©Copyright 2014

Meghana Rawal

Cross-Conjugated Moieties as Design Motifs for a Class of Novel Electro-Optic Chromophores

Meghana Rawal

A dissertation

submitted in partial fulfillment of the

requirements for the degree of

Doctor of Philosophy

University of Washington

2014

Reading Committee:

Larry Dalton, Chair

Samson Jenekhe

Bruce Robinson

Program Authorized to Offer Degree:

Department of Chemistry

University of Washington

Abstract

Cross-Conjugated Moieties as Design Motifs for a Class of Novel Electro-Optic Chromophores

Meghana Rawal

Chair of the Supervisory Committee:
Professor Larry R. Dalton
Department of Chemistry

Organic electro-optic materials are at the forefront of current photonics applications that enable high speed data transmission, micro-scale sensors, and terahertz applications. Typically linearly conjugated push-pull type chromophores are the primary molecules of choice for various second and third order non-linear optical (NLO) applications. However, intra-molecular charge transfer responsible for many NLO properties can take place in molecules through other means such as σ-conjugation, cross-conjugation and omniconjugation as well. In Chapter 2 a study of electronic transitions, excited states and first hyperpolarizibility (β) of a series of molecules with a cross-conjugated bridge functionalized with a dialkylaminobenzene donor on one end and varying strength acceptors on the other end is reported. A lowered excited state dipole moment compared to the ground state dipole was indicated for an asymmetric cross-conjugated molecule with a relatively stronger acceptor confirming that the cross-conjugated bridge does in fact break the over-all molecular dipole into two constituent parts. The primary charge-transfer transition was, however still identified to occur from the donor across the cross-conjugated bridge to the acceptor. X-ray diffraction (XRD) found the molecules to be twisted significantly resulting in further isolation of the highest occupied molecular orbital (HOMO) and the lowest unoccupied

molecular orbital (LUMO). This reduced overlap of the HOMO and the LUMO in cross-conjugated systems may in fact enable independent modulation of donor and acceptor strengths while minimizing unfavorable effects on electronic transitions and dipole moments. Comparison of hyperpolarizabilities with a control molecule found that cross-conjugation did not completely diminish β.

In Chapter 3, a tricyanopyrroline (TCP) type acceptor was substituted on the cross-conjugated molecules to observe the effects of cross-conjugation on the molecular structure, the ground and excited states of the molecules and consequently β. Through XRD the cross-conjugated motif was found to be perpendicular to the conjugated TCP chromophore and the TCP acceptor was twisted out of plane from the donor despite being conjugated to the donor. Further the aromatic substituents on the cross-conjugated side group were found to interact with each other influencing crystal packing. The dihedral twist and the aromatic interactions are indicated as the cause of reduced aggregation behavior. Hyper-Raleigh scattering measurements found the compounds to have β values comparable to their fully conjugated control molecules. The β values were expected to be influenced by the cross-conjugated side groups acting as auxiliary acceptors as well as by the dihedral twist observed in these molecules resulting in larger spatial isolation between the HOMO and LUMO.

In conclusion the use of a cross-conjugated motif by itself (Chapter 2) and in conjunction with a conjugated chromophore (Chapter 3) was studied and found to be useful towards affecting aggregation, solubility and hyperpolarizability of NLO chromophores.

Table of Contents

List of Figures

List of Tables

List of Abbreviations

1,1,2-TCE	1,1,2-trichloroethane
2PF	two photon fluorescence
APC	amorphous polycarbonate
B3LYP	a hybrid DFT functional
BCOG	binary chromophore organic glasses
BLA	bond length alternation
CAM-B3LYP	a range separated DFT functional
$CHCl_3$	chloroform
CPKS	coupled-perturbed Kohn-Sham
CS	charge separated
Cy	cyclohexane
DFG	difference frequency generation
DFT	density functional theory
DMSO	dimethylsulfoxide
DR1	Disperse Red 1, a chromophore with an azo bridge and nitro-benzene acceptor
EO	electro-optic
E_p	electric field poling voltage
$E_T(30)$	empirical solvent polarity parameter
EZ-FTC	chromophore with thiophene bridge and dimethyl-TCF acceptor
GC-MS	gas chromatography-mass spectrometry
HF	Hartree-Fock
HOMO	highest occupied molecular orbital
HRMS (ESI)	high-resolution mass spectrometry (electrospray ionization)
HRS	hyper-Rayleigh Scattering
iso-PDA	*iso*-polydiacetylenes
LUMO	lowest unoccupied molecular orbital
MP2	second-order Møller-Plesset perturbation theory
NLO	nonlinear optics
NMR	nuclear magnetic resonance
OEO	organic electro-optics
PCM	polarizable continuum method
PMMA	polymethyl methacrylate
pNA	para-nitroaniline
SHG	second harmonic generation
TCF	tricyanofuran, a strong electron accepting moiety
TCP	tricyanopyrroline, a strong electron accepting moiety
T_g	glass transition temperature
THF	tetrahydrofuran
TICTOID	twisted intramolecular charge transfer systems

TLM	two-level model
TTF	tetrathiafulvalene
XRD	X-ray diffraction
YLD-124	chromophore with isophorone bridge and CF3-phenyl TCF acceptor
YLD-156	chromophore with thiophene bridge and CF3-phenyl TCF acceptor

Units

µm	micrometer
Å	Angstrom
D	Debye
dB	decibel
Gbit	gigabit
GHz	gigahertz
mm	millimeter
nm	nanometer
ns	nanosecond
pm	picometer
ps	picosecond
THz	terahertz
V	volts

NMR

$CDCl_3$	deuterated chloroform
d	doublet
dd	doublet of doublets
DMSO-d6	deuterated dimethyl sulfoxide
J	coupling constant in Hz
m	multiplet
MHz	megahertz
s	singlet
t	triplet
δ	chemical shift in parts per million

Acknowledgements

Foremost, I would like to thank my advisor Prof. Larry R. Dalton for supporting me and allowing me the opportunity and the freedom to work on projects that interested me. I also thank Dr. Dinesh Patel who was my first mentor in graduate school and his patient yet rigorous mentoring was essential to my conversion from a polymer engineer to an organic chemist.

During my time as a graduate student, many people guided me and sowed seeds of ideas that would later create the basis of some of my thesis work. Dr. Arumugasamy Elangovan provided me with ideas for my first projects in the Dalton lab and his synthetic guidance and confidence in me allowed me the courage to try new ideas. Dr. Bruce Eichinger's expertise in theoretical chemistry, his ability to explain intricate quantum mechanical concepts in simple terms and his enthusiasm towards research were a great resource and an inspiration to me. Dr. Eichinger's theoretical predictions were driving force for most of my research. Working with Prof. Bruce Robinson taught me the elegance of asking simple questions to problems with convoluted solutions. His approach to problem solving was very insightful and showed me a different way of approaching synthetic strategies.

Nathan Sylvain has been an amazing colleague. His bold and creative approach to organic chemistry helped me overcome many synthetic hurdles. Kerry Garret performed all the quantum mechanical calculations presented in this thesis. I am thankful to her for her patience and her rigorous scientific approach towards the theoretical predictions. Prof. David Shelton at the University of Nevada, Las Vegas performed all the hyper-Rayleigh scattering experiments and I am grateful to him for collaborating with us as well as for his time and expertise in the matter. Dr. Denise Bale not only helped me find direction in my work but also painstakingly helped me understand hyper-Rayleigh scattering experiments and data thereof. Crystallographers Evgheni Jucov and Prof. Tatiana Timofeeva from New Mexico Highlands University and Dr. Werner Kaminsky at University of Washington were very instrumental in my understanding of structure property relationships of organic materials.

I'd like to thank Dr. Ilya Kosilkin for being a great friend and a very supportive lab-mate and for encouraging me through all my ups and downs in graduate school. Many important scientific discussions with Andreas Tillack guided my final thesis work and his critical reading

of the many drafts is highly appreciated. Monte-Carlo simulations by Andreas provided an important outlook for my research.

Prof. Phil Sullivan provided many hours of education on the basics of electro-optics and was always eager to explain the fundamentals. Dr. Delwin Elder and Dr. Jinsheng Song provided many valuable scientific discussions on organic synthesis. My research would not have been possible without the excellent work that Dr. Martin Sadelik, Loren Kruse, Dr. Rajan Paranji and Dr. Paul Miller do in our department in the instrumentation labs. Many undergraduates that I mentored contributed indirectly to the work presented here; most notably I'd like to thank Terry Villarreal and George Kimpel for their significant contributions to my research projects and for allowing me the opportunity to both teach and learn from them by constantly asking great questions.

I'd like to thank both old friends from India and new friends I made in Seattle that supported and motivated me including Vikram Nair, Sharbari Dey, Ravi Ravichandran, Elena Wendelyn and Julie Steele. And finally I thank my parents Asha and Dr. Shuban Rawal and my brother Dr. Aditya Rawal for their confidence in me and for always pushing me to follow my ideas!

I have had many wonderful teachers along the way; I am ever in their debt and to them ever grateful.

Dedication

Dedicated to my grandfather Pt. Prem Nath Rawal and my Guru for being my guides through life.

And also to my parents Asha Rawal and Dr. Shuban Kishen Rawal for teaching me to persevere and be independent.

Chapter 1 Introduction

1.1. Objective and Perspective:

The focus of this thesis is the experimental study of cross-conjugated molecules and the potential for the use of cross-conjugated motifs in non-linear optical chromophores. Due to the time and expense involved in the synthesis of novel chromophores, close collaboration between the experimental and theoretical fields of research is essential both for theoretical guidance of design as well as for understanding observed experimental phenomena. This allows for the creation of significantly improved electro-optic materials. Organic electro-optic materials have the potential to become critical components of next generation computer, telecommunication, and sensor technologies. As will be discussed in more detail shortly, organic electro-optic materials offer clear advantages over competing technologies (inorganic electro-optics, inorganic electro-absorptive, organic liquid crystalline technologies, silicon devices based on free-carrier depletion or injection in pn-diode or metal-oxide semiconductor structures) in terms of one or more of the following properties: response time, electro-optic activity, optical loss, and/or processability. Large macroscopic electro-optic activity deriving from large molecular hyperpolarizability has permitted operational voltages required to convert electronic data into data encoded on optical transmissions to be as low as 0.5V for a 1 mm device[1]. Such low voltages permit record energy efficiency of 0.6 femtojoules/bit to be achieved for digital signal transduction[2]. The short device lengths permit low insertion loss and operational bandwidths of 100 Gbit/s to be achieved for digital signals and 100 GHz bandwidths to be achieved for analog signal processing. Compared to the voltage-length parameter ($V\pi$) value of 500 V-mm for 40 Gbit/s lithium niobate devices[3] , organic electro-optic materials currently offer a thousand fold improved $V\pi$ of 0.5 V-mm. Such small voltage-length parameters, made possible by large

electro-optic activity (180 pm/V) of organic materials are critical for chipscale integration of electronics and photonics as well as for nano-antenna sensitivity used in phased array radar and cell phone applications. Continued improvement in electro-optic activity will permit even smaller and more energy efficient devices to be developed and is the fundamental motivation for this thesis research.

Electro-optics is one class of second-order nonlinear optics. Second order nonlinear optics can be broken down into the following effects (classified according to frequency of the applied electric fields):

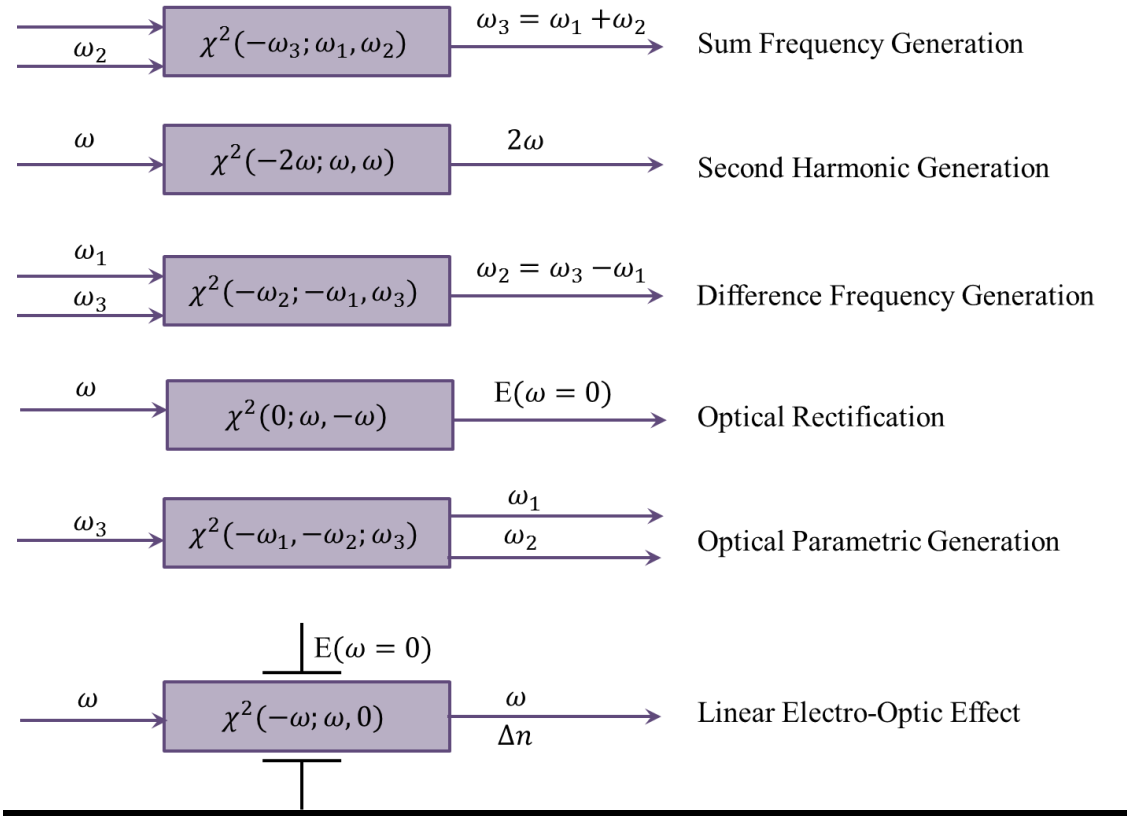

Figure 1.1: A list of second order non-linear effects

While the motivation for this thesis is the potential improvement of organic electro-optic materials it is important to understand other second order effects as these can be used to measure second order nonlinear optical susceptibility. In the subsequent sections of this chapter, a general discussion of nonlinear optics is presented alongside further insights into the importance and impact of organic electro-optic materials to modern information technology.

1.2. Nonlinear Optics

Electro-optics lies at the intersection of electronics and photonics and organic electro-optics (OEO) in particular studies the interaction between electrical (low frequency) and optical (high frequency) electromagnetic fields mediated by an organic material. Nonlinear optics (NLO) focuses on the creation of systems where the optical properties of a material are modified by electrical fields through a nonlinear perturbation of the charge density of the material.

Advances in the field of photonics have led to the use of light to carry data through fiber optic cables for telecommunications. The use of light to transmit data has significantly increased bandwidth and allowed for the possibility of transmission of hundreds of terabits/s of data[4]. Signal processing and transduction have seen tremendous improvements in the last few decades driven by advances in computer chip technology. The doubling of the number of transistors per chip every two years (Moore's Law)[5] has resulted in a large increase in information processing speeds in silicon-based circuits. Silicon devices continue to become smaller and their architectures more complicated while processor chips are becoming more powerful, energy efficient and less expensive[6]. They are however reaching a fundamental physical limit with respect to transistor scaling. As gate length gets smaller, quantum tunneling is likely to occur between the source and drain. Also as the density of transistors per chip and operating speeds increase, the removal of heat from the system is expected to become more problematic resulting

ultimately limiting performance. The use of electro-optic (EO) materials and photonics technology for not only long-range transmission but also for routing information between computer processors and between processors and memory elements would result in greatly improved bandwidths as well as reduced power consumption allowing for less complex processor design. This is an important next step in telecommunications and information technology. Electronic to optical signal transduction is central to the application of this technology and is performed by an EO modulator.

EO modulators are based on the principle of Pockels effect (linear electro-optic effect), which is the change in refractive index of a material due to application of an electric field. The Mach-Zehnder modulator (**figure 1.2**) consists of an optical waveguide made of electro-optic material that is split into two waveguides of equal length and then recombined. One arm is subject to an electric field, which can change the refractive index of the material in that arm. When coherent light is introduced into the waveguide, it travels through one arm unchanged. However, as it travels through the other arm, the change in refractive index causes light to travel more slowly through the material resulting in a phase shift of light in one arm before recombination at the other end. If the appropriate voltage (V_π) is applied to the active arm, a phase shift of π can be introduced resulting in destructive interference of the two beams of light and the modulator creates a binary 0. When no voltage is applied to the active arm, the interference is constructive creating a binary 1; data is thus coded onto a beam of light. Of course, Mach-Zehnder modulators can be used for both analog and digital signal modulation although this simple illustration has focused on digital signal transduction.

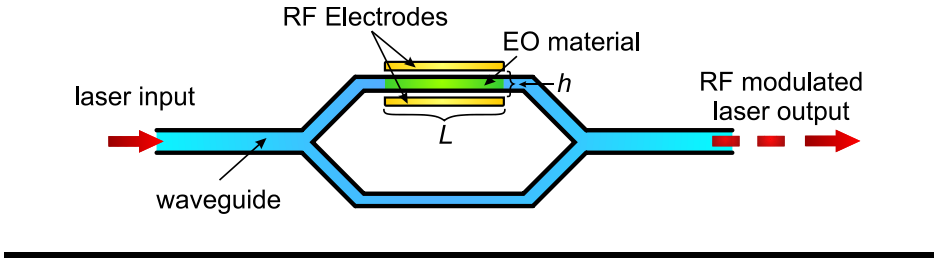

Figure 1.2: Simplified Schematic of a Mach-Zehnder Modulator
(reproduced with permission from Andreas Tillack)

As illustrated in **figure 1.1** of the preceding section, electro-optic (second order nonlinear optical) materials also enable various nonlinear optical processes such as second harmonic generation (SHG) and difference frequency generation (DFG) (*i.e.* terahertz (THz) frequency generation and detection). These are leading to the many applications in the fields of (civilian and military) surveillance, image sensing, detection, etc.

1.3. Materials used for EO applications

Currently most of the materials used for electro-optic applications are inorganic compounds such as crystalline lithium niobate ($LiNbO_3$). As industrial standards, these materials have various advantages such as high optical transparency at the telecommunication wavelengths (0.1-0.2 dB/cm for $LiNbO_3$ at 1.53μm). The Pockels' effect in inorganic materials arises due to displacement of ions within the crystal due to the applied electric field. The speed of response of the material depends on the speed of movement of ions, which is in the region of 10^{-10}s for inorganics and is fairly fast. Another figure of merit for the application of Pockels' effect is the electro-optic tensor r which quantifies the phase shift of light in the active arm with respect to the modulating electric field. For $LiNbO_3$ this coefficient is 30pm/V at 1.3μm which is adequate for long (e.g., centimeter) path-length devices. $LiNbO_3$ devices have high dielectric constants (ε~28) which results in a velocity mismatch between the optical and electrical fields leading to lower bandwidths[3]. The large dielectric permittivity of lithium niobate also reduces gain in

signal-concentrating antennae structures. Drive voltages for $LiNbO_3$ devices are often in the range of 2.8 to 6 V for centimeter devices, which is an impediment (both in terms of energy efficiency and size) for VLSI applications[7,8]. Inorganic materials are typically used as highly polished, optical quality crystals, which require time-consuming and costly processing.

These disadvantages present an opportunity for the replacement of inorganic compounds by organic materials, which have the potential of affording improvements in size, weight, power, performance, cost, and reliability. Many organic EO materials have shown great promise and have been incorporated in electro-optic devices such as ring microresonators and Mach-Zehnder interferometers. Whereas crystalline inorganic modulators are currently working at 40 GHz or less, organic electro-optic modulators with 40-100 GHz bandwidths are already being offered in the market[9].

The bandwidth of organic electro-optic devices is currently limited by the conductivity of metal drive electrodes and bandwidths of 30 THz have been observed in THz signal generation and detection applications. The 10 femtosecond response time of the p-electrons of organic electro-optic materials has also been confirmed by pulsed optical measurements and by all-optical modulation experiments[10]. The advantages of organic modulators over inorganic modulators stem in part from the fact that their EO response results from a distortion in the π electron cloud of the molecules, which occurs in 10^{-14} s as compared to ionic displacement (10^{-10}s) in the case of inorganic devices. Organic materials also allow for better velocity matching of the optical and electric fields due to their low dielectric ($\varepsilon \sim 3$). Through theory-guided design, organic EO materials have steadily improved upon their r values. Numbers as high as 300 pm/V[11] have been reported with 500-1000 pm/V[12] being theoretically possible. Such electro-optic coefficients permit drive voltages (V_π) below 1V for millimeter length devices and thus

allow for organic EO materials to be integrated quite easily into VLSI systems[13]. Organic molecules possess tunable properties that can be designed into the molecular structure such as ease of processability, crosslinking or hydrogen-bonding and liquid crystalline groups to improve performance through soft interactions that are not possible with inorganic crystals.

1.4. Fundamentals of Optical Nonlinearity

1.4.1. Microscopic and Macroscopic Polarization and Electro-Optic Coefficient r_{33}:

In order to understand the origins of nonlinear optical effects one must delve into the influence of an intense electromagnetic field (such as a laser) on the polarization response of these materials. The polarization response of nonlinear materials is defined both micro- and macroscopically; **p** and **P** respectively are described by the following power series expansions of the electric field:

$$p = p_0 + \alpha_{ij}E_j + \beta_{ijk}E_jE_k + \gamma_{ijkl}E_jE_kE_l + \cdots \quad (1)$$

$$P = P_0 + \chi_{ij}^{(1)}E_j + \chi_{ijk}^{(2)}E_jE_k + \chi_{ijkl}^{(3)}E_jE_kE_l + \cdots \quad (2)$$

In equation (1) the term p_0 is the polarization at zero field, α_{ij} is the linear polarizibility and the terms β_{ijk} and γ_{ijkl} are the first and second order molecular hyperpolarizibilities. Higher order terms beyond γ_{ijkl} are negligible and are ignored. The β tensor describes second order processes such as Pockels effect (EO), sum frequency generation (SFG) and difference frequency generation (DFG) (see **figure 1.1**). In this thesis, we ignore $\gamma_{ijkl}$and higher order effects.

Similarly, in equation (2), P_0 is the intrinsic bulk polarization, $\chi_{ij}^{(1)}$is the linear optical susceptibility and $\chi_{ijk}^{(2)}$ and $\chi_{ijkl}^{(3)}$ are the second order and third order nonlinear optical susceptibilities respectively. In both equations, E_j, E_k and E_l are vectors of the applied electric field within the molecular framework.

In equation (1), all even terms become zero for molecules in which polarization in either direction of the molecular axis is equal and opposite. This is the case for centrosymmetric molecules whose β is therefore zero. For a molecule to exhibit any second order effects, it must possess a non-zero β which is induced by possessing a non-centrosymmetric molecular electronic structure. An example of such a chromophore is shown in **figure 1.3**. The basic motif in these molecules is an electron donor-π bridge- electron acceptor type structure and the dominant tensor element of the first hyperpolarizability β_{zzz} is along the molecular dipolar axis.

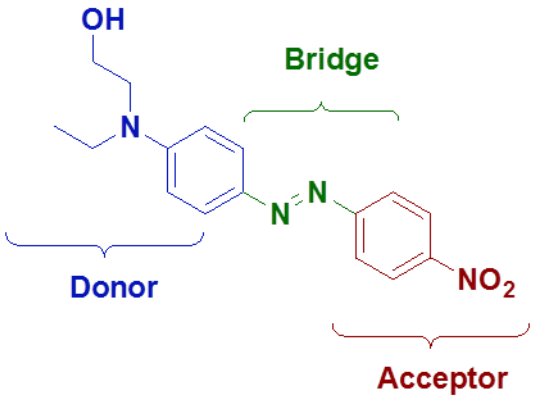

Figure 1.3: Structure of Disperse Red 1 (DR1) chromophore

At the bulk level, the material must also be ordered anisotropically for the second order susceptibility $\chi_{ijk}^{(2)}$ to be non-zero. Since they are designed as donor-π-acceptor systems, most chromophores are highly dipolar in nature and centrosymmetric dipole-dipole interactions are favored in the bulk phase between chromophores. They are therefore only weakly acentrically aligned in the bulk phase. Therefore their order parameter $< cos^3\theta >$ which indicates the degree of non-centrosymmetric alignment along the z direction will be low. A few other factors also affect χ^2 under bulk conditions. Most devices are made by preparing an NLO chromophore guest-polymer host solution followed by a film forming process such as spin casting. As would be expected therefore, the number density (N) of chromophores in the polymer matrix is important as is the dielectric of the surrounding medium, in this case the polymer and the Lorentz-Onsager field factor $f(\omega)$ takes this into account.

The term r_{33}, known as the EO response coefficient ties together all the molecular parameters and can be understood as the control of the index of refraction of a material by application of a voltage. The application of an electric field causes a change in the charge distribution of a molecule thereby causing a change in the velocity of light propagating through it. In the bulk, randomly ordered chromophores will cause this effect to cancel out as the light propagates through the material. However if all the molecules are ordered anisotropically then the effect will be augmented as light travels from chromophore to chromophore through the material. r_{33} is defined as follows:

$$r_{33}(\omega) = \frac{-2\chi_{zzz}^2}{\eta_\omega^4} = \left|\frac{2Nf(\omega)\beta_{zzz}(\omega,\varepsilon) < cos^3\theta >}{\eta_\omega^4}\right| \qquad (3)$$

Where N is the chromophore number density (molecules/cm^3), $f(\omega)$ is the Lorentz-Onsager local field factor (at operating frequency ω) that accounts for change in applied field due to the dielectric of the media surrounding the chromophores and η_ω is the refractive index of the material. The degree of acentric alignment of the chromophore in the matrix is given by the order parameter $< cos^3\theta >$ where θ is the angle between the axis of the molecular dipole and the poling axis.

1.4.2. Structure Property Relationships for Electro-Optic Effect r_{33}

1.4.2.1. Optimizing β_{zzz}: Modifying Donors, Acceptors and Bridges

As inferred from equation (4), one way to optimize r_{33} would be to design and chromophores with higher molecular hyperpolarizibility (β_{zzz}) values. Oudar and Chemla[14] in 1977 developed the two-level model (TLM) to determine theoretically the total β of a given molecule. They found that enhanced β occurs due to intra-molecular charge transfer between the electron donor on one end and the electron acceptor on the other end of the molecule and could be described by a two-level system in which the ground and first excited states are influential. The ground and excited state dipole moments μ_{gg} and μ_{ee}, the transition dipole moment μ_{ge} (which is related to the oscillator strength) and the molecular bandgap ΔE_{ge} (energy difference between highest occupied molecular orbital (HOMO) and lowest unoccupied molecular orbital (LUMO) levels of the molecule influence β. This relationship is given by equation (5) which is known as the two level charge-transfer model, where

$$\beta_{zzz} \propto \frac{(\mu_{ee} - \mu_{gg})(\mu_{ge})^2}{(\Delta E_{ge})^2} \qquad (5)$$

Strong donors typically increase the energy of the HOMO whereas strong acceptors decrease the energy of the LUMO. In either case, this leads to a reduction in ΔE_{ge} thereby increasing β. Indeed strong donor (arylamines and triarylamines) and strong acceptor (2-(dicyanomethylene)-2,5-dihydro-4,5,5-trimethylfuran-3-carbonitrile (dimethyl-TCF) and 2-(dicyanomethylene)-2,5-dihydro-4-methyl-5-oxo-1H-pyrrole-3-carbonitrile (TCP)) moieties are typically part of the structure of some of the current high β molecules that have been developed (**figure 1.4**). The drawback however, is that lowering of the band gap results in a bathochromic shift of the maximum absorption wavelength of the molecule. As this wavelength approaches telecommunication wavelengths (1310nm and 1550nm), absorptive losses within the electro-optic device become significant. Modification of the bridge by increasing the conjugation length (polyene type bridge) also leads to higher hyperpolarizibilities (via reduction in band gap). As the bridge length increases, however, it reduces the photo- and thermal stability of the molecule. This is overcome by using ring-locked (CLD type and substituted) isophorone bridges[13,12,15,16,17] as seen in YLD-124. Heteroaromatic thienyl-vinylene bridges (FTC type)[16,18,19] as seen in YLD-156 and EZ-FTC offer high thermal and photostability without significant loss in β along with relatively easier syntheses (**figure 1.4**). Thiophene moieties also offer a point of substitution for further modification of the chromophore. These organic molecules can be modified not only towards the goal of higher β but also towards other favorable properties such as better photo-, thermal-, and temporal stability, reduction of optical loss at telecommunication wavelengths and much improved processability[15,20, 21,22].

Although great strides have been made in the improvement of β by this method, there is still a gap between the quantum limit and the experimentally observed hyperpolarizibilities that must be bridged[23].

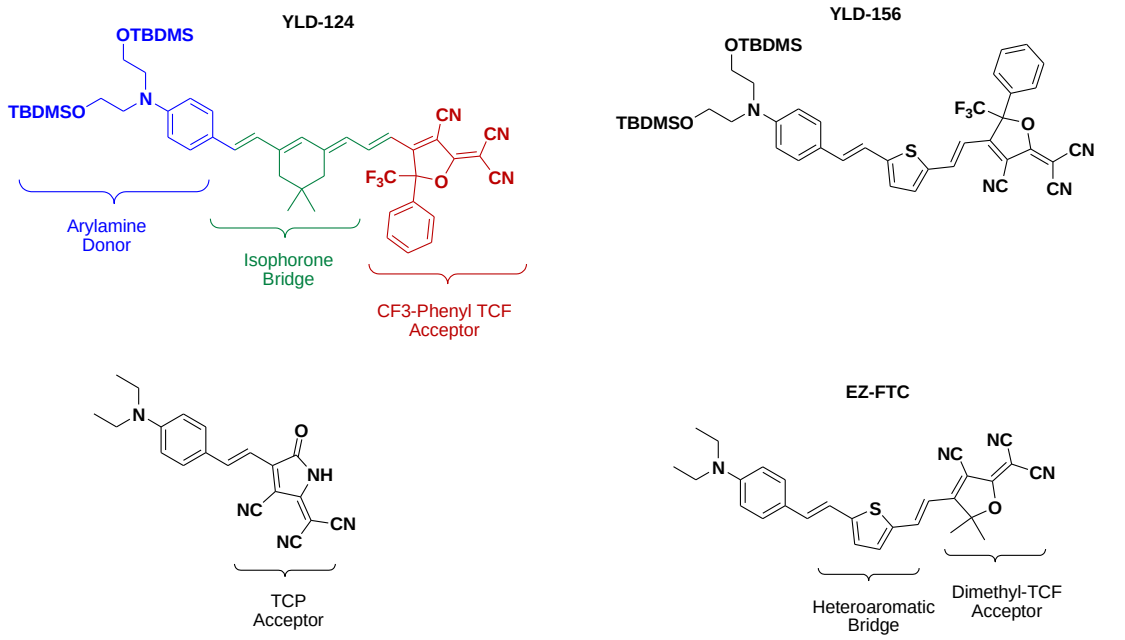

Figure 1.4: Molecular structures of some important chromophores in electro-optics

1.4.2.2. Alternate strategies towards improving β: Bond Length Alternation Theory

Polyene chromophores consisting of π-conjugated bridges are the mainstay of organic EO chromophores. As discussed in the previous section, their modification by changing the length and chemical composition has a significant effect on the molecular hyperpolarizibility of the molecule. The bridge connects the donor and acceptor within the molecule plays a role in determining the degree of charge separation in the ground state of the molecule which is essential to the understanding of β. Bond length alternation (BLA) has furthered the realization of the structure-property relationships within polyene molecules and the use of optimal donor and acceptor strengths for a given bridge[24–27].BLA parameter $< \Delta r >$ is defined as the average difference in length between adjacent carbon-carbon bonds of a molecule. In the case of conjugated bridges these adjacent bonds are alternating single and double bonds[24]. For the

simplest case the BLA is calculated as $1.45\text{Å} - 1.34\text{Å} = +0.11\text{Å}$ which is the largest positive $< \Delta r >$ possible. Marder and coworkers used this parameter to explain why increasing the donor and acceptor strengths for a given bridge does not always increase molecular hyperpolarizibilities[24–29]. They used the sum-over-states model to observe the effect of an external static field on a simple donor-acceptor molecule, 9-(dimethylamino)nona-2,4,6,8-tetraenal (DAO) with a polyene bridge (**figure 1.5**) and the resulting change in hyperpolarizibility[30]. The change in electric field would effectively simulate the change in the strength of the donor and acceptor. They proposed that for weak values of donor and acceptor strengths, the ground state was neutral (**figure 1.5, (*left*) structure (a)**) and $< \Delta r >$ large (~0.1Å). This implies that since the large difference in energy between the two resonance states results in very little mixing of the two states. Therefore, even though $(\mu_{ee} - \mu_{gg})$ would be high, β values would be small due to high ΔE_{ge}.

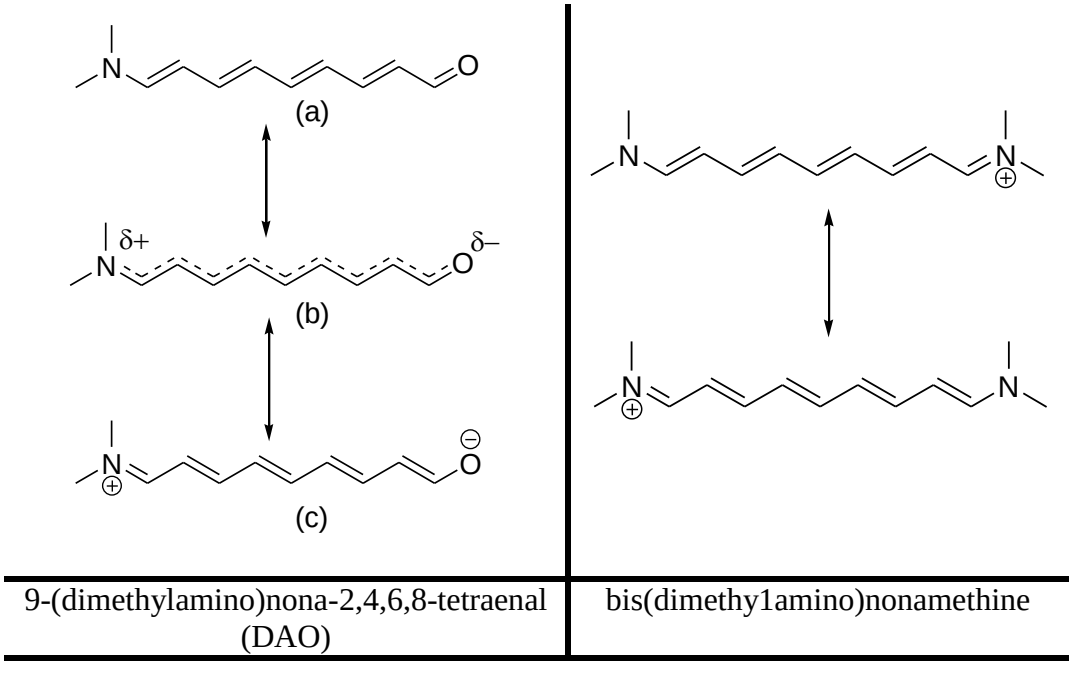

Figure 1.5: *(left)* The molecule used to study the change in BLA with donor and

acceptor strengths. *(right)* Example of a cyanine type molecule with two degenerate resonance structures

As the strengths of the donor and acceptors increased, BLA decreased causing a reduction in ΔE_{ge} due to increased mixing of the resonance states thereby increasing β. In other words, initially as the contribution of the charge separated resonance structure to the ground state increased, β increased until it peaked at an optimum BLA parameter (in this case $< \Delta r >$~0.04Å). As the contribution of the two resonance forms to the ground state becomes equivalent, BLA becomes zero. This however translates to a zero β value as well since the term $(\mu_{ee} - \mu_{gg})$ becomes zero due to degeneracy of the two states. This trend is shown in **figure 1.6** below[24]. This limit at which BLA becomes zero is known as the cyanine limit after the cyanine type molecules that are represented by two degenerate resonance forms (**figure 1.5 (*right*)**).

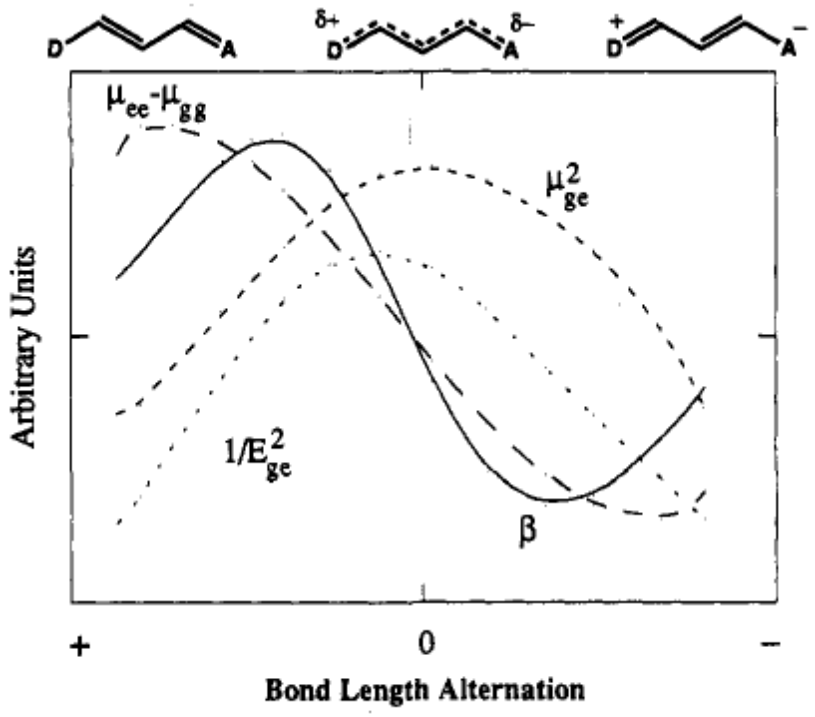

Figure 1.6: Dependence of β (−),$\mu_{ee} - \mu_{gg}$ (− − −), μ^2_{ge} (---) and $1/\Delta E^2_{ge}(\cdots)$ on bond length alternation

On the other side of the cyanine limit, the charge separated state dominates the ground state while the neutral state has higher energy. Such molecules are categorized as "zwitterionic ground state" molecules and their ground states are more polar than their excited states. This leads to a negative BLA with an increase in β in the negative direction where it once again reaches a maximum (negative) value at optimal $< \Delta r >$.

Molecular hyperpolarizability can thus be influenced and tuned to large values by changing the relative contribution of the neutral form or the charge separated form to the ground state.

1.4.2.3. Alternate strategies towards improving β: Twisted intramolecular charge transfer (TICTOID) structures:

Theory has also predicted that the degree of the HOMO-LUMO orbital overlap between donor and acceptor to be dependent on the twist angle with the optimal dihedral angle (θ) being 70°-85°[31]. The dihedral angle between the donor and acceptor parts of these molecules serves to modulate the magnitude of the response by changing the nature of the bond between quinoid and aromatic states. Quinopyran and merocyanine type twisted intramolecular charge transfer (TICTOID) type structures have been shown to demonstrate some of the largest non-linear responses to date. The molecules are reported to show high μβ values of -488000 x 10-48 esu (at 1907nm) compared to that of CLD (35000 x 10-48esu at 1907nm). They also however possess large ground state dipole moments in the region of 50D[32]. While this results in significant aggregation and solubility issues, never the less r_{33} values of 300 pm/V (Teng-Man at 1.33 microns, Ep = 100V/micron) have been reported. The biggest drawback for these molecules however is aggregation caused by the high dipoles in the aromatic states. An increase in the first order molecular hyperpolarizability by modification of the π orbital strengths and overlap

typically results in high dipole moments (13-30 Debye and as high as 50.6 Debye for the TICT chromophores).

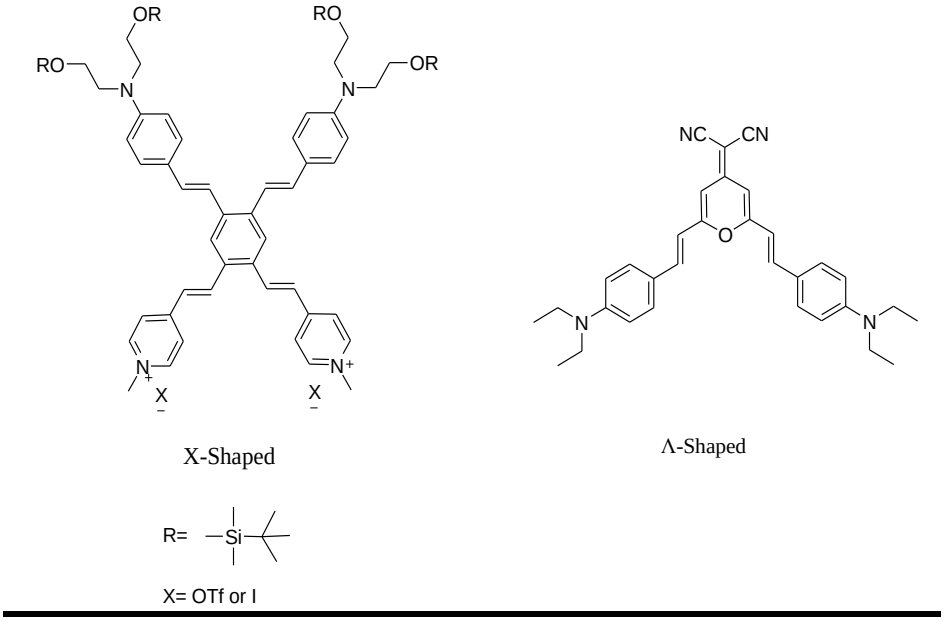

Figure 1.7: Examples of X- and λ–shaped molecules

While a large body of research is based on one dimensional (1D) dipolar chromophores described above, multiple donor/acceptor substitution creates X- and λ–shaped molecules (**figure 1.7**) with a two dimensional β tensor character[33]. In most dipolar molecules, an increase in β, brought about by increasing donor/acceptor strengths or increasing bridge length, inevitably leads to a bathochromic shift of the charge transfer band. Two dimensional and multipolar strategies become relevant when the trade-off between nonlinearity and transparency becomes important[34] since these compounds combine larger molecular non-linearities with hypsochromic shifts of the charge transfer band relative to corresponding control (1D) molecules. It has been shown that the larger β associated with X-shaped chromophores is possibly related to maximum conjugation of the two donor groups and the two acceptor groups respectively and larger spatial

asymmetry between the HOMOs and the LUMOs to promote charge transfer in the excited state[35]. Second harmonic generation (SHG) is an example of such an application where the conversion of light to its second harmonic frequency must be efficient but reabsorption of the generated frequency must be low

1.4.2.4. Optimizing Loading Parameter ($N < cos^3\theta >$)

While considerable attention has been paid to the prediction, understanding and improvement of β_{zzz}, this has not translated into equivalent gains in terms of macroscopic properties. High dipole moments in organic NLO materials result in strong electrostatic dipole-dipole interactions which prevent the molecules from ordering non-centrosymmetrically. Improving the acentric order ($< cos^3\theta >$) or more accurately the loading parameter ($N < cos^3\theta >$) of the current organic NLO materials would be advantageous for commercializing these systems. One must recognize however that the two terms N and ($< cos^3\theta >$) are interdependent as an increase in the number density causes increased dipolar interactions between chromophores and making the realization of improved $< cos^3\theta >$ more difficult.

Attempts at increasing the loading parameter fall into two categories: (1) processing methods such as electric field poling and laser assisted electric field poling and (2) variation in the chromophore structure towards either reduced dipole-dipole interactions or introduction of soft interactions that direct acentric order.

Electric field poling is one of the most commonly used methods for inducing order. In this technique, the NLO active material is spun cast (neat or in a polymer host) on to a glass slide followed by vapor deposition of gold electrodes. This device is heated to and held at just below the glass transition temperature (T_g) of the polymer to soften the matrix followed by application of a strong electric field of voltage E_p. The soft matrix allows the chromophores to align with the

applied field and the device is then cooled in the presence of the electric field to preserve the order achieved. The efficiency of this poling method is measured as a ratio of r_{33} obtained to the electric field applied $E_{p.}$ Current work in our group shows the highest poling efficiency (r_{33}/E_p) for a guest/host system of a chromophore guest at 25 wt.% loading in a polymethyl methacrylate (PMMA) host to be approximately 1.5 nm^2/V^2.

Laser assisted electric field poling utilizes the cis-trans photoisomerization of low β azo-chromophores such as Disperse Red 1 (DR1) to induce order in a higher β chromophore such as YLD-124. Up to 2.5 fold increase in poling efficiencies have been reported with this technique as compared to electric field poling[36].

The concept of shape engineering of chromophores takes into account that the design of the chromophore itself not only affects β_{zzz} but also the electrostatic interactions between chromophores. Substitution of bulky side groups onto a chromophore bridge has shown to reduce chromophore dipole-dipole interactions resulting in improved electro-optic activity[37]. Isolation of chromophores by attachment of dendritic[38,39] units changes the shape of the molecule towards more spherical dimensions. This strategy has been employed with significant success towards improving poling efficiencies. In an approach similar to dendronized chromophores, multi-chromophore dendrimer systems are molecules in which multiple chromophores are attached to a single dendritic core[16,24,40–42]. Dendritic NLO systems easily exhibit high poling efficiencies and are often cast as neat films with high number densities[43–45] as high as ~ 6x 10^{20} molecules/cm^3. These materials have also been designed to exhibit high thermal stability[46] and by substituting with photo-crosslinkable groups, highly improved temporal stability[44,46].

Dendronized polymers[18] and hyper-branched polymers[41,44,45] are another class of shape engineered molecules that have resulted in an improvement of poling efficiencies 2 to 2.5 times

higher than guest-host systems. These polymeric systems also allow for improvement of thermal and temporal properties.

Introduction of soft interactions such as hydrogen bonding[47,48], aryl-fluoroaryl interactions[11], liquid crystalline mesogens[49–53] and as binary chromophore organic glasses[54,55] (BCOG) help increase the concentration of the chromophore (N) in the bulk and can even enhance $< cos^3\theta >$. In these materials, a competing interaction is introduced into the bulk system to induce a reduction in dimensionality (degrees of freedom) of the material. Enhancements in efficiencies of as high as 3 times that of chromophores in simple polymeric materials have been reported[12,50,56].

1.5. References

(1) Leuthold, J.; Koos, C.; Freude, W.; Alloati, L.; Palmer, R.; Korn, D.; Pfeifle, J.; Lauermann, M.; Dinu, R.; Wehrli, S.; Jazbinsek, P.; Gunter, P.; Waldow, M.; Wahlbrink, T.; Bolten, J.; Fedeli, J.-M.; Yu, H.; Bogaerts, W. *J. Sel. Top. Quantum Electron.* **2013**, *19*, 3401413.

(2) Koos, C.; Leuthold, J.; Freude, W. *Nat. Photonics* **2010**, *4*, 583–584.

(3) EOSPACE Electro-Optic Modulators, Switches and Custom Integrated Optical Circuits http://www.eospace.com/product_index.htm.

(4) Hecht, J. Ultrafast fibre optics set new speed record http://www.newscientist.com/article/mg21028095.500-ultrafast-fibre-optics-set-new-speed-record.html#.Uk35lIasim5.

(5) Moore, G. E. *Electronics*. 1965, p. 4.

(6) Bohr, M.; Mistry, K. Intel's Revolutionary 22nm Transistor Technology http://www.intel.com/content/www/us/en/silicon-innovations/revolutionary-22nm-transistor-technology-presentation.html.

(7) Agere Systems Data Sheet LiNbO3 Modulators http://www.lightwavestore.com/product_datasheet/OSC-MOD-10Gb-011C_pdf1.pdf.

(8) Lucent Technologies Product Definition Sheet http://www.oocities.org/electroabsorption/eam/linbo3-40gbps-lucent.pdf.

(9) Gigoptix Modulator http://www.gigoptix.com/products/17-tfps-mach-zehnder-modulators.

(10) Koos, C.; Vorreau, P.; Vallaitis, T.; Dumon, P.; Bogaerts, W.; Baets, R.; Esembeson, B.; Biaggio, I.; Michinobu, T.; Diederich, F.; Freude, W.; Leuthold, J. *Nat. Photonics* **2009**, *3*, 216–219.

(11) Kim, T.-D.; Kang, J.-W.; Luo, J.; Jang, S.-H.; Ka, J.-W.; Tucker, N.; Benedict, J. B.; Dalton, L. R.; Gray, T.; Overney, R. M.; Park, D. H.; Herman, W. N.; Jen, A. K.-Y. *J. Am. Chem. Soc.* **2007**, *129*, 488–489.

(12) Dalton, L. R.; Sullivan, P. A.; Bale, D. H.; Olbricht, B. C. *Solid-State Electron.* **2007**, *51*, 1263–1277.

(13) Shi, Y.; Zhang, C.; Zhang, H.; Bechtel, J. H.; Dalton, L. R.; Robinson, B. H.; Steier, W. H. *Science* **2000**, *288*, 119–122.

(14) Oudar, J. L.; Chemla, D. S. *J. Chem. Phys.* **1977**, *66*, 2664–2668.

(15) Sullivan, P. A.; Dalton, L. R. *Acc. Chem. Res.* **2010**, *43*, 10–18.

(16) Zhang, C.; Dalton, L. R.; Oh, M.-C.; Zhang, H.; Steier, W. H. *Chem. Mater.* **2001**, *13*, 3043–3050.

(17) Zhang, C. H.; Todorova, G.; Wang, C.; Londergan, T.; Dalton, L. R. In *Proceedings of SPIE*; 2000; Vol. 4114, pp. 77–87.

(18) Liao, Y.; Anderson, C. A.; Sullivan, P. A.; Akelaitis, A. J. P.; Robinson, B. H.; Dalton, L. R. *Chem Mater* **2006**, *18*, 1062–1067.

(19) Dalton, L. R.; Sullivan, P. A.; Olbricht, B. C.; Takimoto, Y.; Rehr, J. J.; Eichinger, B. E.; Mistry, A. A.; Bale, D.; Rommel, H.; Robinson, B. In *Proceedings of SPIE*; Noginov, M. A.; Zheludev, N. I.; Boardman, A. D.; Engheta, N., Eds.; 2007; p. 66380I–66380I–9.

(20) Prasad, P. N.; Williams, D. J. *Introduction to nonlinear optical effects in molecules and polymers*; Wiley, 1991.

(21) Dalton, L. R.; Lao, D.; Olbricht, B. C.; Benight, S.; Bale, D. H.; Davies, J. A.; Ewy, T.; Hammond, S. R.; Sullivan, P. A. *Opt. Mater.* **2010**, *32*, 658–668.

(22) Pereverzev, Y. V.; Gunnerson, K. N.; Prezhdo, O. V.; Sullivan, P. A.; Liao, Y.; Olbricht, B. C.; Akelaitis, A. J. P.; Jen, A. K.-Y.; Dalton, L. R. *J. Phys. Chem. C* **2008**, *112*, 4355–4363.

(23) Tripathy, K.; Moreno, J. P.; Kuzyk, M. G.; Coe, B. J.; Clays, K.; Kelley, A. M. *J. Chem. Phys.* **2004**, *121*, 7932–7945.

(24) Bourhill, G.; Bredas, J.-L.; Cheng, L.-T.; Marder, S. R.; Meyers, F.; Perry, J. W.; Tiemann, B. G. *J. Am. Chem. Soc.* **1994**, *116*, 2619–2620.

(25) Marder, S. R.; Beratan, D. N.; Cheng, L.-T. *Science* **1991**, *252*, 103–106.

(26) Marder, S. R.; Perry, J. W.; Bourhill, G.; Gorman, C. B.; Tiemann, B. G.; Mansour, K. *Science* **1993**, *261*, 186–189.

(27) Marder, S. R.; Cheng, L.-T.; Tiemann, B. G.; Friedli, A. C.; Blanchard-Desce, M.; Perry, J. W.; Skindhøj, J. *Science* **1994**, *263*, 511–514.

(28) Marder, S. R.; Gorman, C. B.; Tiemann, B. G.; Cheng, L. T. *J. Am. Chem. Soc.* **1993**, *115*, 3006–3007.

(29) Marder, S. R.; Gorman, C. B.; Meyers, F.; Perry, J. W.; Bourhill, G.; Bredas, J.-L.; Pierce, B. M. *Science* **1994**, *265*, 632–635.

(30) Meyers, F.; Marder, S. R.; Pierce, B. M.; Bredas, J. L. *J. Am. Chem. Soc.* **1994**, *116*, 10703–10714.

(31) Keinan, S.; Zojer, E.; Bredas, J.-L.; Ratner, M. A.; Marks, T. J. *J. Mol. Struct. THEOCHEM* **2003**, *633*, 227–235.

(32) Kang, H.; Facchetti, A.; Jiang, H.; Cariati, E.; Righetto, S.; Ugo, R.; Zuccaccia, C.; Macchioni, A.; Stern, C. L.; Liu, Z.; Ho, S.-T.; Brown, E. C.; Ratner, M. A.; Marks, T. J. *J. Am. Chem. Soc.* **2007**, *129*, 3267–3286.

(33) Kang, H.; Evmenenko, G.; Dutta, P.; Clays, K.; Song, K.; Marks, T. J. *J. Am. Chem. Soc.* **2006**, *128*, 6194–6205.

(34) Kang, H.; Zhu, P.; Yang, Y.; Facchetti, A.; Marks, T. J. *J Am Chem Soc* **2004**, *126*, 15974–15975.

(35) Kinnibrugh, T.; Bhattacharjee, S.; Sullivan, P.; Isborn, C.; Robinson, B. H.; Eichinger, B. E. *J Phys Chem B* **2006**, *110*, 13512–13522.

(36) Olbricht, B. C.; Sullivan, P. A.; Wen, G.-A.; Mistry, A. A.; Davies, J. A.; Ewy, T. R.; Eichinger, B. E.; Robinson, B. H.; Reid, P. J.; Dalton, L. R. *J. Phys. Chem. C* **2008**, *112*, 7983–7988.

(37) Hammond, S. R.; Clot, O.; Firestone, K. A.; Bale, D. H.; Lao, D.; Haller, M.; Phelan, G. D.; Carlson, B.; Jen, A. K.-Y.; Reid, P. J.; Dalton, L. R. *Chem. Mater.* **2008**, *20*, 3425–3434.

(38) Ma, H.; Liu, S.; Luo, J.; Suresh, S.; Liu, L.; Kang, S. h.; Haller, M.; Sassa, T.; Dalton, L. r.; Jen, A. k.-Y. *Adv. Funct. Mater.* **2002**, *12*, 565–574.

(39) Luo, J.; Ma, H.; Haller, M.; Jen, A. K.-Y.; Barto, R. R. *Chem. Commun.* **2002**, 888–889.

(40) Bale, D. H.; Eichinger, B. E.; Liang, W.; Li, X.; Dalton, L. R.; Robinson, B. H.; Reid, P. J. *J. Phys. Chem. B* **2011**, *115*, 3505–3513.

(41) Robinson, B. H.; Dalton, L. R. *J. Phys. Chem. A* **2000**, *104*, 4785–4795.

(42) Sullivan, P. A.; Bhattacharjee, S.; Eichinger, B. E.; Firestone, K. A.; Robinson, B. H.; Dalton, L. R. In *Proceedings of SPIE*; 2004; Vol. 5351, pp. 253–259.

(43) Sullivan, P. A.; Rommel, H.; Liao, Y.; Olbricht, B. C.; Akelaitis, A. J. P.; Firestone, K. A.; Kang, J.-W.; Luo, J.; Davies, J. A.; Choi, D. H.; Eichinger, B. E.; Reid, P. J.; Chen, A.; Jen, A. K.-Y.; Robinson, B. H.; Dalton, L. R. *J. Am. Chem. Soc.* **2007**, *129*, 7523–7530.

(44) Ma, H.; Chen, B.; Sassa, T.; Dalton, L. R.; Jen, A. K.-Y. *J. Am. Chem. Soc.* **2001**, *123*, 986–987.

(45) Gopalan, P.; Katz, H. E.; McGee, D. J.; Erben, C.; Zielinski, T.; Bousquet, D.; Muller, D.; Grazul, J.; Olsson, Y. *J. Am. Chem. Soc.* **2004**, *126*, 1741–1747.

(46) Sullivan, P. A.; Olbricht, B. C.; Akelaitis, A. J. P.; Mistry, A. A.; Liao, Y.; Dalton, L. R. *J. Mater. Chem.* **2007**, *17*, 2899–2903.

(47) Zhu, P.; Kang, H.; Facchetti, A.; Evmenenko, G.; Dutta, P.; Marks, T. J. *J. Am. Chem. Soc.* **2003**, *125*, 11496–11497.

(48) Facchetti, A.; Annoni, E.; Beverina, L.; Morone, M.; Peiwang Zhu; Marks, T. J.; Pagani, G. A. *Nat. Mater.* **2004**, *3*, 910–917.

(49) Benight, S. J.; Bale, D. H.; Olbricht, B. C.; Dalton, L. R. *J. Mater. Chem.* **2009**, *19*, 7466–7475.

(50) Benight, S. J.; Johnson, L. E.; Barnes, R.; Olbricht, B. C.; Bale, D. H.; Reid, P. J.; Eichinger, B. E.; Dalton, L. R.; Sullivan, P. A.; Robinson, B. H. *J. Phys. Chem. B* **2010**, *114*, 11949–11956.

(51) Dalton, L. R.; Benight, S. J.; Johnson, L. E.; Knorr, D. B.; Kosilkin, I.; Eichinger, B. E.; Robinson, B. H.; Jen, A. K.-Y.; Overney, R. M. *Chem. Mater.* **2011**, *23*, 430–445.

(52) Grote, J. G.; Dalton, L. R.; Sullivan, P.; Robinson, B. H.; Eichinger, B.; Jen, A. K.-Y.; Benight, S.; Kosilkin, I.; Bale, D. H. *Nonlinear Opt. Quantum Opt. Concepts Mod. Opt.* **2010**, *40*, 15–26.

(53) Koch, A. T. H.; Fridrikh, S. V.; Warner, M.; Schwarzwälder, C. E.; Moratti, S. C.; Friend, R. H. *Synth. Met.* **1999**, *101*, 244 – 245.

(54) Kim, T.-D.; Luo, J.; Cheng, Y.-J.; Shi, Z.; Hau, S.; Jang, S.-H.; Zhou, X.-H.; Tian, Y.; Polishak, B.; Huang, S.; Ma, H.; Dalton, L. R.; Jen, A. K.-Y. *J. Phys. Chem. C* **2008**, *112*, 8091–8098.

(55) Halter, M.; Liao, Y.; Plocinik, R. M.; Coffey, D. C.; Bhattacharjee, S.; Mazur, U.; Simpson, G. J.; Robinson, B. H.; Keller, S. L. *Chem. Mater.* **2008**, *20*, 1778–1787.

(56) Yang, Z.; Mutter, L.; Stillhart, M.; Ruiz, B.; Aravazhi, S.; Jazbinsek, M.; Schneider, A.; Gramlich, V.; Günter, P. *Adv. Funct. Mater.* **2007**, *17*, 2018–2023.

Chapter 2 Study of Cross Conjugated Systems

2.1 **Introduction:**

In the field of non-linear optics, linearly conjugated push-pull type chromophores are the primary motifs of choice for various second and third order applications. The ground state and the excited state configurations, the transition dipole moment and the energy gap between the two states are of consequence in defining the non-linear properties of such molecules. It has been hypothesized and observed in many cases however, that charge transfer can occur in molecules through other means such as σ-conjugation through sp^3 carbons, cross-conjugation and omni-conjugation[57]. Cross-conjugated frameworks (**figure 2.1**) especially are seen extensively in molecules comprising dendralenes (**1**), benzoquinonedimethanes (**2**), radialenes (**3**), fulvalenes (**4**), azulenes (**5**) etc. The term "cross-conjugation" typically refers to molecules that contain three groups, two of which are conjugated to the third but not to each other. Cross-conjugation has, however, come to cover molecules where this definition is not strictly applied; e.g. fulvalenes, where the cyclic structure creates conjugation between the two groups that would otherwise not be connected.

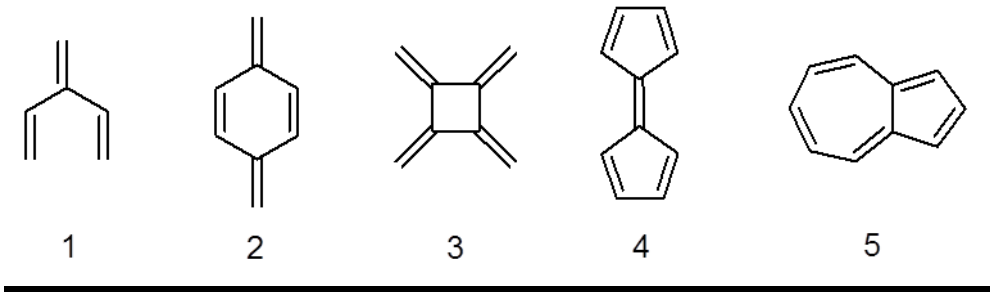

Figure 2.1: Various cross-conjugated motifs

The effect of broken conjugation and cross-conjugation on the molecular first and second hyperpolarizibilities, β and γ has been studied by several groups in the past. Theoretical calculations led by the Brédas and Marder[58] groups investigated the relationship between the length of a saturated spacer group in a push-pull polyene chromophore and the degree of π-conjugation on molecular hyperpolarizibilities. It was reported that charge transfer did indeed occur at a certain applied external field from the donor to the acceptor and larger spacer groups (two carbons long) caused more abrupt charge transfers resulting in large predicted β values. In 2000, Brédas and coworkers[59] published theoretical and experimental work on oligo vinylthiophenes in which an electron donating segment and an electron withdrawing segment were separated by various spacers in the bridge to gauge the modulation of charge transfer by the spacers.

A study of [3]dendralenes by Almenningen and coworkers[60] showed that these molecules do not adopt a planar conformation as would be expected for the molecules to maintain a conjugated network. The molecules were revealed to exist in an anti, skew conformation with a dihedral angle of 40°. Ultra violet-visible (UV-vis) spectroscopy study of [3]dendralenes oligomers by Grubbs and Swager[61] also pointed to a twisted backbone with the largest conjugation length consisting of a triene unit. Increasing the length of the polymer did not significantly influence the absorbance spectra of the molecules.

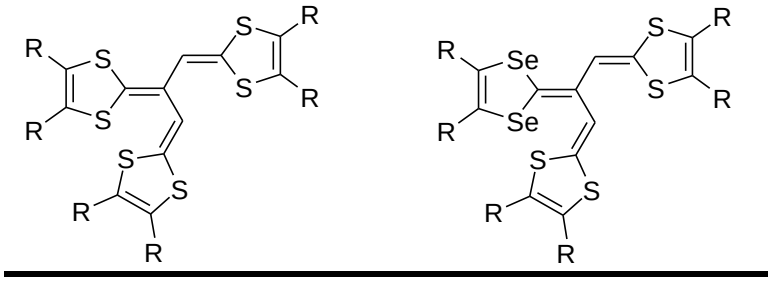

Figure 2.2: Tetrathiafulvalene vinylogs

Various tetrathiafulvalene [TTF] analogues of dendralenes (**figure 2.2**) have also been studied by Cava and coworkers and found to be strong electron donating groups[62]. Studies by Bryce and coworkers found dendralene based TTF molecules also to be slightly twisted with little electron delocalization along the main backbone[63].

Diederich and coworkers reported on the synthesis and electronic characterization of a series of cross-conjugated dicyanovinyl substituted 2,3-diphenyl-1,4-butadiene derivatives (**figure 2.3**) in which they found efficient intramolecular charge transfer interactions and high third order non-linear responses[64,65] in spite of a substantial twist[66] between the two adjacent dicyanovinyl groups.

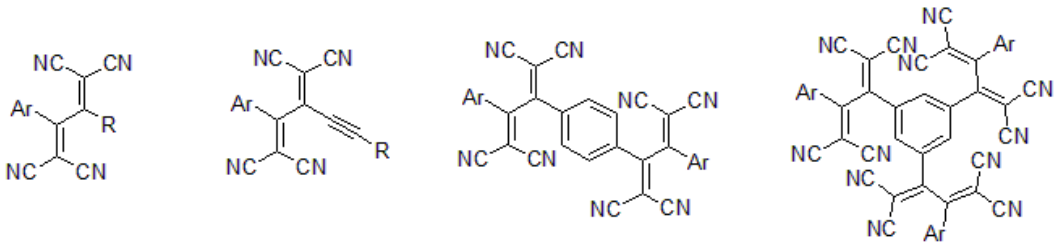

Figure 2.3: Dicyanovinyl substituted 2,3-diphenyl-1,4-butadiene derivatives

The Tykwinski group started studies on *iso*-polydiacetylenes (*iso*-PDA) (**figure 2.4**) with the synthesis of isopropylidenic small molecules and oligomers[67,68] followed by more complex cyclohexylidene[69] and adamantylidene[70] type *iso*-PDAs and found the π electron communication to extend along the enyne backbone. Evidence for intramolecular charge transfer through cross-conjugation was also seen in donor-acceptor type monomeric *iso*-PDAs[71] (**10**) (**figure 2.4**) but was absent in the case of the oligomers.

Using fluorescence and UV-vis spectroscopy experiments van Walree and coworkers[72] have shown the existence of charge separated states with charge transport occurring though a cross-conjugated bridge in donor-acceptor substituted 1,1-diphenylethenes (**11,12**) (**figure 2.5**). The weak ground state interactions in these molecules cause a larger degree of charge separation than the corresponding stilbenoid chromophores.

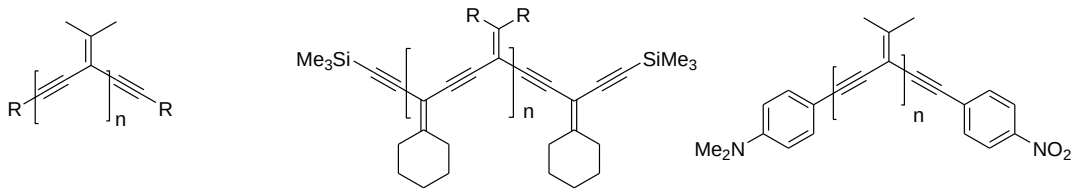

6 R = Me_3Si (n = 1, 3-5, 7)
7 R = *i*-Pr_3Si (n = 1, 3-5, 7, 9)

8 R = -(CH2)5- (n = 1,2)
9 R = Me (n = 1,2)

10 (n = 1-3)

Figure 2.4: Structures of *iso*-polydiacetylenes

Quinopyran and merocyanine type twisted intramolecular charge transfer (TICTOID) type structures (**13**) (**figure 2.5**) have been shown to demonstrate some of the largest molecular non-linear responses to date. The dihedral angle between the donor and acceptor parts of these molecules serves to modulate the magnitude of the response by changing the nature of the bond between quinoid and aromatic states. The biggest drawback for these molecules however is aggregation caused by the high dipoles in the aromatic states[31,73–76].

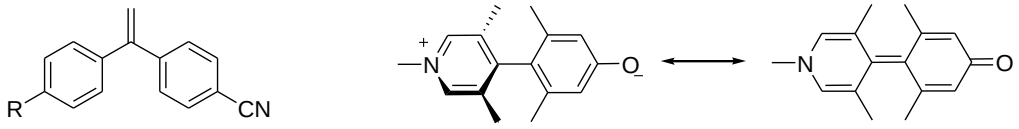

11 R = OMe
12 R = NMe_2

13 TICTOID Molecules

Figure 2.5: Structure of 1,1-diphenylethenes (**11** and **12**) and TICTOID molecules (**13**)

A theory paper by Ratner *et al*. studied the difference in electron transfer between cross-conjugated and linearly conjugated molecules[77]. They found strong quantum interference effects to be dominant in cross-conjugated molecules suggesting that the prediction of charge transfer in these molecules may not be straightforward.

In summary the class of cross-conjugated molecules hold promise for overcoming the drawbacks in linearly conjugated molecules such as electronic transparency in the visible region[78], low dipole moments as well as independent modulation of donor and acceptor functionalities with minimal effect on the electronic transition energy; it is of importance to study the photo-physics of such molecules and how variation in structure affects properties.

2.2 **Proposed Molecules and Synthesis:**

Herein we report on the theoretical simulation of electronic transitions as well as the molecular first hyperpolarizability β and comparison with experimental results of a series of cross-conjugated molecules shown in **figure 2.6**. In each case, the cross-conjugated spacer carbonyl group was functionalized with a donor (dialkylanilino) on one end and varying strengths of acceptor on the other end. Here the donor and acceptor are linearly conjugated to the carbonyl group but not to each other. Control molecules consisting of simply the donor or acceptor were either purchased or synthesized. Further, as discussed in Chapter 3 tricyanopyrroline type acceptor was substituted on each of the cross-conjugated molecules to observe the effects of a strong electron withdrawing group on the ground and excited stated of the molecules and their effect on β.

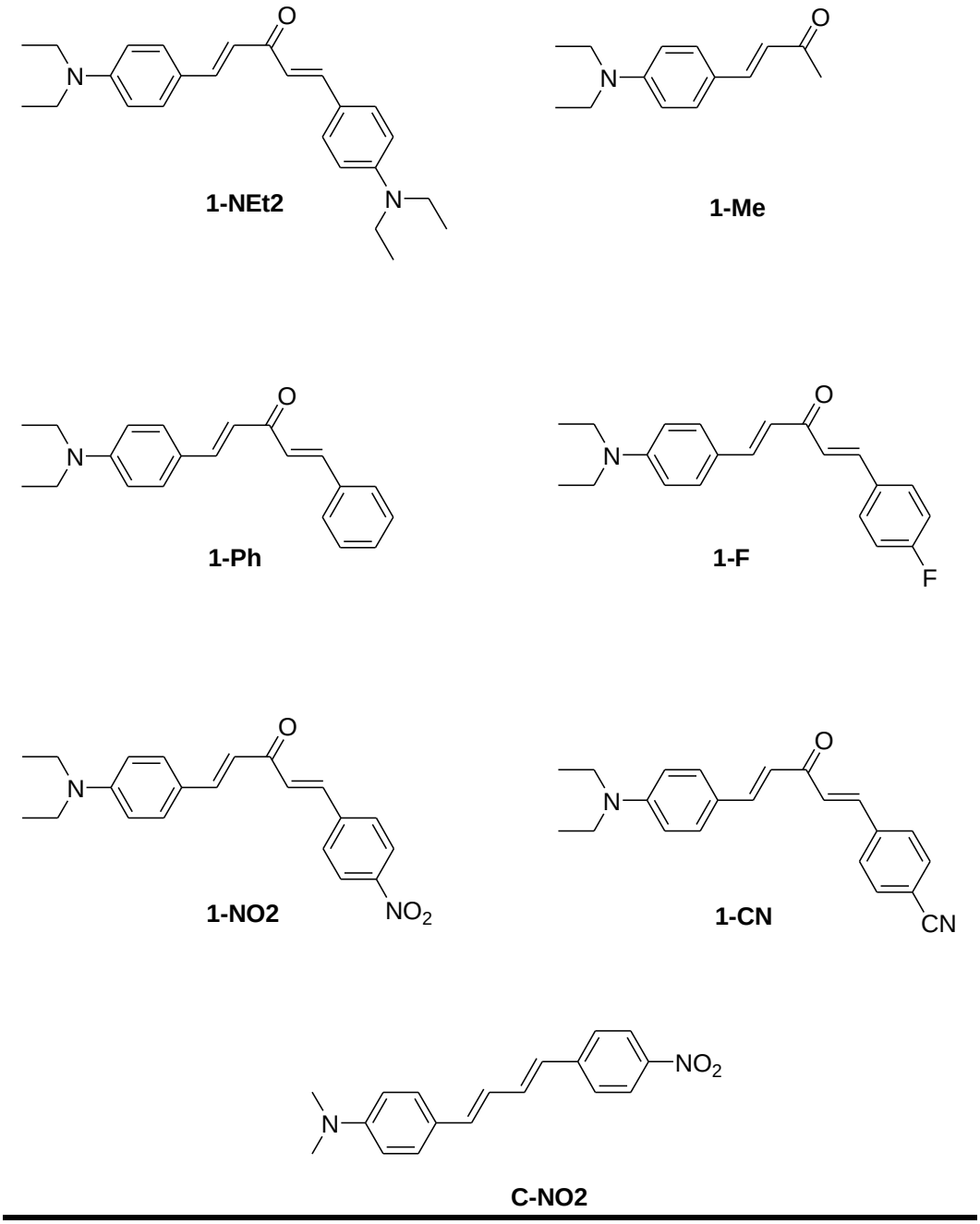

Figure 2.6: Cross-Conjugated Chromophores

2.2.1 **Synthesis of cross-conjugated chromophores:**

The reaction schemes for synthesis of the cross-conjugated molecules are shown in **figure 2.7**[79]. Compound **1-NEt2** was synthesized in one step via aldol condensation of 4-(diethylamino)benzaldehyde and acetone in 2-butanol without need for further purification. Using other solvents, ethanol, isopropanol or 1-butanol, or reducing the reaction time gave a mixture of mono- and di substituted acetone. **1-Me** was prepared in good yield by reacting 4-(diethylamino)benzaldehyde and excess acetone at 60°C in 24h. Compound **1-Ph**, **1-F** and **1-NO2** were synthesized from **1-Me** which was deprotonated using sodium methoxide in ethanol followed by an aldol condensation with benzaldehyde (**A**) to give **1-Ph**, 4-fluorobenzaldehyde (**B**) to give **1-F** and 4-nitrobenzaldehyde (**C**) to give **1-NO2**. Reaction times and yields varied depending on the electronegativity of the benzaldehydes (**A**, **B** and **C**) used; with strong electron-withdrawing groups allowing for shorter reaction times and greater yields than the weaker electron-withdrawing groups. Heating reduced yields possibly from decomposition of products or generation of side products. **1-CN** was synthesized from the aldol condensation of **1-Me** with 4-cyanobenzaldehyde using piperidine as base and a 1:1 mixture of acetonitrile/ethanol as solvent. The control molecule **C-NO2** was synthesized as shown in **figure 2.8**[80] by reacting 4-(dimethylamino)cinnamaldehyde with 4-nitrophenylacetic acid in piperidine at 100°C. The condensation proceeds rapidly followed by decarboxylation to produce the final product in good yield after purification. Synthetic details, NMR and ESI/MS spectra are given in appendix to Chapter 2

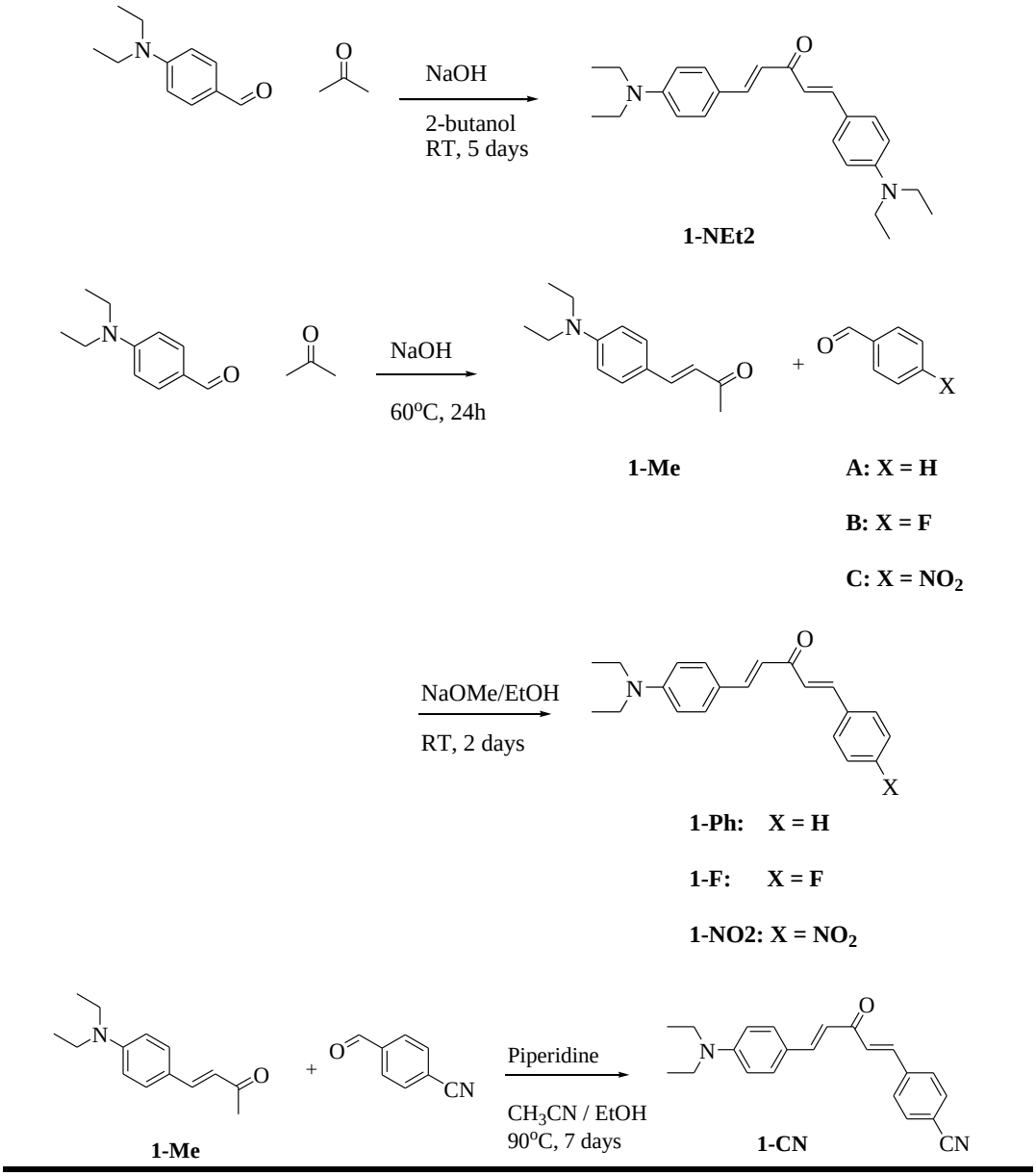

Figure 2.7: Synthesis of Cross-Conjugated Chromophores

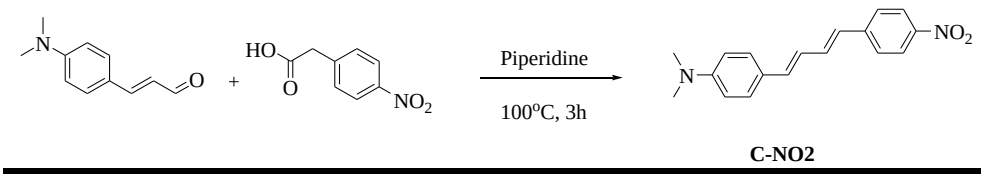

Figure 2.8: Synthesis of C-NO2

2.3 **UV-vis Spectroscopy:**

2.3.1 **Cross-conjugated series: Comparison of UV-vis spectroscopy in chloroform**

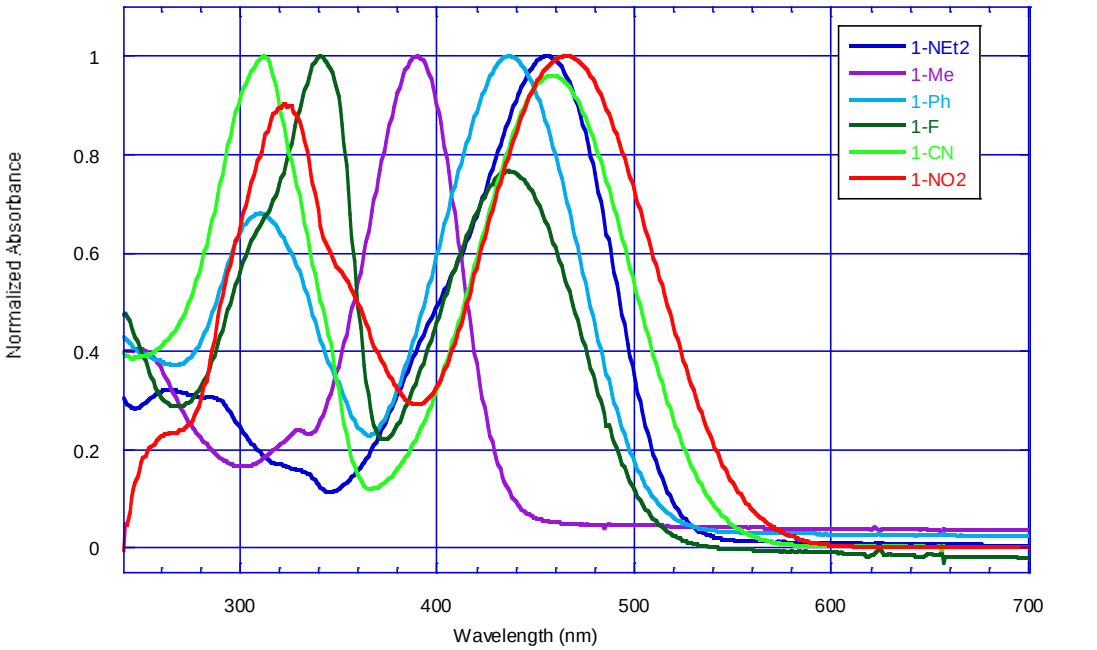

Figure 2.9: UV-vis spectra of cross-conjugated chromophores in chloroform

Name	1-NEt2	1-Me	1-Ph	1-F	1-CN	1-NO2
Structure	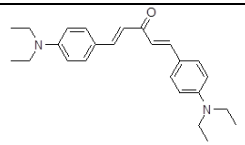	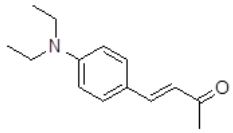	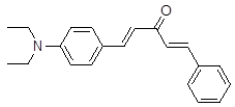	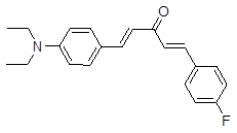	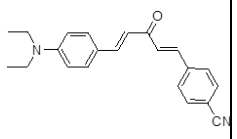	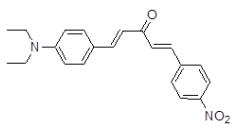
Wavelength λ_{max} (nm)	455	390	310 436	341 436	312 458	322 465

Table 2.1: Absorbance maxima of cross-conjugated chromophores in chloroform

UV-visible spectroscopy of cross-conjugated dyes in chloroform ($E_T(30)$ = 39.1 kcal/mol) shows two $\pi \rightarrow \pi^*$ transition absorbances (**figure 2.9, table 2.1**) for the molecules with weak acceptors; benzene (**1-Ph**) and fluorobenzene (**1-F**), as well as strong acceptors; cyanobenzene (**1-CN**) and nitrobenzene (**1-NO2**). The high energy peaks range (**figure 2.10**) from 310nm to 340nm. A bathochromic trend is observed for these peaks with the fluorophenyl acceptor absorbance being an outlier to the trend. The low energy peaks range (**figure 2.11**)from 436nm to 464 nm showing a red (bathochromic) shift with increasing acceptor strength. The symmetric donor substituted molecule, **1-NEt2** and the methyl substituted **1-Me** both show a single ($\pi \rightarrow \pi^*$ transition) peak situated around 455nm and 390nm respectively. A comparison with the theoretically predicted absorbance values in the next section will help with understanding the experimental UV-vis plots for these cross conjugated molecules.

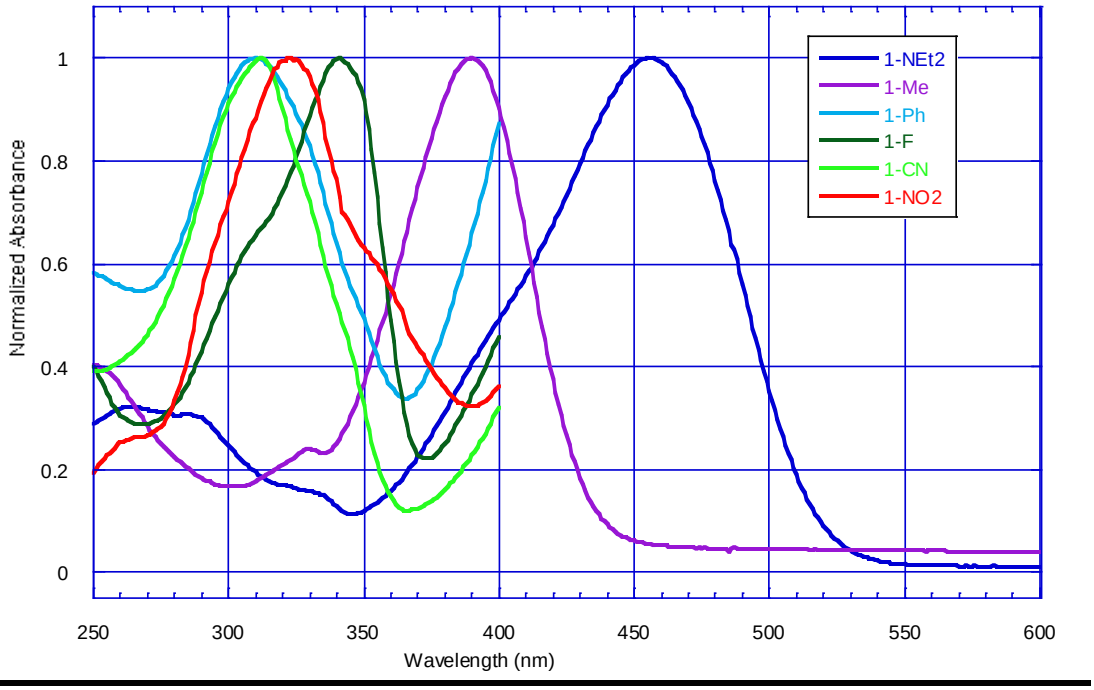

Figure 2.10: High energy peak of cross conjugated chromophores in chloroform

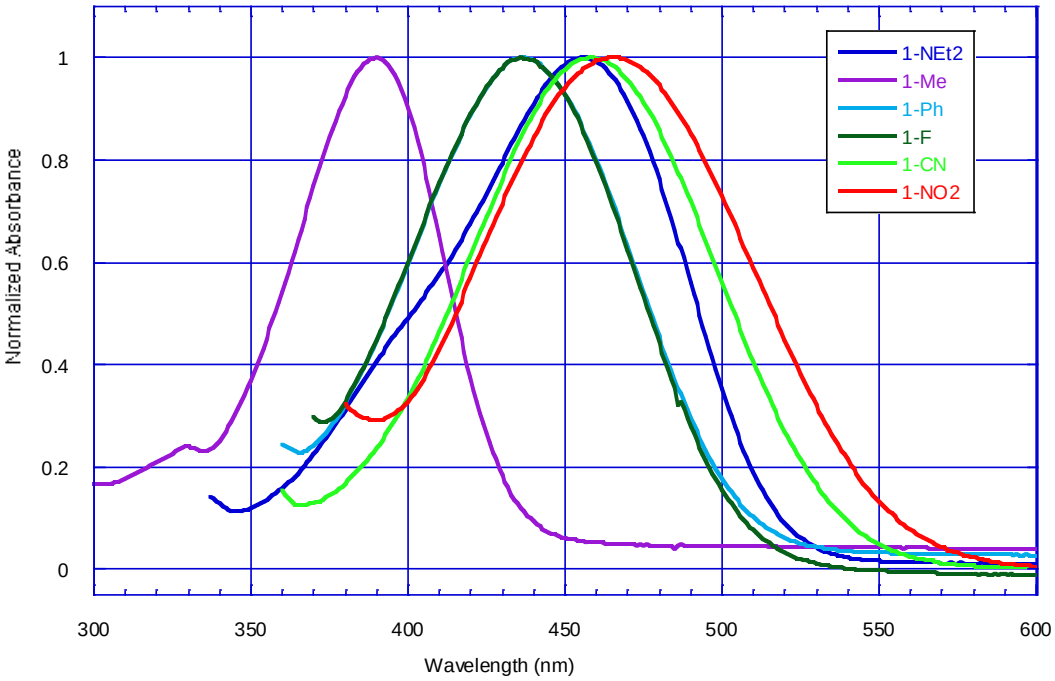

Figure 2.11: Low energy peak of cross conjugated chromophores in chloroform

2.3.2 **UV-Vis spectroscopy: Comparison with calculated values in chloroform:**

Quantum chemical calculations were performed using the Gaussian-09 package. Molecular geometries were optimized using the B3LYP hybrid functional with the 6-31+G* basis set (B3LYP/6-31+G*). Electronic transitions and respective oscillator strengths in chloroform (with the polarization continuum model (PCM) reaction field) were calculated using the long-range corrected hybrid functional CAM-B3LYP with the 6-31+G* basis set (CAM-B3LYP/6-31+G*).

The results are compared in table 2.2 with experimental optical data in chloroform. The molecules are listed going from the symmetric donor substituted **1-NEt2** to the asymmetric molecules with increasing acceptor strengths going from **1-Ph** (with a weak phenyl acceptor) to **1-NO2** (with a stronger nitrophenyl acceptor). The theoretical values for the major transitions for

the cross conjugated molecules are all blue shifted by around 21 to 36 nm. The primary transitions indicated by density functional theory (DFT) for all the cross conjugated molecules are from the highest occupied molecular orbital (HOMO) to the lowest unoccupied molecular orbital (LUMO) (HOMO→LUMO transitions). These are the lower energy transitions around 409nm to 478nm (theoretical) and 436nm to 465nm (experimental). The theoretical values follow the experimental trend and show a bathochromic shift with increasing acceptor strength from **1-Ph** to **1-NO2**.

The HOMO for **1-NEt2** lies on the diethylamino benzene donor on either side of the carbonyl carbon at the center while the LUMO lies largely on the carbonyl carbon (**figure 2.12**). Since the ketone moiety is only weakly electron withdrawing, the LUMO appears to be quite delocalized. **1-Me** is quite similar to 1-NEt2 except for the absence of the second diethylamino benzene group. The HOMO is located on the donor and the LUMO while delocalized, extends across the carbonyl to the methyl group.

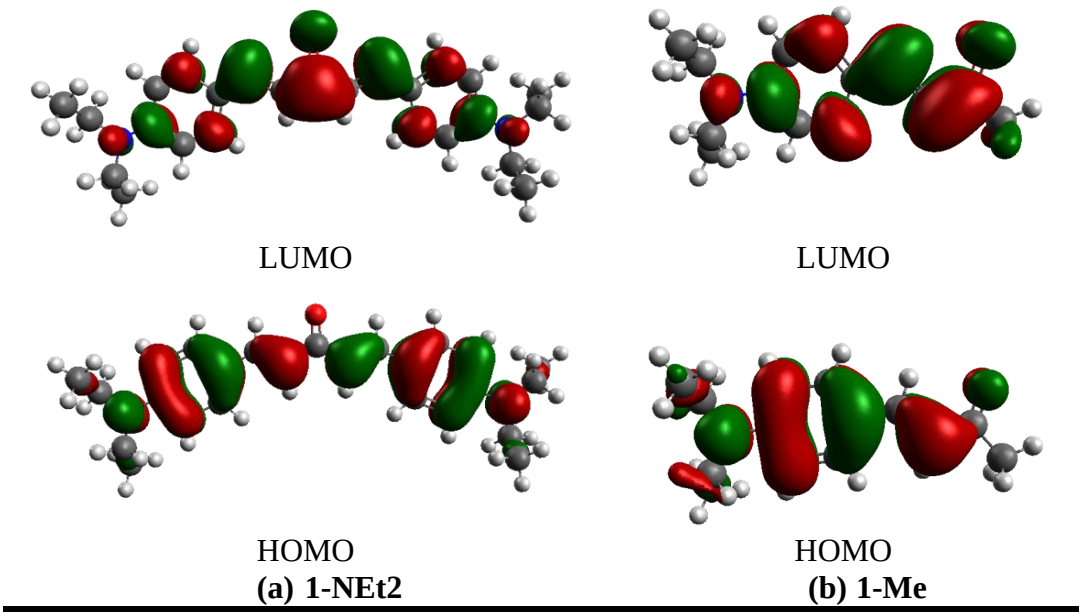

Figure 2.12: HOMO to LUMO transition for (a) **1-Net2** and (b)**1-Me**

Name	Experimental λ_{max} (nm)	CAM-B3LYP/6-31+G*		
		λ_{max} (nm)	f^{a}	Transition
1-NEt	455	358.75 419.94	0.2035 2.1009	HOMO-1→LUMO HOMO→ LUMO
1-Me	390	363.00	1.1906	HOMO→ LUMO
1-Ph	310 436	309.38 409.70	0.4679 1.5379	HOMO-1→LUMO HOMO→ LUMO
1-F	341 436	308.51 410.77	0.4717 1.5285	HOMO-1→LUMO HOMO→ LUMO
1-CN	312 458	311.00 427.04	0.6968 1.5008	HOMO-1→LUMO HOMO→LUMO
1-NO2	322 465	317.68 327.28 440.21	0.3983 0.4926 1.4113	HOMO→LUMO+1 HOMO-1→LUMO HOMO→ LUMO

Table 2.2: Absorption maxima $\boldsymbol{\lambda_{max}}$of chromophores in chloroform: Experimental Vs Calculated values

a: calculated oscillator strengths

The HOMOs on the asymmetrical acceptor substituted molecules **1-Ph**, **1-F**, **1-CN** and **1-NO2** are quite identical and are once again located on the donor side of the molecules (**figure 2.13** and **figure 2.14**). The change in LUMO is where the major difference lies in these molecules. The LUMOs on **1-Ph** and **1-F** (**figure 2.13**) are only slightly biased towards the phenyl and fluorophenyl groups respectively. They are in fact quite delocalized and extend beyond the cross-conjugated center to the diethylamino benzene group. The LUMOs on **1-CN** and **1-NO2** on the other hand are localized primarily on the cyanobenzene and the nitrobenzene groups respectively.

The existence of these HOMO→LUMO transitions in the experimentally observed spectra indicates that the major charge transfer in these cross conjugated molecules occurs from the donor on one side of the cross-conjugated center across to the acceptor on the other side. The cross-conjugated center does not truly break the conjugation between the donor and acceptor groups across the molecules.

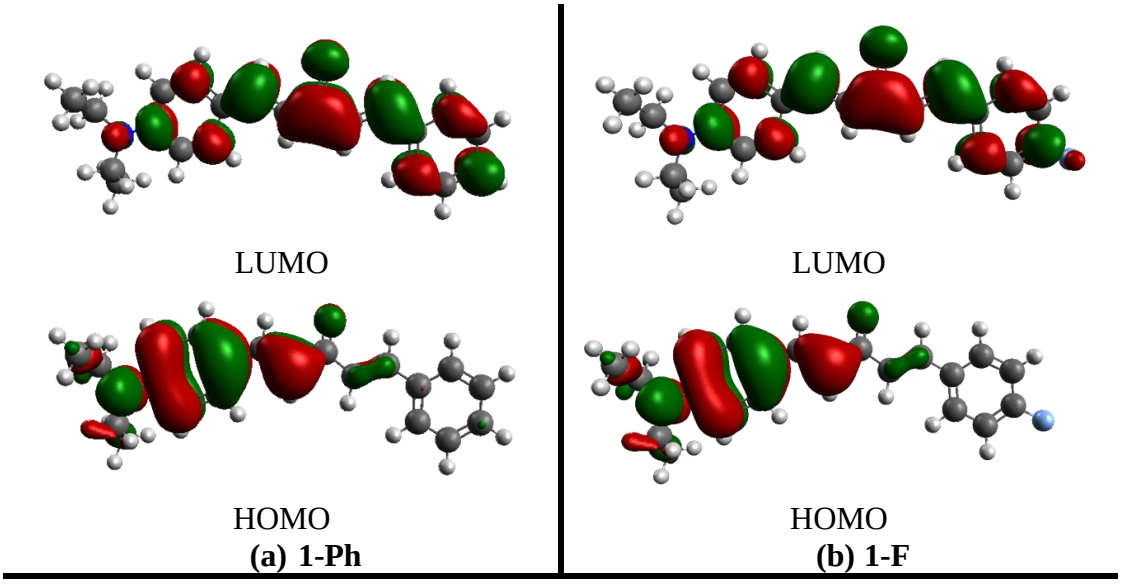

Figure 2.13: HOMO to LUMO transition for (a) **1-Ph** and (b) **1-F**

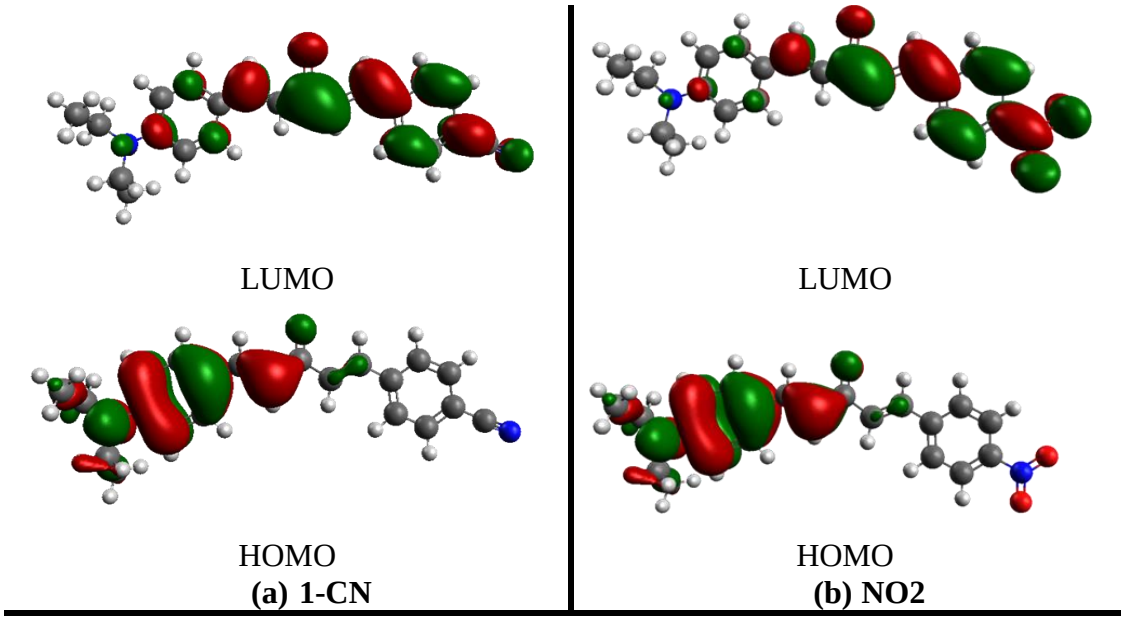

Figure 2.14: HOMO to LUMO transition for (a) **1-CN** and (b) **1-NO2**

For the acceptor substituted cross-conjugated molecules **1-Ph**, **1-F**, **1-CN** and **1-NO2**, secondary transition are predicted by DFT. These correspond to the absorbances around 310 nm to 341nm (experimental) and 308nm to 322nm (theoretical) and are HOMO-1→LUMO transitions. The HOMO-1 for all four molecules are located primarily on the acceptor side of the cross-conjugated center (**figure 2.15 and figure 2.16**). The absolute values for the secondary transitions for **1-Ph**, **1-CN** and **1-NO2** are predicted quite accurately by theory. Theory also predicts a bathochromic shift with increasing acceptor strengths for this transition in going from **1-Ph** (310nm (theoretical) and 309nm (experimental)) to **1-CN** (311nm (theoretica)l and 312nm (experimental)) and finally to **1-NO2** (327nm (theoretica)l and 322nm (experimental)). This can be explained by the fact that the energy of the HOMO-1 orbital would in fact increase with an increase in the strength of the donor thus reducing the HOMO-1→LUMO gap resulting in a bathochromic trend. The value of 308.5nm predicted for **1-F** is red shifted in the experimental spectra (341nm) and the experimental data does not fit in the theoretically predicted

bathochromic trend. It is unclear at this point why 1-F would be an outlier to the trend observed in theory.

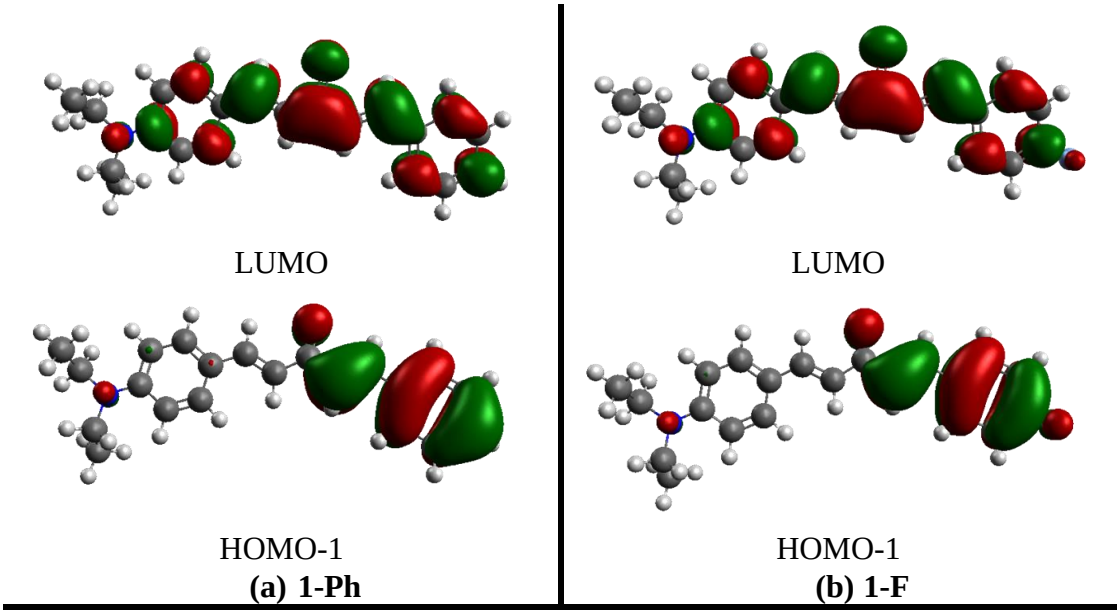

Figure 2.15:HOMO-1 to LUMO transition for (a) **1-Ph** and (b) **1-F**

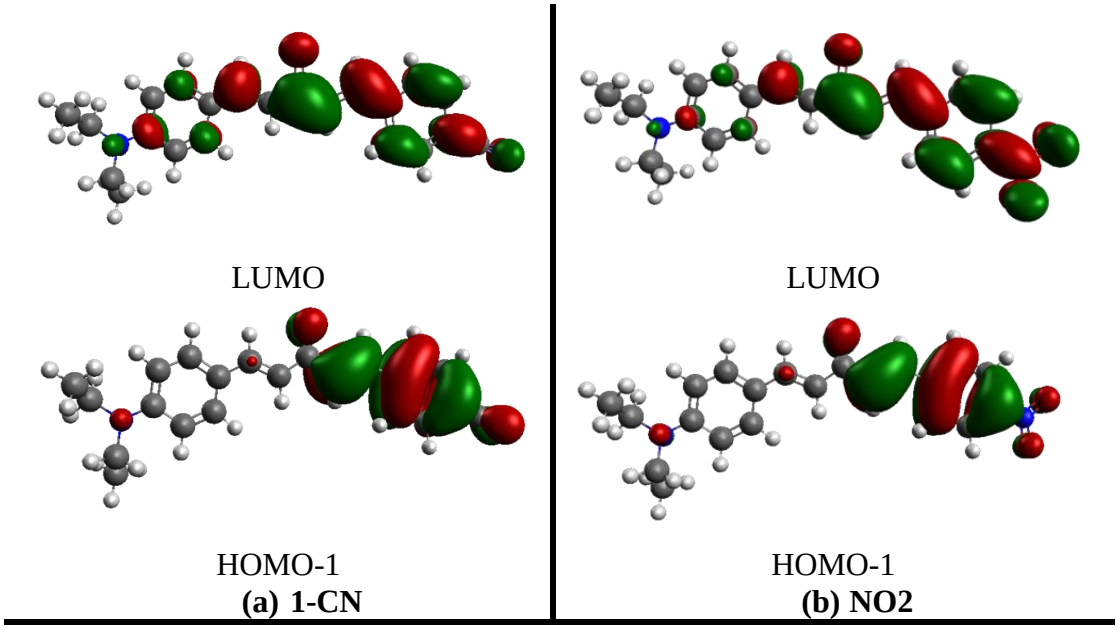

Figure 2.16:HOMO-1 to LUMO transition for (a) **1-CN** and (b) **1-NO2**

The prediction of a secondary transition for **1-Net2** at 358nm by DFT is not clearly observed in the experimental spectra (**figure 2.10**) although a broad absorbance around 280nm and also a shoulder around 400nm is observed in the experimental plot. It is possible that due to the low calculated oscillator strength, the peak might be one of the two peaks mentioned above.

2.3.3 **UV-vis spectroscopy in cyclohexane:**

UV-vis spectra of the dyes in a non-polar solvent like cyclohexane ($E_T(30)$ = 30.9 kcal/mol) (**figure 2.17** and **table 2.3**) are similar to those in chloroform. However, in cyclohexane, many of the peaks have shoulders predominantly on the red side of the main peak. This could signify presence of J-aggregates. **1-NEt2** also has shoulders on both blue and red side of its main absorbance peak suggesting the presence of both H and J aggregates. Once again, the trend observed is a bathochromic shift for the asymmetric molecules with acceptors for both the low energy as well as the high energy absorbances. **1-F** is once again an outlier to the trend. With the exception of **1-NO2**, all the peaks are blue (hypsochromic) shifted compared to those in chloroform. These shifts are more pronounced for the low energy peaks than the high energy peaks (**table 2.4** and **table 2.5**). The spectrum for **1-NO2** is unusual in that not only is the low energy peak red shifted in cyclohexane compared to chloroform but also that the relative intensities of the two peaks are reversed.

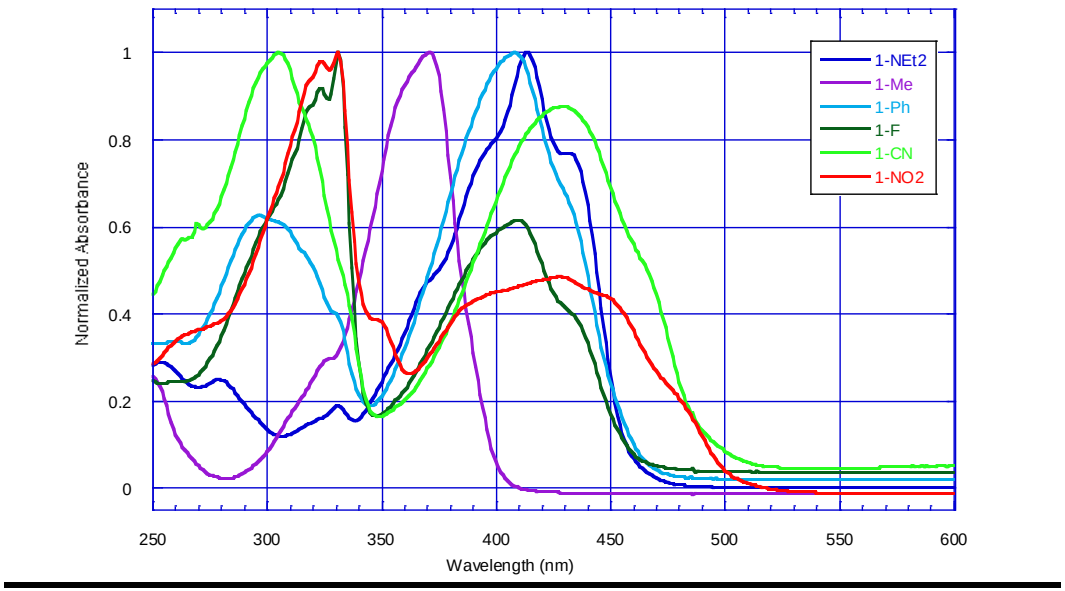

Figure 2.17: UV-vis spectra of cross-conjugated chromophores in cyclohexane

Name	1-NEt2	1-Me	1-Ph	1-F	1-CN	1-NO2
Structure	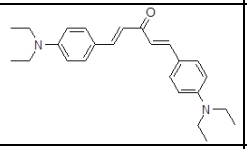	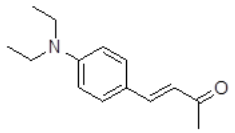	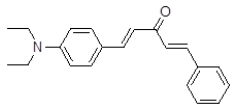	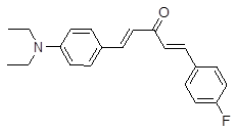	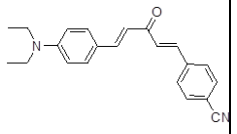	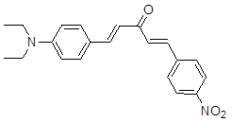
Wavelength λ_{max} (nm)	413	371	296 408	331 409	305 430	331 427

Table 2.3: Absorbance maxima of cross-conjugated chromophores in cyclohexane

2.3.3.1 **Cross-conjugated series: Comparison of λmax in cyclohexane and chloroform**

The shifts in absorbance for the series in going from cyclohexane to cyclohexane are listed in **tables 2.4** and **2.5**. The shifts seen for the high energy peak of the asymmetric molecules **1-Ph**, **1-F**, **1-CN** and **1-NO2** are comparable to that seen for **1-Me** with reducing difference seen as the acceptors get stronger. **1-Ph**, **1-F** and **1-CN** display positive solvatochromism while **1-NO2** displays negative solvatochromism in going from cyclohexane to chloroform.

Such behavior is atypical of most $\pi \rightarrow \pi^*$ transitions seen in polar chromophores. As discussed previously this high energy peak is a transition from the HOMO-1 (on the acceptor) to the LUMO of the cross conjugated dyes. It appears that although the HOMO-1 energy levels for the molecules decreases with a decrease in polarity of the solvent causing the positive solvatochromism as expected (**1-Ph**, **1-F** and **1-CN**), this decrease in the energy level diminishes with the strength of the acceptor ultimately resulting in the negative solvatochromism observed for **1-NO2**.

Solvent	Wavelength λ_{max} (nm)					
	1-NEt2	1-Me	1-Ph	1-F	1-CN	1-NO2
Cyclohexane	413	371	296	331	305	331
Chloroform	455	390	310	341	312	322
Difference $\lambda_{max(CDCl3)}$- $\lambda_{max(Cy)}$	42	19	14	10	7	-9

Table 2.4: Difference in λ_{max} in chloroform and cyclohexane for the high energy peaks

The shifts seen in low energy peaks are more comparable to that seen for **1-NEt2**. All the shifts in absorbance in going from cyclohexane to chloroform show a positive solvatochromic trend. In going from **1-Ph** to **1-F** to **1-CN** the amount of shift observed remains the same. It is only with the stronger acceptor (**1-NO2**) and the stronger donor (**1-NEt2**) that is the solvatochromism more pronounced suggesting that the low energy electronic excitations for these molecules are likely more complex than typical HOMO→LUMO transitions seen in most push-pull type molecules.

Solvent	Wavelength λ_{max} (nm)					
	1-NEt2	1-Me	1-Ph	1-F	1-CN	1-NO2
Cyclohexane	413	371	408	409	430	427
Chloroform	455	390	436	436	458	464
Difference $\lambda_{max(CHCl3)}$- $\lambda_{max(Cy)}$	42	19	28	27	28	37

Table 2.5: Difference in λ_{max} in chloroform and cyclohexane for the low energy peaks

2.3.4 **Cross-conjugated series: polarity study**

In general the dyes show bathochromic shifts with increase in solvent polarity. Dyes with strong donors (**1-NEt2**) (**figure 2.18**) and strong acceptors (**1-NO2**) (**figure 2.21**) show the largest shifts of the HOMO→LUMO transition compared to the molecules with a weaker donor (**1-Me**) (**figure 2.19**) and weaker donor (**1-CN**) (**figure 2.20**).

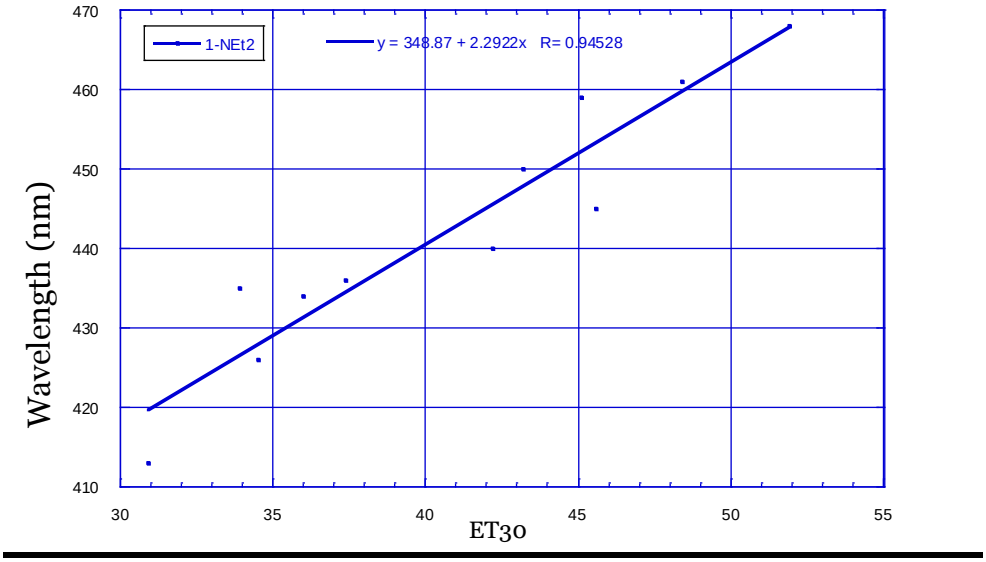

Figure 2.18: 1-NEt2 Solvatochromism study

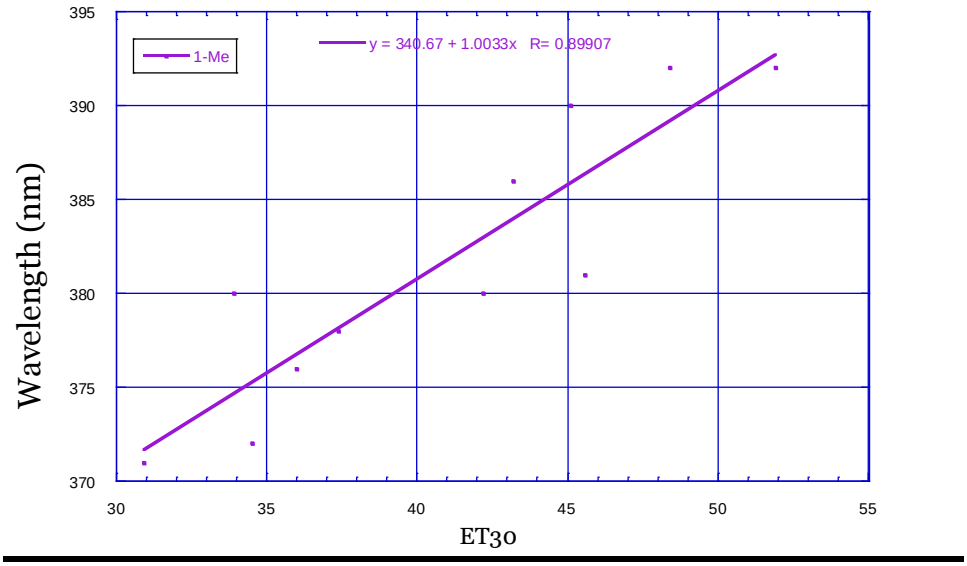

Figure 2.19: 1-Me Solvatochromism study

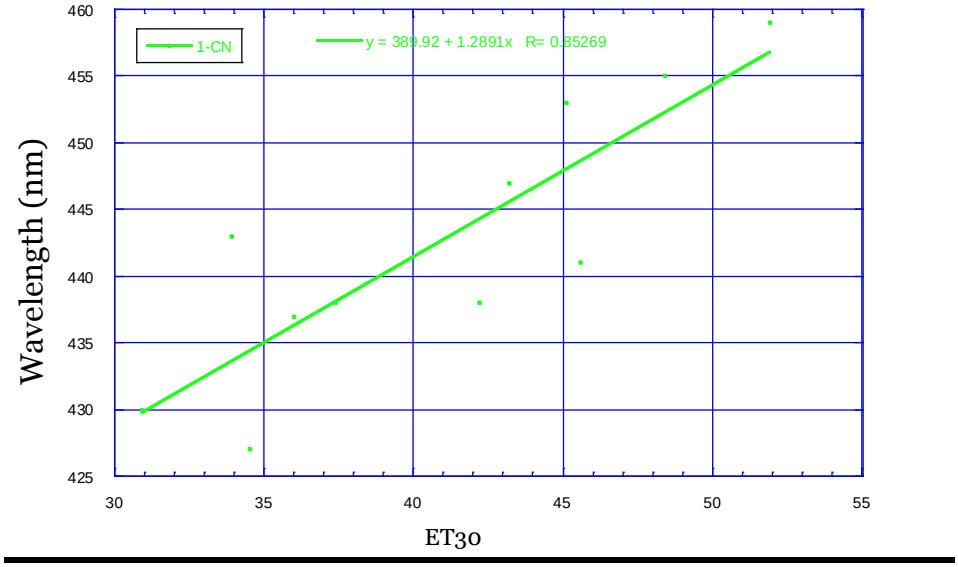

Figure 2.20: 1-CN Solvatochromism study

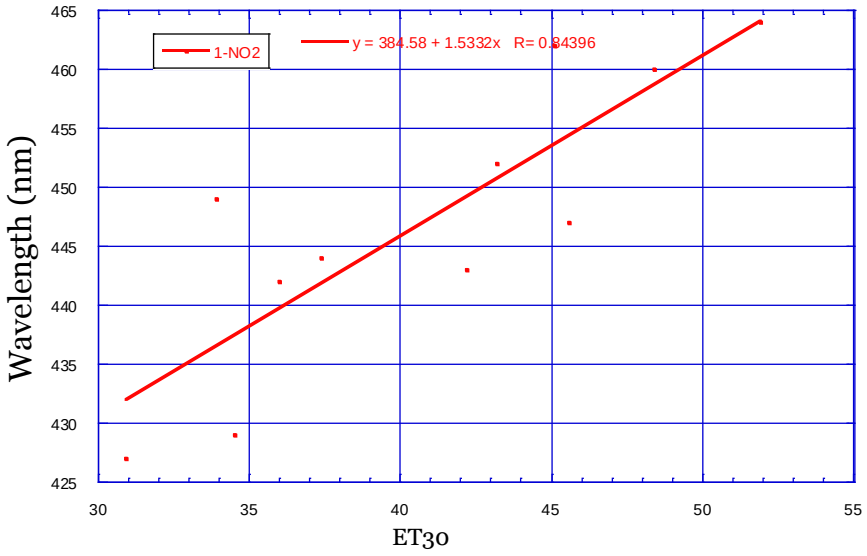

Figure 2.21: 1-NO2 Solvatochromism study

2.3.5 UV-vis spectroscopy: Control molecule (C-NO2) and comparison with cross-conjugated molecule 1-NO2:

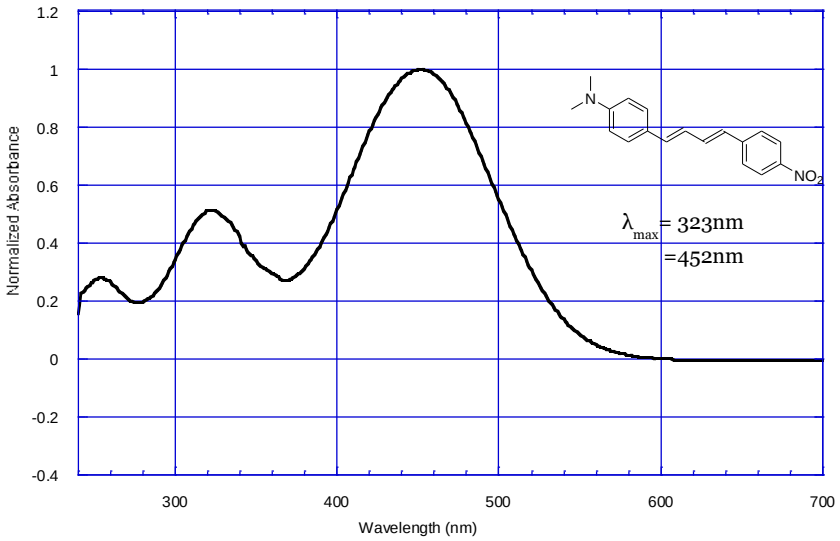

Figure 2.22: UV-vis spectra of control (**C-NO2**) chromophore in chloroform

The fully conjugated control molecule **C-NO2** was synthesized for comparison with cross-conjugated molecule **1-NO2**. UV-vis spectrum in chloroform shows two peaks at 323nm and 452 nm (**figure 2.22**). Comparing the molar absorptivity and the energies of the two peaks (**figure 2.23**) however, it is observed that the molar absorptivity at 323 nm is half that observed at 452nm and energy at 323 nm is approximately double the energy at 452 nm. It is most likely that the 323 nm peak is a vibronic absorption.

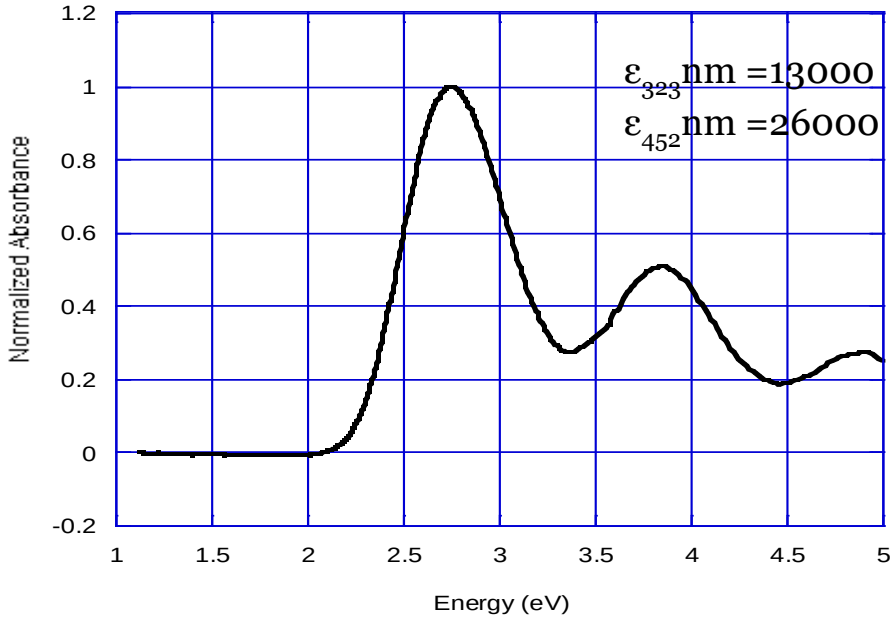

Figure 2.23:UV-vis spectra of control (**C-NO2**) chromophore in chloroform (Normalized absorbance Vs Energy)

Comparing **C-NO2** to **1-NO2** and **1-Me** in chloroform (**figure 2.24**), it is clear that the low energy (HOMO→LUMO) absorbance is red shifted for **1-NO2** (464nm) compared to that of **C-NO2** (452nm). It is unclear why a red shift of 12nm would be observed in absorbance in going from a conjugated system to a cross-conjugated system.

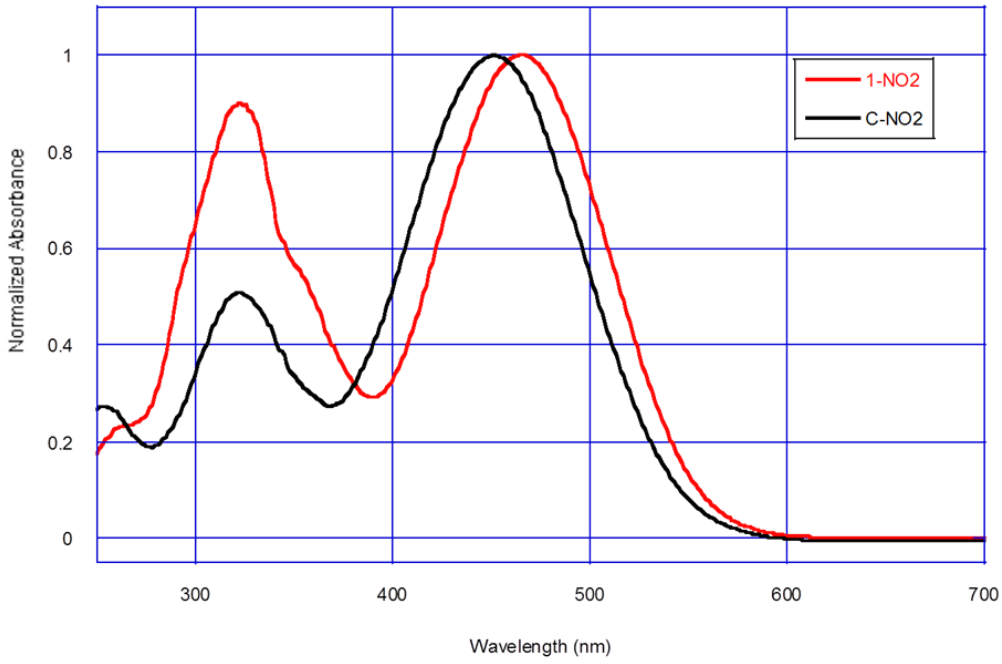

Figure 2.24: Comparison UV-vis spectra of control **C-NO2** and **1-NO2** in chloroform

Name	C-NO2	1-NO2
Structure	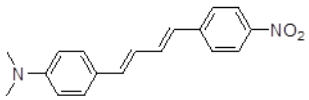	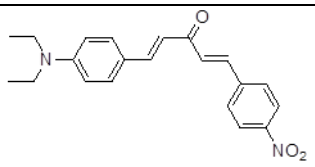
Wavelength λ_{max} (nm)	323 452	322 464
Table 2.6: $\boldsymbol{\lambda_{max}}$ values in chloroform for **C-NO2** and **1-NO2**		

2.3.6 **UV-vis spectroscopy - Summary:**

The asymmetric acceptor substituted cross-conjugated molecules **1-Ph**, **1-F**, **1-CN** and **1-NO2** exhibit two absorbances in their experimental UV-vis spectra. The major transitions are the lower energy absorbances around 436nm to 465nm. Theoretical values for these transitions are only slightly blue-shifted and correctly predict the bathochromic trend observed with increasing acceptor strength. These are HOMO→LUMO charger transfer transitions. The HOMO in these molecules is located on the donor while the LUMO is located across the cross-conjugated bridge on the acceptor. This picture is especially clear in the case of the molecules with relatively strong acceptors (**1-CN** and **1-NO2**)

The high energy secondary absorbances around 310nm to 341nm arise from HOMO-1→LUMO transitions and both their values as well as red-shifted trends are accurately predicted by theory.

In summary, based on the experimental UV-vis data and theoretical calculations, a major charge transfer transition is indeed observed in cross-conjugated molecules. This occurs from the diethylamino benzene donor on one side of the cross-conjugated center to the acceptor on the other side of the cross-conjugation (especially in **1-CN** and **1-NO2**) indicating that the carbonyl carbon does not prevent charge transfer even though it isolates the HOMO and the LUMO.

2.4 **Fluorescence Spectroscopy:**

When obtaining fluorescence data, the fluorophore is typically excited to the first singlet state (S1) of the molecule within which it relaxes to the lowest vibrational state, followed by emission from the excited state. The excited states of typical fluorophores exhibit larger dipole moments than the ground states. Since fluorescence lifetimes (1-10ns) are at least an order of magnitude slower than solvent relaxation times (10-100ps), the dipole of the excited fluorophore can therefore be affected by the dipole moment of the surrounding solvent. Solvent dipoles can orient themselves along the dipolar axis of the excited molecule thereby reducing its energy and lowering the emission wavelength. Solvatochromic effects in fluorescence spectra for polar molecules are often significantly pronounced compared to non-polar molecules. The study of fluorescence data and the shifts observed thus gives us important information about the excited state of the molecules.

Four compounds were picked for fluorescence measurements to cover the range of molecules from those cross-conjugated with a strong donor, weak donor and strong acceptor; **1-NEt2**, **1-Me** and **1-NO2** respectively and the fully conjugated molecule **C-NO2**.

Due to the presence of strong electron donors, **1-NEt2** demonstrates strong fluorescence intensity in all solvents (**figure 2.25** and **table 2.7**) and increasing quantum yields with increase in solvent polarity. In non-polar solvents (cyclohexane and toluene), red shoulders are seen suggesting possible J-aggregates. While **1-Me** is not very fluorescent and has low quantum yields in all solvents (**figure 2.26** and **table 2.7**), its quantum yields increase with increasing solvent polarity before dropping off again in higher polarity solvents.

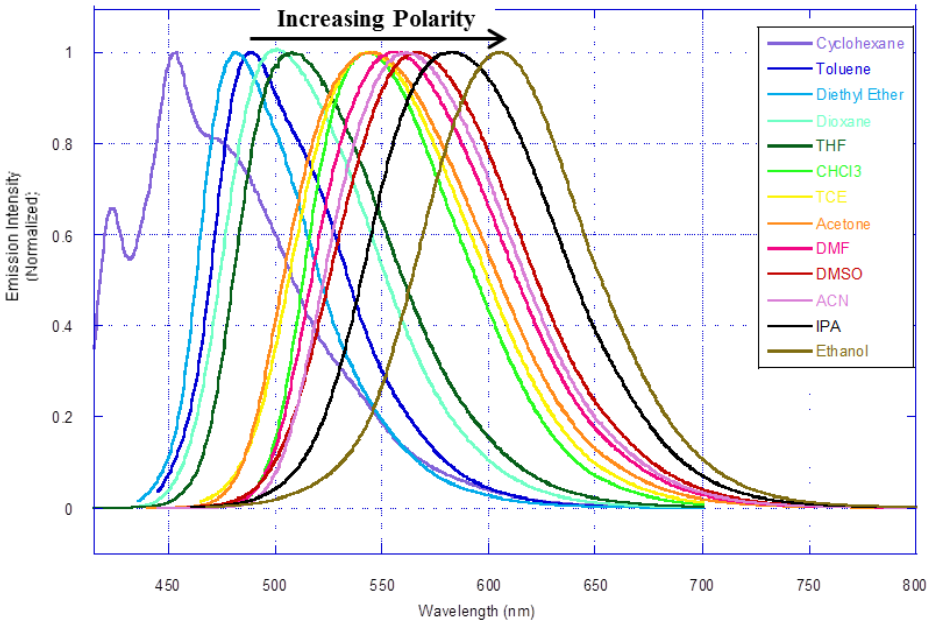

Figure 2.25: Normalized fluorescence for **1-NEt2**
Solvents in the key are listed in order of increasing $E_T(30)$

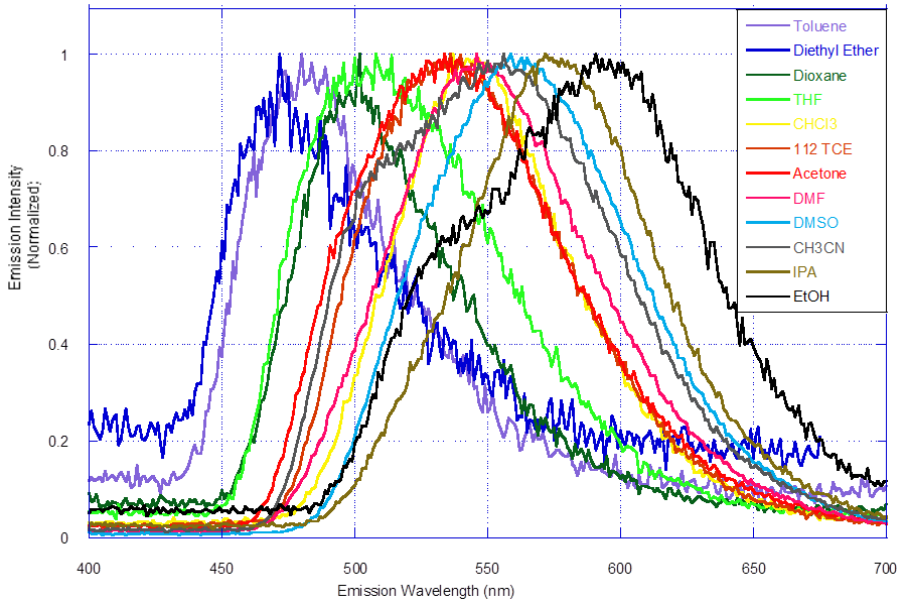

Figure 2.26: Normalized fluorescence for **1-Me**
Solvents in the key are listed in order of increasing $E_T(30)$

Fluorescence emission data is listed in table 2.7 below for comparison.

Solvent	**$E_T(30)$**	**Emission Wavelength[a] (λ_{em})**			
		1-NEt2	**1-Me**	**1-NO2**	**C-NO2**
Cyclohexane	30.9	451 (0.8)	(*b*)	503 (0.3)	527 *(b)*
Toluene	33.9	488 (3.0)	480 (0.0)	579 (4.0)	593 (54.2)
Diethylether	34.5	480 (2.4)	474 (0.2)	607 (0.8)	612 (38.4)
1,4-dioxane	36.0	499 (13.2)	502 (0.4)	607 (1.6)	616 (37.7)
Tetrahydrofuran	37.4	508 (11.1)	507 (0.5)	562 (0.1)	670 (6.7)
Chloroform	39.1	543 (17.1)	543 (0.5)	563 (0.2)	595 (2.0)
1,1,2-Trichloroethane	40.3	544 (7.1)	536 (1.0)	601 (0.3)	608 (29.4)
Acetone	42.2	545 (19.9)	535 (1.1)	582 (0.1)	608 (1.1)
N,N-dimethylformamide	43.2	555 (14.5)	546 (2.3)	*c*	617 (0.8)
Dimethylsulfoxide	45.1	566 (13.5)	562 (2.1)	586 (0.1)	613 (0.3)
Acetonitrile	45.6	561 (20.1)	552 (1.3)	*c*	610 (0.2)
Isopropanol	48.4	583 (32.6)	577 (0.6)	587 (0.2)	*c*
Ethanol	51.9	605 (20.4)	592 (0.6)	617 (0.1)	606 (0.2)

Table 2.7: Fluorescence emission data for cross-conjugated chromophores

*a:*Percent quantum yields in parentheses
b: Omitted due to aggregation.
c: No fluorescence data due to low fluorescence intensity or low solubility.

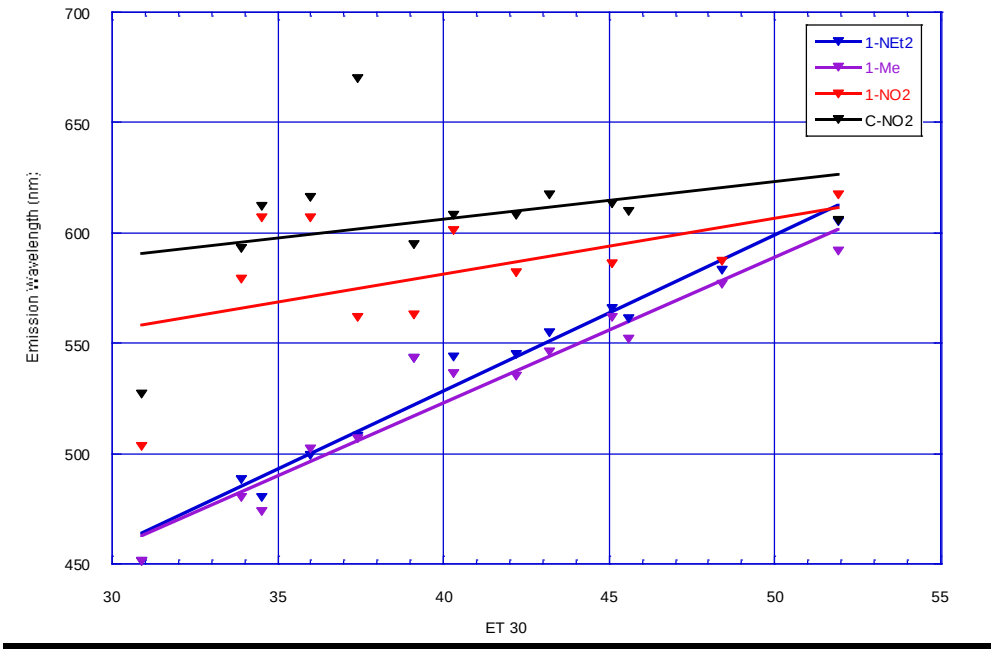

Figure 2.27: Solvatochromic trends of the emission spectra.
The linear fits are shown only to guide the eye.

Fluorescence maxima of compounds **1-NEt2** and **1-Me** show strong positive solvatochromic trends (**figure 2.27**). The maximum shift from cyclohexane to ethanol is 154nm for **1-NEt2** and 141nm for **1-Me**. While **1-Me** absorbance wavelengths are significantly blue-shifted (between 40-96nm) compared to **1-NEt2**, the emission wavelengths in different solvents only differ by 13 nm (seen in ethanol) at the most (**table 2.7**). This would suggest similar excited state structures from which the molecules emit. An approximation of the charge separated (CS) structure depicted in **figure 2.28** (top) for **1-NEt2** has two resonance forms which would account for the slightly lower energy emission wavelength compared to **1-Me** but is quite similar to the CS structure (**figure 2.28** (bottom)) for **1-Me**. While the exact structure of the lowest lying electronically excited singlet (the emissive species) for the molecules in different solvents may be elusive, it is helpful to see the similarities in the two structures based on the CS species.

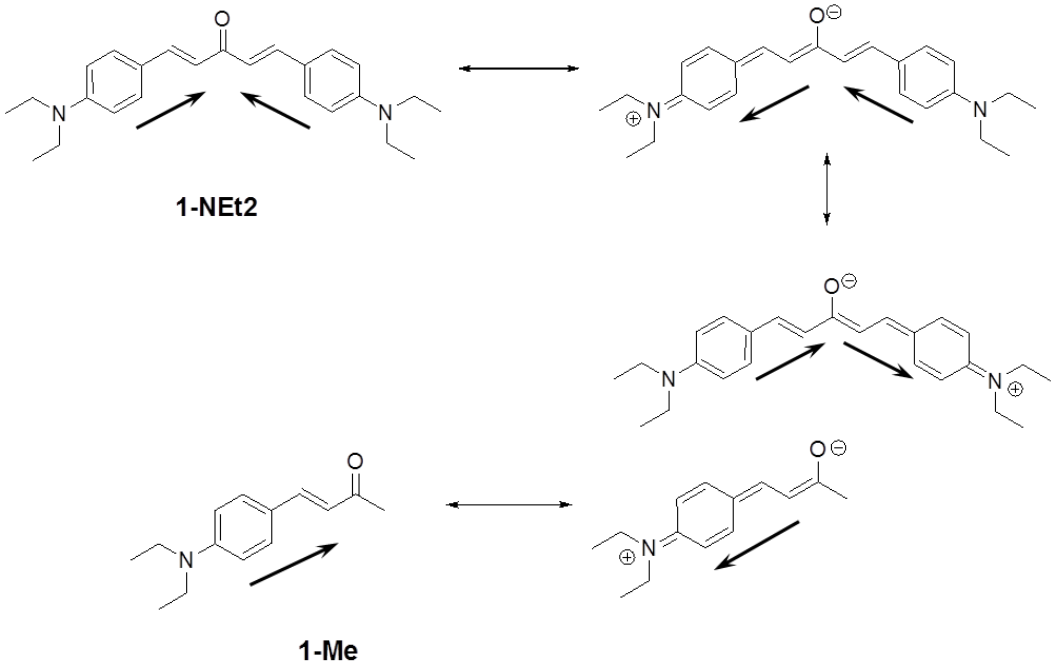

Figure 2.28: Neutral and charge separated states for **1-NEt2** (*top*), **1-Me** (*bottom*)
The arrows next to the structures represent dipole moments

Both molecules also show increasing stokes shift with increasing solvent polarity (**figure 2.29**). The increase in stokes shift is quite pronounced for **1-Me** compared to **1-NEt2** suggesting that the difference in ground state polarization and excited state polarization is higher for **1-Me** than for **1-NEt2**. This is to be expected since **1-NEt2** has two degenerate resonance forms (**figure 2.28**) in the CS state, delocalizing the charge and reducing the difference between the excited state dipole moment and the ground state dipole moment ($\mu_e - \mu_g$).

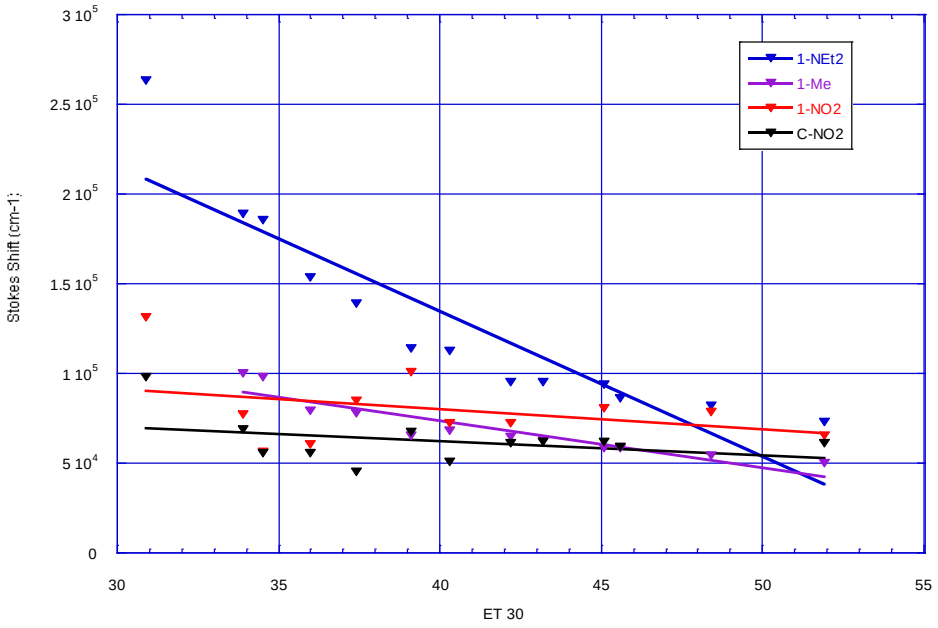

Figure 2.29: Stokes shifts trends for the cross conjugated dyes.
The linear fits are only to guide the eye.

As discussed in the previous section, calculations of the HOMO obtained from CAM-B3LYP/6-31G* calculations (**figure 2.12**) show that the electron density in the ground state is predominantly located on the diethylaminobenzene donor for **1-NEt2** and the LUMO while significantly delocalized shifts the electron density to the central carbonyl group. The molecule being symmetric, the HOMO is also symmetric on either side of the carbonyl group. This indicates that the individual dipoles on either side of the carbonyl are indeed as depicted in **figure 2.28** and that the excited state would have two degenerate resonance structures.

The HOMO for **1-Me** (**figure 2.12**) is present on the diethylaminobenzene donor as anticipated and no electron density observed on the methyl group indicating a lack of conjugation on two sides of the carbonyl group. Since the methyl group isn't a strong acceptor, the LUMO is more delocalized on the donor part of the molecule.

In the case of **1-NO2** the presence of an electron withdrawing group results in significantly lower fluorescence quantum yields than are seen for **1-NEt2** (**table 2.7 and figures 2.30**). Quantum yields drop off quite significantly as solvent polarity increases indicating solvent interaction and quenching of the fluorescent species. The conjugated **C-NO2** is a stronger fluorophore (**table 2.7** and **figure 2.32**) than **1-NO2** due to its longer conjugation length. However, as seen with **1-NO2** quantum yields drop in more polar and hydrogen bonding solvents.

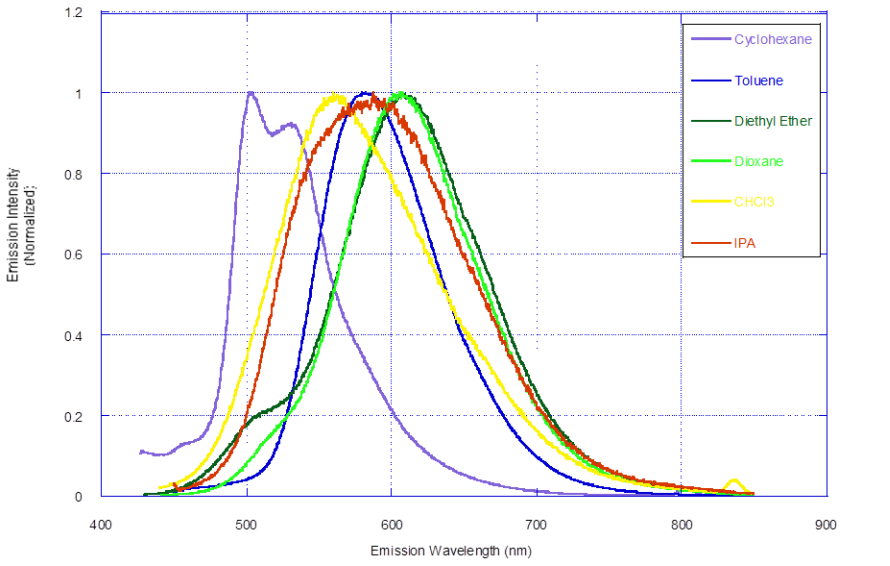

Figure 2.30: Normalized fluorescence for **1-NO2**
Solvents in the key are listed in order of increasing $E_T(30)$

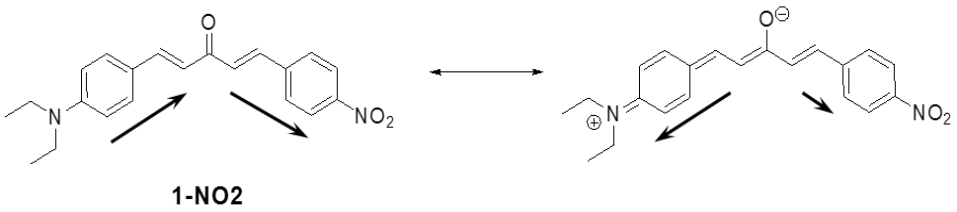

1-NO2

Figure 2.31: Neutral and charge separated states for **1-NO2**
The arrows next to the structures represent dipole moments

Compound **1-NO2** also shows positive solvatochromism of the emission spectra, however the correlation to solvent polarity (**figure 2.27**) is more complex than that seen for **1-Me** and **1-NEt2**. **1-NO2** emission wavelengths are higher than those for **1-NEt2** even though the absorption wavelengths for the two molecules are quite close indicating a lower energy excited state. This also leads to higher observed stokes shifts (**figure 2.29**) especially in low polarity solvents. Looking at the neutral and CS structures for **1-NO2** (**figure 2.31**), one can see that the nitro group stabilizes the charge separated state leading to lowering of the energy of the CS state compared to **1-NEt2**. While the CS state shown in **figure 2.31** is an approximation of the first excited state, it suggests that the as **1-NO2** tends towards an excited state structure, a partial lowering of the dipole is to be expected. This would explain the low energy emission wavelengths observed in non-polar solvents such as toluene, diethyl ether and 1,4-dioxane (**table 2.7**) as they would better stabilize a lower dipole moment excited state.

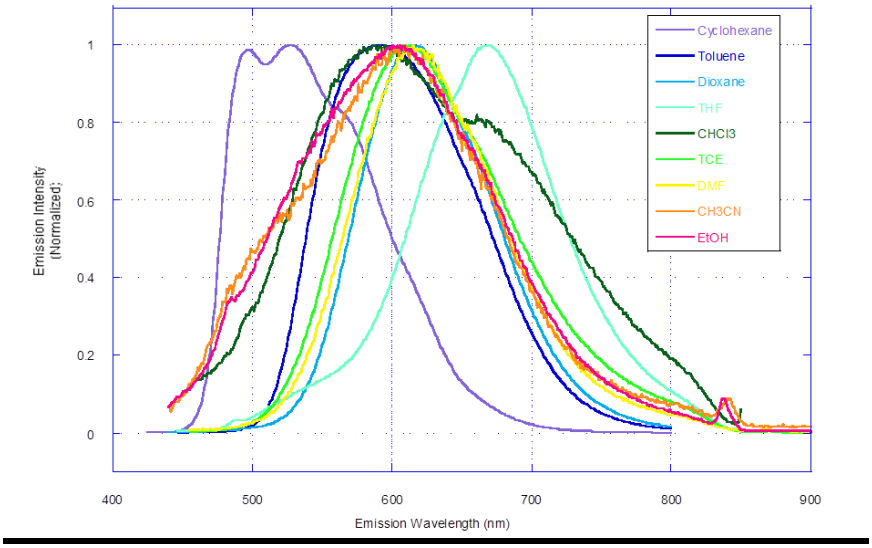

Figure 2.32: Normalized fluorescence for **C-NO2**
Solvents in the key are listed in order of increasing $E_T(30)$

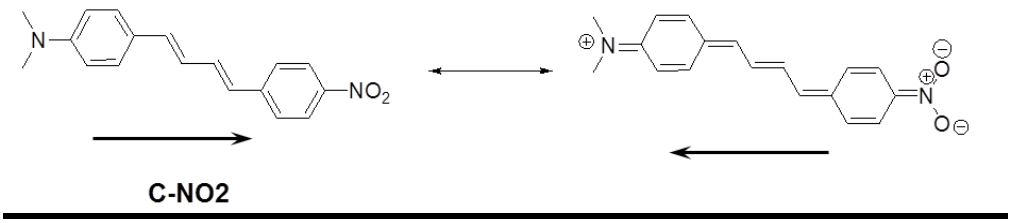

Figure 2.33: Neutral and charge separated states for **C-NO2**
The arrows next to the structures represent dipole moments

Emission wavelength data for conjugated control molecule **C-NO2** (**table 2.7**, **figure 2.27** and **figure 2.32**) shows no clear trend in solvatochromism. It seems to show a positive trend initially in going from cyclohexane to tetrahydrofuran and then a negative trend from tetrahydrofuran to ethanol. As seen in **figure 2.32** however, most of emission wavelengths are centered around 600nm except for cyclohexane and THF. While the absorbance wavelengths for **1-NO2** and **C-NO2** are similar, the emission wavelengths for **C-NO2** are red-shifted due to stabilization by the conjugated bridge. Stokes shift for this molecule does not change a lot signifying that the difference in ground state and excited state dipoles ($\mu_e - \mu_g$) is not high. Both states are expected to be highly polar as depicted in **figure 2.33.**

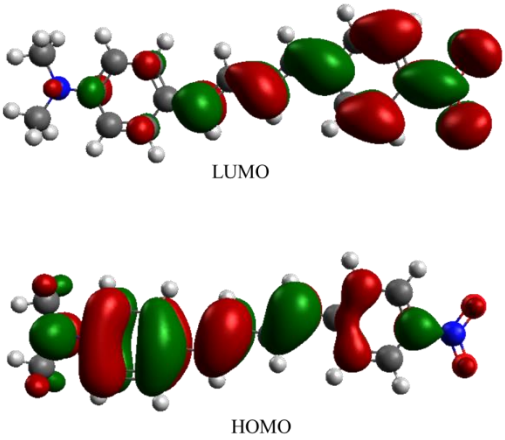

Figure 2.34: HOMO and LUMO diagrams for **C-NO2**

The molecular orbital picture obtained from CAM-B3LYP/6-31G* calculations for 1-NO2 indicate that the HOMO is located on the donor and the LUMO on the acceptor with very little overlap between the two (**figure 2.16**). This further supports the excited state structure as depicted in **figure 2.31**. **C-NO2** demonstrates a similarly situated HOMO and LUMO but with substantial overlap (**figure 2.34**) which likely results in high dipole moments in both ground and excited states.

2.4.1 **Fluorescence spectroscopy-Summary:**

In general the excited state of the donor substituted cross conjugated compounds **1-NEt2** is expected to be very similar to that of the methyl substituted cross conjugated compound **1-Me**. **1-NEt2** likely has a lower excited state dipole moment than **1-Me** due to the presence of two resonance structures in the possible excited state. **1-NEt2** and **1-Me** show strong, positive solvatochromic trends suggesting that the excited states are more polar than the ground states.

Acceptor substituted cross-conjugated compound **1-NO2** exhibits a lower energy excited state than **1-NEt2** due to stabilization of the charge separated species by the acceptor. The dipole of the excited state for this asymmetric molecule, while likely lower than the ground state, is also tuned by the polarity of the solvent. It is important to note that while the possibility of a biradical excited state has not been discussed here, it is conceivable that **1-NO2** may show a propensity for such a species due to dihedral twist between the donor and acceptor parts of the molecule. This may also explain its erratic behavior with regards to solvent polarity. Control molecule **C-NO2** shows the lowest energy emission wavelengths as well as low Stokes shifts due to its conjugated bridge.

2.5 **X-ray Diffraction (XRD):**

Due to the nature of the cross-conjugated center, the groups on either side of the carbonyl carbon can be viewed as independent units; hence the dipoles on cross-conjugated molecules are expected to be weaker than those for conjugated molecules. As seen in the UV-vis and fluorescence experiments, they are also strongly affected by their dielectric environment. Structure elucidation thus becomes essential to the understanding of their behavior.

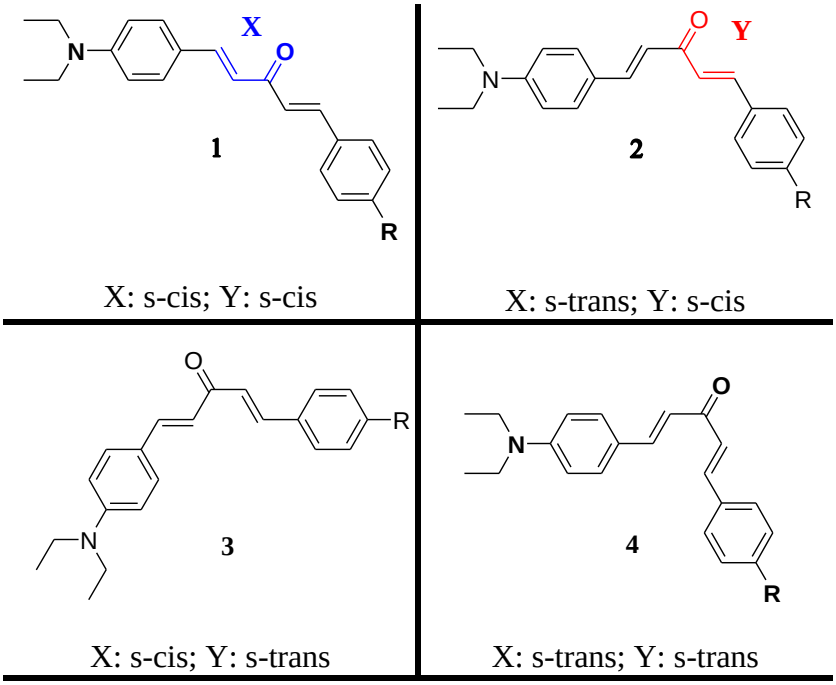

Figure 2.35: Cross-conjugated molecules; Possible rotational isomers

There are two important components to the structure of these molecules: (**a**) the stereochemistry of the two vinylic double bonds (depicted as X and Y in **figure 2.35**) and (**b**) the dihedral angle between the planes of the phenyl rings (depicted as A and B in **figure 2.36**) on either side of the ketone .

The double bond stereochemistry (**figure 2.35)** can either be s-cis or s-trans based on the relative position of the vinylic double bond to the ketone double bond. It must be noted that all the double bonds have trans configurations and are fixed based on lowest energy structures. This creates four possible rotational isomers as shown. The various O---H and H---H interactions from the carbonyl oxygen and the vinylic hydrogens being energetically inequivalent determine the likelihood of the existence of a conformer. For example, isomer **4** (**figure 2.35)** with two s-trans motifs in the cross-conjugated structure introduces two sterically hindered vinylic hydrogen atoms on the benzylic carbons making this isomer highly energetically unfavorable. Isomers **1**, **2** and **3** however are not hindered from inter-conversion as long as they do not go through isomer **4**.

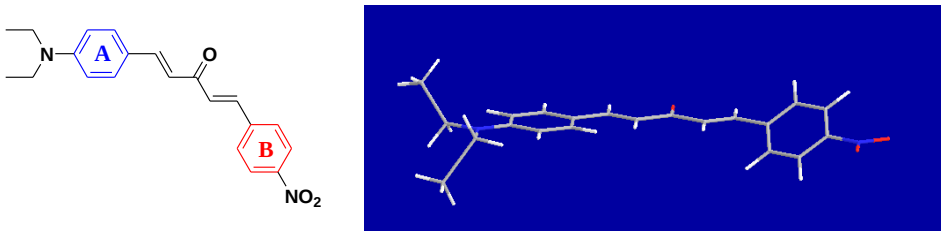

Figure 2.36: Possible twisted structure for cross conjugated molecules.

The dihedral angle between the two phenyl groups A and B as shown in **figure 2.36** on either side of the cross-conjugation center affects the conjugation from either end of the molecule to the center. The change in shape of molecules is known to affect dipole moments and hyperpolarizability of the molecule. Push-pull molecules that exist in a twisted conformation in the ground state but are planar in the excited state would conceivably have a large change in the dipole moments between ground and excited states. Such a phenomenon can lead to a large molecular first hyperpolarizibility β.

There is often a trade-off between dipole moment and poling efficiency. Typical high β chromophores with higher dipole moments interact more strongly with the applied electric field than chromophores with lower dipole moments. The disadvantage however is that chromophore dipole-dipole interactions are much stronger (as they scale with the square of the chromophore dipole moment (μ)) than dipole-electric field interactions (which scale linearly with μ). A lowering of the dipole moments due to twisted structures and cross-conjugated structures can give rise to higher poling efficiencies due to lower dipole-dipole interactions.

2.5.1 **Calculated geometries:**

Gaussian 09C was used to calculate optimized geometries using the B3LYP hybrid functional and the 6-31+G* basis set (**figure 2.37** and **figure 2.38**). These geometries were further used to calculate molecular hyperpolarizibilities (as discussed in the next section) as well as electronic transition energies (as discussed in the UV-Vis section).

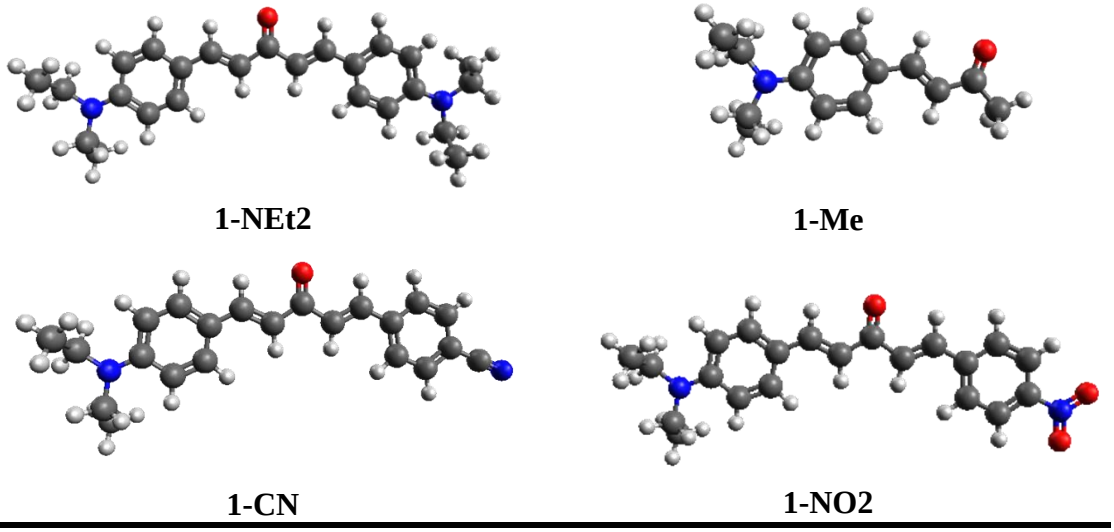

Figure 2.37: Optimized geometries of cross conjugated molecules from B3LYP calculations

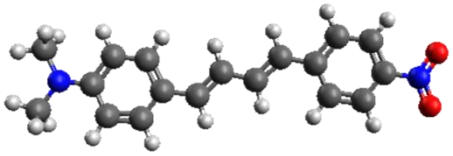

Figure 2.38: Optimized geometry of conjugated molecule **C-NO2** from B3LYP calculations

Calculated geometries indicate all s-cis conformations for the vinylic double bonds with respect to the ketone. The dihedral angle between the phenyl rings on either side of the cross conjugation center was found to be zero and the all molecules appear to be planar.

2.5.2 **Experimentally determined structures**

Crystals were grown of compounds **1-NEt2**, **1-Me**, **1-CN**, **1-NO2** and **C-NO2** (**figure 2.6**) and analyzed using X-ray diffraction. Crystals could not be grown of **1-Ph** and **1-F** (**figure 2.6**) as they were viscous liquids.

X-ray crystallographic data was collected at -173^{o}C on a Bruker APEX II single crystal X-ray diffractometer, Mo-radiation. The data was integrated and scaled using SAINT, SADABS within the APEX2 software package by Bruker. Complete crystallographic details and data tables can be found in the appendix to Chapter 2.

1-NEt2

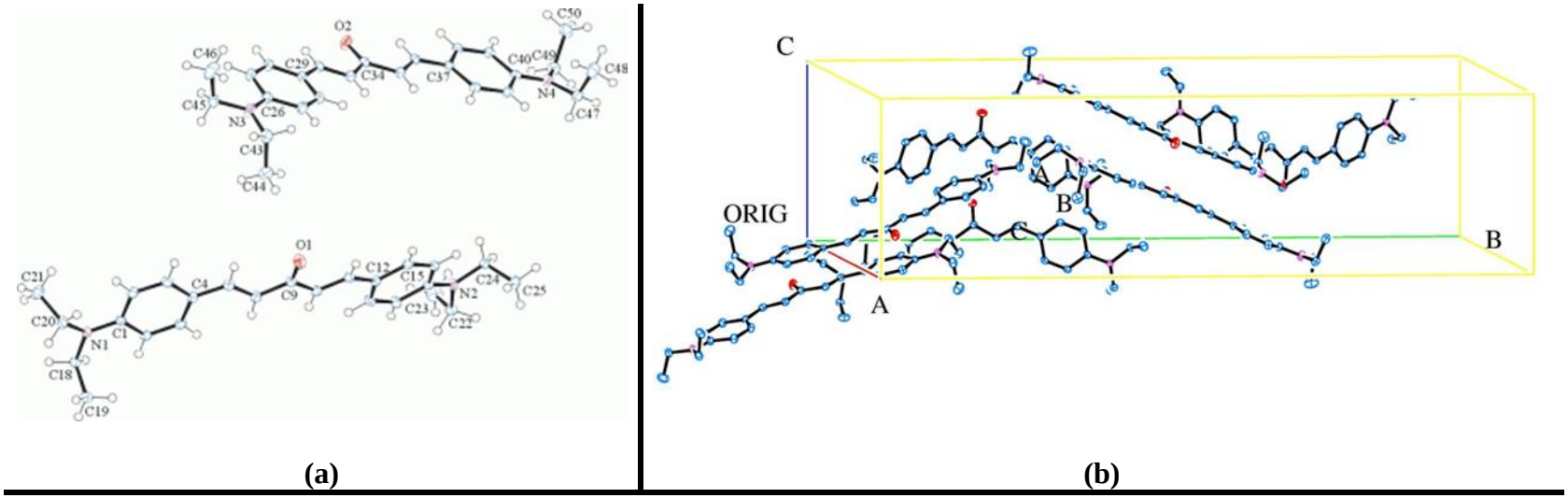

Figure 2.39: (a) ORTEP of the structure of **1-NEt2** with thermal ellipsoids at the 50% probability level. **(b)**Packing diagram of **1-NEt2**, omitting hydrogen for clarity.

Orange crystals of **1-NEt2** were grown from hot ethyl acetate. **Figure 2.39(a)** shows the crystal structure of **1-NEt2**. Trans stereochemistry is observed for both double bonds and s-cis geometries are indicated for double bonds with respect to the central ketone. No other isomers were seen. The two phenyl groups were found to be slightly twisted with respect to each other. **Figure 2.39(b)** shows the crystal packing of **1-NEt2**. It is a centrosymmetric molecule and the molecules in the crystal are connected via week van der Waals interactions. A zigzag plus ca. 90° tilt motif describes the packing structure best.

1-Me

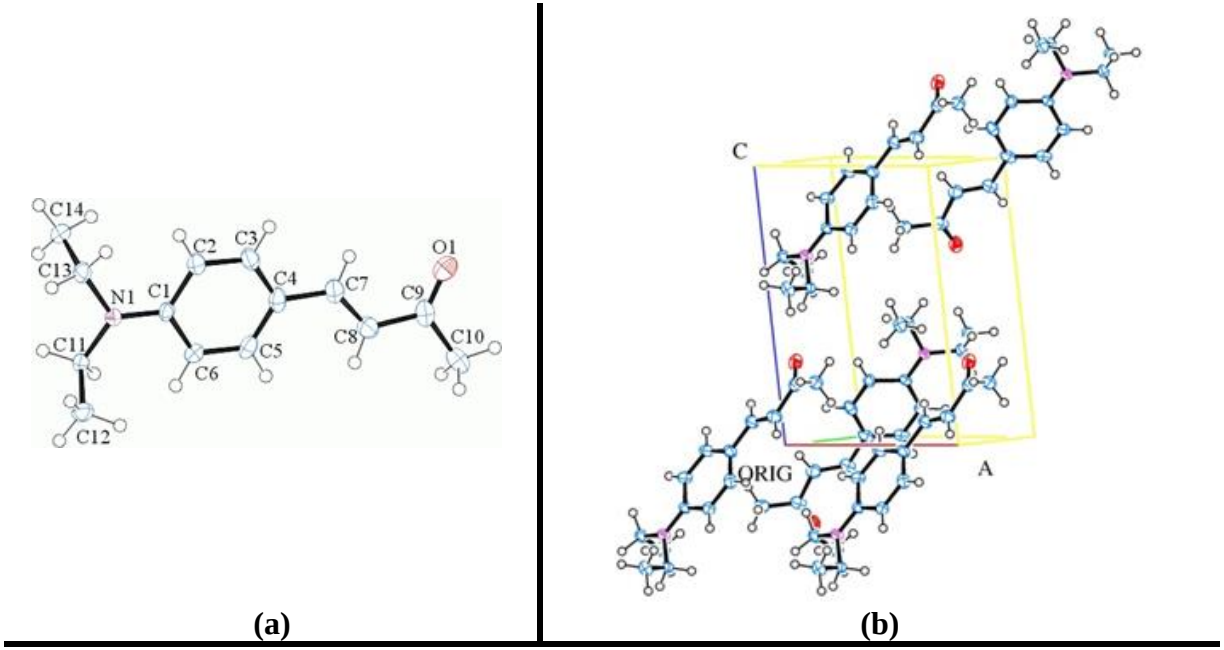

Figure 2.40: **(a)**ORTEP of the structure of **1-Me** with thermal ellipsoids at the 50% probability level. **(b)**Packing diagram of **1-Me**

Ethyl acetate/hexanes (8/2 v./v.) was used for growing yellow-orange **1-Me** crystals. **1-Me** shows a fairly planar structure (**figure 2.40(a)**). The double bond stereochemistry is trans and the vinylic double bond is in a s-cis configuration with respect to the ketone. The molecular structure itself is non-centrosymmetric but the crystal is ordered centrosymmetrically and the molecules are aligned with their long elongation parallel. Weak van der Waals interactions between ketones and methyl hydrogen atoms hold the molecules together.

1-CN

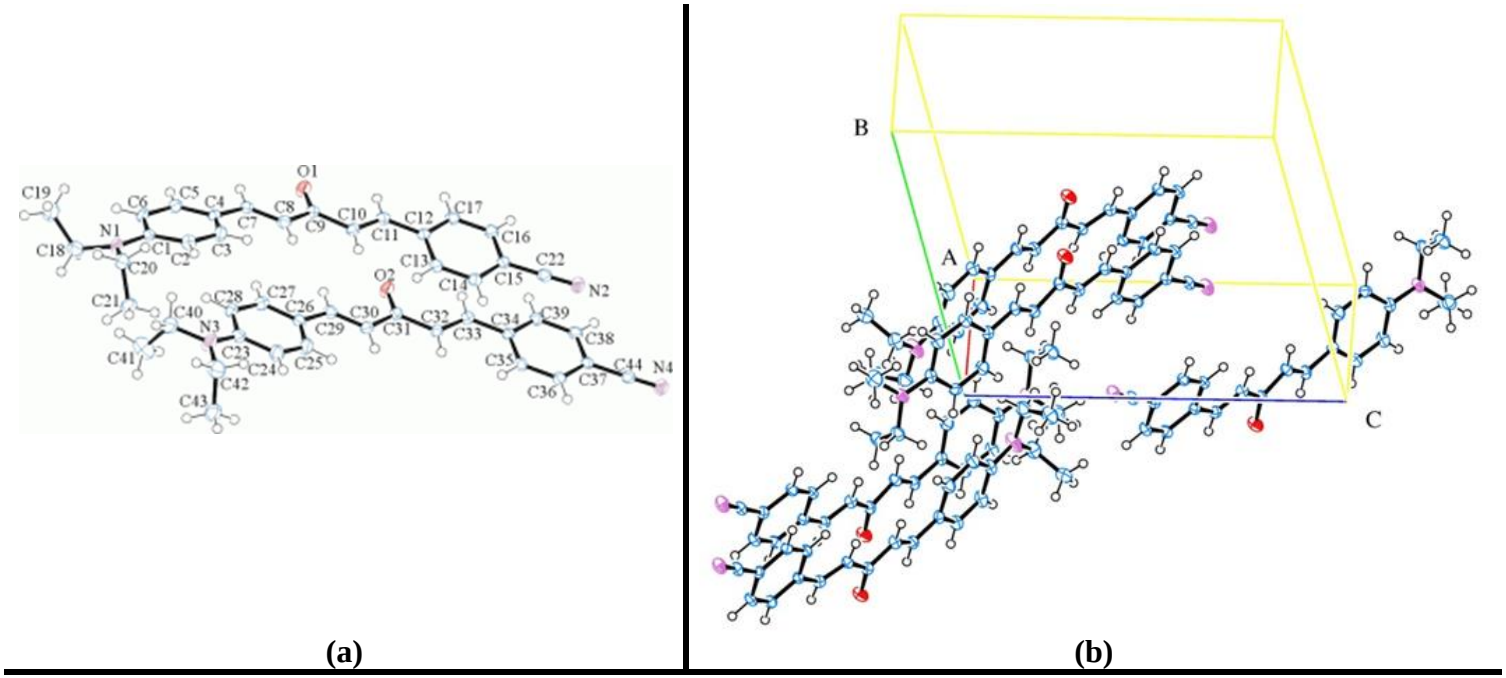

Figure 2.41: (a)ORTEP of the structure of **1-CN** with thermal ellipsoids at the 50% probability level. **(b)**Packing diagram of **1-CN**

Dark red crystals of **1-CN** were grown from hot ethyl acetate. The X-ray structure (**figure 2.41(a)**) shows s-cis geometries for both double bonds as well as trans stereochemistries. The cyano-benzene acceptor appears twisted slightly out of plane with respect to the diethylamino benzene donor. A pseudo-translational symmetry is observed between the two slightly different representations of the chromophore in the crystal structure (**figure 2.41(b)**). The crystal packing is centrosymmetric.

1-NO2

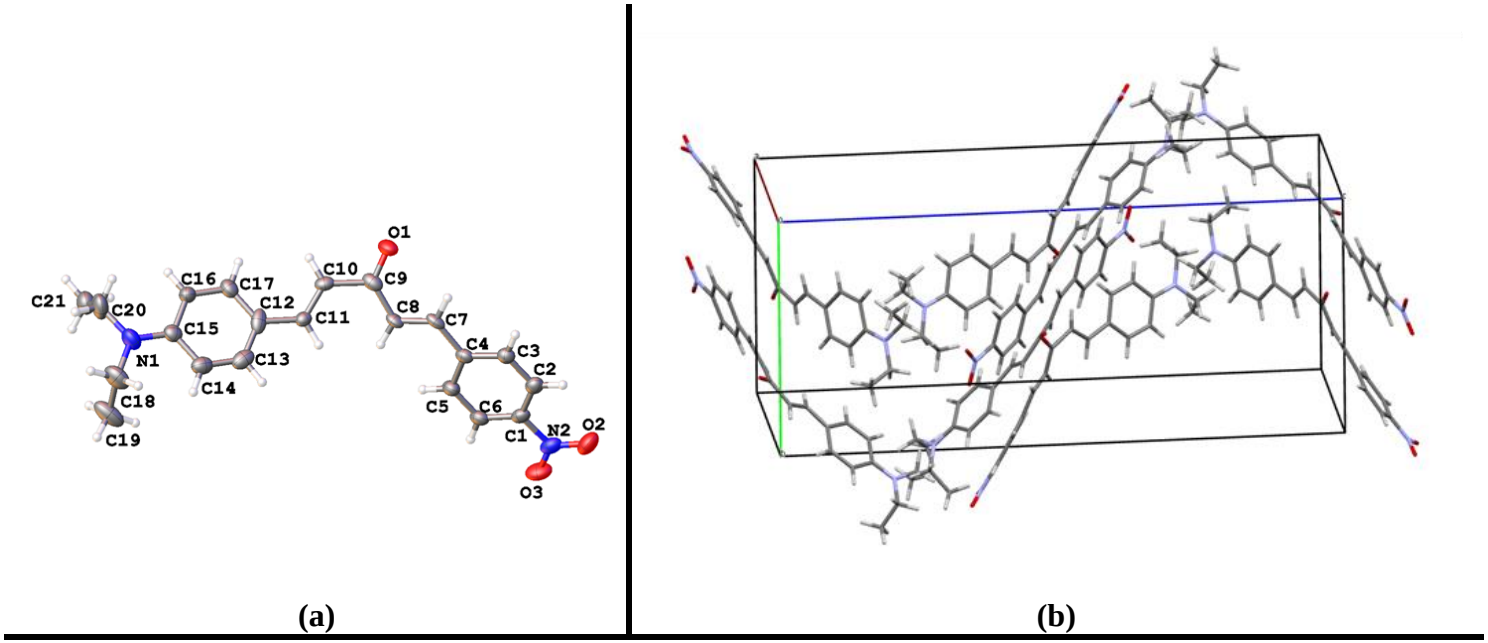

Figure 2.42: (a) ORTEP of the structure of **1-NO2** with thermal ellipsoids at the 50% probability level. **(b)**Packing diagram of **1-NO2**

Red **1-NO2** crystals were grown from hot ethyl acetate. Both double bond geometries were found to be trans (**figure 2.42(a)**). The X-ray data indicates that some parts of molecule are disordered and the crystal is centrosymmetric (**figure 2.42(b)**). The fragment NO2-Ph-C7-C8-C10-C11 is disordered over two positions (**figure 2.43**) with the occupancy ratio of 0.797(5):0.203(5). This means that the molecules in crystal statistically occupy two positions with a population of around. 8:2. The major structure is the one with s-

trans(C10-C11:C9-O1), s-cis (O1-C9:C8-C7) geometry while the minor structure has s-cis (C10-C11:C9-O1), s-trans (O1-C9:C8-C7)geometry. Both ethyl substituents at N1 atom are also disordered over two positions with the occupancy ratio of 0.896(6):0.104(6).

There also seems to be a substantial rotation of the nitrophenyl group with respect to the diethylaminobenzene. This is discussed later in this section

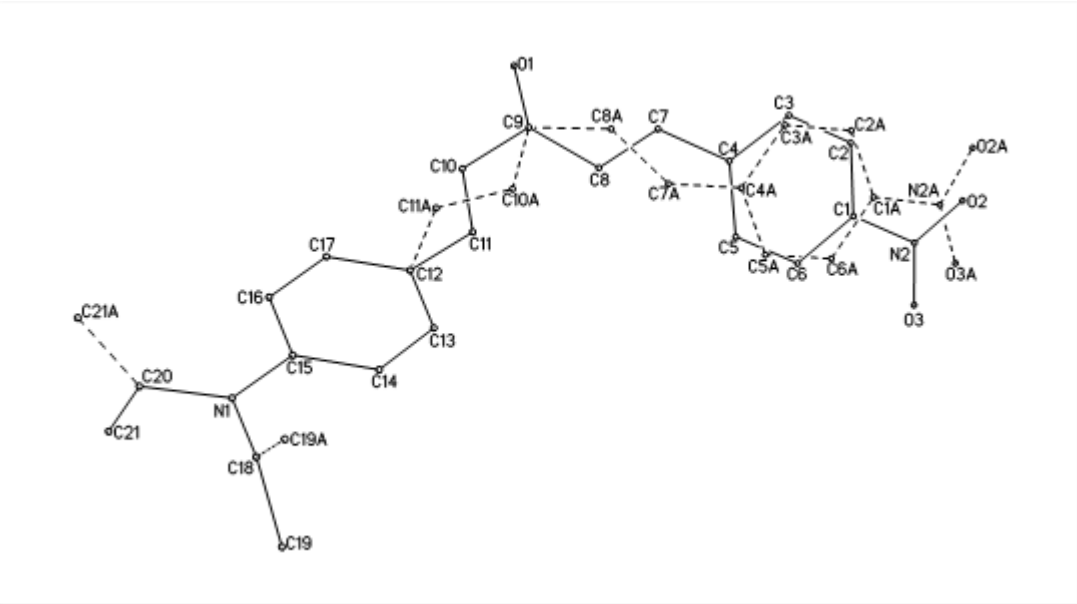

Figure 2.43: Scheme of disorder in the molecule **1-NO2**; bonds of the minor part are shown with dashed lines.

C-NO2

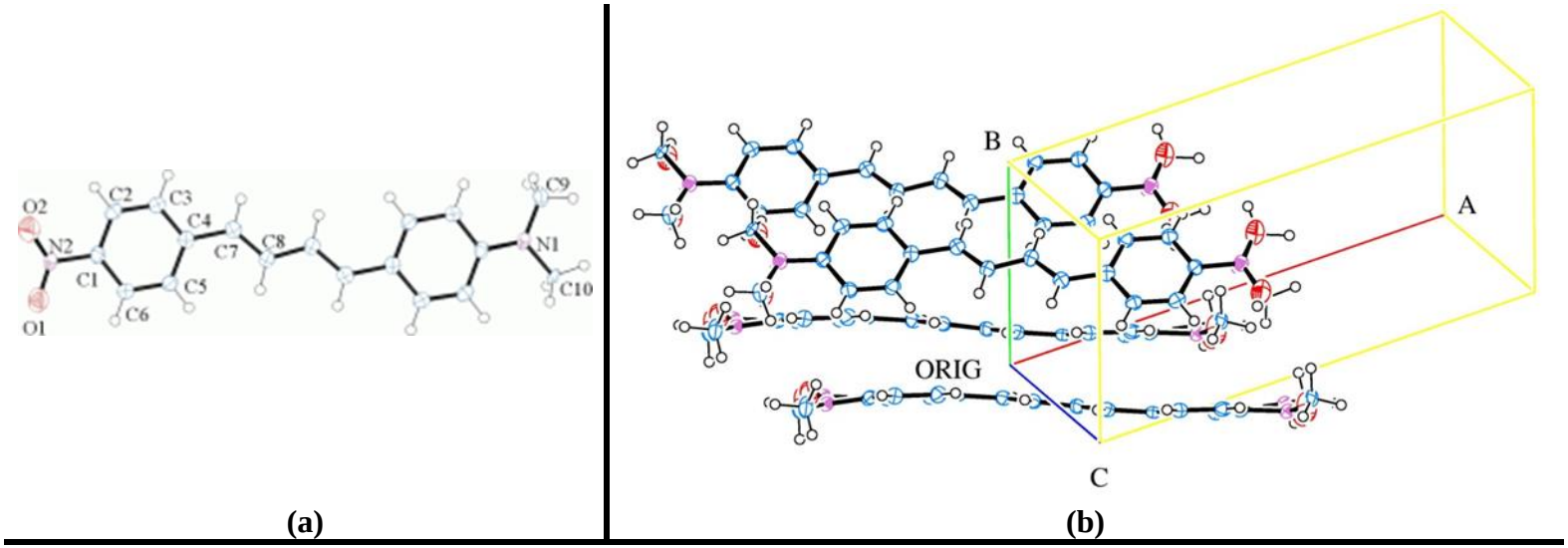

Figure 2.44: (a) ORTEP of the structure of **C-NO2** with thermal ellipsoids at the 50% probability level. (b)Packing diagram of **C-NO2**

Toluene was used for recrystallization of **C-NO2**. Crystal structure (**figure 2.44(a)**) shows trans stereochemistry for both double bonds. The terminal NO_2 and $N(CH_3)_2$ moieties are disordered with each other, where a twofold rotation reproduces the full molecule out of a half one. The molecules are aligned with their long elongation parallel and the crystal packing is centrosymmetric. A zig-zag rotation between neighboring molecules appears perpendicular to that direction. The structure is planar with a dihedral angle of 0°, as would be expected for a fully conjugated molecule.

2.5.3 **Dihedral angles:**

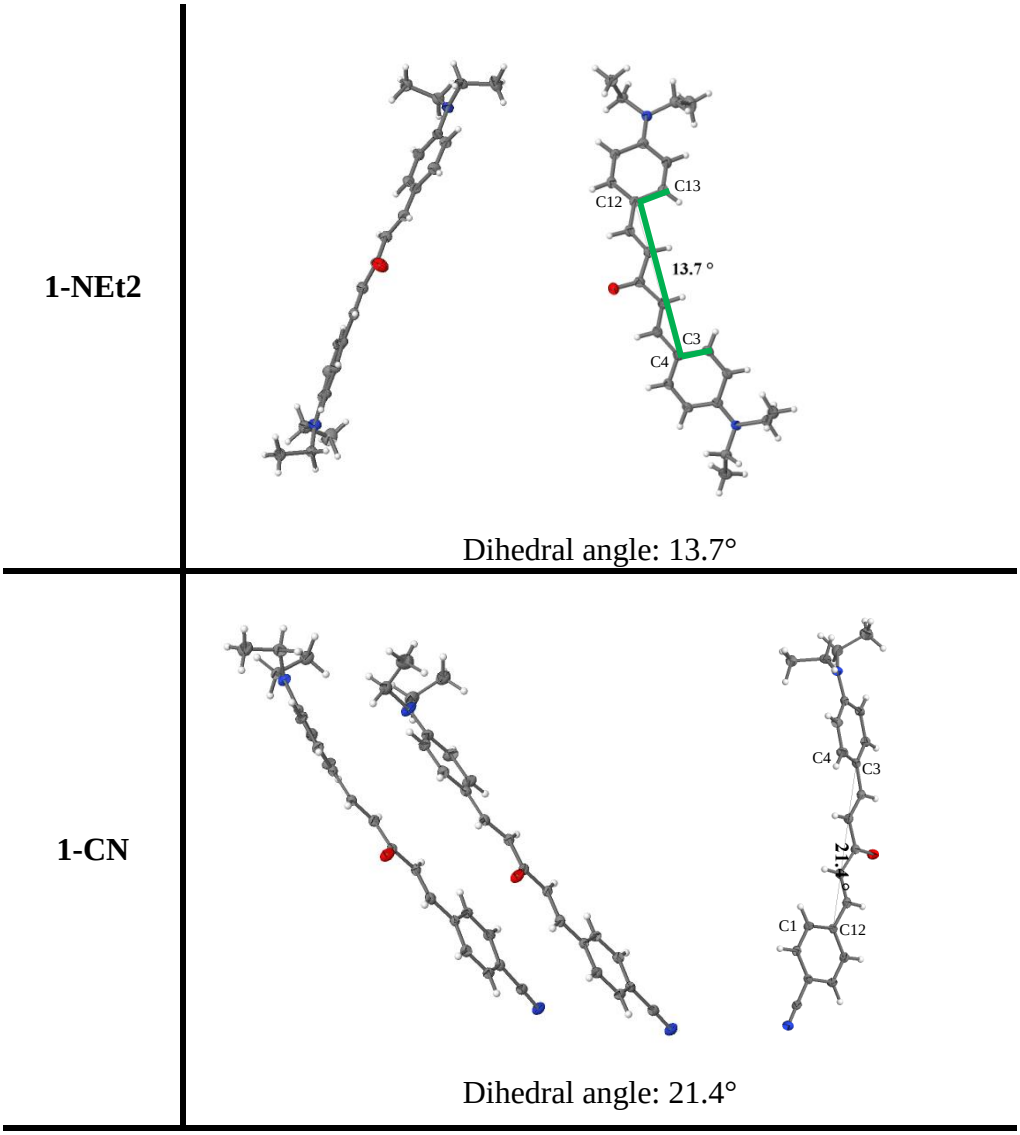

Figure 2.45: Dihedral angles between phenyl groups on either side of cross-conjugation center of molecules **1-NEt2** and **1-CN**

The dihedral angle between the planes of the two phenyl rings on either side of the carbonyl was measured using the carbons C3-C4-C12-C13 from crystallographic structures for molecules **1-NEt2**, **1-CN**. The angle was found to be 13.7° in **1-NEt2** (**figure 2.45(top**))and 21.4° in **1-CN** (**figure 2.45(bottom)**). The dihedral angle between the diethylamino phenyl donor and the nitrophenyl acceptor for **1-NO2** (measured using carbons C4-C5-C12-C13) is

significantly larger at 59.5° (**Figure 2.46(top)**). **C-NO2** has planar geometry with no twisting about any of the phenyl rings (**figure 2.46(bottom)**).

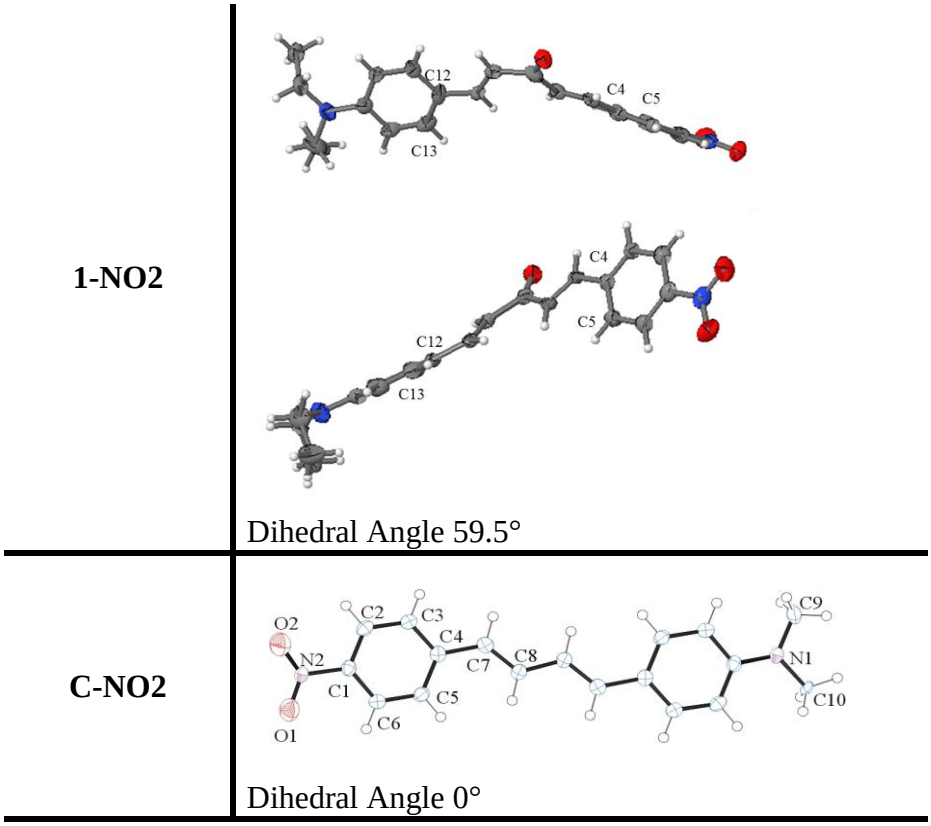

Figure 2.46: Dihedral angles between phenyl groups on either side of cross-conjugation center of molecules **1-NO2** and **C-NO2**.

The lack of planarity between the aromatic rings in the cross-conjugated molecules is an indication of the lack of orbital overlap between the two ends. The twist between the two phenyl rings increases with increasing strength of acceptor. It must be noted that for **1-NO2**, the angle between the diethylamino phenyl group and the ketone is 25° and that between the nitrophenyl group and the ketone is 28.5° indicating that the short conjugation existing between the two ends and the bridge is further compromised in the case of **1-NO2**.

2.6 **Hyper-Rayleigh Scattering (HRS) Measurements:**

2.6.1 **Experimental details:**

All HRS measurements were performed by Prof David Shelton (Department of Physics, University of Nevada, Las Vegas, NV).

The β values for the chromophores in $CDCl_3$ solution were determined from hyper-Rayleigh scattering (HRS) measurements at a laser wavelength of 1064 nm (using a pulsed Nd:YAG laser) and sample temperature 25°C. Calibration of the HRS results used 4-nitroaniline (pNA) in $CDCl_3$ solution as a reference standard. Dilute solutions of pNA (36.4mM), **1-NO2** (38.4μM) and **C-NO2** (43μM) in $CDCl_3$ were freshly prepared for each measurement. The solution concentrations were chosen to give comparable signals for the chromophore and reference solutions, and the much smaller HRS signal measured for the neat solvent was subtracted. Sample and reference HRS signals were compared using the same laser focusing, collection optics and polarization configuration, using apparatus and techniques as previously described[81]. The laser power incident on the sample was adjusted without affecting the alignment or focusing of the laser beam using a half-wave plate and polarizer combination. The sample absorption at the 532 nm second harmonic wavelength was measured and the HRS signals were corrected for the small self-absorption of the scattered light along the 1.5 mm path to the cuvette exit face. The HRS signal at 532 nm was corrected for thermal lensing effect as well as any two photon fluorescence contribution. Further details are provided in the appendix to Chapter 2.

2.6.2 **Theory details:**

All quantum mechanical calculations for these molecules were performed by Kerry E. Garrett. Quantum calculations for were performed using three levels of theory:

1) The mild hybrid density functional B3LYP, which includes a constant 20% Hartree-Fock (HF) exchange over the electronic interaction range to correct for the asymptotic decay of the exchange potential at long range.
2) CAM-B3LYP which divides the exchange into short-range and long-range parts with 19% and 46% HF exchange respectively and
3) Second order Møller-Plesset perturbation (MP2), a computationally-feasible correlated wavefunction method that was used for comparison with DFT.

The static hyperpolarizabilities, $\beta_{HRS}(0)$ were corrected for dispersion at 1064 nm with a damping factor, γ, set to 100 nm chosen so to match the full-width at half-maximum of the experimental spectra. The theoretical absorption wavelengths, used in the two-state model were provided using CAM-B3LYP/6-31+G*. Additionally, for comparison with the two-state model, frequency-dependent hyperpolarizabilities, $\beta_{HRS}(2\omega)$, were calculated at 1064 nm using the coupled-perturbed Kohn-Sham (CPKS) method for both B3LYP and CAM-B3LYP functionals. All of the above methods – B3LYP, CAM-B3LYP, and MP2 –consistently used 6-31+G* basis and with solvent effects according to the polarizable continuum method (PCM) for all of the properties calculations on PCM-B3LYP/6-31+G* optimized geometries. All quantum calculations were performed using Gaussian 09 Rev. D.01 suite of QM codes.

The experimental HRS measurements give frequency dependent hyperpolarizability values with respect to a reference molecule (**pNA** in this case) thus the data obtained from HRS experiments are the $(\beta_{HRS}/\beta_{pNA})_{1064}$ values in **table 2.10**. It must be noted that resonance enhancement at the

frequency doubled 532 nm of the β_{HRS} values it is expected for **1-NO2** and **C-NO2** although they are likely to be of a similar magnitude for both molecules since their absorption wavelengths and molar absorptivities are are quite similar as observed in their optical transition data (**figure 2.24**). To account for any enhancement observed in the measurement, the experimental static hyperpolarizability ratios, $\beta_{HRS(0)}/\beta_{pNA(0)}$ (**table 2.11**) were extrapolated from the frequency dependent ratios using the two level model (TLM) equation developed by Oudar and Chemla[14]. Extrapolation to the static limit becomes increasingly unreliable however as resonance is approached because line broadening effects need to be taken into account. A correction factor thus applied to the TLM equation to give the damped two level model dispersion fit (see appendix to Chapter 2).

The experimentally obtained value for β_{HRS} at 1064 nm for 4-nitroaniline, 11.4×10^{-30} esu was used to convert the $(\beta_{HRS}/\beta_{pNA})_{1064}$ ratios to $\beta_{HRS(1064)}$ for both molecules (**table 2.8)**. The static $\beta_{HRS(0,TLM)}$ value for pNa was extrapolated using the TLM expression in a fashion similar to that described above. This value was used multiplied with the $\beta_{HRS(0)}/\beta_{pNA(0)}$ values to give the static hyperpolarizibilities for both molecules (**table 2.9)**. Structures for the **pNA**, **1-NO2** and **C-NO2** are shown in **figure 2.47** for convenience

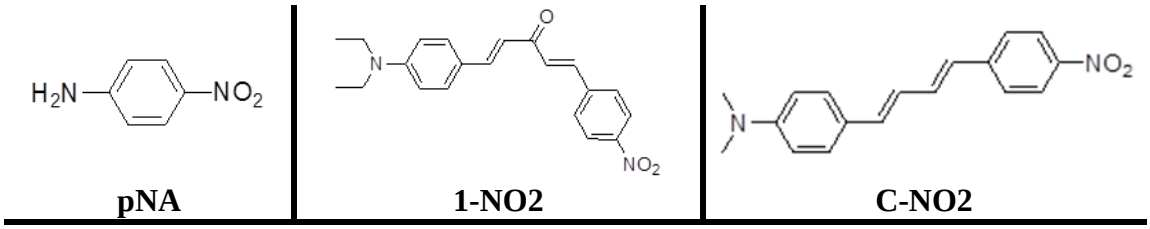

Figure 2.47: Structures for **pNA**, **1-NO2** and **C-NO2**

2.6.3 **Hyper-Rayleigh scattering - Discussion:**

The frequency dependent hyperpolarizability $\beta_{HRS(1064)}$ for **1-NO2** was significantly overestimated (by a factor of ~1.73) by B3LYP calculations and largely underestimated by both CAM B3LYP and MP2 calculations by factors of 2.6 and 2.5 respectively. MP2 calculations for C-NO2 were quite accurate however and the CAM B3LYP value was underestimated by only a factor of 1.25.

Compound	$\beta_{HRS(1064)}$ (10^{-30} esu)			
	Experimental	B3LYP/ 6-31+G*	CAM B3LYP/ 6-31+G*	MP2/ 6-31+G*
pNA	11.4	20.2	14.6	13.1
1-NO2	627	1084	277.5	247
C-NO2	700	1816	559.8	641

Table 2.8: Experimental and Calculated Frequency Dependent β_{HRS} values.

For the static values once again B3LYP, overestimating by a factor of 1.25 was found to be a better predictor for **1-NO2** compared to CAM B3LYP and MP2 functionals which underestimate by factors of 2.4 and 2 respectively. B3LYP was found to overestimate static hyperpolarizability values for **C-NO2** by a factor of 1.7 and CAM B3LYP and MP2 were found to underestimate this value by factors of 1.8 and 1.4 respectively.

Compound	$\beta_{HRS(0,TLM)}$ (10^{-30} esu)			
	Experimental	B3LYP/ 6-31+G*	CAM B3LYP/ 6-31+G*	MP2/ 6-31+G*
pNA	6.29	9.21	8.02	7.76
1-NO2	156.63	196	66.43	77
C-NO2	197.04	338	111	141

Table 2.9: Experimental and Calculated β_0 values

All three methods do catch the trend of higher hyperpolarizability values for **C-NO2** than for **1-NO2** albeit to different extents

Hyperpolarizability ratios are often more helpful in analyzing the accuracy and trends of the values obtained by quantum calculations as most calculations may over or underestimate the absolute hyperpolarizability values by a consistent factor.

The experimental values for $(\beta_{HRS}/ \beta_{pNA})_{1064}$ of **1-NO2** was predicted quite accurately by B3LYP calculations. Both CAM B3LYP and MP2 calculations on the other hand significantly underestimate this ratio by a factor of around 2.9. A similar trend is observed for the static ratios, $\beta_{HRS(0)}/\beta_{PNA(0)}$ where the B3LYP value (21.3) comes close to the experimental ratio (24.9) while CAM B3LYP (8.28) and MP2 (9.92) once again significantly underestimate the values by factors of 3 and 2.5 respectively.

The frequency dependent ratios for **C-NO2** were underestimated only by a factor of ~1.25 by MP2 and by a factor of ~1.6 by CAM B3LYP calculations while B3LYP overestimated the ratio by a factor of ~1.86. The static ratios for **C-NO2** were better predicted by B3LYP calculations while CAM B3LYP and MP2 calculations were underestimated by factors of 2.27 and 1.7 respectively.

Compound	$(\beta_{HRS}/\beta_{pNA})_{1064}$			
	Experimental	B3LYP/ 6-31+G*	CAM B3LYP/ 6-31+G*	MP2/ 6-31+G*
pNA	1	1	1	1
1-NO2	55	53.66	18.97	19
C-NO2	61.4	89.84	38.27	49

Table 2.10: Experimental and Calculated Frequency Dependent β_{HRS}/β_{pNA} values

Compound	$\beta_{HRS(0)}/\beta_{pNA(0)}$			
	Experimental	B3LYP/ 6-31+G*	CAM B3LYP/ 6-31+G*	MP2/ 6-31+G*
pNA	1	1	1	1
1-NO2	24.9	21.3	8.28	9.92
C-NO2	31.32	36.8	13.8	18.17

Table 2.11: Experimental and Calculated Static β_{HRS}/β_{pNA} values

Comparing the β_{HRS}/β_{pNA} values for the conjugated versus the cross-conjugated molecule the frequency dependent value for **C-NO2** was found to be higher than that of **1-NO2** by a factor of ~1.12 while the static value was higher by a factor of 1.26. It is there for safe to say that while the introduction of a cross-conjugated center might reduce the molecular hyperpolarizability β slightly, it is not so detrimental so as to render the motif impractical for use in second order non-linear materials.

2.6.4 **Hyper-Rayleigh scattering measurements-Summary**

The frequency dependent $\boldsymbol{\beta_{HRS(1064)}}$ value for **1-NO2** was not predicted very well by any of the methods investigated here and only the B3LYP functional comes closest to the experimental value. The $\boldsymbol{\beta_{HRS(1064)}}$ value for the conjugated **C-NO2** molecule was predicted accurately by CAM-B3LYP and MP2 methods. The static hyperpolarizability $\boldsymbol{\beta_{HRS(0,TLM)}}$ value for **1-NO2** was found to be predicted best once again by B3LYP much better than the frequency dependent value. The static value for C-NO2 was found to be predicted most accurately by the MP2 functional albeit off by a factor of 1.4

Overall, B3LYP provided fairly accurate values for static ratios $\beta_{HRS(0)}/\beta_{PNA(0)}$ for both the cross conjugated **1-NO2** and the conjugated **C-NO2**. MP2 calculations were found to be better for the frequency dependent ratios $(\beta_{HRS}/\beta_{pNA})_{1064}$ of the conjugated molecule and B3LYP once again worked well for the cross conjugated molecule.

Most importantly, experimental hyperpolarizability numbers for **1-NO2** were lower than those of **C-NO2** only by factors of 1.12 for frequency dependent values and 1.26 for the static values. This suggests that cross-conjugated motifs are reasonable for use in second order non-linear molecules.

2.7 **Conclusions to Chapter 2:**

The synthesis and characterization of six cross-conjugated molecules **1-NEt2**, **1-Me**, **1-Ph**, **1-PhF**, **1-CN** and **1-NO2** and one conjugated control molecule **C-NO2** has been described. Their electronic properties were investigated using UV-vis spectroscopy and compared with quantum mechanical calculations. The primary optical absorbance of the cross-conjugated molecules was identified as a charge-transfer transition from the HOMO on the diethylamino donor to the LUMO on the acceptor. These transitions were especially evident for **1-CN** and **1-NO2** clearly indicating that the primary transition occurs across the cross-conjugated carbonyl bridge.

The presence of the cross-conjugated bridge also causes unusual behavior in the fluorescence spectrum of the asymmetric molecule **1-NO2**, i.e. lower energy emission wavelengths in non-polar solvents. This suggests a lower excited state dipole in **1-NO2** that can be explained by breaking the molecular dipole into two constituent parts as shown in **figure 2.31**.

The crystal structures of the cross-conjugated molecules **1-NEt2**, **1-Me**, **1-CN** and **1-NO2** and the conjugated molecule **C-NO2** were studied using X-ray diffraction. It was found that the quite unexpectedly, cross-conjugated molecules exhibited dihedral twists ranging from ~14° (for **1-NEt2**) to 59.5° (for **1-NO2**)

Finally HRS measurements comparing **1-NO2** and **C-NO2** found that the cross-conjugation reduces hyperpolarizability only by about 12-26% compared to the full conjugated molecule.

2.8 **Appendix to Chapter 2**

2.8.1 **Synthesis of cross-conjugated chromophores:**

Experimental:

All reactions were carried out under a nitrogen atmosphere in flame-dried glassware. Standard air-free techniques were used for handling air and moisture sensitive reagents. All solvents were used as received from commercial suppliers. All NMR spectra were recorded using Bruker 300 MHz and Bruker 500 MHz spectrometers. Chemical shifts (δ) are given in parts per million (ppm) and measured against residual solvent peaks as internal standards. Coupling constants (J) are given in Hertz (Hz). UV-Vis spectra were recorded on the Agilent 8453 spectrophotometer. Fluorescence spectra were recorded on the Horiba FL3-21tau fluorescence spectrophotometer. Fresh solvents were used for solution preparation.

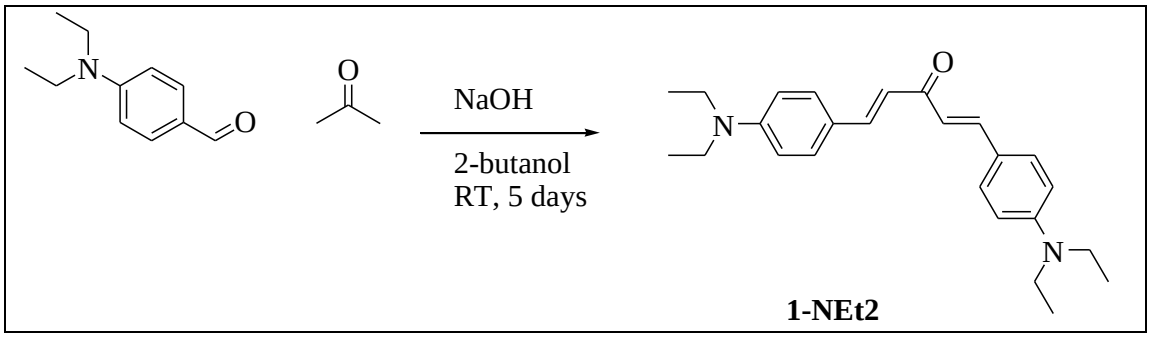

1-NEt2

1-NEt2: 4-Diethylaminobenzaldehyde (1.77g, 9.98mmol), acetone (0.29g, 4.99mmol), NaOH (1.4 g 25% aq., 62.5mmol) and 2-butanol (25 mL) were charged into a 100mL round bottom flask and stirred at room temperature under nitrogen for 5 days. Orange solids had crashed out of solution; these were filtered over a Buchner funnel, washed with 2-butanol and dried under vacuum for 2 days. The solid was then re-dissolved in dichloromethane (100mL), washed with NH_4Cl (3x100mL) dried over $MgSO_4$, filtered and stripped of solvent. The solids

were dried under vacuum to give pure product. (0.4g, 11%). ^{1}H NMR (300MHz,$CDCl_3$): δ 7.67 (d, J = 15.7Hz, 1H), 7.49 (d, J = 8.9Hz, 2H), 6.86 (d, J = 15.7Hz, 1H), 6.65 (d, J = 8.9Hz, 2H), 3.41 (q, J = 7.1Hz, 4H), 1.2 (t, J = 7.1Hz, 6H). HRMS (ESI) (M+, $C_{25}H_{32}N_2O$): calcd, 376.2515; found, 377.26232 [M+H].

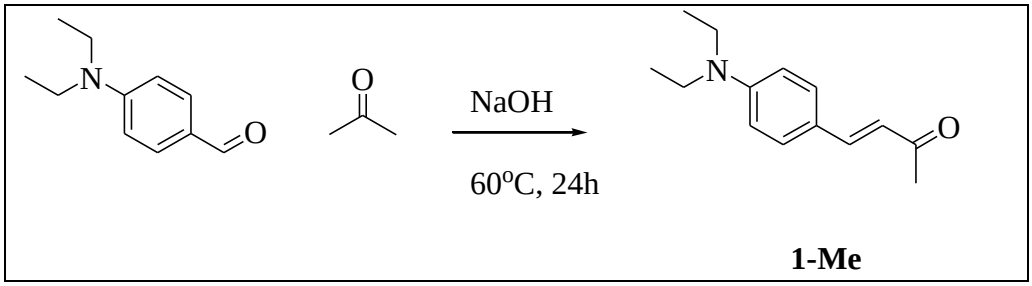

1-Me

1-Me: 4-Diethylaminobenzaldehyde (2g, 11.28mmol) was added to acetone (5mL) in a 50mL round bottom flask and allowed to stir until dissolved. 50% aqueous NaOH (2mL) was added and stirred for 5 min followed by addition of deionized water (4mL) and heating at 60°C overnight. Heating was stopped and the solvent was removed by rotary evaporation. The crude reaction was made acidic by dropwize addition of 6M HCl. The reaction was redissolved in CH_2Cl_2 (150mL) and washed with aq. sat. NH_4Cl (4x50mL), dried over $MgSO_4$, filtered and stripped of solvent. Purification was achieved by silica gel chromatography in Ethyl Acetate/Hexanes 2/8 to yield pure product. (1.77g, 72%). ^{1}H NMR ($CDCl_3$): δ 7.45 (d, J = 15.9Hz, 1H), 7.41 (d, J = 9Hz, 2H), 6.64 (d, J = 9Hz, 2H), 6.52 (d, J = 15.9Hz, 1H), 3.4 (q, J = 7.2Hz, 4H), 2.33 (s, 3H), 1.19 (t, J = 7.2Hz, 6H). HRMS (ESI) (M+, $C_{14}H_{19}NO$): calcd, 217.1467; found, 218.1564 [M+H].

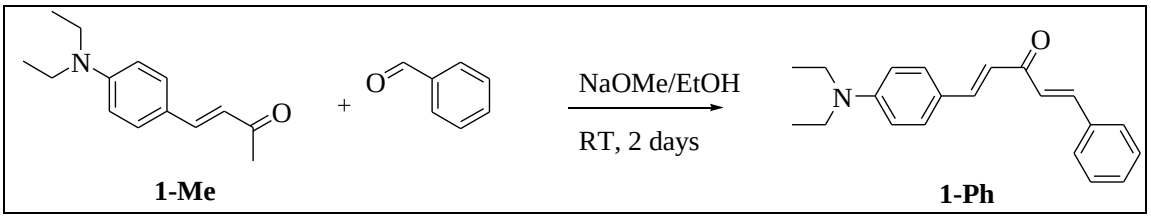

1-Me **1-Ph**

1-Ph: All glassware was flame-dried prior to use. **1-Me** (0.5g 2.3mmol) and benzaldehyde (0.465mL, 4.6mmol) were dissolved in ethanol (6mL) in a 25mL round bottom flask. NaOMe solution was prepared by reacting sodium (0.116g, 3.9mmol) with methanol (6mL) in a separate 25mL flask. It was then added to the reaction dropwise and the reaction was allowed to stir at room temperature for 2-3 days. Reaction was monitored via GC-MS until there was no more increase in formation of product was seen. All the solvent was evaporated. The reaction was redissolved in dichloromethane (50mL), washed with aq. sat. NH_4Cl (3x50mL), dried over $MgSO_4$, filtered and stripped of solvent. Column chromatography (0.5/1.5/8.5 acetonitrile/ethyl acetate petroleum ether) was performed to give final product. (0.14g, 24%). ^1H NMR ($CDCl_3$) δ 7.75 (d, J = 15.6Hz, 1H), 7.74 (d, J = 15.9Hz, 1H), 7.638 (m, 2H), 7.52 (d, J = 9Hz, 2H), 7.41 (m, 3H), 7.13 (d, J = 15.9Hz, 1H), 6.89 (d, J = 15.6Hz, 1H), 6.67 (d, J = 9Hz, 1H), 3.41 (q, J = 7.06Hz, 4H), 1.21 (t, J = 7.06Hz, 6H). HRMS (ESI) (M+, $C_{21}H_{23}NO$): calcd, 305.178; found, 306.18849 [M+H].

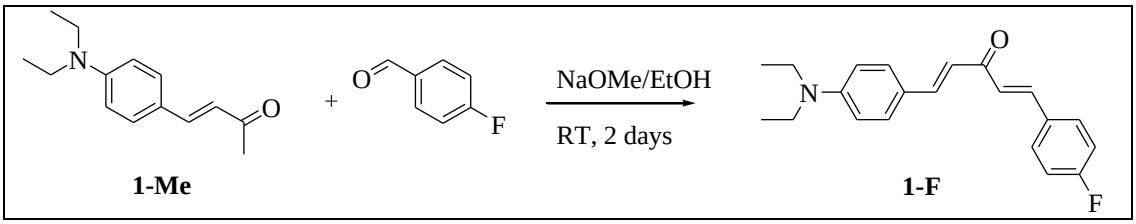

1-Me **1-F**

1-F: All glassware was flame-dried prior to use. **1-Me** (0.15g 0.69mmol) and 4-fluorobenzaldehyde (0.111mL, 1.035mmol) were dissolved in ethanol (13mL) in a 25mL round bottom flask. NaOMe solution was prepared by reacting sodium (0.027g, 1.17mmol) with methanol (2.5mL) in a separate 25mL flask. It was then added to the reaction dropwise and the reaction was allowed to stir at room temperature for 2 days. All the solvent was evaporated. The reaction was re-dissolved in dichloromethane (50mL), washed with aq. sat NH_4Cl (3x50mL), dried over $MgSO_4$, filtered and stripped of solvent. Column chromatography (1/1 dichloromethane/hexanes to 100 % dichloromethane to 5% ethyl acetate/dichloromethane) was performed to give final product. (0.12g,54%). ^{1}H NMR ($CDCl_3$, 500MHz) δ 7.71 (d, J = 15.5Hz, 1H), 7.66 (d, J = 16Hz, 1H), 7.588 (dd J = 8.76Hz, J = 8.75Hz, 2H), 7.49 (d, J = 8.94Hz, 2H), 7.08 (dd, J = 8.07Hz, J = 8.09Hz, 2H), 7.02 (d, J = 16Hz, 1H), 6.83 (d, J = 15.5Hz, 1H), 6.65 (d, J = 8.94Hz, 2H), 3.41 (q, J = 7.1Hz, 4H), 1.2 (t, J = 7.1Hz, 6H) ^{19}F NMR ($CDCl_3$) δ 110.88. HRMS (ESI) (M+, $C_{21}H_{22}FNO$): calcd, 323.1685; found, 324.17903 [M+H].

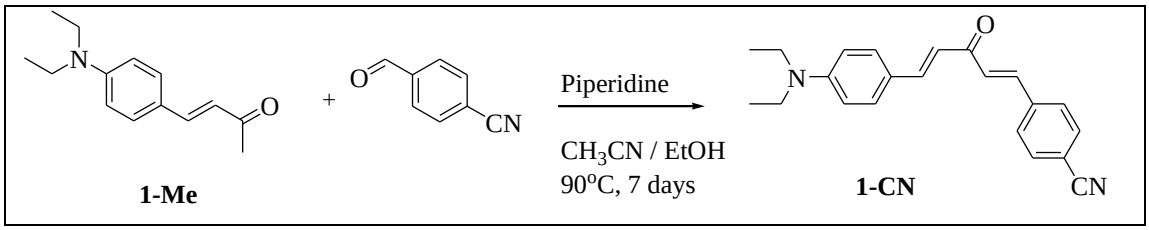

1-CN: 1-Me (0.5g, 2.3mmol) and 4-cyanobenzaldehyde (0.452g, 3.45mmol) were added to a 50 mL round bottom flask and dissolved in 13mL of 1/1 acetonitrile/ethanol solution. Piperidine (15 drops, catalytic) was added, a water jacketed condenser was attached to the flask and the reaction was heated to 90°C for 7 days. Heating was stopped and the solvent was stripped from the reaction. The resulting crude was redissolved in dichloromethane and washed with aq. sat. NH_4Cl (3x75mL). The organic layer was dried over $MgSO_4$, filtered and stripped of solvent. The product was purified by column chromatography (acetonitrile/ethyl acetate/petroleum ether = 0.5/1.5/8.5) followed by recrystallization in ethyl acetate to give final product. (0.2g, 26%). ^{1}HNMR ($CDCl_3$) δ 7.73 (d, J = 15.8Hz, 1H), 7.66 (d, J = 15.8Hz, 1H), 7.69 (m, 4H), 7.51 (d, J = 8.83Hz, 2H), 7.16 (d, J = 15.8Hz, 1H), 6.83 (d, J = 15.73Hz, 1H), 6.68 (m, 2H), 3.43 (q, J = 7.1Hz, 4H), 1.21 (t, J = 7.1Hz, 6H). HRMS (ESI) (M+, $C_{22}H_{22}N_2O$): calcd, 330.1732; found, 331.18401 [M+H].

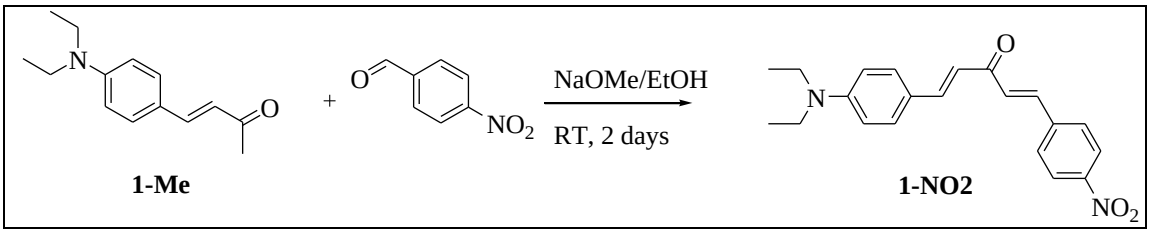

1-NO2: A 2.6M NaOMe solution was made by reacting sodium (0.24g, 10.4mmol) with methanol (4mL) in a flame dried 10mL round bottom flask. A 500mL rbf was flame dried and charged with **1-Me** (2g, 9.2mmol), 4-nitrobenzaldehyde (2.086g, 13.8mmol) and ethanol (185mL). The solution was stirred until all the solids dissolved. The NaOMe solution was added dropwize to the reaction flask over a period of 6-7 min. The solution changed colour from reddish orange to dark red. The reaction was stirred at room temperature for 2 days. The solvent was evaporated to give a red solid. This was rinsed with water and hexanes to remove any residual methanol and ethanol. The red solid was dissolved in CH_2Cl_2 (100mL) and washed with aq. sat. NH_4Cl (4x50mL) followed by drying over $MgSO_4$, filtering and removal of solvent by rotary evapouration. Crude was purified on a silica gel column using gradient elution (100% Dichloromethane to 5% Ethyl Acetate/ Dichloromethane). (1.55g,48 %). ^{1}HNMR ($CDCl_3$) δ 8.29 (d, J = 8.82Hz, 2H), 8.05 (d, J = 8.85Hz, 2H), 7.78 (d, J = 15.87Hz, 1H), 7.74 (d, J = 15.99Hz, 1H), 7.58 (m, 3H), 6.98 (d, J = 15.85Hz, 1H), 6.72 (d, J = 8.94Hz, 2H), 3.42 (q, J = 6.99Hz, 4H), 1.12 (t, J = 6.98Hz, 6H). HRMS (ESI) (M+, $C_{21}H_{22}N_2O_3$): calcd, 350.163; found, 351.17032 [M+H].

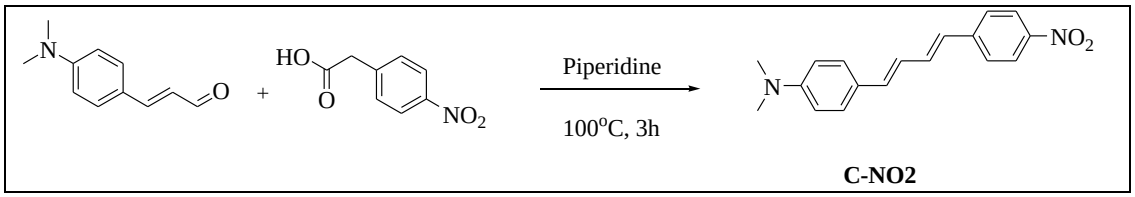

C-NO2: A 25mL rbf was charged with 4-(dimethylamino)cinnamaldehyde (0.5g, 2.85mmol), 4-nitrophenylacetic acid (0.622g, 3.42mmol) and piperidine (5mL). The reaction was heated to 100°C for 3 hr. Heating was stopped and after cooling back down to room temperature all of the piperidine was stripped on a rotary evaporator. Crude reaction mixture was redissolved in dichloromethane (100mL) and washed with DI water (3x100mL). Aq. Sat. NH_4Cl was used to break up any emulsions formed. The organic phase was dried over $MgSO_4$, filtered and stripped of solvent. Column chromatography was done (3/7/0.1 dichloromethane/hexanes/methanol to 10/0.1 dichloromethane/methanol). Final purification was done by recrystallization from toluene to give red solid. (0.5g, 59.5%). ^{1}H NMR ($CDCl_3$) δ 8.16 (d, J = 8.5Hz, 2H), 7.5 (d, J = 8.7Hz, 2H), 7.37 (d, J = 8.66Hz, 2H), 7.1 (dd, J = 15.3Hz, J = 9.3Hz, 1H), 6.77 (m, 4H), 6.59 (d, J = 15.37Hz, 1H), 3.01 (s, 6H). HRMS (ESI) (M+, $C_{18}H_{18}N_2O_2$): calcd, 294.1368; found, 295.14712 [M+H].

2.8.2 **Nuclear magnetic resonance (NMR) spectroscopy and mass spectrometry data:**

^{1}HNMR of 1-NEt2

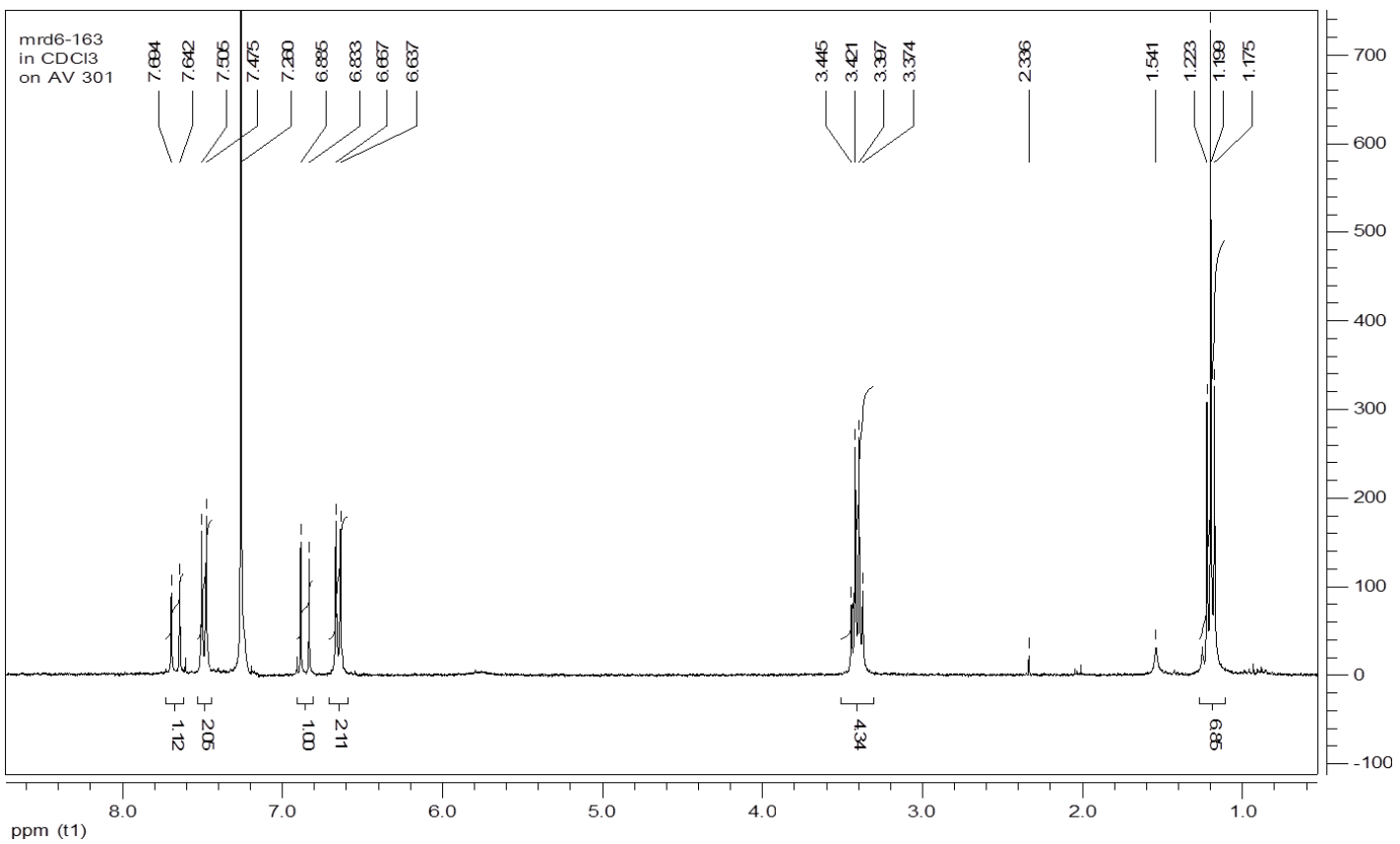

HRMS (ESI) of 1-NEt2

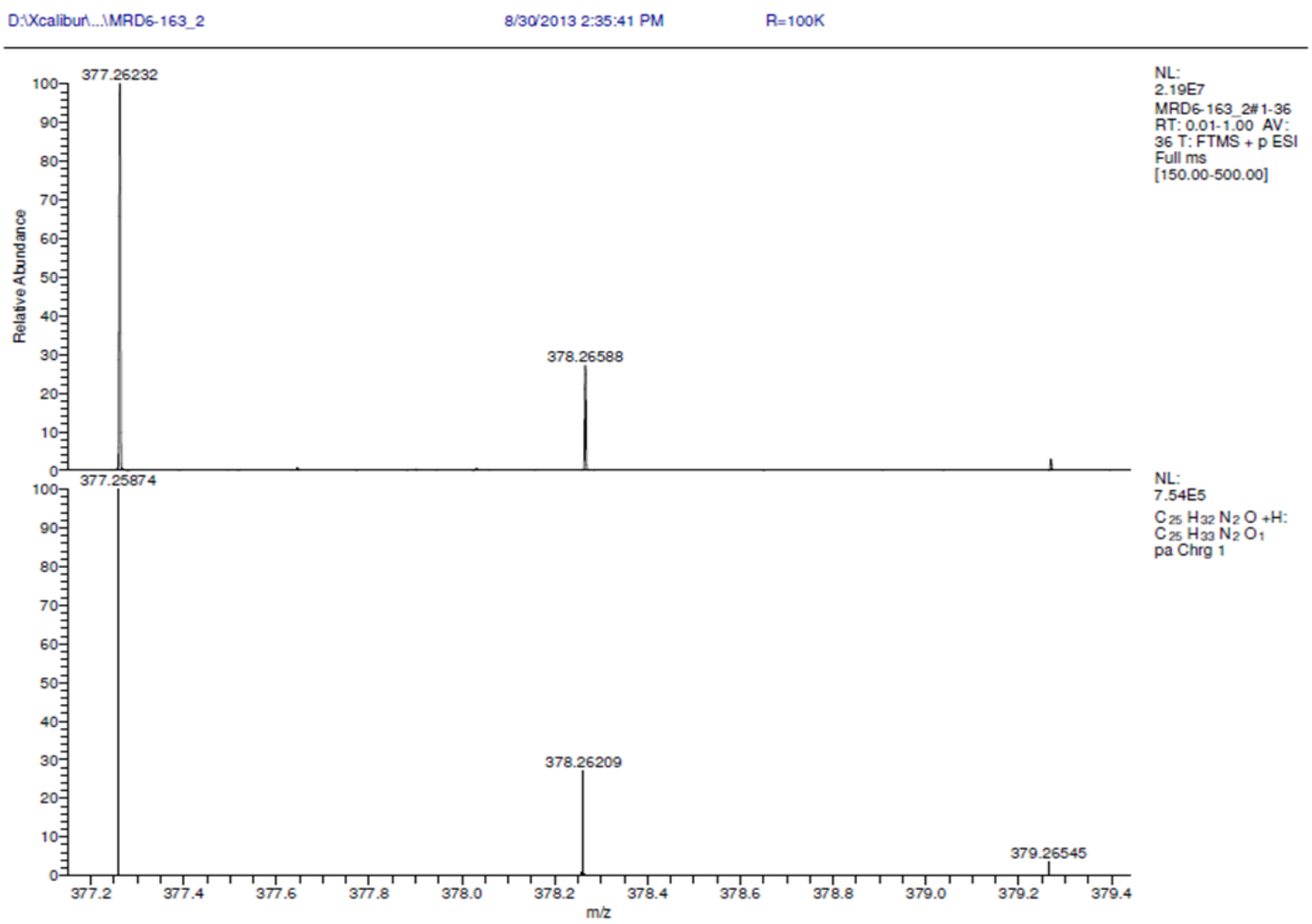

^{1}HNMR of 1-Me

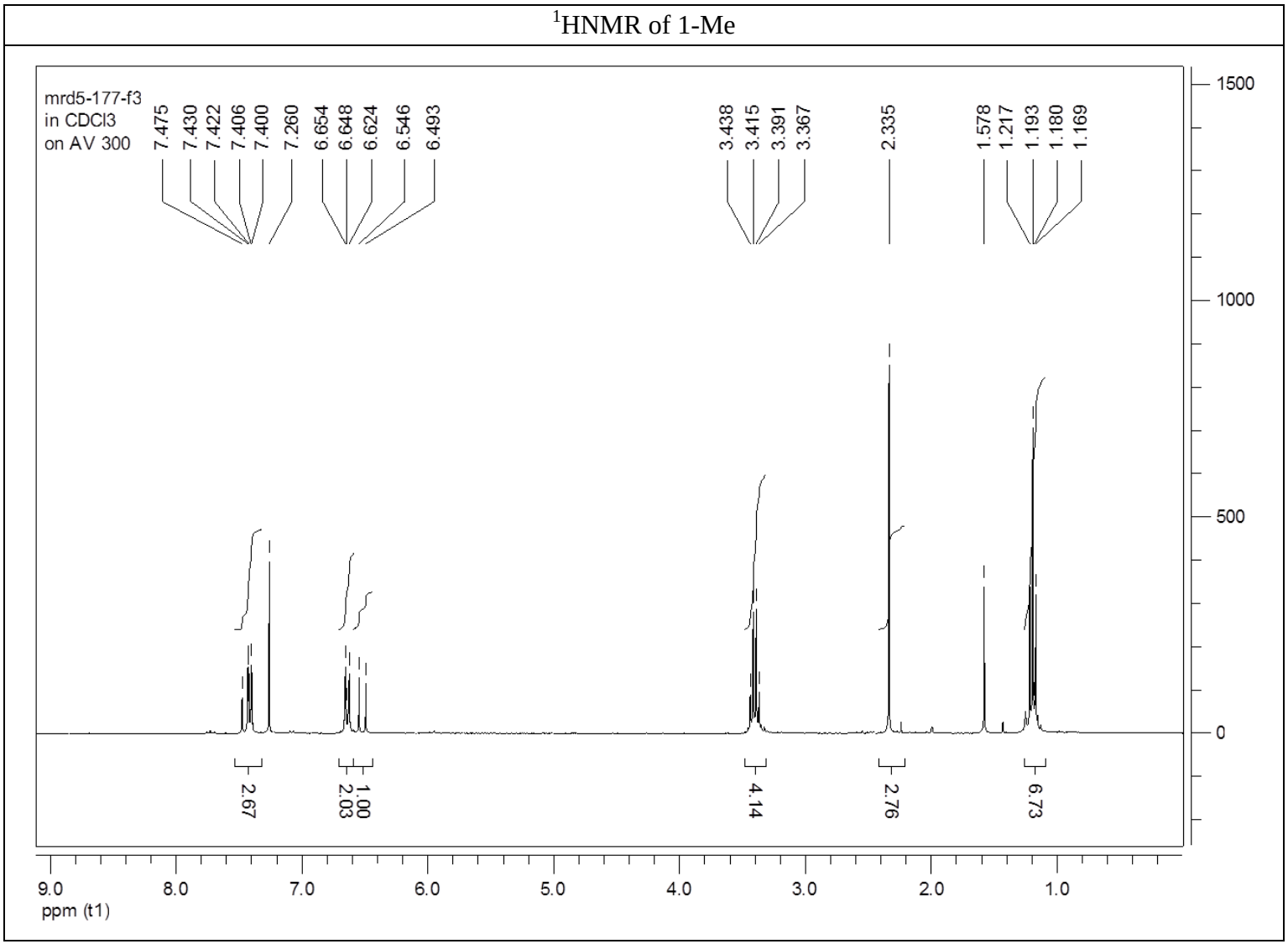
mrd5-177-f3
in CDCl3
on AV 300
7.475
7.430
7.422
7.406
7.400
7.260
6.654
6.648
6.624
6.546
6.493
3.438
3.415
3.391
3.367
2.335
1.578
1.217
1.193
1.180
1.169
1500
1000
500
0
2.67
2.03
1.00
4.14
2.76
6.73
9.0
8.0
7.0
6.0
5.0
4.0
3.0
2.0
1.0
ppm (t1)

HRMS (ESI) of 1-Me

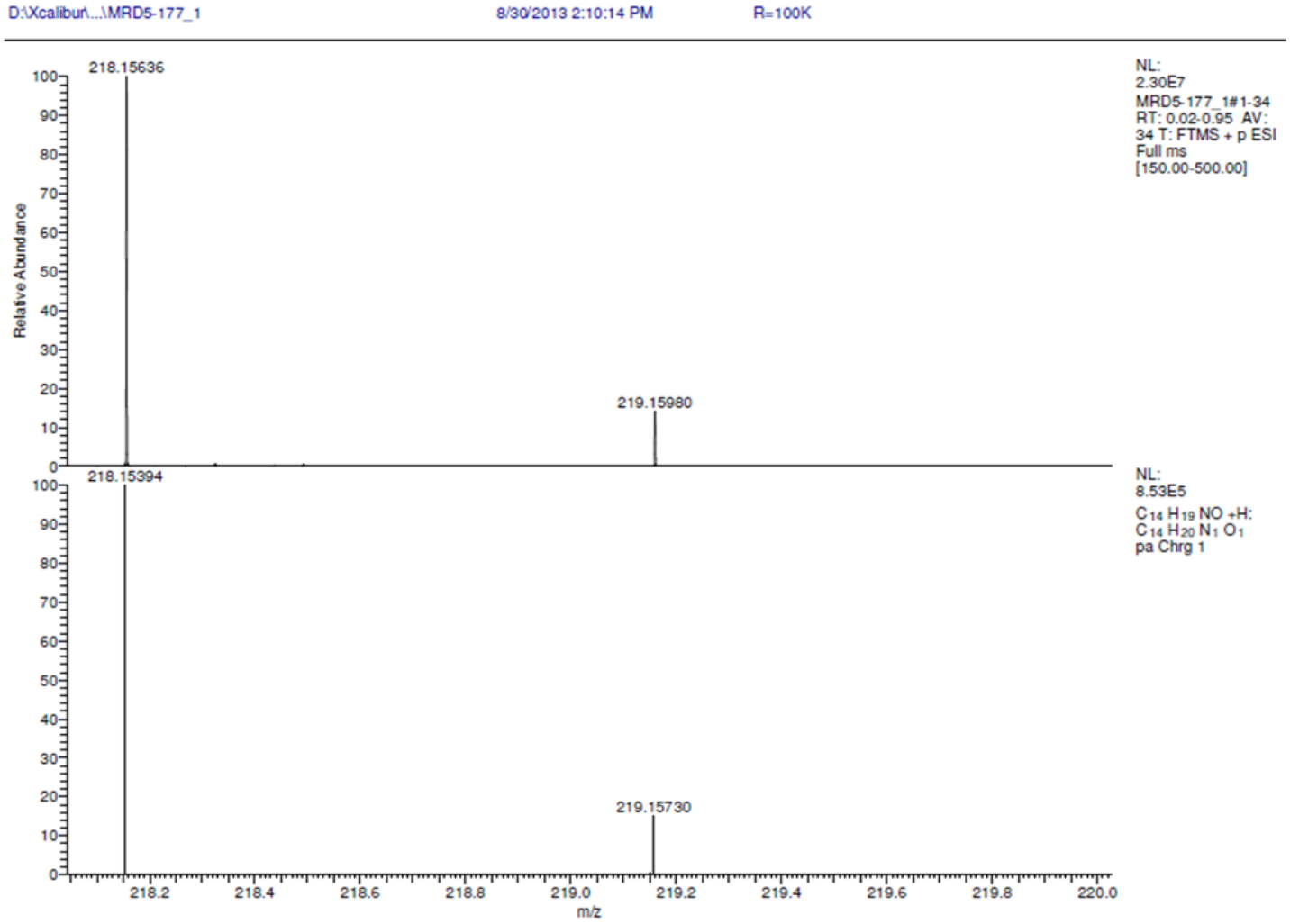

^{1}HNMR of 1-Ph

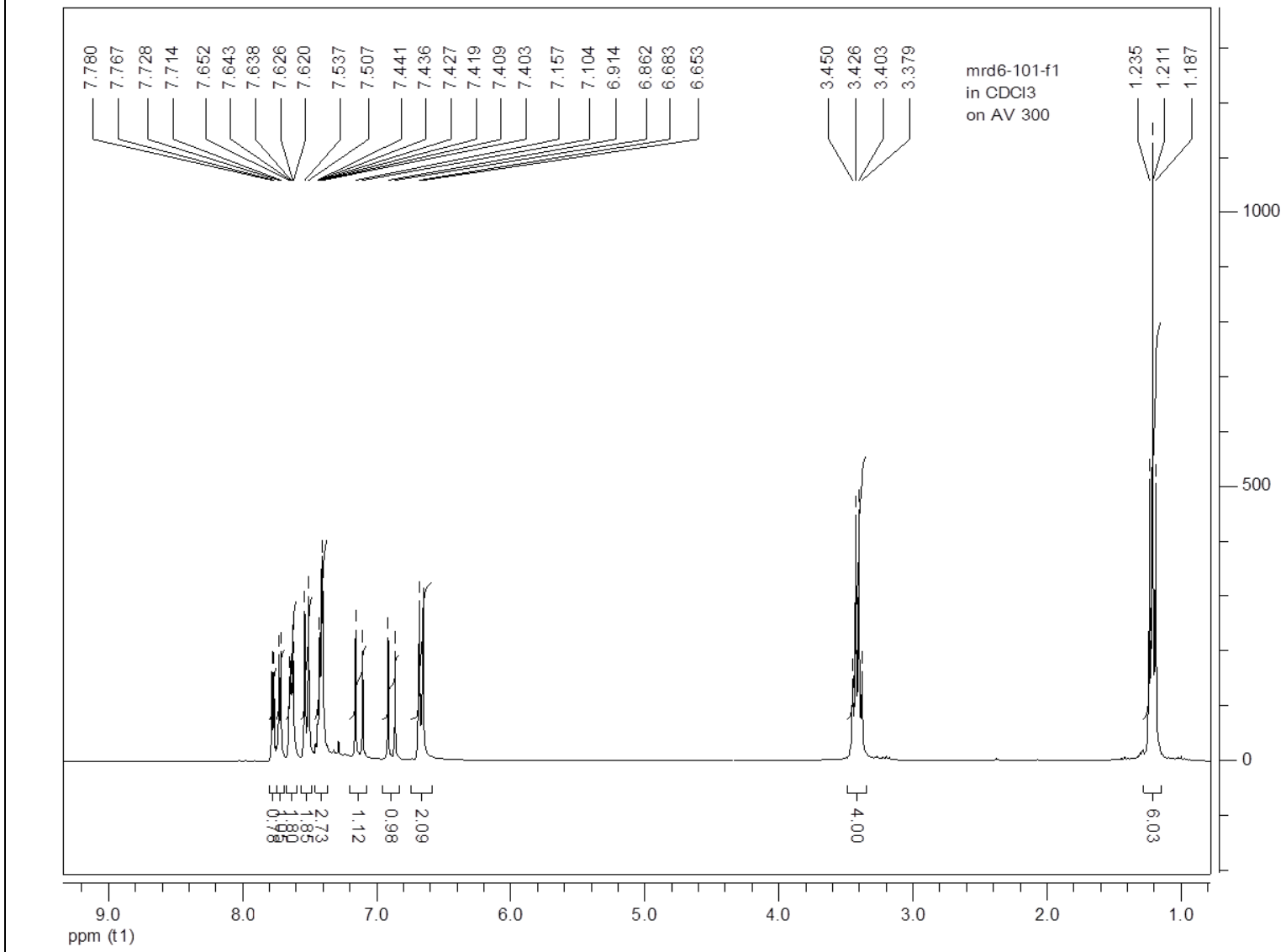
7.780
7.767
7.728
7.714
7.652
7.643
7.638
7.626
7.620
7.537
7.507
7.441
7.436
7.427
7.419
7.409
7.403
7.157
7.104
6.914
6.862
6.683
6.653
3.450
3.426
3.403
3.379
1.235
1.211
1.187
mrd6-101-f1
in CDCl3
on AV 300
1000
500
0
0.78
1.00
2.73
1.85
1.80
1.12
0.98
2.09
4.00
6.03
9.0
8.0
7.0
6.0
5.0
4.0
3.0
2.0
1.0
ppm (t1)

HRMS (ESI) of 1-Ph

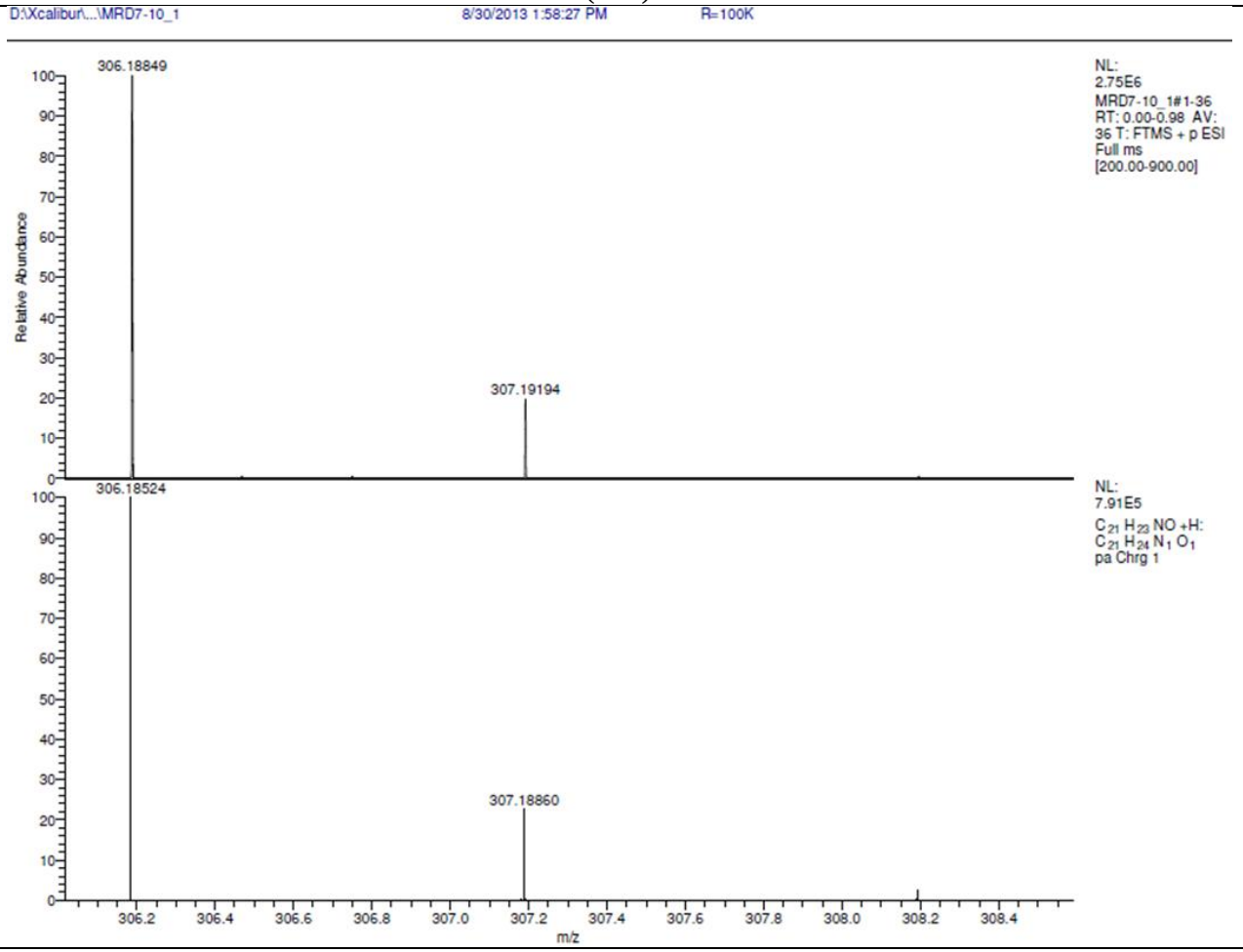

^{1}HNMR of 1-Ph

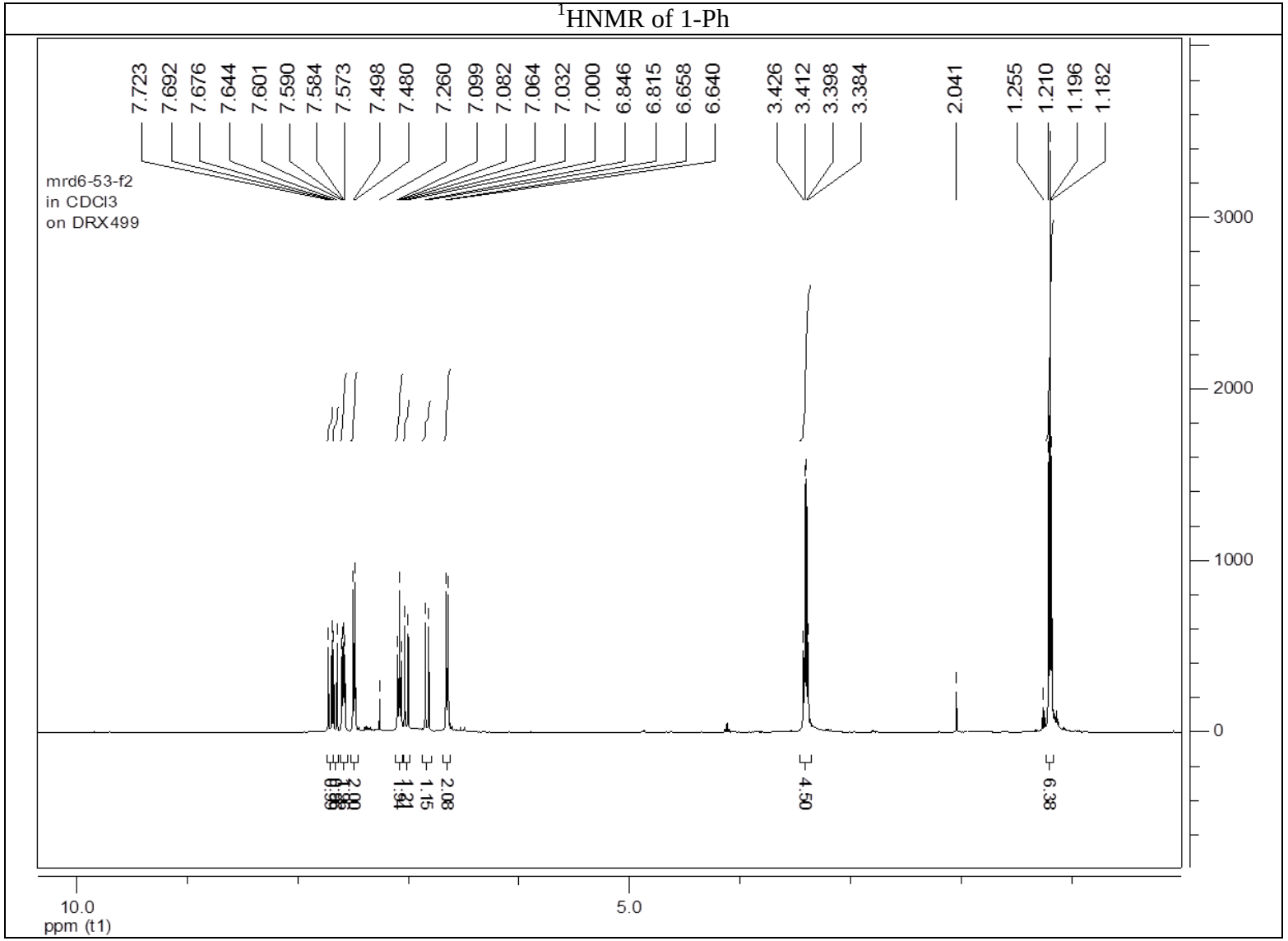
7.723
7.692
7.676
7.644
7.601
7.590
7.584
7.573
7.498
7.480
7.260
7.099
7.082
7.064
7.032
7.000
6.846
6.815
6.658
6.640
3.426
3.412
3.398
3.384
2.041
1.255
1.210
1.196
1.182
mrd6-53-f2
in CDCl3
on DRX499
3000
2000
1000
0
2.00
1.94
1.15
2.08
4.50
6.38
10.0
ppm (t1)
5.0

2D-COSY of 1-PhF

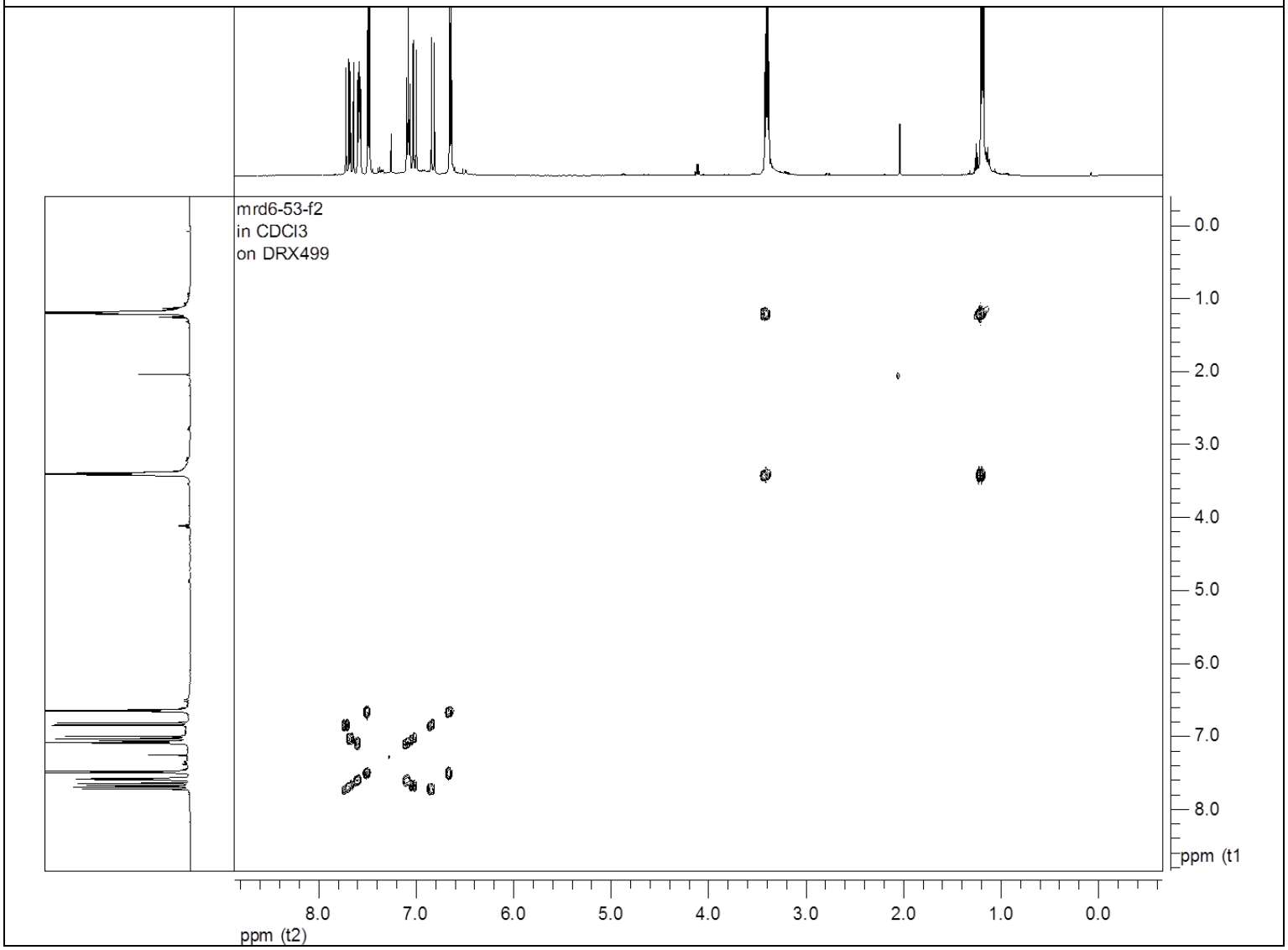

2D-COSY of 1-PhF

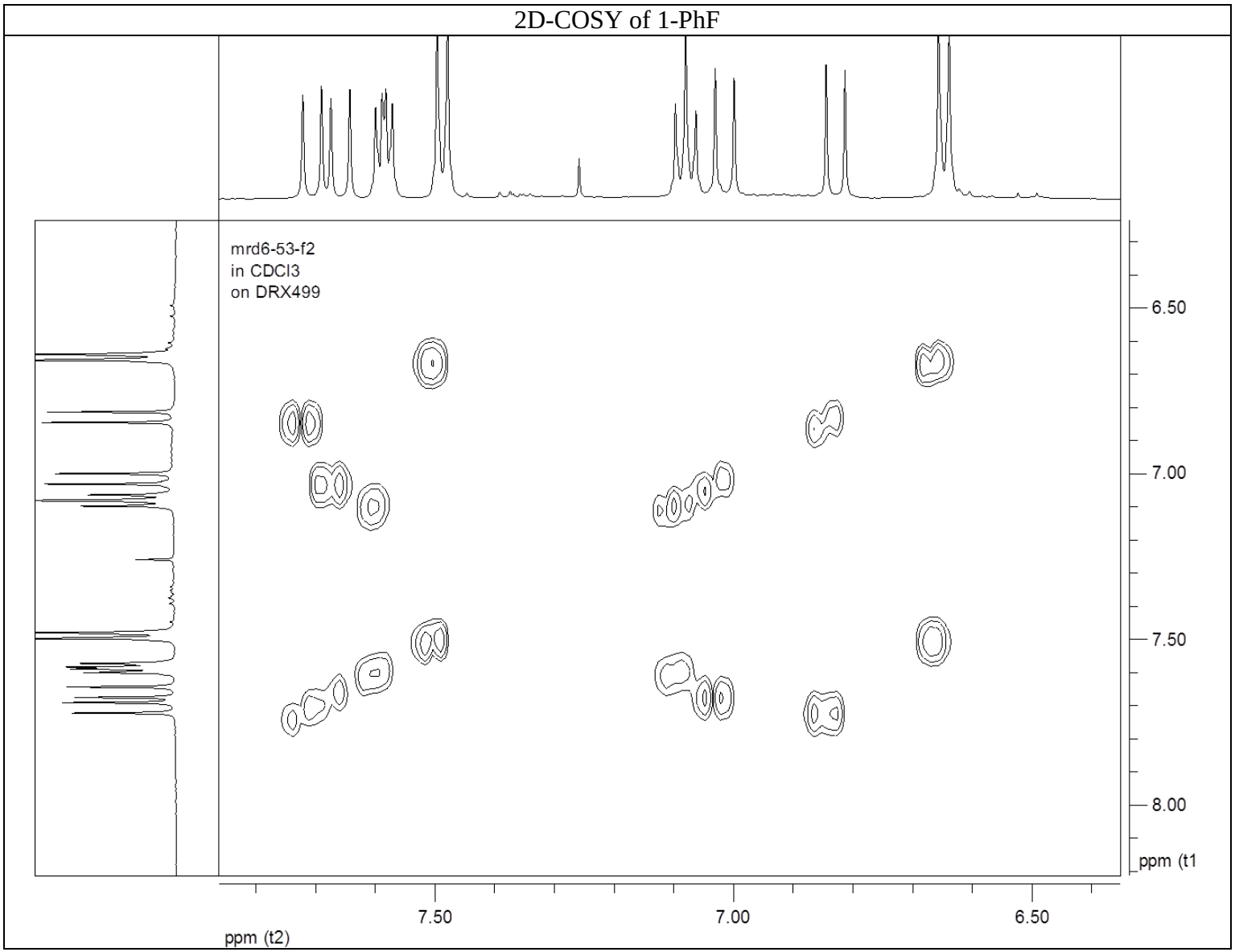

^{19}FNMR of 1-PhF

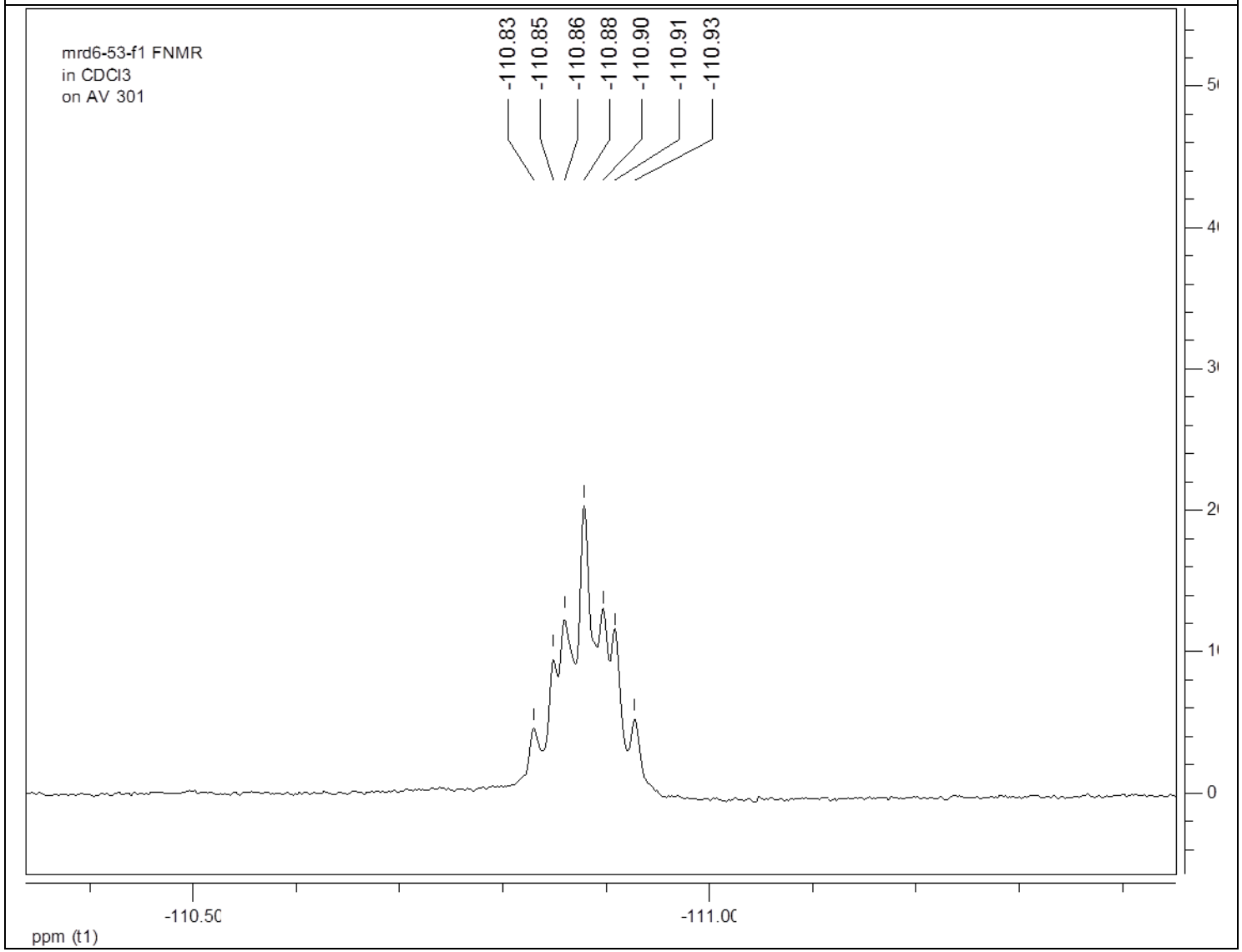

HRMS (ESI) of 1-PhF

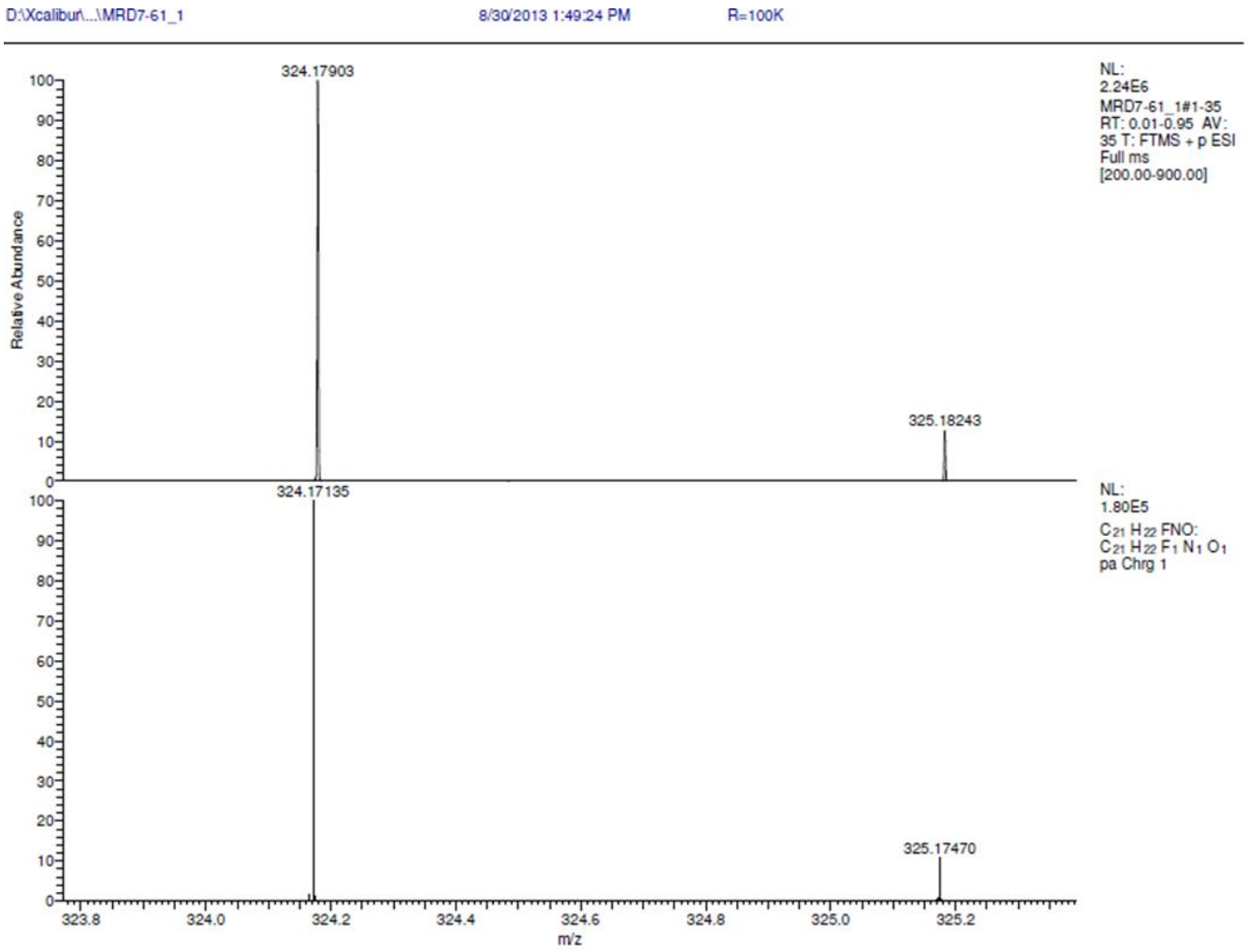

^{1}HNMR of 1-CN

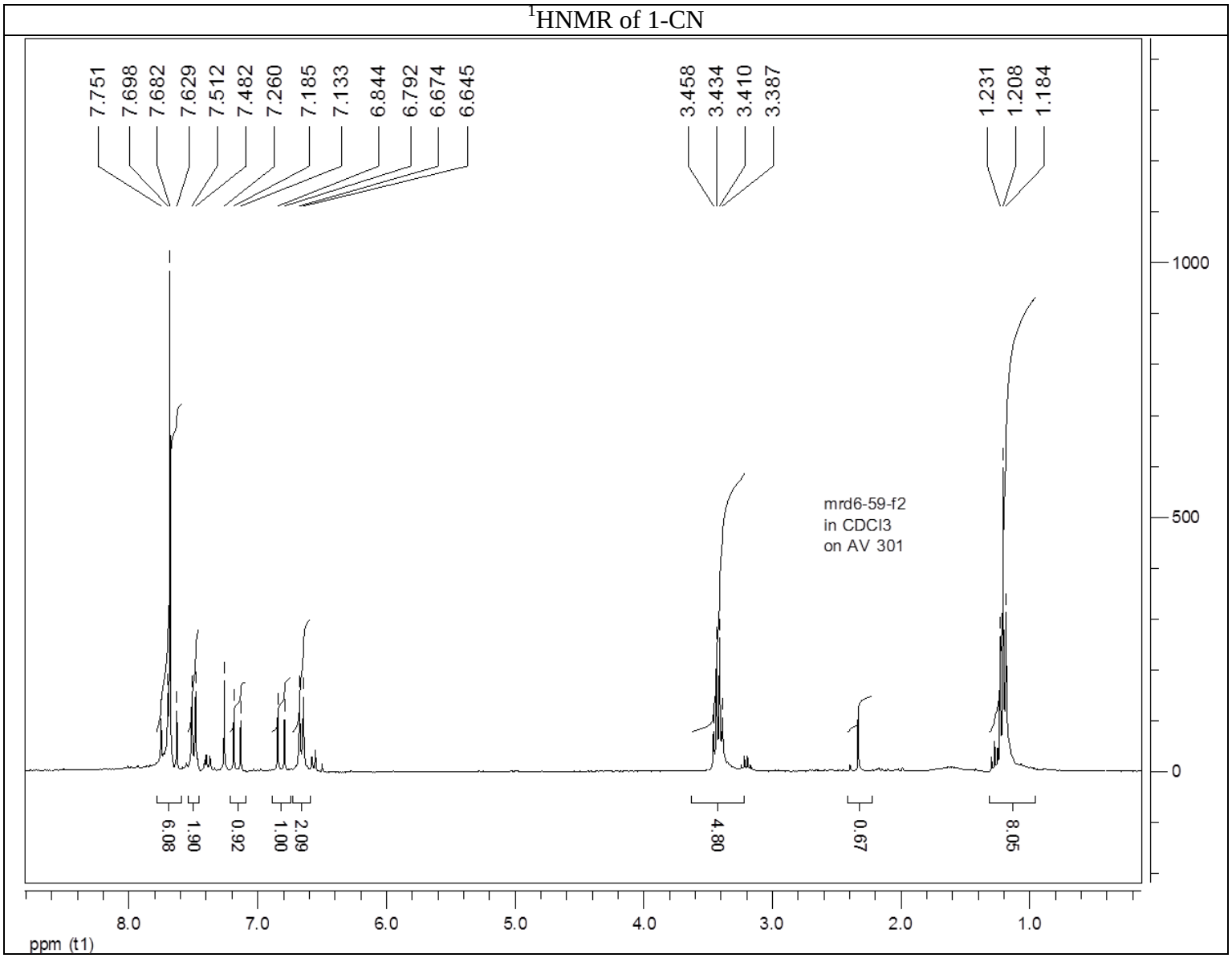
7.751
7.698
7.682
7.629
7.512
7.482
7.260
7.185
7.133
6.844
6.792
6.674
6.645
3.458
3.434
3.410
3.387
1.231
1.208
1.184
mrd6-59-f2
in CDCl3
on AV 301
1000
500
0
6.08
1.96
0.92
1.00
2.09
4.80
0.97
8.05
8.0
7.0
6.0
5.0
4.0
3.0
2.0
1.0
ppm (t1)

HRMS (ESI) of 1-CN

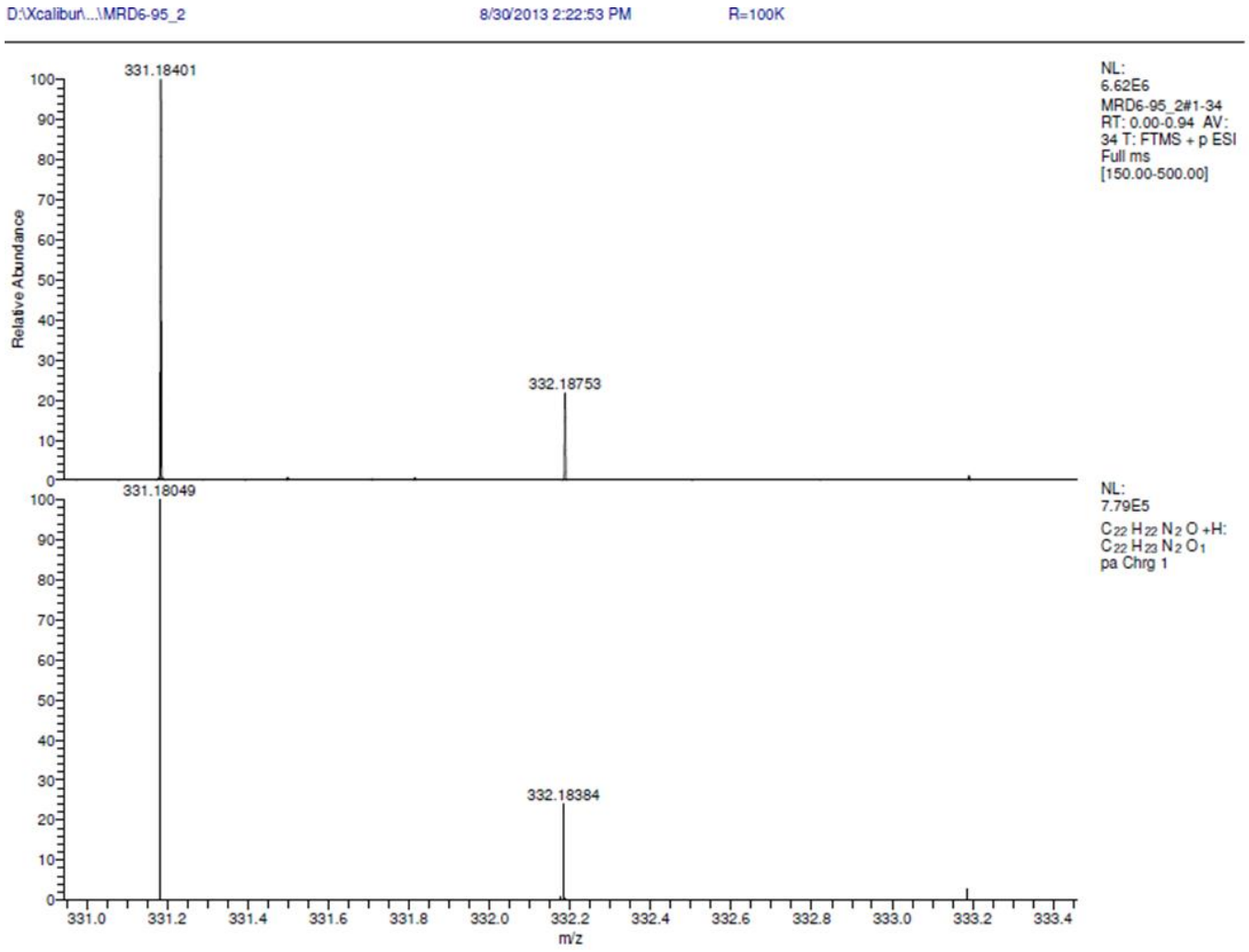

^{1}HNMR of 1-NO2

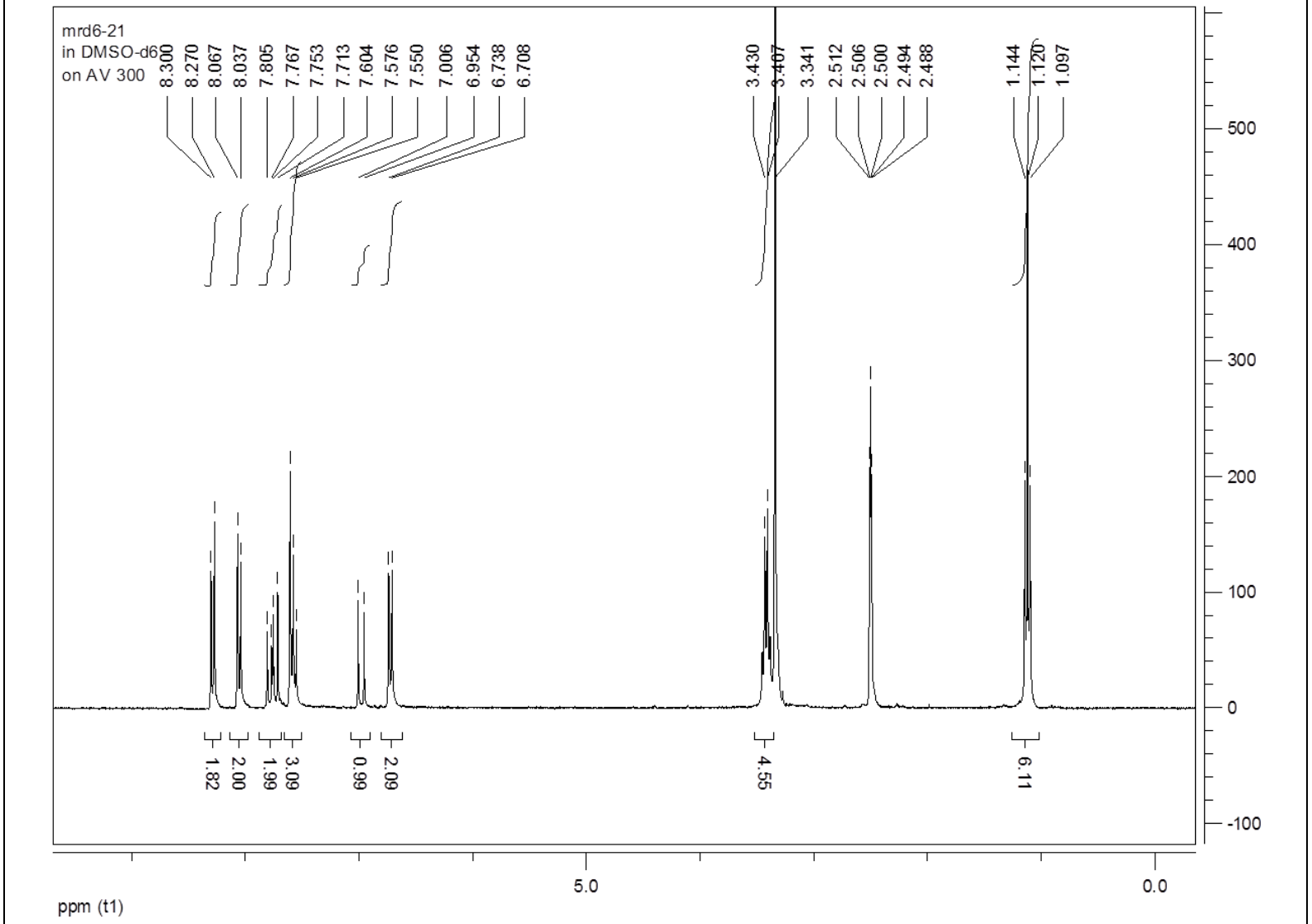

HRMS (ESI) of 1-NO2

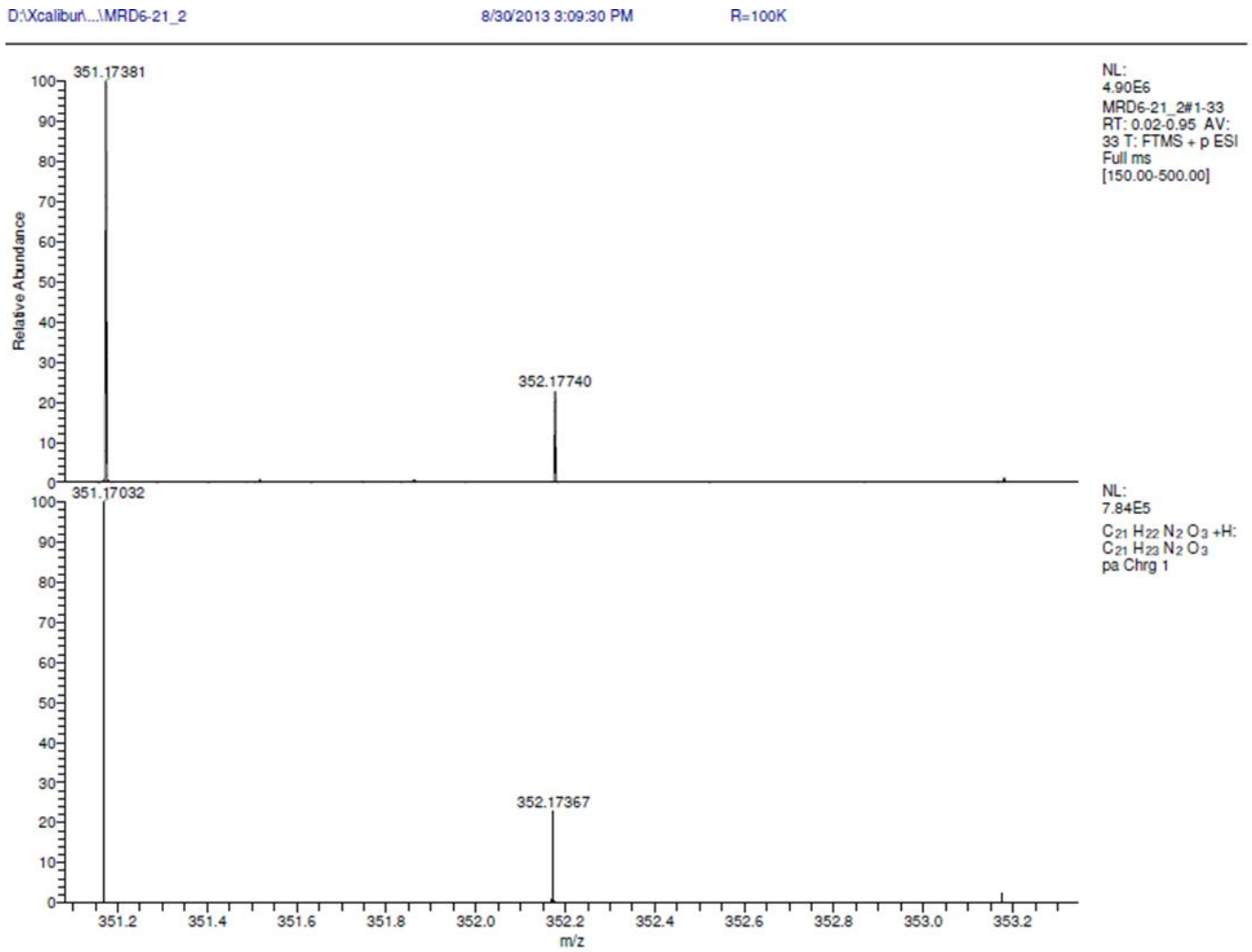

^{1}HNMR of C-NO2

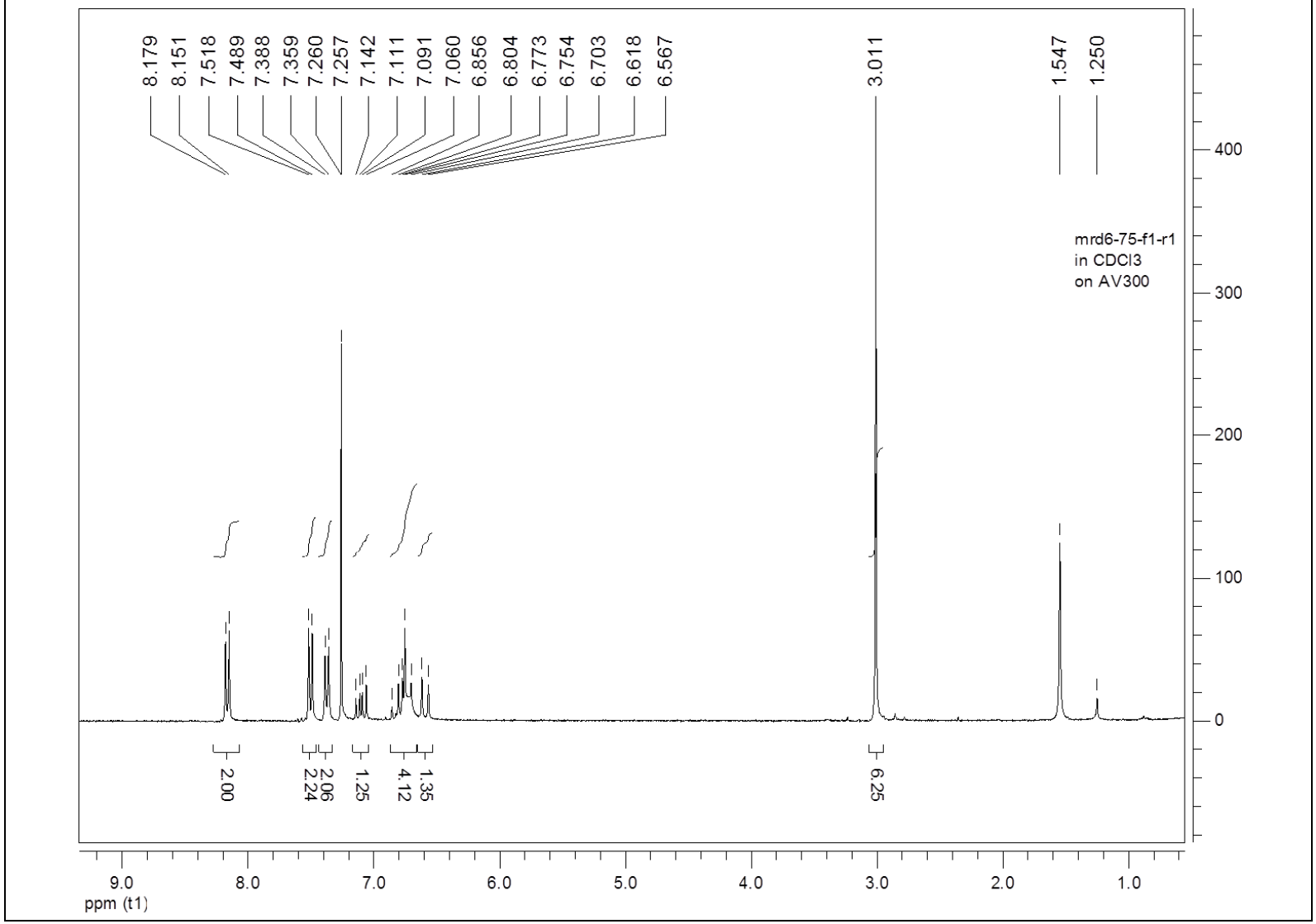

HRMS (ESI) of C-NO2

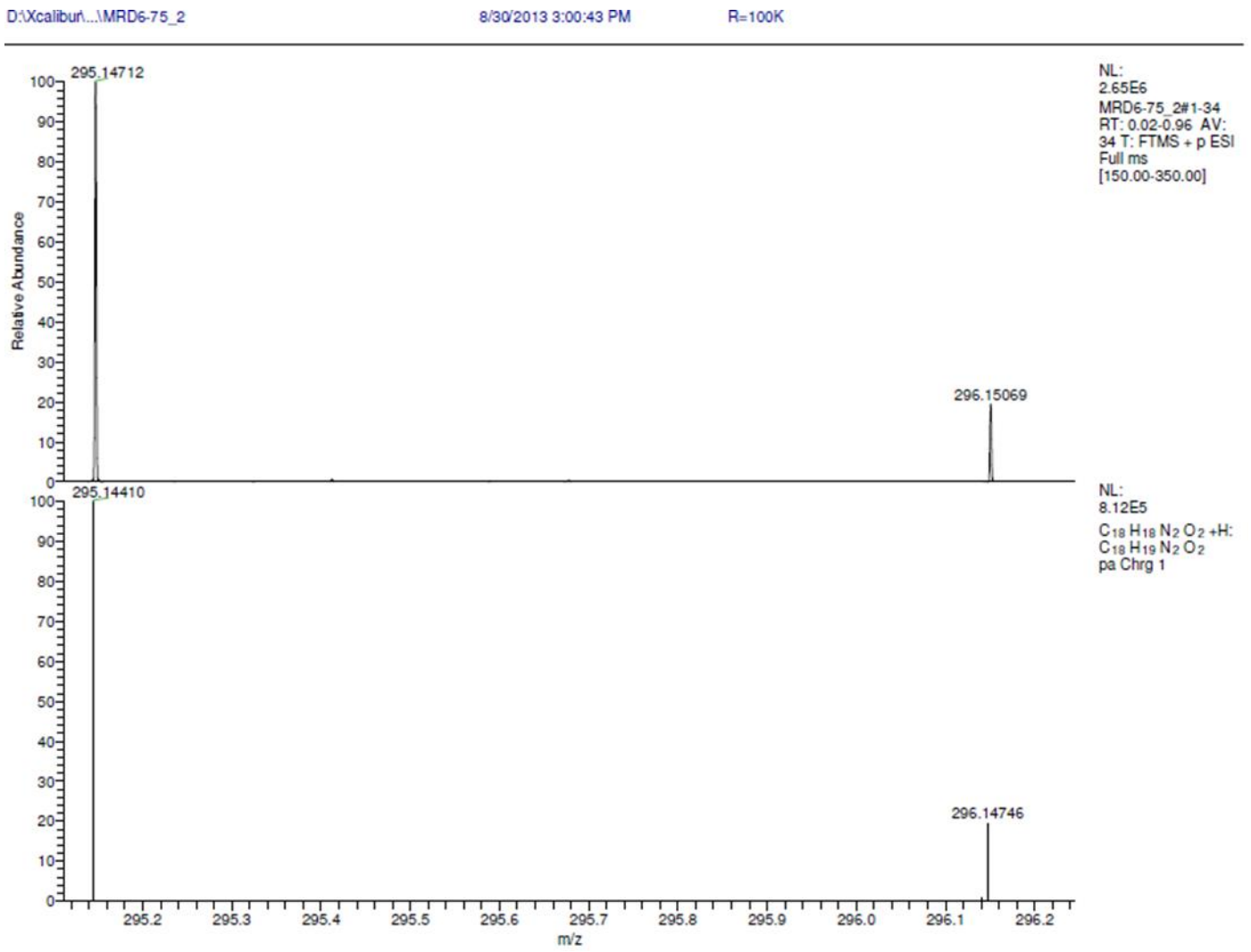

2.8.3 **X-ray diffration data:**

Experimental:

Crystallographic experiments and structure elucidation of **1-NEt2**, **1-Me**, **1-CN** and **C-NO2** were performed by Prof. Werner Kaminsky, Department of Chemistry, University of Washington, Seattle, WA.

Crystallographic experiments and structure elucidation of **1-NO2** was performed by Evgheni V. Juckov, Department of Chemistry, New Mexico Highlands University, Las Vegas, NM.

X-ray crystallographic data was collected at -173^{o}C on a Bruker APEX II single crystal X-ray diffractometer, Mo-radiation. The data was integrated and scaled using SAINT, SADABS within the APEX2 software package by Bruker.

1-NEt2 Crystal Packing Structure

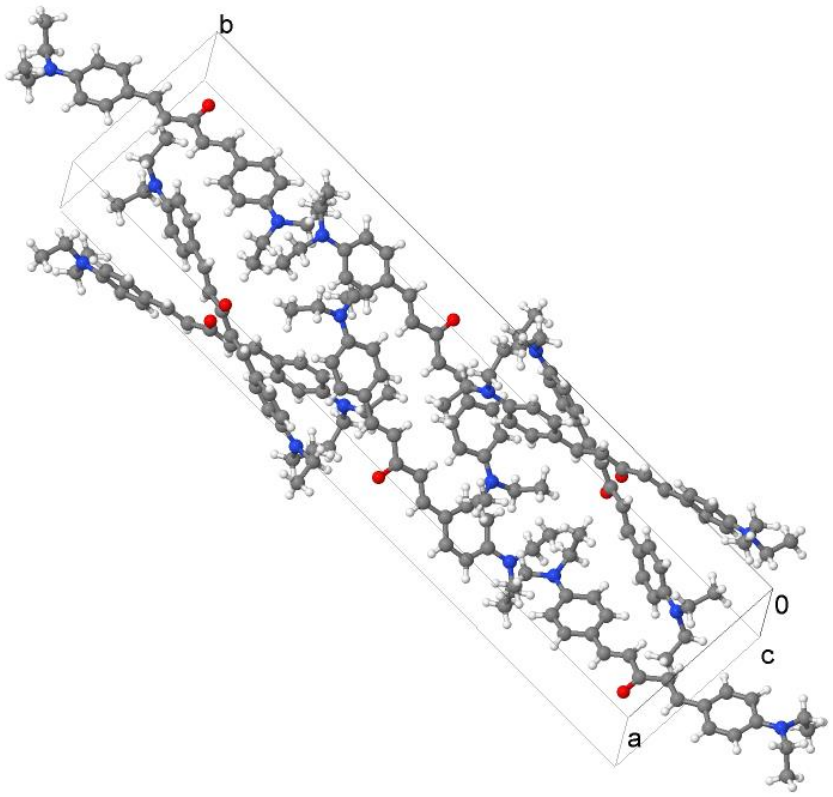

Crystal data for 1-NEt2

Identification code	mrd_6_163_0ma	
Empirical formula	C25 H32 N2 O	
Formula weight	376.53	
Temperature	100(2) K	
Wavelength	0.71073 Å	
Crystal system	Monoclinic	
Space group	P 2_1/c	
Unit cell dimensions	a = 10.6803(8) Å	α= 90°.
	b = 40.253(3) Å	β= 100.715(4)°.
	c = 10.1636(8) Å	γ = 90°.
Volume	4293.3(6) $Å^3$	
Z	8	
Density (calculated)	1.165 Mg/m^3	
Absorption coefficient	0.071 mm^{-1}	
F(000)	1632	
Crystal size	0.20 x 0.17 x 0.10 mm^3	
Theta range for data collection	1.94 to 28.56°.	
Index ranges	-14<=h<=14, -53<=k<=53, -13<=l<=13	
Reflections collected	207280	
Independent reflections	10850 [R(int) = 0.0425]	
Completeness to theta = 25.00°	99.9 %	
Max. and min. transmission	0.9930 and 0.9860	
Refinement method	Full-matrix least-squares on F^2	
Data / restraints / parameters	10850 / 0 / 513	
Goodness-of-fit on F^2	1.028	
Final R indices [I>2sigma(I)]	R1 = 0.0401, wR2 = 0.0968	
R indices (all data)	R1 = 0.0487, wR2 = 0.1034	
Largest diff. peak and hole	0.318 and -0.196 $e.Å^{-3}$	

1-Me Crystal Packing Structure
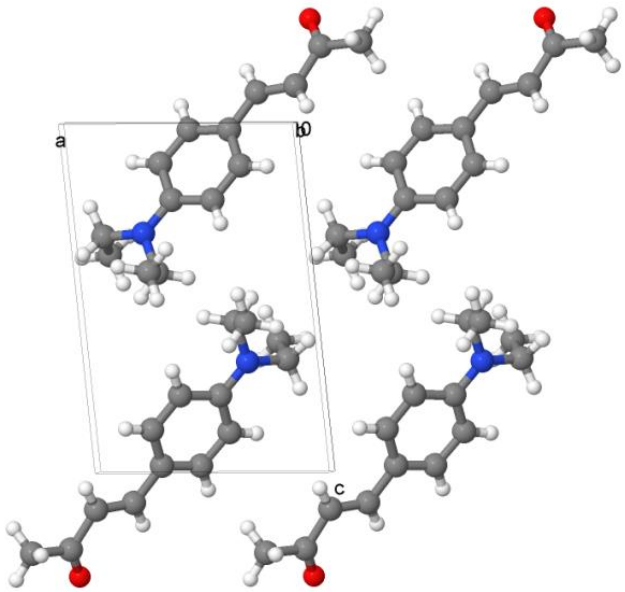

Crystal data for 1-Me

Identification code	mrd_5_177_0m	
Empirical formula	C14 H19 N O	
Formula weight	217.30	
Temperature	100(2) K	
Wavelength	0.71073 Å	
Crystal system	Monoclinic	
Space group	P 2_1	
Unit cell dimensions	a = 7.2907(9) Å	α= 90°.
	b = 7.8314(9) Å	β= 95.859(6)°.
	c = 10.9265(13) Å	γ = 90°.
Volume	620.60(13) $Å^3$	
Z	2	
Density (calculated)	1.163 Mg/m^3	
Absorption coefficient	0.072 mm^{-1}	
F(000)	236	
Crystal size	0.32 x 0.16 x 0.14 mm^3	
Theta range for data collection	1.87 to 28.59°.	
Index ranges	-9<=h<=9, -10<=k<=10, -14<=l<=14	
Reflections collected	23647	
Independent reflections	3035 [R(int) = 0.0299]	
Completeness to theta = 25.00°	96.0 %	
Max. and min. transmission	0.9899 and 0.9772	
Refinement method	Full-matrix least-squares on F^2	
Data / restraints / parameters	3035 / 2 / 148	
Goodness-of-fit on F^2	1.039	
Final R indices [I>2sigma(I)]	R1 = 0.0525, wR2 = 0.1329	
R indices (all data)	R1 = 0.0565, wR2 = 0.1370	
Absolute structure parameter	0.3(18)	
Largest diff. peak and hole	0.773 and -0.228 $e.Å^{-3}$	

1-CN Crystal Packing Structure

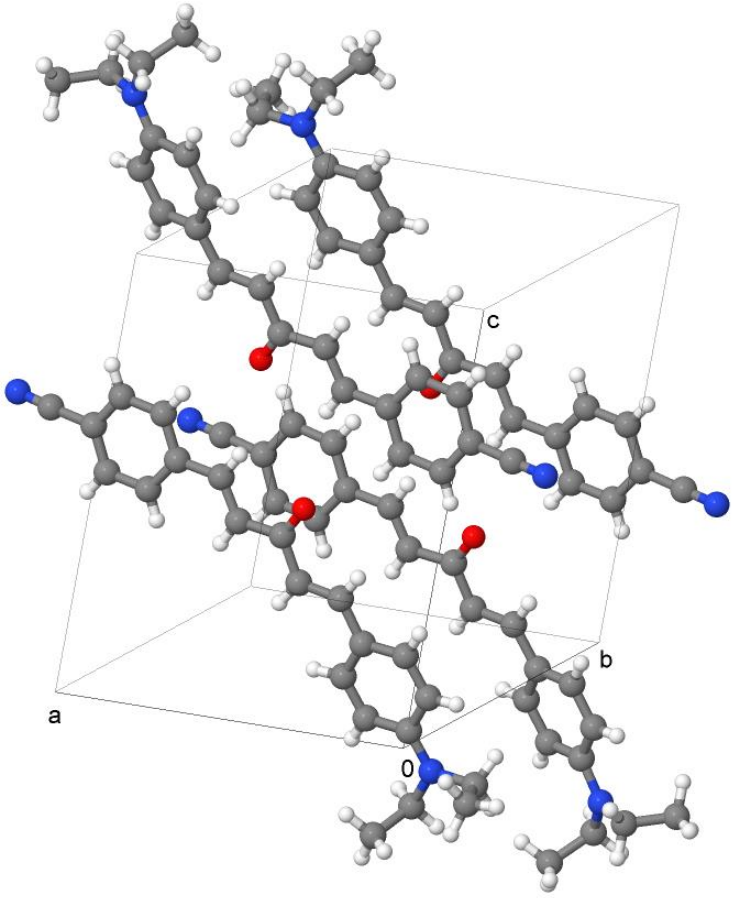

Crystal data for 1-CN

Identification code	mrd_6_95_0m	
Empirical formula	C22 H22 N2 O	
Formula weight	330.42	
Temperature	100(2) K	
Wavelength	0.71073 Å	
Crystal system	Triclinic	
Space group	P -1	
Unit cell dimensions	a = 10.4577(13) Å	α = 97.245(8)°.
	b = 12.0506(15) Å	β = 98.964(7)°.
	c = 14.4789(18) Å	γ = 99.147(8)°.
Volume	1758.0(4) $Å^3$	
Z	4	
Density (calculated)	1.248 Mg/m^3	
Absorption coefficient	0.077 mm^{-1}	
F(000)	704	
Crystal size	0.17 x 0.10 x 0.04 mm^3	
Theta range for data collection	2.01 to 26.65°.	
Index ranges	-13<=h<=13, -15<=k<=15, -18<=l<=18	
Reflections collected	35264	
Independent reflections	7249 [R(int) = 0.0507]	
Completeness to theta = 25.00°	98.6 %	
Max. and min. transmission	0.9969 and 0.9870	
Refinement method	Full-matrix least-squares on F^2	
Data / restraints / parameters	7249 / 0 / 455	
Goodness-of-fit on F^2	1.017	
Final R indices [I>2sigma(I)]	R1 = 0.0613, wR2 = 0.1399	
R indices (all data)	R1 = 0.1264, wR2 = 0.1771	
Largest diff. peak and hole	0.592 and -0.302 $e.Å^{-3}$	

1-NO2 Crystal Packing Structure

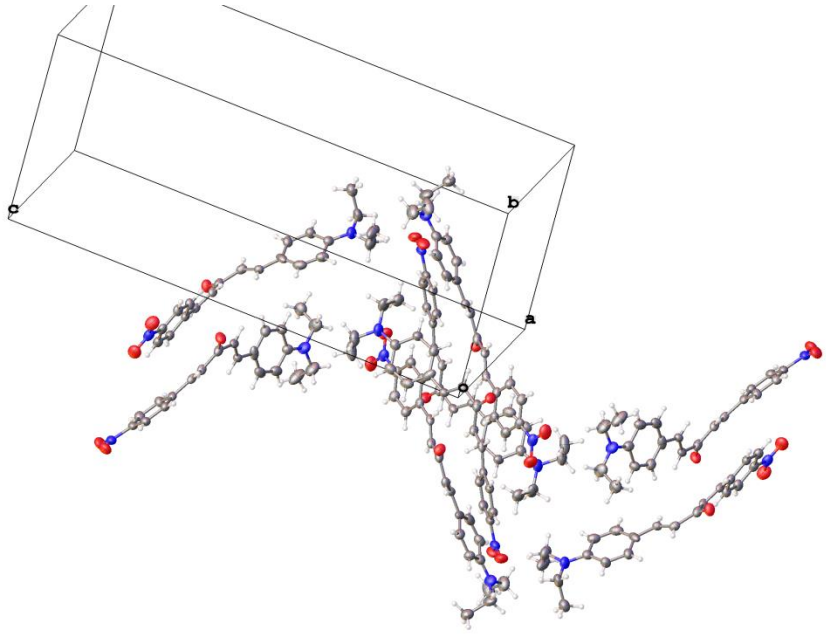

Crystal data for 1-NO2

Identification code	DALTON	
Empirical formula	C21 H22 N2 O3	
Formula weight	350.41	
Temperature	100(2) K	
Wavelength	0.71073 Å	
Crystal system	Orthorhombic	
Space group	Pbca	
Unit cell dimensions	a = 10.7185(5) Å	α = 90°.
	b = 12.0728(5) Å	β = 90°.
	c = 27.9854(12) Å	γ = 90°.
Volume	3621.4 (3) $Å^3$	
Z	8	
Density (calculated)	1.285Mg/m^3	
Absorption coefficient	$0.087mm^{-1}$	
F(000)	1488.0	
Crystal size	0.32 x 0.26 x 0.16 mm^3	
2θ range for data collection	4.78 to 54°.	
Index ranges	-13<=h<=13, -15<=k<=15, -35<=l<=35	
Reflections collected	35472	
Independent reflections	3918 [R(int) = 0.0381]	
Max. and min. transmission	0.9983 and 0.9913	
Refinement method	Full-matrix least-squares on F^2	
Data / restraints / parameters	3918 / 6 / 285	
Goodness-of-fit on F^2	1.037	
Final R indices [I>2sigma(I)]	R1 = 0.0626, wR2 = 0.1558	
R indices (all data)	R1 = 0.0807, wR2 = 0.1728	
Largest diff. peak and hole	0.44 and -0.36 $e.Å^{-3}$	

C-NO2 Crystal Packing Structure

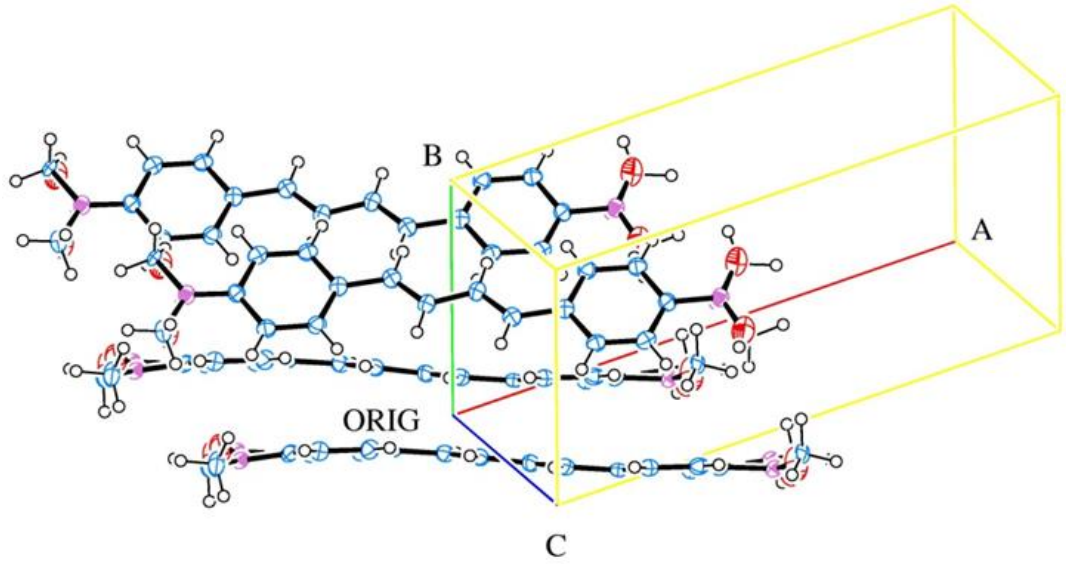

Crystal data for C-NO2

Identification code	mrd_6_75_0ma	
Empirical formula	C18 H18 N2 O2	
Formula weight	294.34	
Temperature	100(2) K	
Wavelength	0.71073 Å	
Crystal system	Monoclinic	
Space group	P 2_1/c	
Unit cell dimensions	a = 17.065(8) Å	α = 90°.
	b = 7.198(3) Å	β = 98.66(3)°.
	c = 6.092(3) Å	γ = 90°.
Volume	739.7(6) $Å^3$	
Z	2	
Density (calculated)	1.322 Mg/m^3	
Absorption coefficient	0.087 mm^{-1}	
F(000)	312	
Crystal size	0.10 x 0.08 x 0.02 mm^3	
Theta range for data collection	2.41 to 25.35°.	
Index ranges	-20<=h<=20, -8<=k<=8, -7<=l<=7	
Reflections collected	12293	
Independent reflections	1304 [R(int) = 0.1407]	
Completeness to theta = 25.00°	96.1 %	
Max. and min. transmission	0.9983 and 0.9913	
Refinement method	Full-matrix least-squares on F^2	
Data / restraints / parameters	1304 / 34 / 124	
Goodness-of-fit on F^2	1.027	
Final R indices [I>2sigma(I)]	R1 = 0.0735, wR2 = 0.1450	
R indices (all data)	R1 = 0.1459, wR2 = 0.1789	
Extinction coefficient	0.16(3)	
Largest diff. peak and hole	0.261 and -0.287 $e.Å^{-3}$	

2.8.4 **Hyper-Rayleigh scattering data:**

Experimental:

All HRS measurements were performed by Prof David Shelton (Department of Physics, University of Nevada, Las Vegas, NV).

The β values for the chromophores in CDCl3 solution were determined from hyper-Rayleigh scattering (HRS) measurements at a laser wavelength of 1064 nm (using a pulsed Nd:YAG laser) and sample temperature 25°C. Calibration of the HRS results used 4-nitroaniline (pNA) in CDCl3 solution as a reference standard. Dilute solutions of p-nitroaniline (pNA) (36.4mM), **1-NO2** (38.4μM) and **C-NO2** (43μM) in $CDCl_3$ were freshly prepared for each measurement. The solution concentrations were chosen to give comparable signals for the chromophore and reference solutions, and the much smaller HRS signal measured for the neat solvent was subtracted. Sample and reference HRS signals were compared using the same laser focusing, collection optics and polarization configuration, using apparatus and techniques as previously described[26]. The laser power incident on the sample was adjusted without affecting the alignment or focusing of the laser beam using a half-wave plate and polarizer combination.

The 532 nm (second harmonic wavelength) HRS light is absorbed by the sample along the 1.5 mm path from the laser focus to the exit window of the cuvette. The self-absorption correction was determined using the 532 nm absorbance measured for the sample in the 10 mm sample cuvette.

The HRS signal at 532 nm selected by the 60 cm^{-1} bandpass filter may be contaminated with two photon fluorescence (2PF). The fraction of the total signal due to HRS is determined from a spectral scan, where the HRS and 2PF appear as a sharp peak and a flat background,

respectively. The directly measured 2PF fractions for **1-NO2** (MRD6-21) and **C-NO2** (MRD6-75) are 65% and 54% respectively.

HRS signal S is measured versus laser power P and S/P^2 is extrapolated to $P = 0$. This extrapolation is necessary since weak absorption of the focused laser beam in the sample heats the sample along the beam path, defocuses the beam, and reduces the HRS signal. In the absence of this thermal lens effect S/P^2 is independent of P. In the usual case of weak linear absorption by the sample at the laser wavelength the extrapolation is done by fitting $S/P^2 = A(1 - B \times P)$ to the data.

The power-normalized HRS signal S/P^2 was independent of laser beam power P for the pNA reference solution, as expected, but S/P^2 for both chromophore solutions exhibited a strong dependence on P. For **1-NO2** (MRD6-21) and **C-NO2** (MRD6-75) there is a strong thermal lens effect that appears to be dominated by two photon absorption, so the appropriate extrapolation function is $S/P^2 = A(1 - B \times P^2)$ instead. For these two molecules significant thermal lensing by linear absorption at 1064 nm is ruled out by direct measurements of the linear absorption at1064 nm and by measurement of the continuous wave thermal lens effect at the same average laser power.

Sample	Conc	A_{532nm} (cm^{-1})	F = HRS/total	T(z)	S/P^2 (cps/W^2)	D (cps/W^2)	E ($cps/\mu M\ W^2$)	β/β_{PNA} $\pm 2\%$
$CDCl_3$					301(5)			
pNA	36.4 mM	0.008	1	0.997	6043(30)	5760	0.15825	1
MRD6-21	38.4 µM	0.335	0.335(7)	0.889	27540(271)	10696	278.55	42.0
MRD6-75	43.0 µM	0.297	0.461(9)	0.901	32798(419)	16480	383.26	49.2

HRS Data Table for 1-NO2 (MRD6-21) and C-NO2 (MRD6-75)

A_{532}= absorbance at 532 nm for 1 cm of solution.

$T(z) = 10^{-Az}$

$S/P^2 =$ power-normalized HRS signal extrapolated to $P^2 = 0$

$D = [(F/T)(S/P^2) - (S/P^2)_{CDCl3}]$

$E = D/conc$

$\beta/\beta_{PNA} = (E/E_{PNA})^{1/2}$

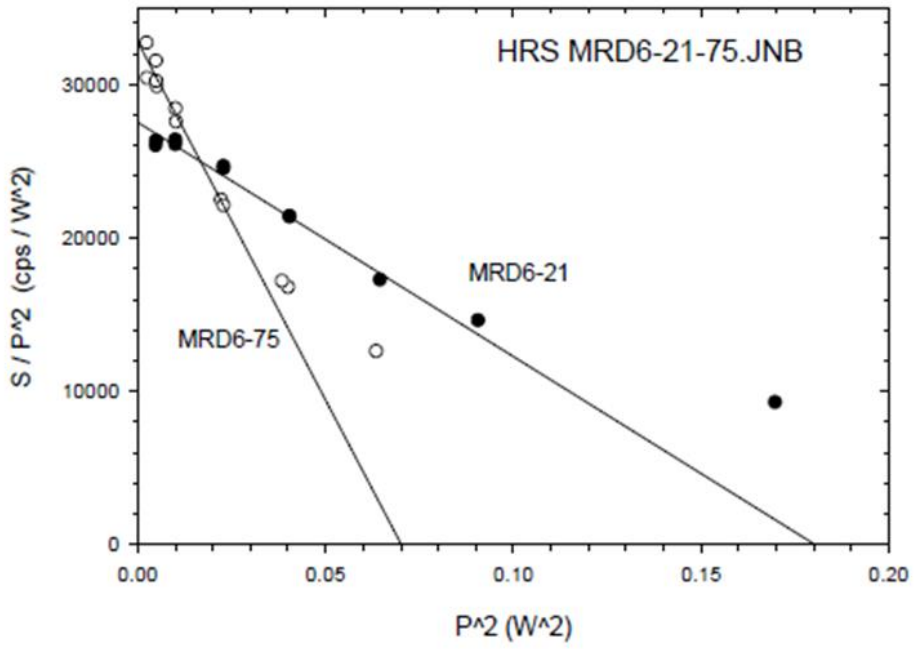

S/P^2 versus $P^2$for 1-NO2 (MRD6-21) and C-NO2 (MRD6-75)

The experimental static hyperpolarizability ratios, $\beta_{HRS(0)}/\beta_{pNA(0)}$ were extrapolated from the frequency dependent ratios, $(\beta_{HRS}/\beta_{pNA})_{1064}$ using the two level model (TLM) equation developed by Oudar and Chemla . Extrapolation to the static becomes increasingly unreliable however as resonance is approached as line broadening effects need to be taken into account. A correction factor known as thus applied to the TLM equation to give the damped two level model dispersion fit shown by **equations 2.1** and **2.2**.

$$\beta^{SHG}(\omega,\omega_{eg},\gamma) = g(\omega,\omega_{eg},\gamma) * \beta^{HRS}(0) \qquad \text{.....(2.1)}$$

$$g(\omega,\omega_{eg},\gamma) = \frac{\omega_{eg}^{\ 2}}{3}\left\{\frac{1}{(\omega_{eg}+i\gamma+2\omega)(\omega_{eg}+i\gamma+\omega)} + \frac{1}{(\omega_{eg}-i\gamma-2\omega)(\omega_{eg}-i\gamma-\omega)} + \frac{1}{(\omega_{eg}+i\gamma+\omega)(\omega_{eg}-i\gamma-\omega)}\right\} \qquad \text{.....(2.2)}$$

These values are tabulated below:

Compound	$(\beta_{HRS}/\beta_{pNA})_{1064}$	$\beta_{HRS(0)}/\beta_{pNA(0)}$
	Experimental	Experimental
pNA	1	1
1-NO2	55	24.9
C-NO2	61.4	31.32

Experimentally obtained Frequency Dependent β_{HRS}/β_{pNA} Values and the Corresponding Extrapolated Static $\beta_{HRS(0)}/\beta_{pNA(0)}$ Values

The experimentally obtained value for β_{HRS} at 1064 for 4-nitroaniline, 11.4×10^{-30} was used to convert the $(\beta_{HRS}/\beta_{pNA})_{1064}$ ratios to $\beta_{HRS(1064)}$ for both molecules. The static $\beta_{HRS(0,TLM)}$ value for pNa 6.29×10^{-30} was extrapolated using the TLM expression in a fashion similar to that described above. This value was used multiplied with the $\beta_{HRS(0)}/\beta_{pNA(0)}$ values to give the static hyperpolarizibilities for both molecules. These results are tabulated below:

Compound	$\beta_{HRS(1064)}$ (10^{-30} esu)	$\beta_{HRS(0,TLM)}$ (10^{-30} esu)
	Experimental	Experimental
pNA	11.4	6.29
1-NO2	627	156.63
C-NO2	700	197.04

Frequency dependent $\beta_{HRS(1064)}$ and static $\beta_{HRS(0,TLM)}$ values

2.9 **References:**

(1) Van der Veen, M. H.; Rispens, M. T.; Jonkman, H. T.; Hummelen, J. C. *Adv. Funct. Mater.* **2004**, *14*, 215–223.

(2) Kogej, T.; Meyers, F.; Marder, S. R.; Silbey, R.; Bredas, J. L. *Synth. Met.* **1997**, *85*, 1141–1142.

(3) Dos Santos, D. .; Kogej, T.; Bredas, J. .; Boutton, C.; Hendrickx, E.; Houbrechts, S.; Clays, K.; Persoons, A.; Xhang, J. .; Dubois, P.; Jérôme, R. *J. Mol. Struct.* **2000**, *521*, 221–230.

(4) Almenningen, A.; Gatial, A.; Grace, D. S. .; Hopf, H.; Klaeboe, P.; Lehrich, F.; Nielsen, C. J.; Powell, D. L.; Trætteberg, M. *Acta Chem. Scand.* **1988**, *42A*, 634–650.

(5) Swager, T. M.; Grubbs, R. H. *J. Am. Chem. Soc.* **1987**, *109*, 894–896.

(6) Amaresh, R. R.; Liu, D.; Konovalova, T.; Lakshmikantham, M. V.; Cava, M. P.; Kispert, L. D. *J. Org. Chem.* **2001**, *66*, 7757–7764.

(7) Bryce, M. R.; Coffin, M. A.; Skabara, P. J.; Moore, A. J.; Batsanov, A. S.; Howard, J. A. K. *Chem. – Eur. J.* **2000**, *6*, 1955–1962.

(8) Michinobu, T.; May, J. C.; Lim, J. H.; Boudon, C.; Gisselbrecht, J.-P.; Seiler, P.; Gross, M.; Biaggio, I.; Diederich, F. *Chem. Commun.* **2005**, 737–739.

(9) May, J. C.; Lim, J. H.; Biaggio, I.; Moonen, N. N. P.; Michinobu, T.; Diederich, F. *Opt. Lett.* **2005**, *30*, 3057–3059.

(10) Michinobu, T.; Boudon, C.; Gisselbrecht, J.-P.; Seiler, P.; Frank, B.; Moonen, N. N. P.; Gross, M.; Diederich, F. *Chem. – Eur. J.* **2006**, *12*, 1889–1905.

(11) Tykwinski, R. R.; Zhao, Y. *Synlett* **2002**, 1939–1953.

(12) Zhao, Y.; Tykwinski, R. R. *J. Am. Chem. Soc.* **1999**, *121*, 458–459.

(13) Eisler, S.; Tykwinski, R. R. *Angew. Chem. Int. Ed.* **1999**, *38*, 1940–1943.

(14) Zhao, Y.; Campbell, K.; Tykwinski, R. R. *J. Org. Chem.* **2002**, *67*, 336–344.

(15) Ciulei, S. C.; Tykwinski, R. R. *Org. Lett.* **2000**, *2*, 3607–3610.

(16) Van Walree, C. A.; Kaats-Richters, V. E. M.; Veen, S. J.; Wieczorek, B.; van der Wiel, J. H.; van der Wiel, B. C. *Eur. J. Org. Chem.* **2004**, *2004*, 3046–3056.

(17) Albert, I. D. L.; Marks, T. J.; Ratner, M. A. *J. Am. Chem. Soc.* **1998**, *120*, 11174–11181.

(18) Keinan, S.; Zojer, E.; Bredas, J.-L.; Ratner, M. A.; Marks, T. J. *J. Mol. Struct. THEOCHEM* **2003**, *633*, 227–235.

(19) Kang, H.; Facchetti, A.; Zhu, P.; Jiang, H.; Yang, Y.; Cariati, E.; Righetto, S.; Ugo, R.; Zuccaccia, C.; Macchioni, A.; Stern, C. L.; Liu, Z.; Ho, S.-T.; Marks, T. J. *Angew. Chem. Int. Ed.* **2005**, *44*, 7922–7925.

(20) Brown, E. C.; Marks, T. J.; Ratner, M. A. *J. Phys. Chem. B* **2008**, *112*, 44–50.

(21) He, G. S.; Zhu, J.; Baev, A.; Samoć, M.; Frattarelli, D. L.; Watanabe, N.; Facchetti, A.; Ågren, H.; Marks, T. J.; Prasad, P. N. *J. Am. Chem. Soc.* **2011**, *133*, 6675–6680.

(22) Solomon, G. C.; Andrews, D. Q.; Van Duyne, R. P.; Ratner, M. A. *J. Am. Chem. Soc.* **2008**, *130*, 7788–7789.

(23) Zhao, Y.; Slepkov, A. D.; Akoto, C. O.; McDonald, R.; Hegmann, F. A.; Tykwinski, R. R. *Chem. – Eur. J.* **2005**, *11*, 321–329.

(24) Cui, M.; Ono, M.; Kimura, H.; Liu, B.; Saji, H. *J Med Chem* **2011**, *54*, 2225–2240.

(25) Peinado, C.; Salvador, E. .; Catalina, F.; Lozano, A. . *Polymer* **2001**, *42*, 2815–2825.

(26) Shelton, D. P. *Rev. Sci. Instrum.* **2011**, *82*, 113103–113103–6.

(27) Oudar, J. L.; Chemla, D. S. *J. Chem. Phys.* **1977**, *66*, 2664–2668.

Chapter 3 Cross-Conjugated Motifs Applied to Tricyanopyrroline Chromophore Systems

3.1 **Introduction:**

The synthesis of the disodium salt of 4-cyano-5-dicyanonethylene-3-hydroxy-2-oxo-3-pyrolline, **2Na-TCP** (**figure 3.1 (a)**) was first disclosed in a patent in 1961 by Rudolph Carboni[82]. It was prepared by reacting 2-amino-1,1,3-tricyano-1-propene with diethyl oxalate in the presence of sodium methoxide in methanol as base. Upon treating with a chlorinating agent such as oxalyl chloride or phosphorous oxychloride, the hydroxyl group was substituted with a chloride generating the strongly electrophilic **Cl-TCP**. By reacting this electrophile and its various analogues with electron rich aromatic compounds (**figure 3.1 (b)**), Carboni created a library of dyes, brilliantly colored ranging from red to green. These dyes were used in the staining of synthetic materials and fabrics made from polymers such as cellulose acetate and nylon.

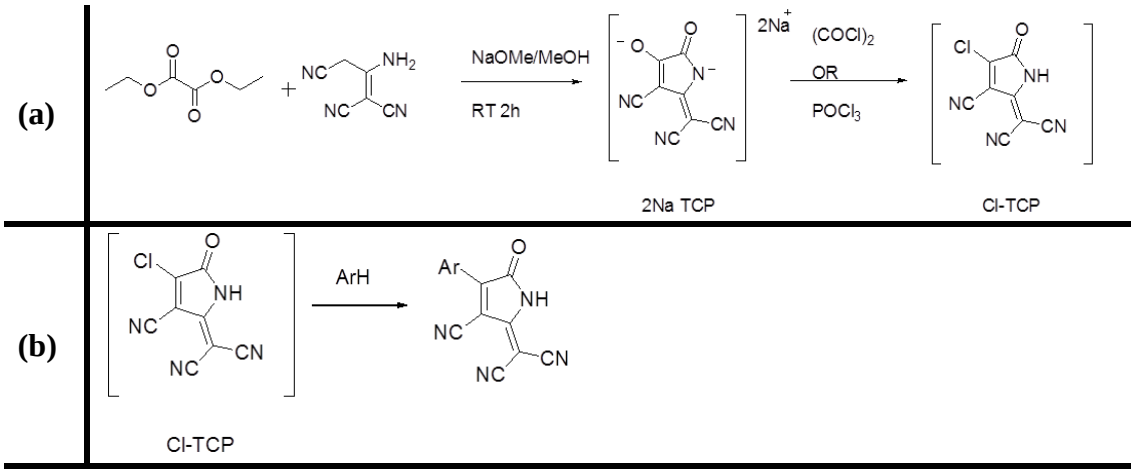

Figure 3.1: (a) Synthesis of **2Na-TCP** and **Cl-TCP**, **(b)** Reaction of **Cl-TCP** with an electron rich aromatic molecule

Since then, much of the work on tricyanopyrroline substituted molecules have used the **2Na-TCP** salt to make many chromophores that found applications not only as dyes for textiles[83–86] but also for thermal transfer printing[87,88] and optical data recording[89]. The merocyanine analogues of TCP chromophores have also been studiedfor use as photographic dyes[90].

In 2005, Kaneko *et al.* published the first series of TCP based molecules especially geared towards applications as second order non-linear systems and measured their β values using hyper-Rayleigh scattering measurements[91]. They found that the chromophores bearing the TCP group as an acceptor had higher hyperpolarizability values than corresponding chromophores bearing the dimethyl-TCF acceptors.

More noteworthy work[92] on TCP based chromophores by Jang et al. provided an alternate route to the synthesis of the TCP acceptor 3-methyl-4-cyano-5-dicyanomethylene-2-oxo-3-pyrroline. (**figure 3.2 (a)**). This methyl analogue of **Cl-TCP** provided a pathway towards synthesizing a new generation of chromophores with TCP acceptors (**figure 3.2 (b)**) via Knoevenagel condensation.

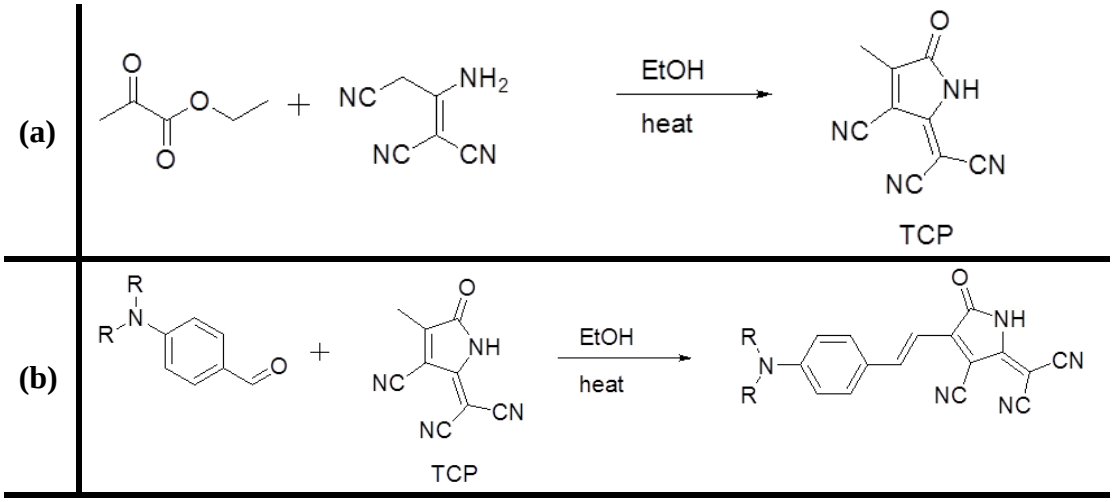

Figure 3.2: Synthesis of **TCP** acceptor and its subsequent reaction with an

aromatic aldehyde.

Once again a comparative study of the hyperpolarizabilities of TCP substituted chromophores with analogous dimethyl-TCF and CF_3-TCF chromophores indicated that β_{zzz} values of the TCP chromophores were around 1.5 times greater than those of their corresponding CF_3-TCF counterparts. This was also supported by previous theoretical work by Leclercq *et al*[93]. A study of the crystal structure of the TCP chromophores found the molecules to be coplanar as would be expected with no appreciable twist between the donor and the acceptor. The crystal packing diagram indicated head to tail alignment of the chromophores resulting in overall centrosymmetric ordering of the crystal.

A major drawback for this class of small molecules has been the formation of strong dipole-dipole aggregates. Formation of aggregates results in a myriad of issues ranging from low poling efficiencies to broadening of the optical spectra of the film resulting in appreciable loss at telecommunication wavelengths, overall resulting in poor device characteristics. While strong electrostatic interactions are often observed in high β donor-π bridge-acceptor type chromophores, the issue is significantly aggravated in the case of the TCP chromophores due to the planar nature of the TCP acceptor compared to CF_3-TCF acceptors. The authors found that substitution of the NH group on the acceptor with bulky groups did not result in any improvement in the dipole-dipole aggregation behavior[92]. This substitution if done with even a weakly electron donating group can also lead to a reduction in hyperpolarizability by reducing the acceptor strength.

Cho *et al.* synthesized a triphenyl ethane based dendrimer with TCP chromophores in an attempt to enhance r_{33} with moderate success[94]. They also substituted photo-crosslinkable

chalcone groups onto the chromophores to induce UV-curing and improve thermal resistance of these systems for applications in multilayer fabrication processes.

In a later paper Cho *et al.* synthesized a short series of chromophores bearing a phenyl or a thienyl side group (**figure 3.3 (a)**) and found them to maintain high optical quality in films when doped even at 40 wt% in amorphous polycarbonate (APC)[95]. They investigated the electric field poling characteristics of these materials and measured r_{33} values and found that the introduction of a lateral group to the backbone of the chromophores reduced aggregation and improved the electro-optic coefficient. They also substituted the acceptor with benzyl and perfluorobenzyl groups (**figure 3.3 (b)** and **(c)**) but found that this resulted in a reduction in r_{33}.

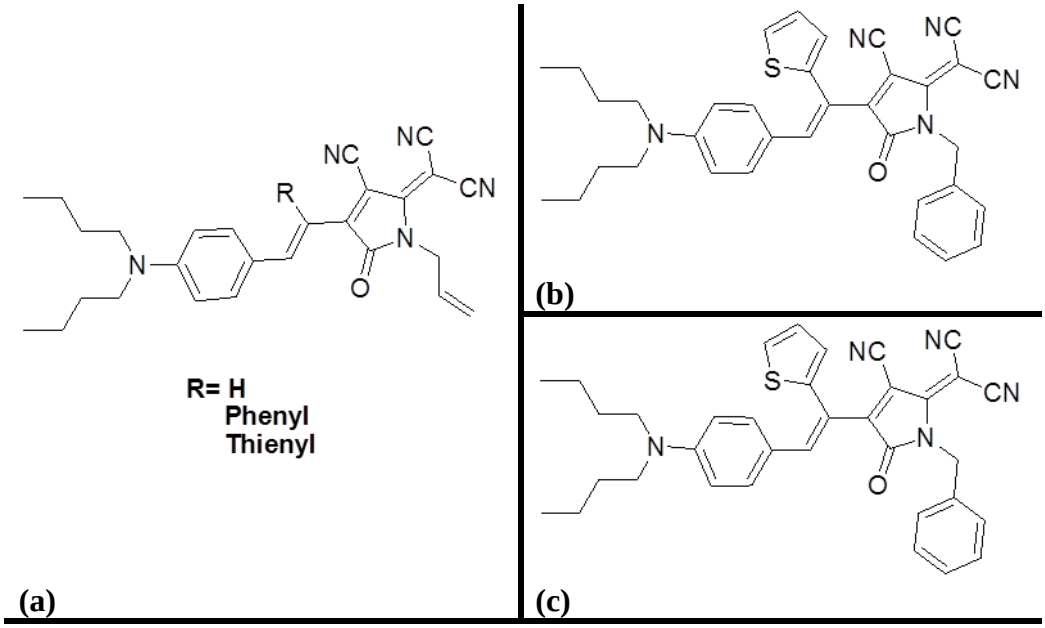

Figure 3.3: TCP chromophore with side groups on the conjugated backbone

In summary, the study and application of TCP small molecules has been hampered by strong electrostatic interactions of the chromophore dipoles causing aggregation in the bulk material. Substitution of the chromophore on the acceptor moiety does not seem to significantly

improve film quality or aid in increasing poling efficiencies. A lateral group on the backbone of these molecules has been shown to improve these characteristics. In Chapter 2 the electronic properties of cross conjugated systems were studied using UV-vis, fluorescence and HRS measurements and their structures were elucidated using X-ray crystallography. It was established that the presence of a cross-conjugated moiety did not prevent charge transfer from the donor to the acceptor and that it did not result in a significant reduction of hyperpolarizability values of these simple chromophores.

In Chapter 3 these cross-conjugated systems will be substituted onto TCP chromophores and the electronic and structural properties will be investigated. To that effect the following series of chromophores were synthesized:

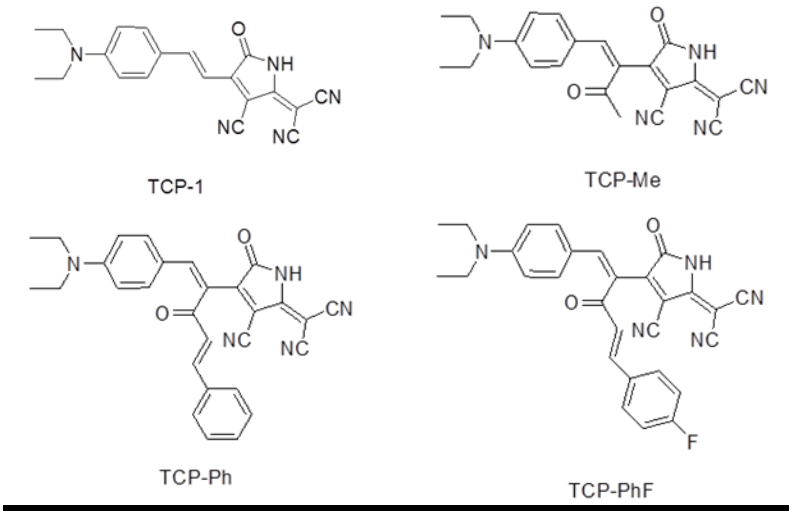

Figure 3.4: Structures of Chromophores Synthesized and Studied

The effect of a cross-conjugated side group on the electronic properties will be studied via UV-vis spectroscopy and the effect on hyperpolarizability will be investigated by HRS measurements. X-ray crystallography will be used to elucidate the structures of these new

molecules and finally quantum mechanical calculations will be used to help explain their observed behavior.

3.2 **Synthesis of TCP Chromophores:**

The reaction schemes for the synthesis of the TCP chromophores are given in **figure 3.5 and figure 3.7**. The synthesis of **TCP-1** has been published in literature. Malononitrile dimer and ethyl pyruvate were refluxed in methanol for 30 minutes followed by addition of N,N-diethylamino benzldehyde (**figure 3.7**). The reaction was refluxed for another hour following which the product was collected by filtration of the reaction and purified by washing with cold ethanol.

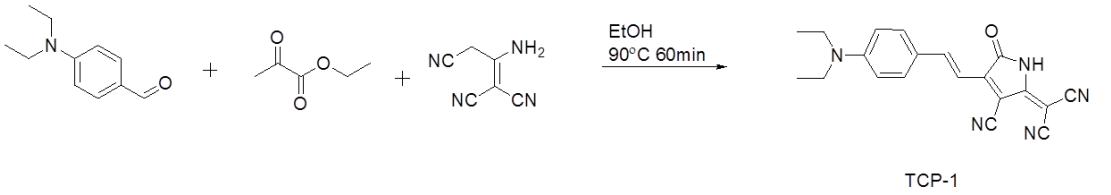

Figure 3.5: Synthesis of **TCP-1**

TCP-Me, **TCP-Ph** and **TCP-PhF** were synthesized from **1-Me**, **1-Ph** and **1-F** respectively. **2NaTCP** was prepared by reacting diethyl oxalate with 1,1,3-tricyano-2-amino-1-propene (malononitrile dimer) in the presence of sodium ethoxide (**figure 3.7; scheme (a)**). The yellow product that precipitated out of solution after 3 hours was collected by filtration and rinsed with benzene to remove impurities. Synthesis of **TCP-Me** (**figure 3.7; scheme (b)**) was carried out by dissolving **1-Me** and **2NaTCP** in N,N-dimethylformamide (DMF) followed by addition of acetic anhydride. The flask was then cooled and phosphorous oxychloride ($POCl_3$) was added to the reaction dropwise; this generated a chlorinated electrophilic intermediate **Cl-**

TCP (**figure 3.6**) *in situ* which upon reaction with **1-Me** for 1 hour generated **TCP-Me**. The product was precipitated by pouring the reaction mixture over ice.

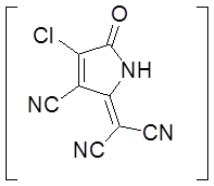

Figure 3.6: Chlorinated TCP (**Cl-TCP**)

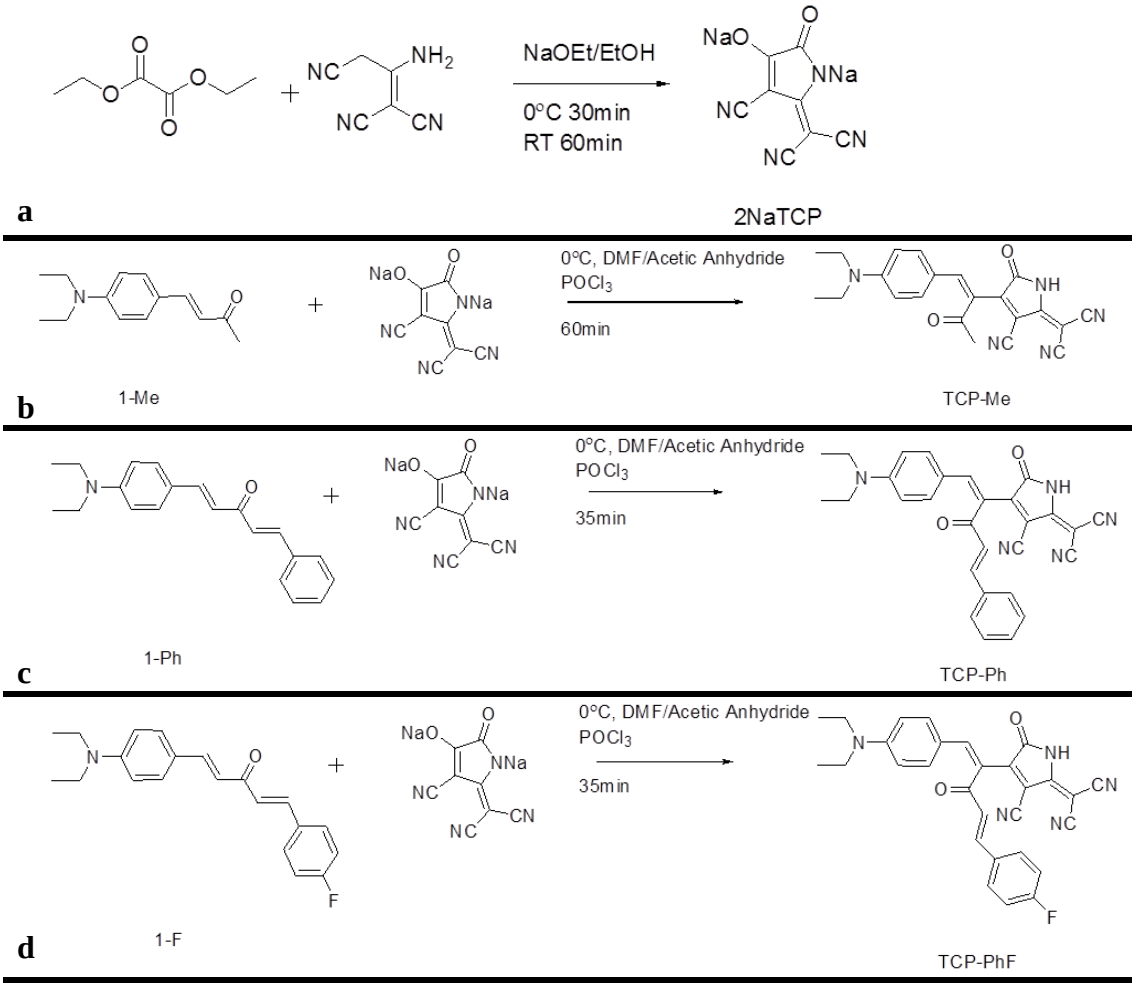

Figure 3.7: Synthesis of substituted TCP chromophores

TCP-Ph and **TCP-PhF** were synthesized (**figure 3.7; scheme (c) and (d)**) similarly with shorter reaction times. Shorter reaction times and lower temperatures gave cleaner products but did result in low yields. It must be noted that addition of excess phosphorous oxychloride or increasing reaction times caused decomposition to occur resulting in complicated purification as the final products do not purify well using column chromatography and prep-TLC methods have to be used for separation. The reaction of **1-NEt2** with **2NaTCP** under similar conditions resulted in no product and less than 5 % product upon switching from DMF to acetonitrile as solvent. Reacting **1-NO2** similarly gave back starting materials.

3.3 **Structure**:

TCP-1 is expected to be planar as published in literature[92]. Based on NMR coupling constants, the double bond geometry is trans. Two possible isomers are possible for **TCP-Me**, **TCP-Ph** and **TCP-PhF**. The TCP group can be either cis or trans to the N,N-dimethylamino donor (**figure 3.8)** .

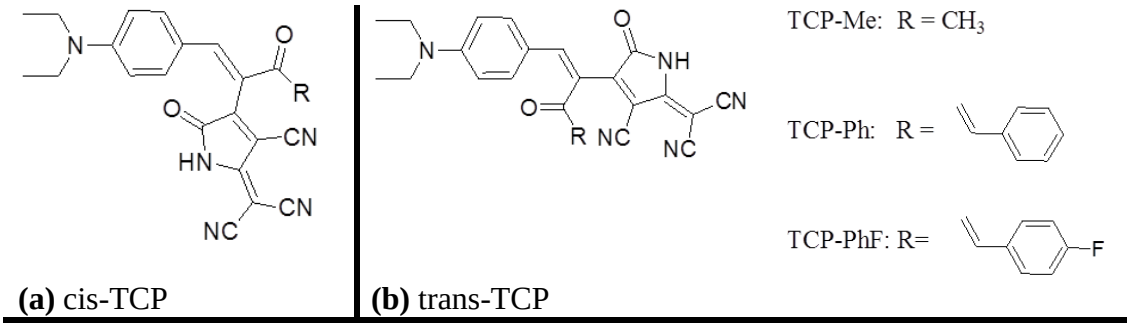

Figure 3.8: Possible isomers of the TCP chromophores: **(a)** TCP group cis to the donor **(b)** TCP group trans to the donor

Both isomers are sterically hindered as the group connected cis to the donor would be in close proximity with the aromatic hydrogens. As a result the cis functional group would likely be out of plane with respect to the rest of the molecule. Cho *et al*. synthesized a similar chromophore[95] with a thiophene side group (**figure 3.3**) and found that the reaction produced exclusively the trans TCP product similar to **figure 3.8 (b)**. The X-ray structure published for the thiophene molecule showed the TCP acceptor coplanar to the plane of the donor and the thiophene moiety nearly perpendicular to the plane of the molecule.

3.3.1 **Optimized structures from quantum mechanical calculations:**

Gaussian 09C was used to calculate optimized geometries (**figure 3.9**) using the B3LYP hybrid functional with the 6-31+G* basis set. The input structure was limited to the transTCP isomer as this was the expected isomer from the reaction.

A planar geometry was predicted for **TCP-1** as expected for this molecule and consequently the dihedral angle between the donor and acceptor was 0°.

In the case of the substituted TCP chromophores **TCP-Me**, **TCP-Ph** and **TCP-PhF**, the plane of the cross-conjugated groups were at 110° to 116° to the plane of the donor moiety. The cause of the significant predicted deviation from a 90° dihedral angle was likely due to Van der Waals interactions between the hydrogens on the α carbon and those on the aromatic ring.

More importantly and unexpectedly, a dihedral angle of between 29° (**TCP-Me**) to 35°(**TCP-Ph** and **TCP-PhF**) was seen between the diethylamino donor and TCP acceptor. This would be quite unusual since the donor and acceptor are conjugated and any deviation from coplanarity would break conjugation. The presence of an auxillary cross-conjugated group seems

to cause this deviation as it is not seen in **TCP-1** or in the thiophene substituted TCP chromophores studied by Cho *et al*[95].

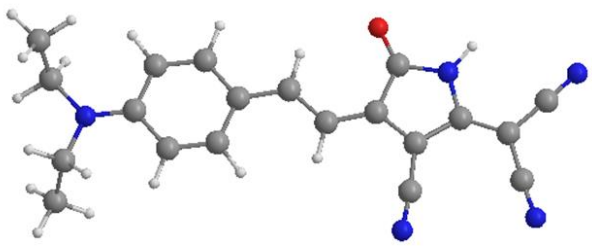

TCP-1
Dihedral Angle: 0°

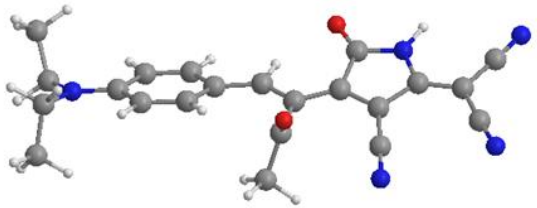

TCP-Me
Dihedral Angles:
Donor-TCP: 29°
Donor-Methyl ketone: 110°

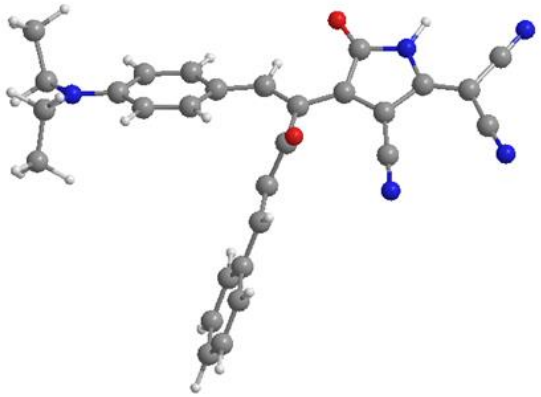

TCP-Ph
Dihedral Angles:
Donor-TCP: 35°
Donor- Phenylvinyl ketone: 115°

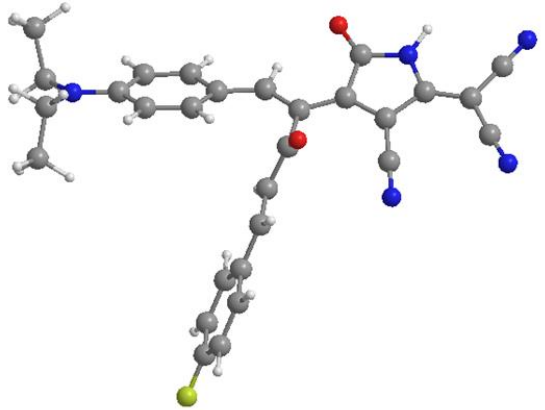

TCP-PhF
Dihedral Angles:
Donor-TCP: 35°
Donor- 4-Fluoro phenylvinyl ketone: 116°

Figure 3.9: B3LYP Optimized geometries of TCP chromophores

3.3.2 **X-ray crystallography- Experimentally determined structures:**

Crystals were grown of compounds **TCP-Me** and **TCP-Ph** and analyzed using X-ray diffraction. X-ray crystallographic data was collected at -173^{o}C on Bruker APEX II single crystal X-ray diffractometer, Mo-radiation. The data was integrated and scaled using SAINT, SADABS within the APEX2 software package by Bruker.

TCP-Me: Lustrous green crystals of TCP-Me were grown from a saturated solution in tetrahydrofuran (THF). The sample, which diffracted rather well, was prepared out of the inside of a larger piece, indicating that the THF solvent may escape easily, since smaller crystals, even if with proper crystalline morphology, would not diffract at all. The oxygen atom, O3 of the THF hydrogen-bonds to nitrogen, N1 on the acceptor moiety. **Figure 3.10 (a)** shows an ORTEP of the asymmetric unit. The TCP moiety is found to be in a trans configuration with respect to the diethylamino benzene donor whereas the cross-conjugated (methyl ketone) group is found to be cis and perpendicular to the plane of the conjugated section. Quite unexpectedly, only one rotational isomer was observed in the crystal structure in which the methyl ketone moiety is pointed into the plane of the paper (away from the viewer) with the donor to the left and the acceptor to the right. Since both the TCP group and the cross-conjugated group are rotatable about their respective single bonds, it is quite possible that with the methyl ketone group, the barrier for rotation from one rotamer to the other is small enough in solution to allow for inter-conversion during crystallization resulting in only one rotamer being preferentially crystallized.

Figure 3.10 (b) shows a packing diagram of the crystal. While THF fills the voids between molecules which are reversely aligned towards each other, the molecules appear slightly tilted towards each other but stay mainly parallel aligned with respect towards their longest elongation. The overall packing is centrosymmetric.

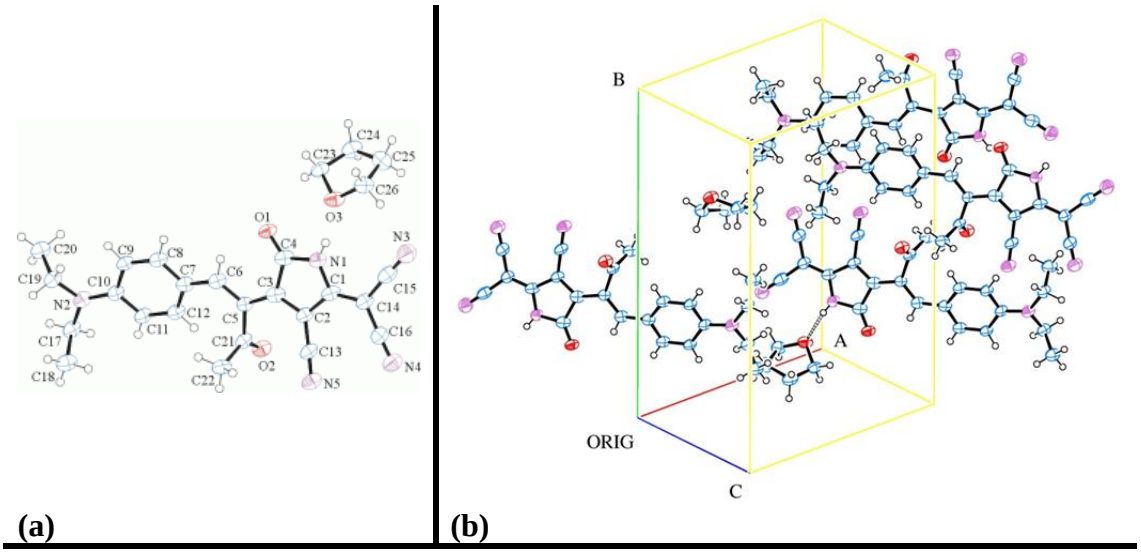

Figure 3.10: **(a)** ORTEP of the structure of **TCP-Me** with thermal ellipsoids at the 50% probability level. **(b)** Packing diagram of **TCP-Me**

TCP-Ph: Green needles of **TCP-Ph** obtained from precipitation of the reaction solution in ethanol were used as is for crystallography. **Figure 3.11 (a)** shows an ORTEP of the asymmetric unit. The structure exhibits triclinic symmetry but with significant twinning. In addition, disorder was observed in a terminal phenol (not shown in **Figure 3.11 (a)**). Once again, the TCP moiety is found to be in a trans configuration with respect to the diethylamino benzene donor and the cross-conjugated (phenylvinyl ketone) group is found to be cis and perpendicular to the plane of the conjugated section. Two rotational isomers were observed in the crystal structure, one in which the phenylvinyl ketone moiety is pointed into the plane of the paper with the donor to the left and the acceptor to the right and one in which the phenylvinyl ketone is pointed out of the plane of the paper (towards the viewer). In this case, the reaction, as expected, generates a 50:50 mixture of each rotamer and since the barrier for rotation of the phenylvinyl ketone and the TCP acceptor in this molecule is expected to be much higher than for the smaller

TCP-Me methyl ketone side group, inter-conversion is prevented in solution during crystallization.

Figure 3.11 (b) shows a packing diagram of the crystal where both rotamers are observed. The phenyl groups on adjacent chromophores lie at a distance of 2.1 Å which indicates that the phenylvinyl group while being perpendicular to the plane of conjugation influences the crystal to crystal distance. At a distance of 2.91Å the phenyl groups also interact weakly with the diethyl amino groups on the donor. The head to tail orientation results in centrosymmetric packing.

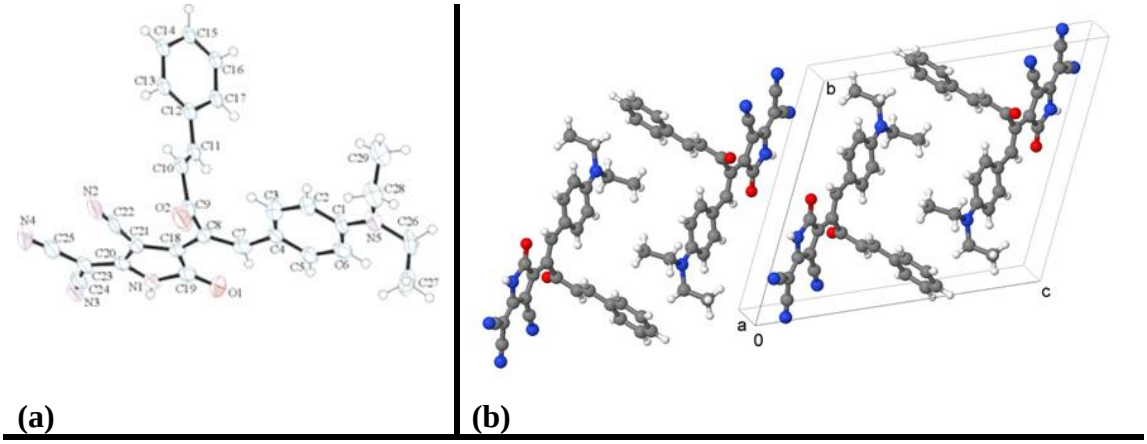

Figure 3.11: (a) ORTEP of **TCP-Ph** with thermal ellipsoids at the 50% probability level. Disorder omitted for clarity **(b)** Packing diagram of **TCP-Ph**

3.3.3 **Dihedral angles:**

TCP-Me: The crystal structure of TCP-Me (**figure 3.12**) indicates a twist between the diethylamino donor and the TCP acceptor very close to the 29° angle predicted by the optimized geometry obtained from theoretical calculations (**Figure 3.9**). Such a deviation from co-planarity for similar chromophores[95] (although not with cross-conjugated side groups) has not been observed previously in literature. The dihedral angle between the donor and acceptor was measured to be ~23°. This angle was difficult to measure due to another feature seen on the donor benzene moiety. The aromatic ring was found to be puckered in one direction and the bond lengths within the aromatic ring indicate an almost quinoid system albeit only within the ring. The puckering also causes the nitrogen on the donor to deviate from coplanarity by ~13°. Such effects can be caused by Van der Waals interaction within the crystal although no clear interactions could be identified in the packing diagram.

The plane of the methyl ketone side group was found to be at an angle of 110° with the plane of the donor indicating that it was slightly rotated towards the acceptor.

TCP-Me	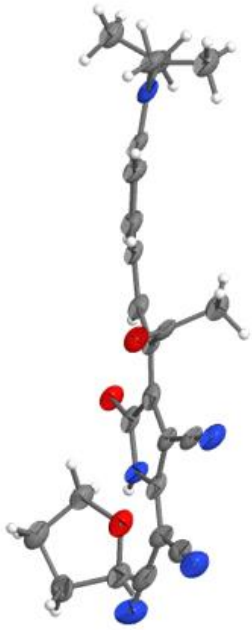	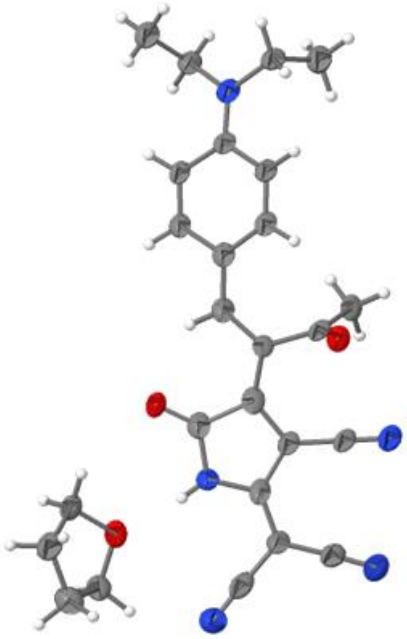
	(a)	**(b)**
	Dihedral Angles:	
	Donor-TCP: 23°	Donor-Methyl ketone 110°

Figure 3.12: (a) Side profile of the crystal structure of **TCP-Me** showing the dihedral twist between donor and acceptor as well as puckering of the aromatic ring. **(b)** Top profile of **TCP-Me** showing twist of the methyl ketone.

TCP-Ph: The crystal structure of TCP-Ph (**figure 3.13**) once again indicates a twist between the diethylamino donor and the TCP acceptor. This twist however, is much lower than the 35° predicted by the optimized geometry obtained from theoretical calculations (f**igure 3.9)**. The dihedral angle between the donor and acceptor was measured to be ~12° which is approximately half of that seen in **TCP-Me** although still significant. The plane of the phenylvinyl ketone side group was found to be at an angle of ~67° with the plane of the donor indicating that it was slightly rotated towards the donor unlike that seen in **TCP-Me**.

TCP-Ph	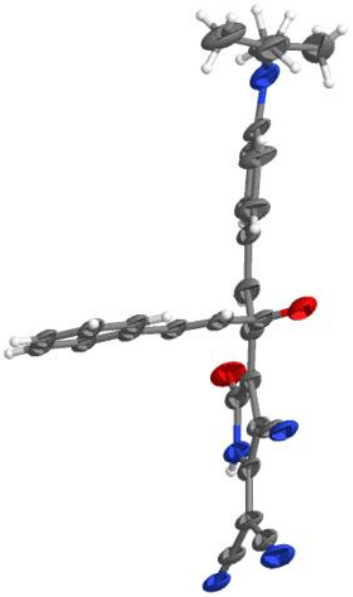	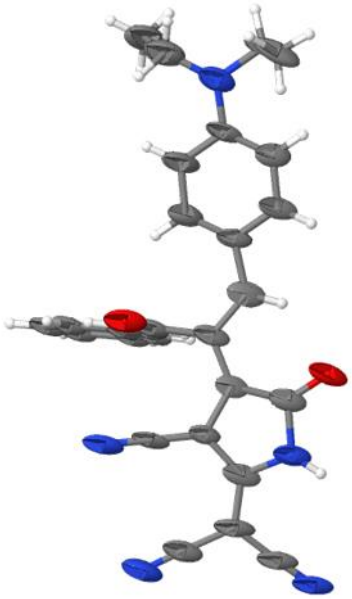
	(a)	**(b)**
	Dihedral Angles: Donor-TCP: 16°	Donor-phenylvinyll ketone 67°

Figure 3.13: (a) Side profile of the crystal structure of **TCP-Ph** showing the dihedral twist between donor and acceptor as well as puckering of the aromatic ring. **(b)**Top profile of **TCP-Ph** showing twist of the phenylvinyl ketone.

3.4 **UV-Vis Spectroscopy of TCP Chromophores:**

3.4.1 **TCP chromophores: Comparison of UV-vis spectroscopy in Chloroform:**

All the TCP chromophores show a strong absorbance around 720-730nm (**figure 3.14**). Molar absorptivity ε, for this absorbance was calculated to be around 77000 L mol^{-1} cm^{-1} for **TCP-1** and 34000 L mol^{-1} cm^{-1} for **TCP-Me**. The substituted chromophores **TCP-Me**, **TCP-Ph** and **TCP-PhF** have slightly blue shifted peaks compared to **TCP-1** by about 8-11nm and the peaks are also slightly broader. The primary transition of **TCP-Me**, **TCP-Ph** and **TCP-PhF** correlate strongly with the main transition of **TCP-1** which indicates that the TCP acceptor in these new chromophores is situated trans to the donor whereas the cross-conjugated section is likely cis to the donor as shown in **Table 3.1**. This was also observed in the X-ray crystal structures shown in **figure 3.10** and **figure 3.11**. Other than the slight hypsochromic shift seen compared to **TCP-1**, the cross-conjugated substitution on the chromophores does not affect this transition and the λ_{max} values are nearly identical for the three substituted molecules.

While **TCP-1** does have some weaker transitions in the 280-500nm region, stronger transitions are indicated in this region for the three substituted chromophores. These higher energy transitions are typically expected to be indicative of cis-trans isomerization within the chromophore. In these new molecules synthesized, however, rotational isomers would be more likely. As indicated in the crystal structure for **TCP-Me** and **TCP-Ph** two rotamers are possible for the substituted chromophores (**figure 3.11**). As the molecules transition from one isomer to another, the cross-conjugated group would transition from being perpendicular to the donor to being parallel and then perpendicular (rotated 180°) again. The TCP group would likewise go from being parallel to the donor to being perpendicular and then parallel (rotated 180°) again.

The absorbances seen in the higher energy regions likely correspond to the donor-cross-conjugated group transitions and are indicative of a distribution of rotational isomers.

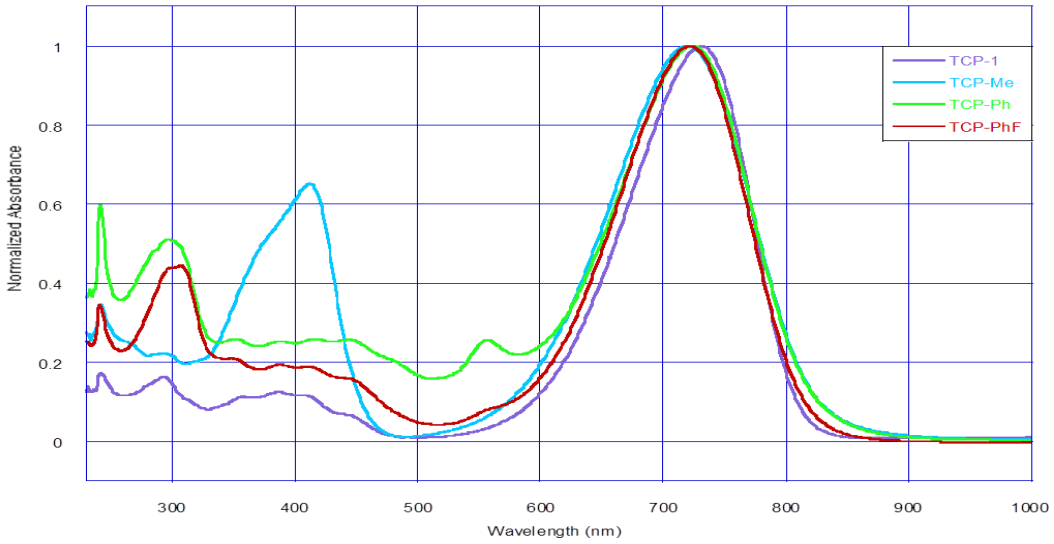

Figure 3.14: UV-vis spectra of TCP chromophores in chloroform

Name	TCP-1	TCP-Me	TCP-Ph	TCP-PhF
Structure	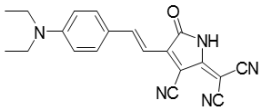	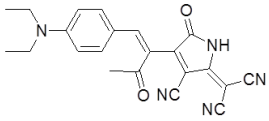	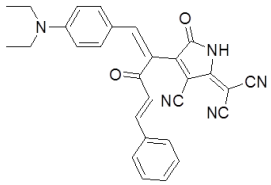	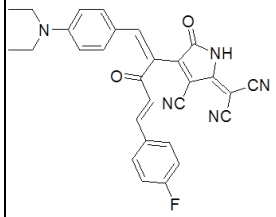
Wavelength λ_{max} (nm)	731	412 720	296 723	307 723

Table 3.1: Absorbance maxima of TCP chromophores in chloroform

Quantum mechanical calculations for electronic transitions in chloroform were performed using CAM-B3LYP functional in chloroform on B3LYP/6-31+G* optimized geometries shown in **figure 3.9**. All the primary transitions (634-647nm) are HOMO to LUMO transitions. The HOMOs for all these molecules lie primarily on the diethylaminobenzene donor while the LUMOs lie on the TCP acceptor and are identical to that shown for **TCP-1** (**figure 3.15**). The primary transition for **TCP-1** (647nm) was predicted at ~84nm lower than the experimental value (731nm) and those predicted for **TCP-Me** (633nm), **TCP-Ph** (~635nm) and **TCP-PhF** (~635nm) are blue shifted from the experimental values by ~87-88 nm .

The values predicted for **TCP-Me**, **TCP-Ph** and **TCP-PhF** are ~12-14nm to the blue of that predicted for **TCP-1** compared to ~8-11nm seen in the experimental data.

All three cross conjugated chromophores have almost identical primary transitions. All these trends are similar to the trends observed in the experimental data and CAM-B3LYP does a good job of predicting both the trends and the actual values for the major transition.

Structure	Experimental λ_{max} (nm)	Theoretical: CAM-B3LYP/6-31+G*		
		λ_{max} (nm)	f^a	Transition
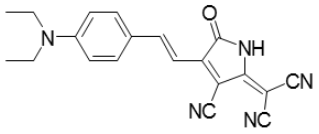 TCP-1	731	647.46 335.68	1.6731 0.4392	HOMO→ LUMO HOMO-2→LUMO
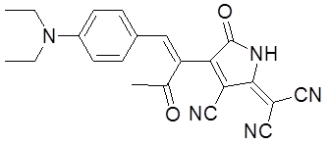 TCP-Me	720 412	633.44 339.25	1.6424 0.3551	HOMO→LUMO HOMO-2→LUMO
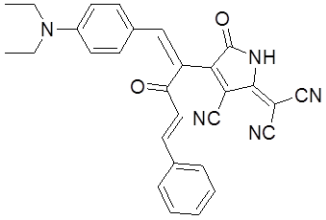 TCP-Ph	723 296	635.44 392.56 339.44	1.5772 0.1803 0.1026	HOMO→LUMO HOMO→LUMO+1 HOMO-2→LUMO
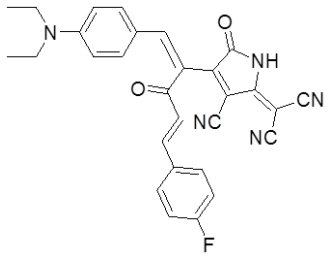 TCP-PhF	723 307	634.61 393.67 339.42	1.5763 0.1779 0.1482	HOMO→LUMO HOMO→LUMO+1 HOMO-2→LUMO

Table 3.2: Absorption maxima $\lambda_{max}$of chromophores in chloroform**:**
Experimental Vs Calculated values
a: calculated oscillator strengths

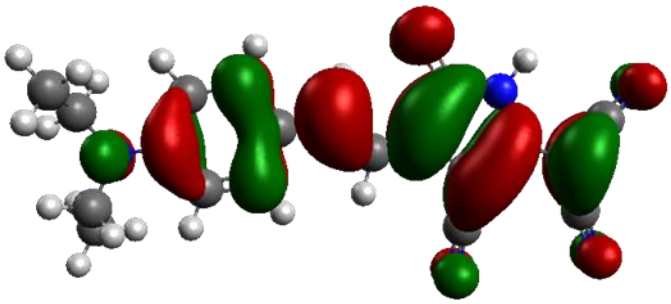

LUMO

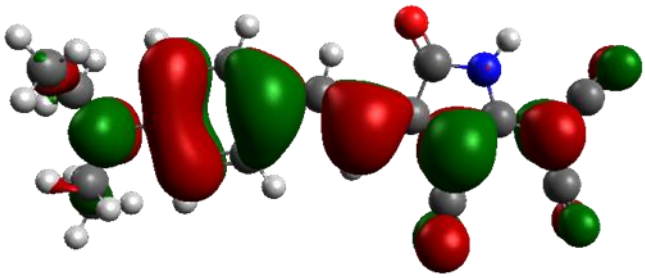

HOMO

Figure 3.15: HOMO and LUMO diagrams for **TCP-1**

Theory also suggests secondary transitions from all molecules. A HOMO-2→LUMO is predicted for all chromophores along with HOMO→ LUMO+1 predicted for **TCP-Ph** and **TCP-PhF**. Considering how close these transitions are in energy and taking into account the error in calculation, if present, they are likely to overlap in experimental optical spectra.

The HOMO-2→LUMO transition predicted for **TCP-1** at ~336nm, expected to have a strong oscillator strength of ~0.4 in chloroform is not well defined in the experimental plot. Similar secondary transitions at 339 nm are predicted for **TCP-Me**, **TCP-Ph** and **TCP-PhF**, all from a lower lying HOMO-2 to LUMO (**figure 3.16**). Based on theoretical calculations, the HOMO-2 orbitals of **TCP-Ph** and **TCP-PhF** (**figure 3.16**) are identical and significantly more delocalized compared to that of **TCP-Me** (which is identical in configuration to HOMO-2 of **TCP-1** (not shown)).

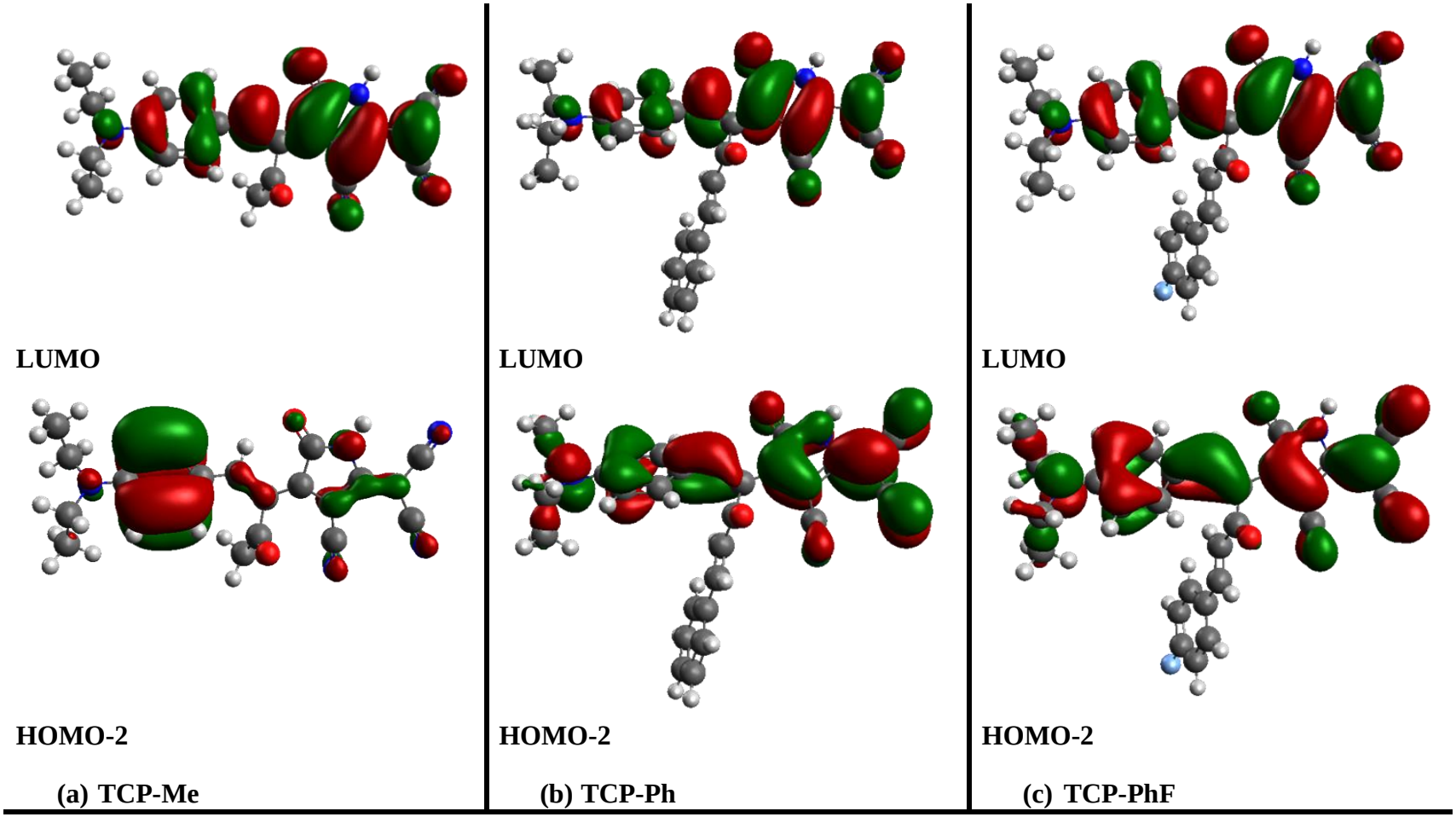

Figure 3.16: HOMO-2 to LUMO transition for **(a) TCP-Me**, **(b) TCP-Ph** and **(c) TCP-PhF**

As a comparison, the UV-vis spectrum of **TCP-Me** was overlaid with **1-Me** (**figure 3.17**) and the high energy absorbance at 412 nm for **TCP-Me** was found to overlap with the major absorbance of **1-Me** at 390nm.

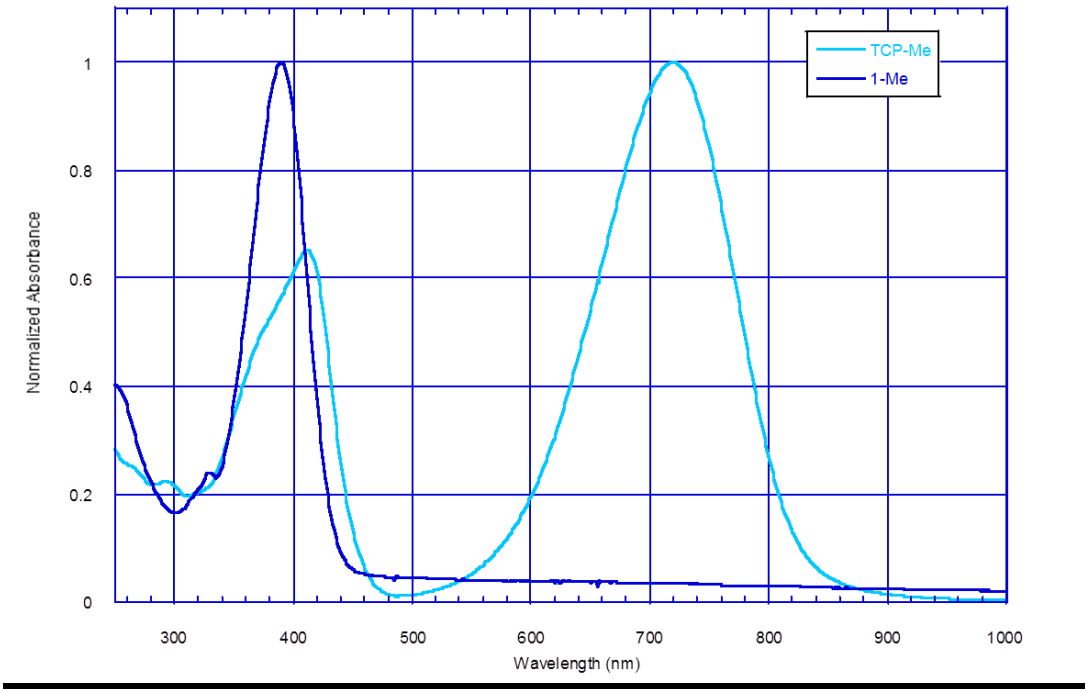

Figure 3.17: UV-Vis of **TCP-Me** and **1-Me** in Chlororform

Similar comparisons for **TCP-Ph** overlaid with **1-Ph** (**figure 3.18**) and **TCP-PhF** overlaid with **1-F** (**Figure 3.19**) indicate clear overlap of the high energy absorbances for **1-Ph**(310nm) and **1-F** (341nm and shoulder at ~300) with the peak at ~300nm seen for both **TCP-Ph** and **TCP-PhF**.

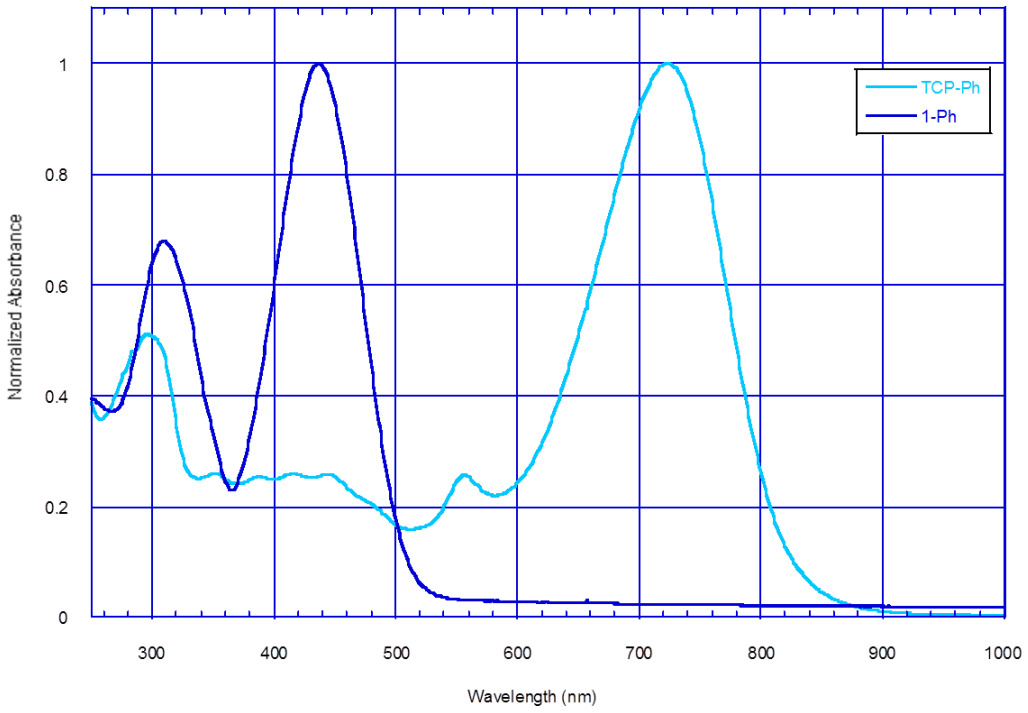

Figure 3.18: UV-Vis of **TCP-Ph** and **1-Ph** in Chlororform

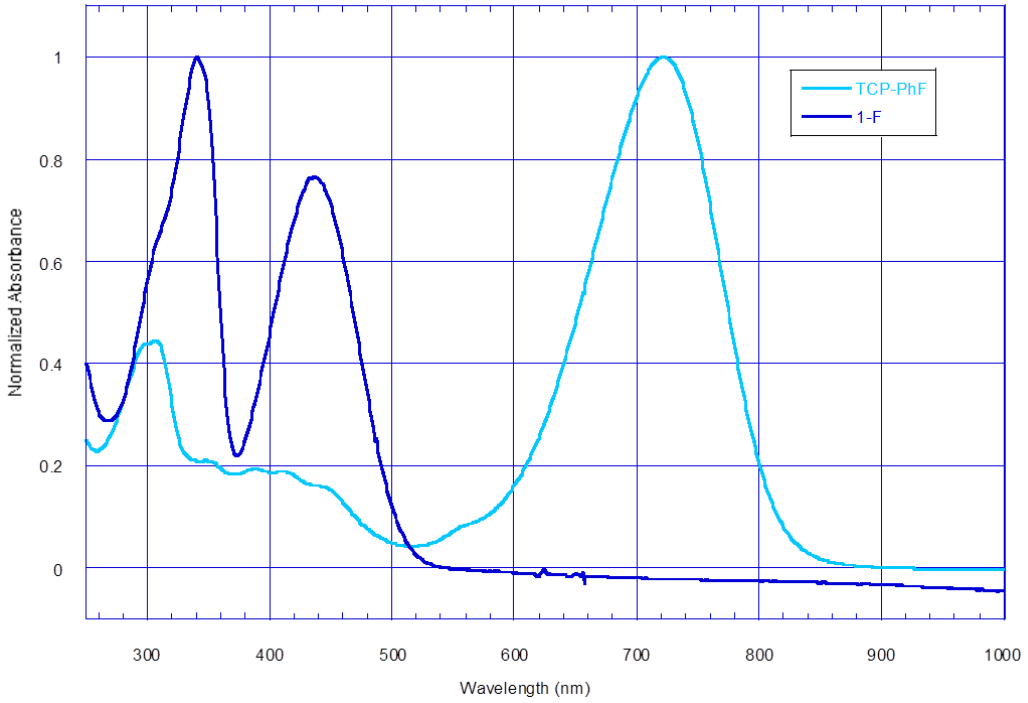

Figure 3.19: UV-Vis of **TCP-PhF** and **1-F** in Chlororform

The HOMO→LUMO+1 transition at ~ 393nm is predicted only for **TCP-Ph** and **TCP-PhF** and have higher oscillator strengths than their respective HOMO-2→LUMO transitions. These predicted HOMO→LUMO+1 transitions are very close in energy to the low energy absorbance seen for **1-Ph** (theoretical:410nm and experimental:436nm) and **1-F** (theoretical:411nm and experimental:436nm) (**Table 2.2**) (**figure 3.18** and **figure 3.19**). These low energy absorbances in **1-Ph** and **1-PhF** were attributed to the charge transfer from the donor across the cross-conjugated center to the acceptor. In **figure 3.20** it is seen that indeed the LUMO+1 of **TCP-Ph** and **TCP-PhF** are located on the cross-conjugated moiety. This suggests that these cross-conjugated groups act as auxiliary acceptors for these molecules.

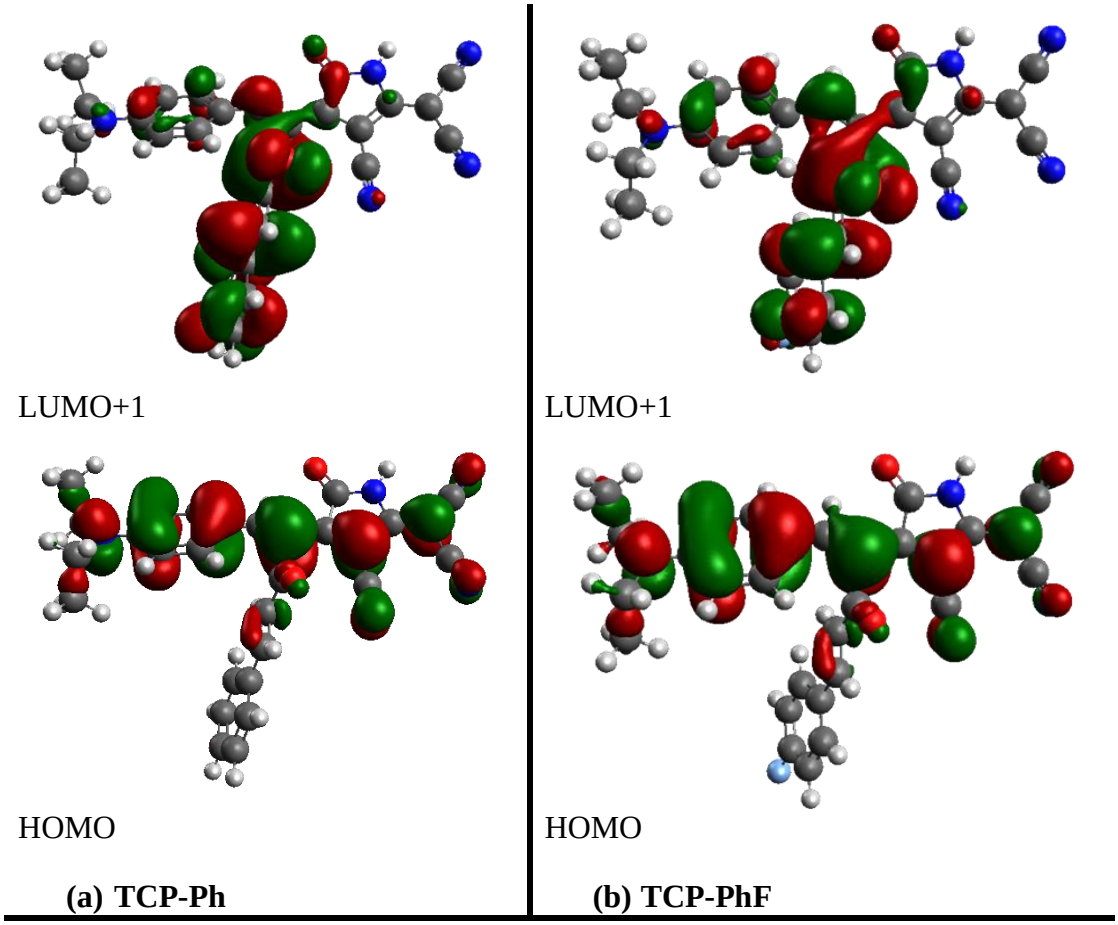

Figure 3.20: HOMO to LUMO+1 transition for **(a) TCP-Ph** and **(b) TCP-PhF**

3.4.2 **TCP chromophores: Polarity study:**

UV-vis spectrum of **TCP-1** chromophore in different solvents (**figure 3.21**) demonstrates a generally bathochromic shift with increasing solvent polarity. Chloroform and 1,1,2-trichloroethane (112-TCE) however, tend to red shift the transition the most even though they are of medium polarity. This is typically seen in chlorinated solvents due to halogen-aromatic π electron interactions.

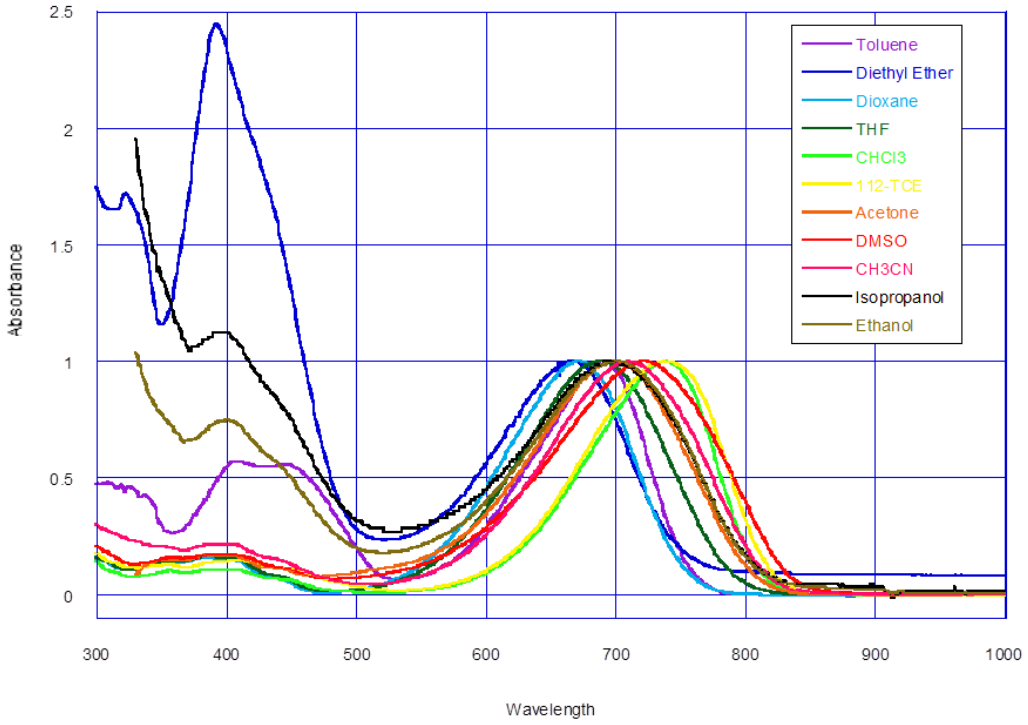

Figure 3.21: Polarity plot of **TCP-1** chromophore
This plot is normalized at the ~730nm peak to show the comparative intensity of the 400nm peak in different solvents

More interestingly though, a second high energy peak was seen distinctly in toluene and diethyl ether, both of lower polarity; isopropanol and ethanol, both of high polarity with hydrogen bonding capabilities. The peak shapes are nearly identical in isopropanol and ethanol at 400nm with a shoulder ~440nm. In toluene it appears as two overlapping peaks at ~405nm and

455nm and in diethyl ether as a strong peak at ~390nm with a shoulder at ~430nm. It must be noted that **TCP-1** was found to be sparingly soluble in toluene, diethyl ether, chloroform, 112-TCE, isopropanol and ethanol. While it is unclear why the peak emerges in low polarity solvents as well as in high polarity but not in the other solvents it is possible that it is from aggregation caused by low solubility or from preferential stabilization of some higher energy isomer in these solvents.

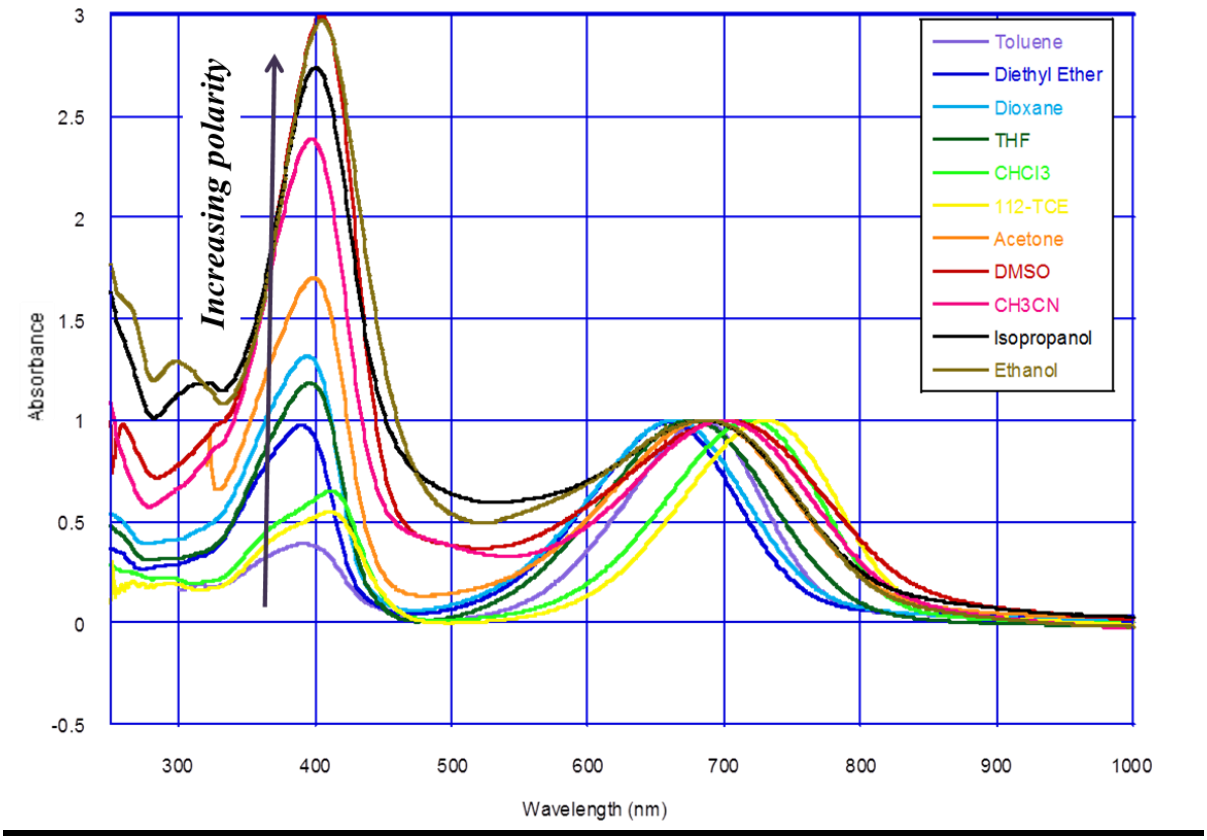

Figure 3.22: Polarity plot of **TCP-Me** Chromophore
This plot is normalized at the ~700nm peak to show the comparative intensity of the 400nm peak in different solvents

TCP-Me was chosen for the polarity study because it showed two very clear absorbances unlike **TCP-Ph** and **TCP-PhF**. UV-vis spectrum of **TCP-Me** chromophore in different solvents

exhibits a generally bathochromic shift of the low energy peat at 720nm with increasing solvent polarity. This peak is the major charge-transfer peak from the HOMO on the diethylamino benzene donor to the LUMO on the TCP acceptor and the trend indicates a highly polar molecule as expected from the molecular structure. This peak also broadens in more polar slovents like dimethylsulfoxide, acetonitrile, isopropanol and ethanol. Once again chloroform and 112-TCE tend to red shift the transition the most even though they are of medium polarity.

The high energy peak at 412nm seen in the chloroform spectrum in **figure 3.14** and **figure 3.22** while blue shifted slightly in all other solvents (except 112-TCE) actually doesn't show any hypsochromic or bathochromic trends in the other solvents. It does however increase in intensity in going from non-polar to polar solvents with chloroform and 112-TCE once again being outliers to this trend. Such an increase in absorbance of a secondary transition has not been described previously in literature for any TCP chromophore. Based on the discussion on the crystal structure of **TCP-Me**, since the TCP and the methyl ketone groups are rotatable about their single bonds, rotational isomers are possible for **TCP-Me** in solution. The simplest explanation for the trend seen in the high energy peak is the preferential stabilization of a rotational isomer in which the TCP moiety is perpendicular (**figure 3.23**, **structure A**) and the methyl ketone is in the plane with the diethylamino benzene donor. With this rotamer, the TCP moiety being perpendicular to the donor would be more isolated from the donor. This conformation would cause an isolation of the charge on the acceptor (due to lowering of electron delocalization). Structure **A** (**figure 3.23**) would be a higher energy rotamer and it would therefore be stabilized more in more polar solvents due to localization of charges. Thus a change in the polarity of the solvent would result in a change in the ratio of rotamer **A** and rotamer **B (figure 3.23)** that would manifest as a change in relative absorbance of the two peaks

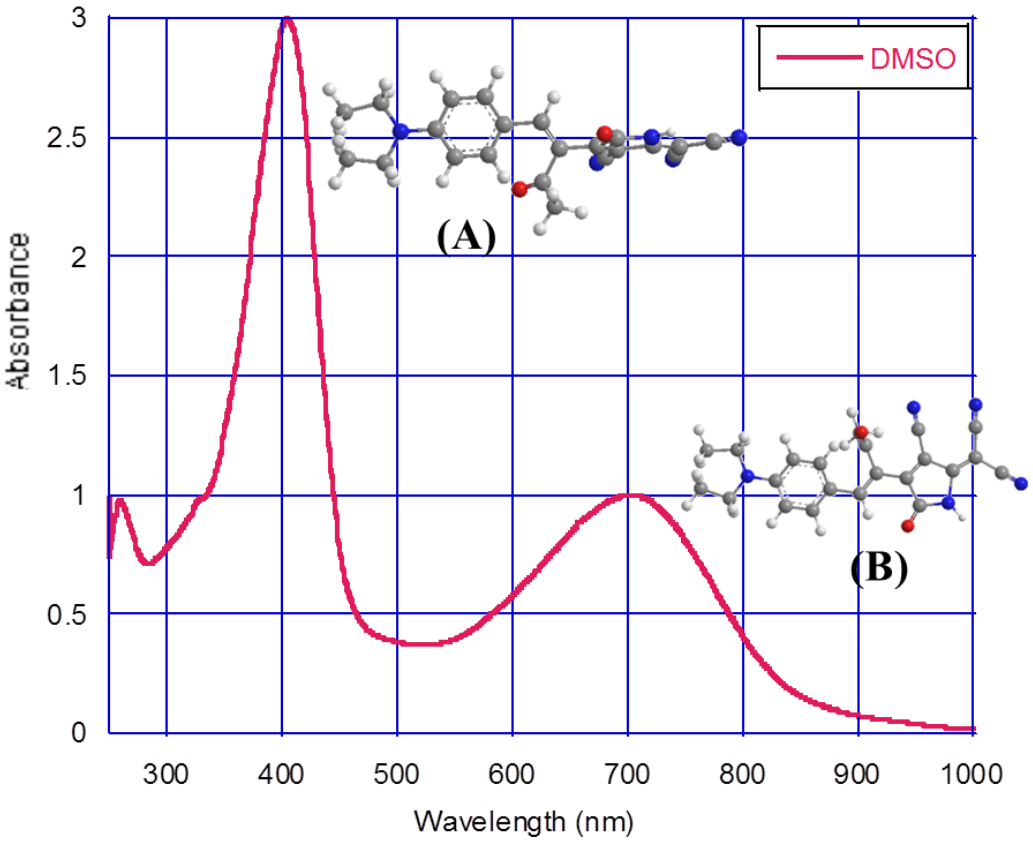

Figure 3.23: UV-vis of **TCP-Me** in DMSO showing the two possible rotamers responsible for the two peaks
This plot is normalized at the ~700nm peak to show the comparative intensity of the 400nm peak .

3.5 **Hyper-Rayleigh Scattering (HRS) Measurements:**

3.5.1 **Experimental details:**

All HRS measurements were performed by Prof David Shelton (Department of Physics, University of Nevada, Las Vegas, NV).

The β values for the chromophores in $CDCl_3$ solution were determined from hyper-Rayleigh scattering (HRS) measurements at a laser wavelength of 1064 nm (using a pulsed Nd:YAG laser) and sample temperature 25°C. Calibration of the HRS results used 4-nitroaniline (pNA) in $CDCl_3$ solution as a reference standard. Dilute solutions of pNA (36.4mM), **TCP-1** (12μM), **TCP-Me** (35.3μM), **TCP-Ph** (36.1μM) and **TCP-PhF** (36.6μM) in $CDCl_3$ were freshly prepared for each measurement. The solution concentrations were chosen to give comparable signals for the chromophore and reference solutions, and the much smaller HRS signal measured for the neat solvent was subtracted. Sample and reference HRS signals were compared using the same laser focusing, collection optics and polarization configuration, using apparatus and techniques as previously described[81]. The laser power incident on the sample was adjusted without affecting the alignment or focusing of the laser beam using a half-wave plate and polarizer combination. The sample absorption at the 532 nm second harmonic wavelength was measured and the HRS signals were corrected for the small self-absorption of the scattered light along the 1.5 mm path to the cuvette exit face. The HRS signal at 532 nm was corrected for thermal lensing effect as well as any two photon fluorescence contribution. Further details are provided in the appendix to Chapter 3.

3.5.2 **Theory details:**

All quantum mechanical calculations for these molecules were performed by Kerry E. Garret and the details are identical to those elucidated in **section 2.6**. These are repeated here for convenience

Quantum calculations for were performed using three levels of theory:

4) The mild hybrid density functional B3LYP, which includes a constant 20% Hartree-Fock (HF) exchange over the electronic interaction range to correct for the asymptotic decay of the exchange potential at long range.
5) CAM-B3LYP which divides the exchange into short-range and long-range parts with 19% and 46% HF exchange respectively and
6) Second order Møller-Plesset perturbation (MP2), a computationally-feasible correlated wavefunction method that was used for comparison with DFT.

The static hyperpolarizabilities, $\beta_{HRS}(0)$ were corrected for dispersion at 1064 nm with a damping factor, γ, set to 100 nm chosen so to match the full-width at half-maximum of the experimental spectra. The theoretical absorption wavelengths, used in the two-state model were provided using CAM-B3LYP/6-31+G*. Additionally, for comparison with the two-state model, frequency-dependent hyperpolarizabilities, $\beta_{HRS}(2\omega)$, were calculated at 1064 nm using the coupled-perturbed Kohn-Sham (CPKS) method for both B3LYP and CAM-B3LYP functionals. All of the above methods – B3LYP, CAM-B3LYP, and MP2 –consistently used 6-31+G* basis and with solvent effects according to the polarizable continuum method (PCM) for all of the properties calculations on PCM-B3LYP/6-31+G* optimized geometries. All quantum calculations were performed using Gaussian 09 Rev. D.01 suite of QM codes.

The experimental HRS measurements give frequency dependent hyperpolarizability values with respect to a reference molecule (pNA in this case) thus the data obtained from HRS experiments are the $(\beta_{HRS}/\beta_{pNA})_{1064}$ values in **table 3.5**. To account for any enhancement observed in the measurement, the experimental static hyperpolarizability ratios, $\beta_{HRS(0)}/\beta_{pNA(0)}$ (**table 3.6**) were extrapolated from the frequency dependent ratios using the two level model (TLM) equation developed by Oudar and Chemla[14]. Extrapolation to the static limit becomes increasingly unreliable however as resonance is approached because line broadening effects need to be taken into account. A correction factor thus applied to the TLM equation to give the damped two level model dispersion fit (see appendix for Chapter 3).

The experimentally obtained value for β_{HRS} at 1064 nm for 4-nitroaniline, 11.4×10^{-30} esu was used to convert the $(\beta_{HRS}/\beta_{pNA})_{1064}$ ratios to $\beta_{HRS(1064)}$ for the TCP molecules (**table 3.3)**. The static $\beta_{HRS(0,TLM)}$ value for pNa was extrapolated using the TLM expression in a fashion similar to that described above. This value was used multiplied with the $\beta_{HRS(0)}/\beta_{pNA(0)}$ values to give the static hyperpolarizibilities for all the molecules (**table 3.4)**. Structures of **TCP-1**, **TCP-Me**, **TCP-Ph** and **TCP-PhF** are shown in **figure 3.24** for convenience.

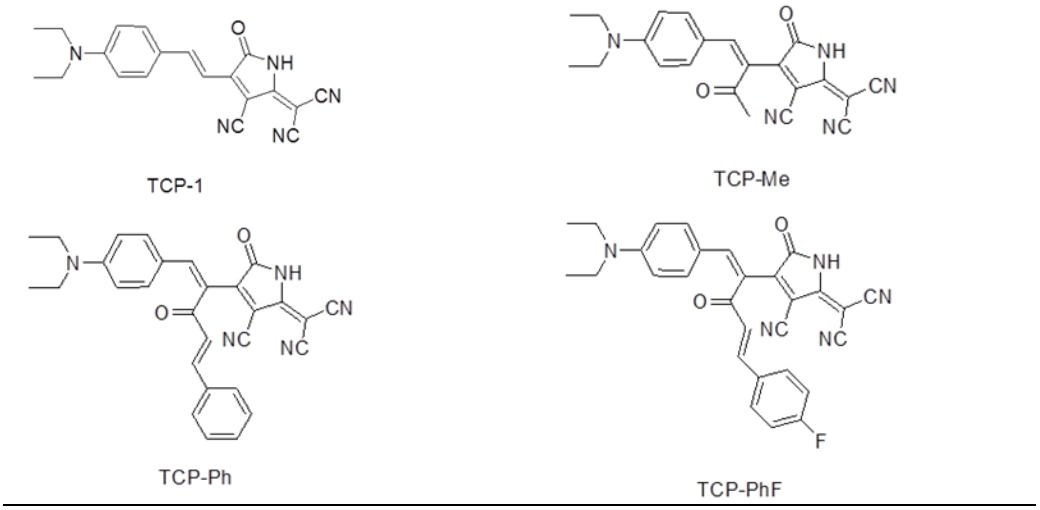

Figure 3.24: Structures of Chromophores Used in HRS Measurements.

3.5.3 **Discussion of Theoretical Trends:**

The frequency dependent hyperpolarizability values $\beta_{HRS(1064)}$ (**table 3.3**) were found to be most accurately predicted by B3LYP calculations. The B3LYP functional does not however pick up on the trends observed in the experimental hyperpolarizability values. Experimental measurements indicate a decrease in $\beta_{HRS(1064)}$ upon going from **TCP-1** to **TCP-Me** followed by a steady increase in hyperpolarizability upon going to **TCP-Ph** and **TCP-PhF**. B3LYP on the other hand predicted much higher $\beta_{HRS(1064)}$ for **TCP-Me** (465.9×10^{-30} esu) than for **TCP-1** (369.42×10^{-30} esu) perhaps picking up on the mild electron withdrawing character of the methyl ketone moiety. It is unclear why lower values were predicted for **TCP-Ph** and **TCP-PhF**. A similar but more exaggerated trend is observed in the CAM B3LYP predictions as the values predicted by this functional are highly overestimated. **TCP-1** was overestimated by a factor of 2.21, **TCP-Me** by a factor of 4.6, **TCP-Ph** by a factor of 2.9 and **TCP-PhF** by a factor of 2.8. MP2 calculations overestimated the hyperpolarizability values by factors of ~2 to 2.6 and predicted a steady decrease $\beta_{HRS(1064)}$ in going from **TCP-1** through to **TCP-PhF** unlike the trend seen in the experimental data

Compound	$\beta_{HRS(1064)}$ (10^{-30} esu)			
	Experimental	B3LYP/ 6-31+G*	CAM B3LYP/ 6-31+G*	MP2/ 6-31+G*
pNA	11.4	20.2	14.6	13.1
TCP-1	479	369.42	1057.9	996
TCP-Me	365	465.9	1646.2	970
TCP-Ph	465	379.46	1355.7	956
TCP-PhF	490	383.07	1371.5	956

Table 3.3: Experimental and Calculated Frequency Dependent β_{HRS} values.

Compound	$\beta_{HRS(0,TLM)}$ (10^{-30} esu)			
	Experimental	B3LYP/ 6-31+G*	CAM B3LYP/ 6-31+G*	MP2/ 6-31+G*
pNA	6.2902	9.21	8.02	7.76
TCP-1	241.35	131	183	342
TCP-Me	174.03	137.97	176.76	303
TCP-Ph	224.61	143.97	177.09	302
TCP-PhF	236.72	145.33	177.11	302

Table 3.4: Experimental and Calculated β_0 values

The static hyperpolarizability values $\beta_{HRS(0)}$ (**table 3.4**) seem to be better predicted by the CAM B3LYP functional although the trends in hyperpolarizability are not predicted well. The B3LYP functional while underestimating the experimental values by factors of ~1.3 to 1.84, once again does pick up on the slight increase in $\beta_{HRS(0)}$ in going from **TCP-Me** to **TCP-Ph** and

TCP-PhF. MP2 values were overestimated by factors of between 1.27-1.74. Based on MP2 methods, the $\beta_{HRS(0)}$ values for **TCP-Me**, **TCP-Ph** and **TCP-PhF** were estimated to be lower than that of **TCP-1** but no difference in values is expected between the three substituted TCP chromophores. This is contrary to what is indicated by the experimental data where an increase in $\beta_{HRS(0)}$ is expected in the substituted chromophores.

Both the static and frequency dependent (β_{HRS}/ β_{PNA}) values (**table 3.5** and **table 3.6**) were largely underestimated by B3LYP calculations by factors of as much as 2.7. CAM B3LYP calculations overestimated the frequency dependent ratios with the largest error seen for TCP-Me (overestimated by a factor of 3.5) while the static values were underestimated. This is similar to the trend seen in the CAM B3LYP values of $\beta_{HRS(0)}$ and $\beta_{HRS(1064)}$. MP2 calculations grossly overestimated the frequency dependent values by a factor of as much as 2.3 (for **TCP-Me**). The static hyperpolarizability ratios were predicted to be slightly higher by MP2 calculations for **TCP-1** and **TCP-Me** and quite accurate for **TCP-Ph** and **TCP-PhF**.

Compound	**$(\beta_{HRS}/\ \beta_{PNA})_{1064}$**			
	Experimental	B3LYP/ 6-31+G*	CAM B3LYP/ 6-31+G*	MP2/ 6-31+G*
pNA	1	1	1	1
TCP-1	42	18.29	72.46	76
TCP-Me	32	23.06	112.75	74
TCP-Ph	40.8	18.785	92.86	73
TCP-PhF	43	18.964	93.94	73

Table 3.5: Experimental and Calculated Frequency Dependent β_{HRS}/β_{pNA} values

Compound	$\beta_{HRS(0)}/\beta_{PNA(0)}$			
	Experimental	B3LYP/ 6-31+G*	CAM B3LYP/ 6-31+G*	MP2/ 6-31+G*
pNA	1	1	1	1
TCP-1	38.37	14.22	22.82	44.07
TCP-Me	27.67	14.98	22.04	39.04
TCP-Ph	35.71	15.63	22.08	38.91
TCP-PhF	37.63	15.78	22.08	38.91

Table 3.6: Experimental and Calculated Static β_{HRS}/β_{pNA} values

Overall, amongst the three theoretical methods, B3LYP was found to be a better predictor of $\beta_{HRS(1064)}$ values while CAM-B3LYP was found to be better at predicting $\beta_{HRS(0)}$ for the TCP chromophores. The trends observed were not accurately predicted by any of the functionals although B3LYP did predict the slight increase in β values observed with the substituted TCP chromophores.

3.5.4 **Discussion of experimental trends:**

The experimentally determined frequency dependent hyperpolarizability $\beta_{HRS(1064)}$values of the four TCP chromophores vary by ca. 125×10^{-30} esu (**table 3.3)**. **TCP-Me** demonstrates the lowest $\beta_{HRS(1064)}$ while TCP-PhF demonstrates the largest value at 490×10^{-30}esu. Upon substitution with a methyl ketone, the hyperpolarizability drops from 479×10^{-30}esu (**TCP-1**) to 365×10^{-30}esu (**TCP-Me**) (a ~24% reduction). Upon further substitution with a phenylvinyl ketone, the hyperpolarizability was significantly recovered (465×10^{-30}esu for **TCP-Ph**). The fluorophenylvinyl ketone substituted **TCP-PhF** was found to have $\beta_{HRS(1064)}$ slightly larger

(490×10^{-30}esu) than **TCP-1**. A similar trend (albeit with lower values) is observed with the experimental static hyperpolarizabilities $\beta_{HRS(0)}$ (**table 3.4**)

The larger loss in β for **TCP-Me** is unusual since the methyl ketone substituent is a weak acceptor and should not have a strongly negative effect on $\beta_{HRS(1064)}$ values. This reduction can be explained by the existence of a distribution of two rotational isomers **A** and **B** as shown in **figure 3.23** and discussed in **section 3.3.2.** Rotamer **A** has the TCP acceptor rotated out of plane with respect to the diethylamino benzene donor and the methyl ketone is closer to a net 0° dihedral angle with respect to the donor. This effectively conjugates the donor to the weak ketone acceptor resulting in a very low hyperpolarizability for rotamer **A**.

As seen in **figure 3.14**, a solution of **TCP-Me** in chloroform shows absorbances for both rotamers **A** and **B**. Thus the effective hyperpolarizability of a mixture of **A** and **B** rotamers of **TCP-Me** in chloroform would be lower than a solution in which only rotamer **B** existed.

The increase in hyperpolarizability observed in going from **TCP-Me** to **TCP-Ph** and finally **TCP-PhF** can be attributed to two factors:

1) the lower rotational freedom expected for the larger phenylvinyl ketone and the fluorophenylvinyl ketone groups in **TCP-Ph** and **TCP-PhF** respectively preventing the formation of corresponding rotamer **A** (seen in **TCP-Me**) versions of these molecules which would have reduced hyperpolarizibilities.
2) the stronger electron withdrawing character of the aromatic substituents in **TCP-Ph** and **TCP-PhF** compared to the methyl substituent in **TCP-Me**.

As has already been discussed in Chapter 2 charge-transfer is indeed possible between donors and acceptors across cross-conjugated motifs. As further elucidated in **section 3.3.1** a HOMO→LUMO+1 transition is observed for **TCP-Ph** and **TCP-PhF**. These are shown again

for convenience in **figure 3.25**. As this transition occurs from the diethylaminobenzene donor to the aromatic cross-conjugated substituents on **TCP-Ph** and **TCP-PhF**, thus indicating that these substituents act as auxiliary acceptors in these chromophores and this effect is indeed observed in the hyperpolarizability trends.

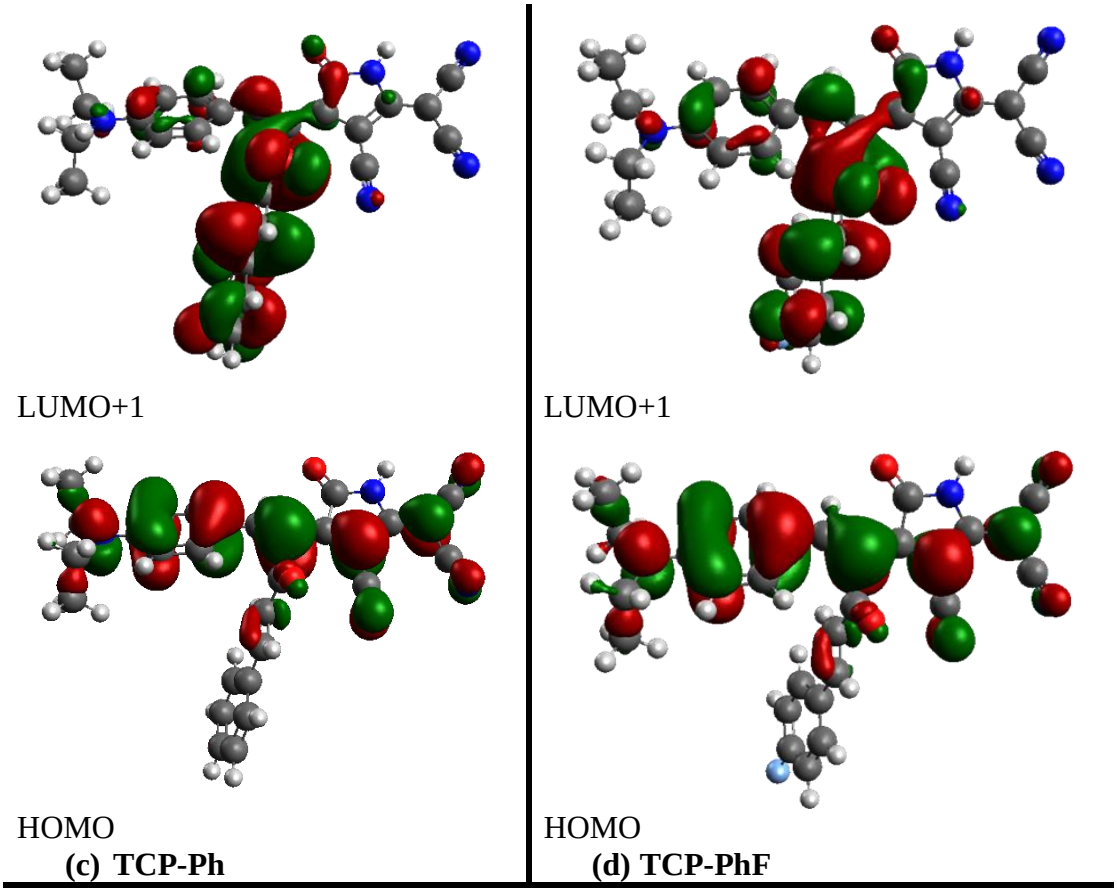

(c) TCP-Ph **(d) TCP-PhF**

Figure 3.25: HOMO to LUMO+1 transition for **(a) TCP-Ph** and **(b) TCP-PhF**

3.6 **Conclusions to Chapter 3:**

In conclusion, the incorporation of a cross-conjugated motif onto a conjugated TCP chromophore was investigated. Four chromophores **TCP-1** (control molecule), **TCP-Me**, **TCP-Ph** and **TCP –PhF** were successfully, characterized and compared.

The crystal structures of **TCP-Me** and **TCP-Ph** were elucidated and compared to the optimized geometries obtained through theoretical calculations. The cross-conjugated side groups were found to be oriented approximately perpendicular to the conjugated backbone of the molecule. This was as expected from theory as well as previously published literature[95]. In addition, a twist was observed along the conjugated bridge between the diethylamino donor and the TCP acceptor. A dihedral angle of 23° (29° theoretical) in **TCP-Me** and 16° (35° theoretical) in **TCP-Ph** was seen. Such a twist in the backbone of a conjugated TCP chromophore has not been reported before. This deviation from co-planarity of the TCP backbone could result in reduction of aggregation behavior (as described in **section 3.1**) and improve film quality. Further, the crystal packing of **TCP-Ph** indicated significant interaction of the perpendicular phenyl side groups between adjacent chromophores. These interactions guide molecular arrangement and could be exploited further and utilized as soft interactions to improve acentric order as described in **Chapter 1**.

The UV-vis spectra of **TCP-Me**, **TCP-Ph** and **TCP-PhF** were understood through comparisons with **1-Me**, **1-Ph**, **1-F** and **TCP-1** as well as through quantum calculations of the electronic transitions. It was evident especially in the case of **TCP-Ph** and **TCP-PhF** that the electronic transitions included charge transfer from the diethylamino donor to the cross-

conjugated moiety (HOMO→LUMO+1, **figure 3.20**) thus indicating that the cross-conjugated substituent acts as an auxiliary acceptor. In the case of **TCP-Me** there is a strong indication that the methyl ketone moiety is able to rotate in solution (**figure 3.22** and **figure 3.23**) and this is the reason for the larger twist is observed between the donor and the acceptor in the crystal structure of **TCP-Me**.

Theoretical calculations of the electronic transitions point towards an increased contribution of the HOMO→ LUMO+1 transition across the cross conjugated part of the molecule in going from **TCP-Me** to **TCP-Ph** and **TCP-PhF** resulting in the larger predicted dihedral angles between the donor and the TCP acceptor. This indicates that increasing the electron-withdrawing character of the cross conjugated side group would in fact increase this HOMO→LUMO+1 contribution and make for a higher β chromophore.

HRS measurements of TCP-Me indicate a β_{HRS} reduced by ~25% compared to **TCP-1** control molecule. This is unexpected unless one takes into account the 23° dihedral twist observed between the donor and acceptor and the ability of the cross-conjugated methyl ketone group to rotate. This corroborates the expectation of the rotational isomers observed in the UV-vis spectrum of **TCP-Me**.

TCP-Ph and **TCP-PhF** have increasing hyperpolarizability values compared to **TCP-Me** once again confirming the electron withdrawing contribution of the cross-conjugated side groups and the reduced rotational freedom expected for the bulkier side groups.

Finally, the substitution of cross conjugated side groups onto the backbone of the conjugated TCP chromophores provides a new design motif through which the following advantages can be gained:

1) Twisting of the conjugated backbone possibility resulting in the lowering of aggregation phenomenon overcoming a major drawback of TCP small molecule chromophores and allowing for improved processing, film characteristics and reduction of optical loss.
2) Introduction of anisotropic “soft” interactions through aryl and possibly aryl-fluoroaryl interactions to improve number densities, order as well as poling efficiencies.
3) The use of cross-conjugated lateral groups as auxiliary acceptors by increasing the electron withdrawing character of these lateral groups and thereby allowing for improvement in hyperpolarizability.

This new design motif is an addition to the ongoing research towards the new and improved materials for electro-optic applications.

3.7 **Appendix to Chapter 3**

3.7.1 **Synthesis of cross-conjugated chromophores:**

Experimental

All reactions were carried out under a nitrogen atmosphere in flame-dried glassware. Standard air-free techniques were used for handling air and moisture sensitive reagents. All solvents were used as received from commercial suppliers. All NMR spectra were recorded using Bruker 300 MHz and Bruker 500 MHz spectrometers. Chemical shifts (δ) are given in parts per million (ppm) and measured against residual solvent peaks as internal standards. Coupling constants (J) are given in Hertz (Hz). UV-Vis spectra were recorded on the Agilent 8453 spectrophotometer. Fluorescence spectra were recorded on the Horiba FL3-21tau fluorescence spectrophotometer. Fresh solvents were used for solution preparation.

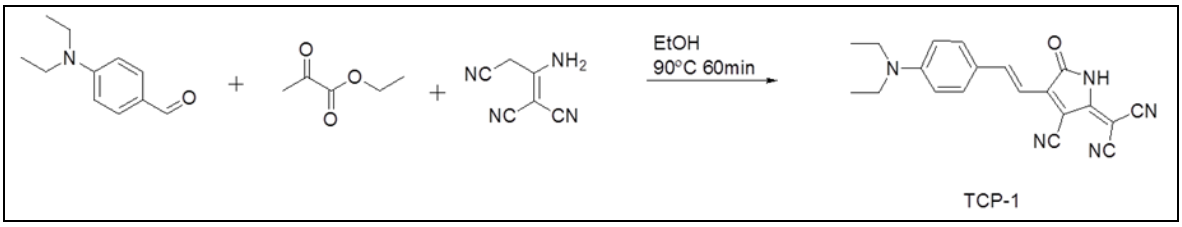

TCP-1:

A 250 mL round bottom flask was charged with a stir bar and connected to a jacketed water condenser. The set up was flushed with nitrogen for 10 min. Ethyl Pyruvate (16 mL, 141.043 mmol), and ethanol (56 mL) were combined in the flask and stirred for 5 minutes under a nitrogen atmosphere. 1,1,3-tricyano-2-amino-1-propene (7.454 g, 56.417 mmol) was then added to the stirring solution. The solution was then refluxed for 100 minutes at 90 °C. At the end of the 100 minutes, diethylamino benzaldehyde (7 g, 39.49 mmol) was added to the solution and

refluxed at 90 °C for 24 hours. The heating was then turned off and the reaction was allowed to cool to room temperature. The reaction was filtered and the green precipitate was washed with dichloromethane until the filtrate looked clear. The green product was then transferred to a vial and placed in a vacuum oven for 2 hours. (6.718 g, 50% yield). ^{1}H NMR (300MHz,DMSO-d6): δ 12.427 (s,1H), 8.403 (d, J = 15.2Hz, 1H), 7.731 (d, J = 8.5Hz, 2H), 6.959 (d, J = 15.1Hz, 1H), 6.857 (d, J = 8.98Hz, 2H), 3.544 (q, J = 6.9Hz, 4H), 1.166 (t, J = 6.9Hz, 6H).

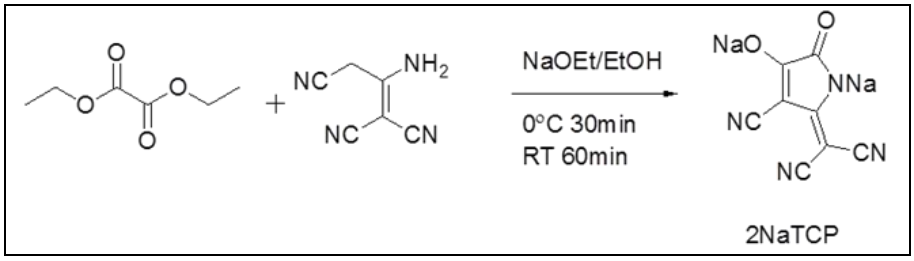

2NaTCP:

A 50mL round bottom flask was flame dried and charged with a stir bar. The flask was cooled under flushing nitrogen. Sodium (0.55g, 24mmol) was added to the flask followed by ethanol (10mL). More ethanol was added as the reaction between sodium and ethanol slowed to allow completion of reaction. Total ethanol added was 16mL. The reaction flask was cooled to 0°C in an ice bath. 1,1,3-tricyano-2-amino-1-propene (1g, 7.6mmol) and diethyl oxalate (1.54mL, 11.35mmol) were added to the flask. The reaction was stirred at 0°C for 30 min during which time a yellow solid precipitated out. The ice bath was removed and the precipitate was broken up to facilitate stirring. The reaction was stirred at room temperature for 3h. After 3h, the reaction was poured into an Erlenmeyer flask containing 100mL of benzene and stirred vigrourously for 5 min. The solids were then filtered and washed with more benzene. The yellow solids were dried under vacuum overnight. (2.271g)

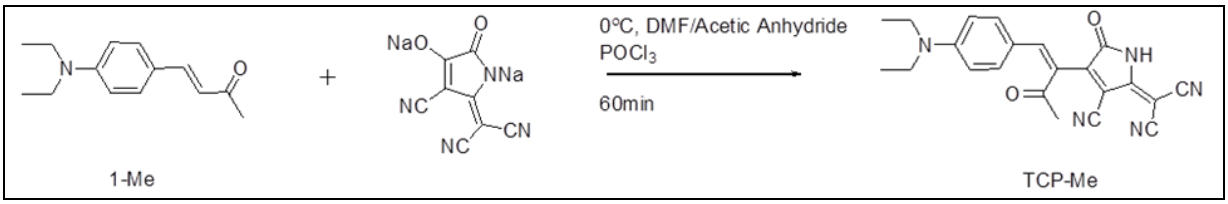

TCP-Me:

A 10mL round bottom flask was flame dried , charged with a stir bar and cooled under flushing nitrogen. **1-Me** (0.15g, 0.69mmol), **2NaTCP** (0.106g, 0.46mmol) and N,N-dimethylformamide (2.3mL) were added to the flask and stirred until all the solids had dissolved. The reaction flask was cooled to -4°C in an ice bath and acetic anhydride (0..044mL, 0.46mmol) was added to the reaction. Phosphorous oxychloride ($POCl_3$) (0.13mL, 1.38mmol) was added dropwise to the reaction and the reaction was allowed to stir and allowed to warm up. After 1h, the reaction had turned green. The reaction mixture was then poured into ice water (50mL). A green precipitate formed which was filtered over a buchner funnel, washed with water and dried under vacuum overnight. Purification of crude product achieved by re-suspending in a 50/50 mixture of dichloromethane/methanol and filtering and further washing with methanol. The final luminous green product was obtained after drying under vacuum overnight. (0.015g, 8.5%) ^{1}H NMR (300MHz,CD_3CN): δ 9.86 (s,1H), 8.156 (s, 1H), 7.308 (d, J =9.1Hz, 2H), 6.721 (d, J = 9.1Hz, 2H), 3.47 (q, J =7.09Hz, 4H), 2.49 (s, 3H), 1.178 (t, J = 7.09Hz, 6H). HRMS (ESI) (M+, $C_{22}H_{19}N_5O_2$) calcd: 385.1539; found, 386.16144 [M+H], 408.1431 [M+Na]

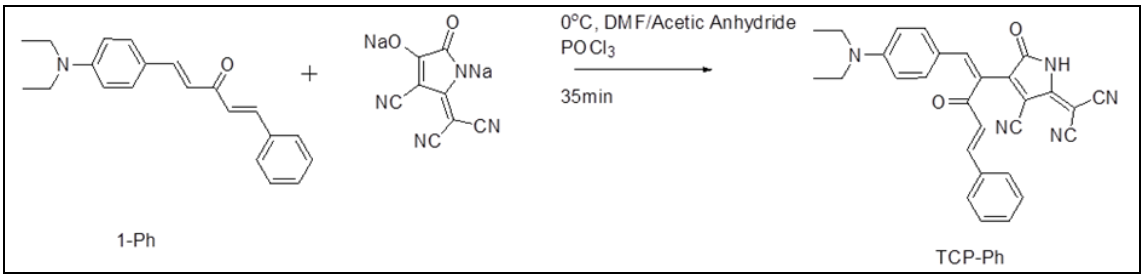

TCP-Ph:

A 10mL round bottom flask was flame dried , charged with a stir bar and cooled under flushing nitrogen. **1-Ph** (0.078g, 0.303mmol), **2NaTCP** (0.059g, 0.256mmol) and N,N-dimethylformamide (0.88mL) were added to the flask and stirred until all the solids had dissolved. The reaction flask was cooled to -4°C in an ice bath and acetic anhydride (0.02mL, 0.211mmol) was added to the reaction. Phosphorous oxychloride ($POCl_3$) (0.05mL, 0.535mmol) was added dropwise to the reaction and the reaction was allowed to stir at -4°C. After 35min, the reaction had turned purple. The reaction mixture was then poured into ice water (50mL). A purple precipitate formed which was filtered over a buchner funnel, washed with water and dried under vacuum overnight. Purification of crude product achieved by re-suspending in methanol and filtering and further washing with methanol. The final luminous green product was obtained after drying under vacuum overnight. (0.006g, 4%) ^{1}H NMR (300MHz,CD_3CN): δ 9.704 (s,1H), 8.621 (s, 1H), 7.64 (m, 3H), 7.436 (m, 6H), 6.736 (d, J =9.3Hz, 2H), 3.478 (q, J =7.1Hz, 4H), 1.158 (t, J = 7.12Hz, 6H). HRMS (ESI): (M+, $C_{29}H_{23}N_5O_2$): calcd: 473.3852; found, 474.194931 [M+H]

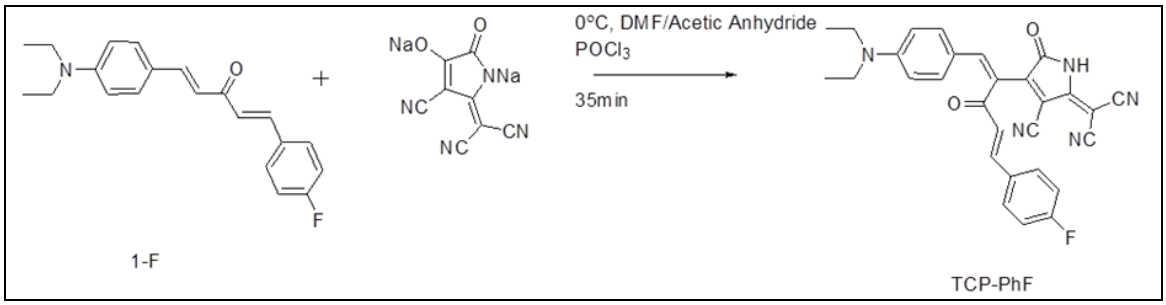

TCP-PhF:

A 10mL round bottom flask was flame dried , charged with a stir bar and cooled under flushing nitrogen. **1-PhF** (0.117g, 0.362mmol), **2NaTCP** (0.047g, 0.206mmol) and N,N-dimethylformamide (2mL) were added to the flask and stirred until all the solids had dissolved. The reaction flask was cooled to -4°C in an ice bath and acetic anhydride (0.02mL, 0.211mmol) was added to the reaction. Phosphorous oxychloride ($POCl_3$) (0.06mL, 0.641mmol) was added dropwise to the reaction and the reaction was allowed to stir at -4°C. After 35min, the reaction had turned purple. The reaction mixture was then poured into ice water (50mL). A purple precipitate formed which was filtered over a buchner funnel, washed with water and dried under vacuum overnight. Purification of crude product achieved by re-suspending in methanol and filtering and further washing with methanol. The final luminous green product was obtained after drying under vacuum overnight. (0.006g, 3.4%) ^{1}H NMR (300MHz,CD_3CN): δ 9.686 (s,1H), 8.617 (s, 1H), 7.688 (dd, J =8.9Hz, 8.7Hz, 2H), 7.59 (d, J =16.145Hz, 1H), 7.44 (d, J =9.3Hz, 2H), 7.165 (dd, J =8.9Hz, 8.8Hz, 2H), 6.74 (d, J =9.3Hz, 2H), 3.481 (q, J =7.1Hz, 4H), 1.16 (t, J = 7.1Hz, 6H). HRMS(ESI) (M+, $C_{29}H_{22}FN_5O_2$): calcd: 491.1758; found, 492.1852 [M+H], 514.1674 [M+Na].

3.7.2 **Nuclear magnetic resonance (NMR) spectroscopy and mass spectrometry data:**

^{1}HNMR of TCP-1

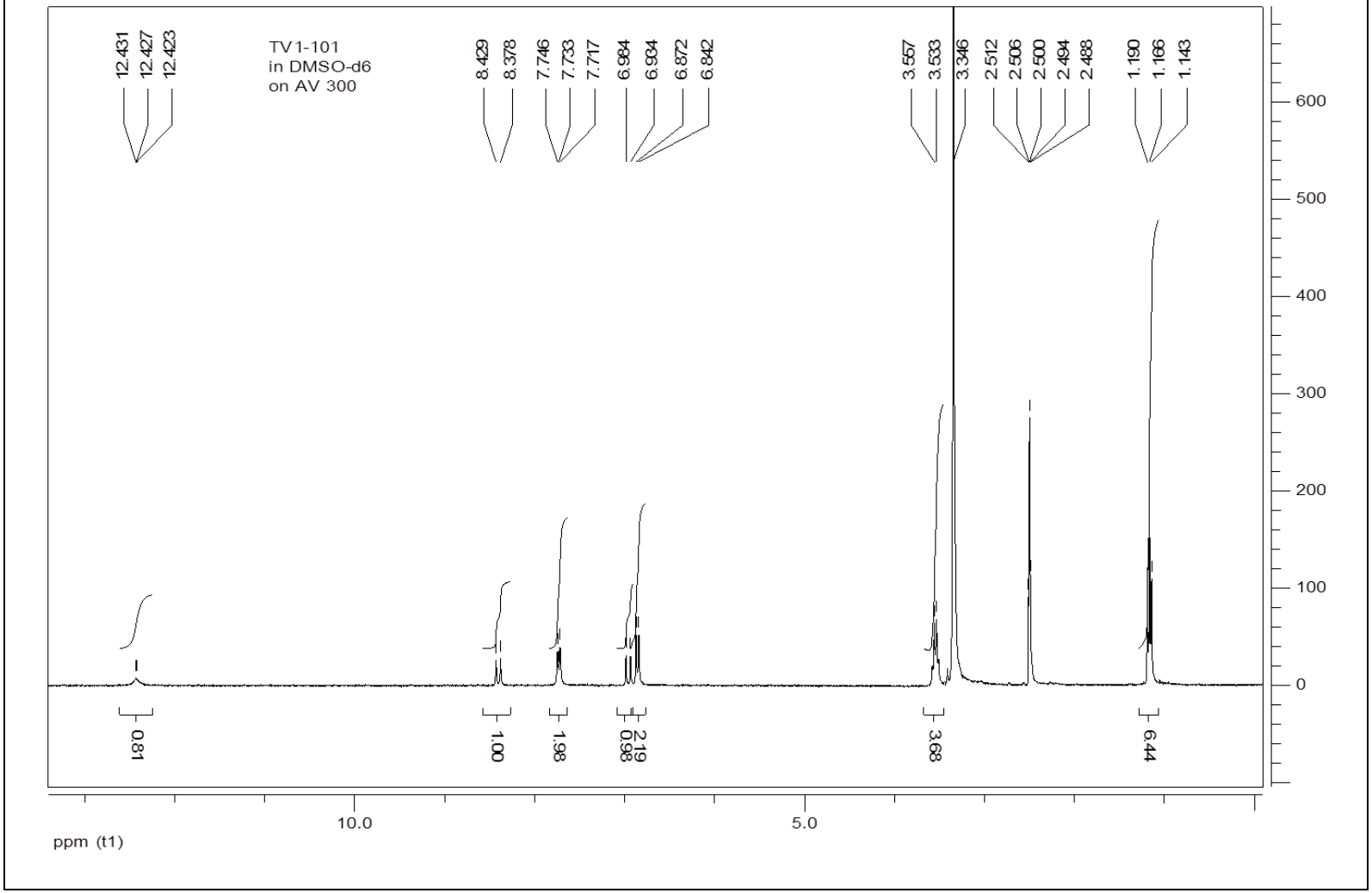

^{1}HNMR of TCP-Me

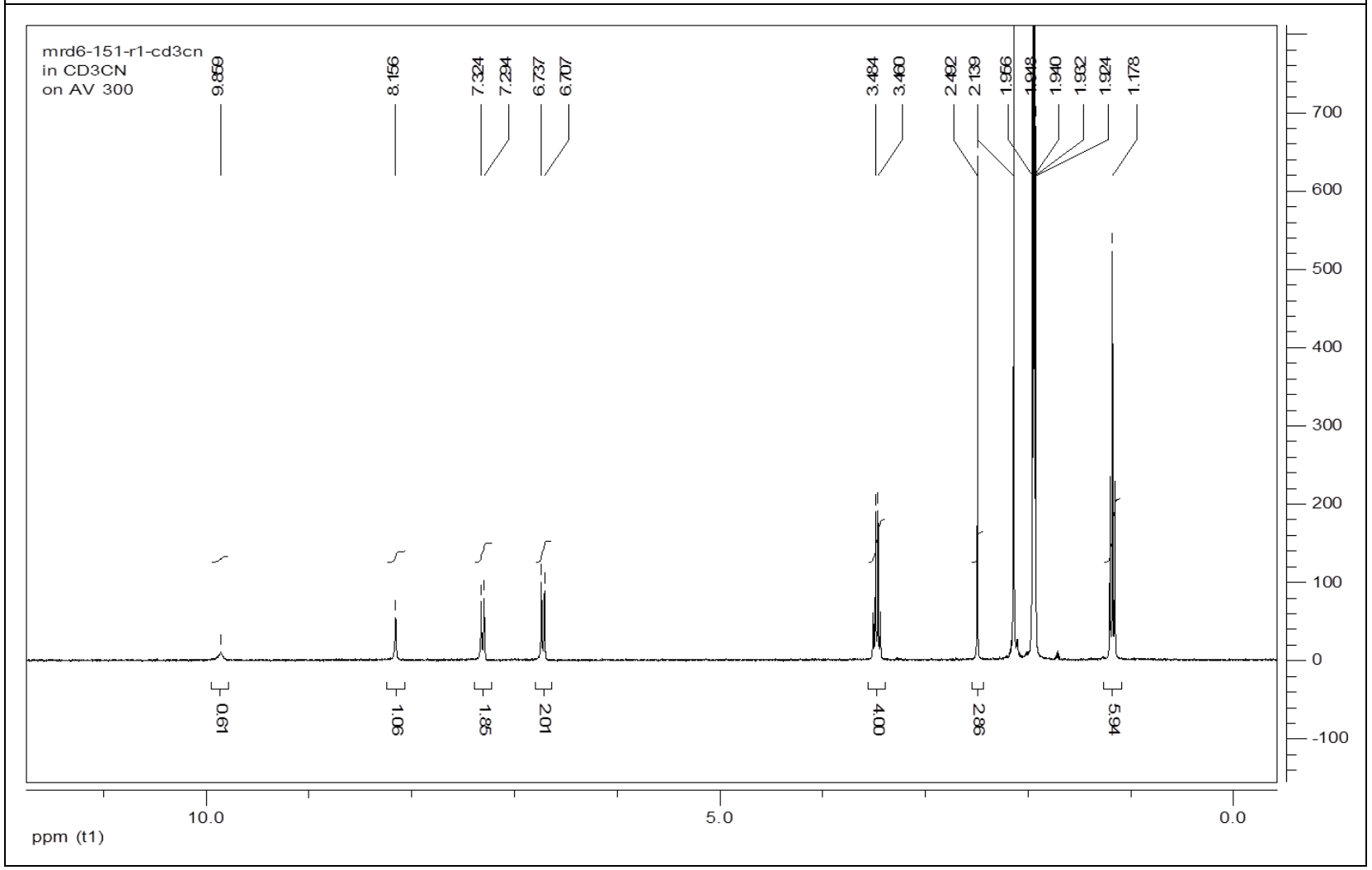

HRMS (ESI) of TCP-Me

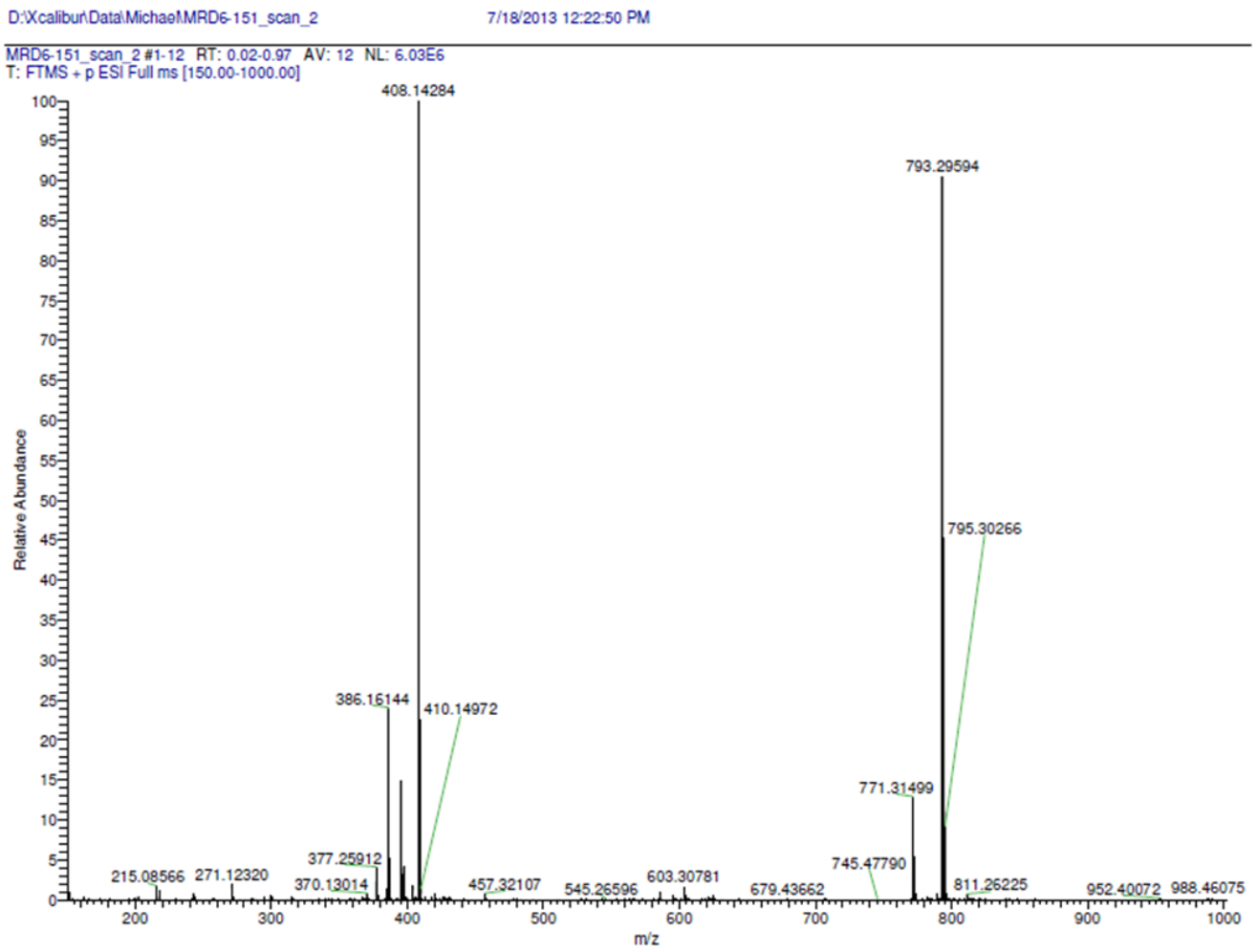

^{1}HNMR of TCP-Ph

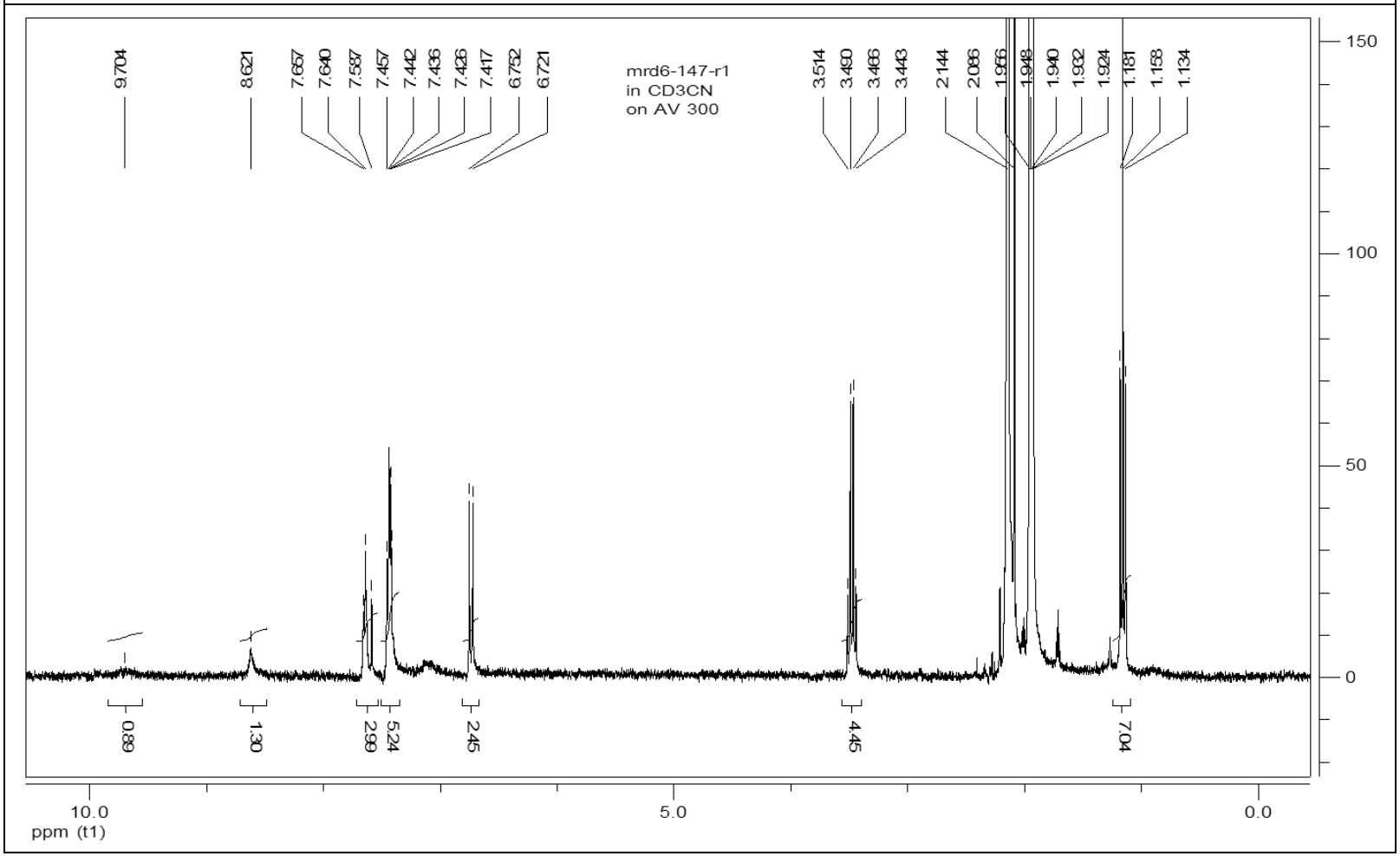

HRMS (ESI) of TCP-Ph

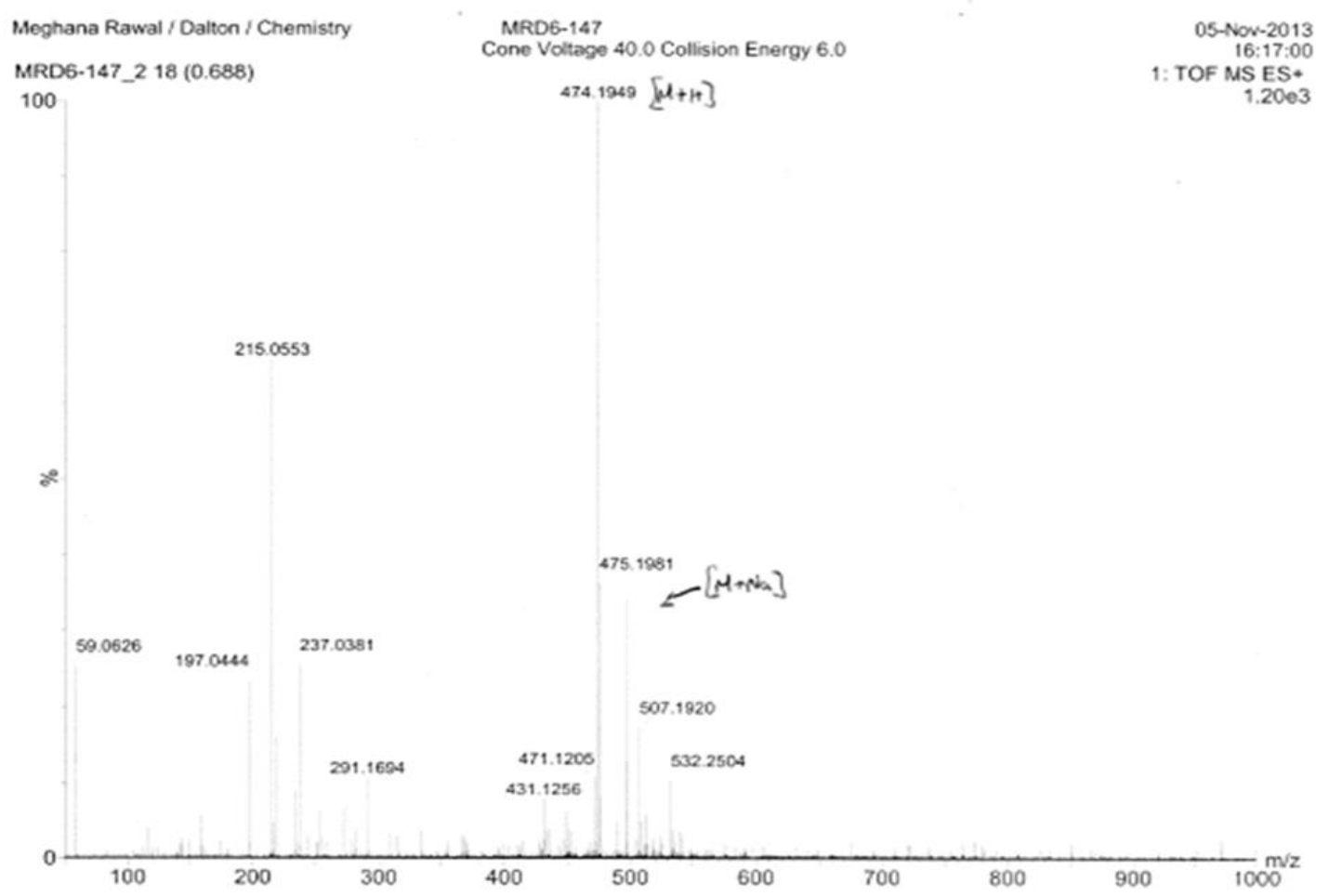

^{1}HNMR of TCP-PhF

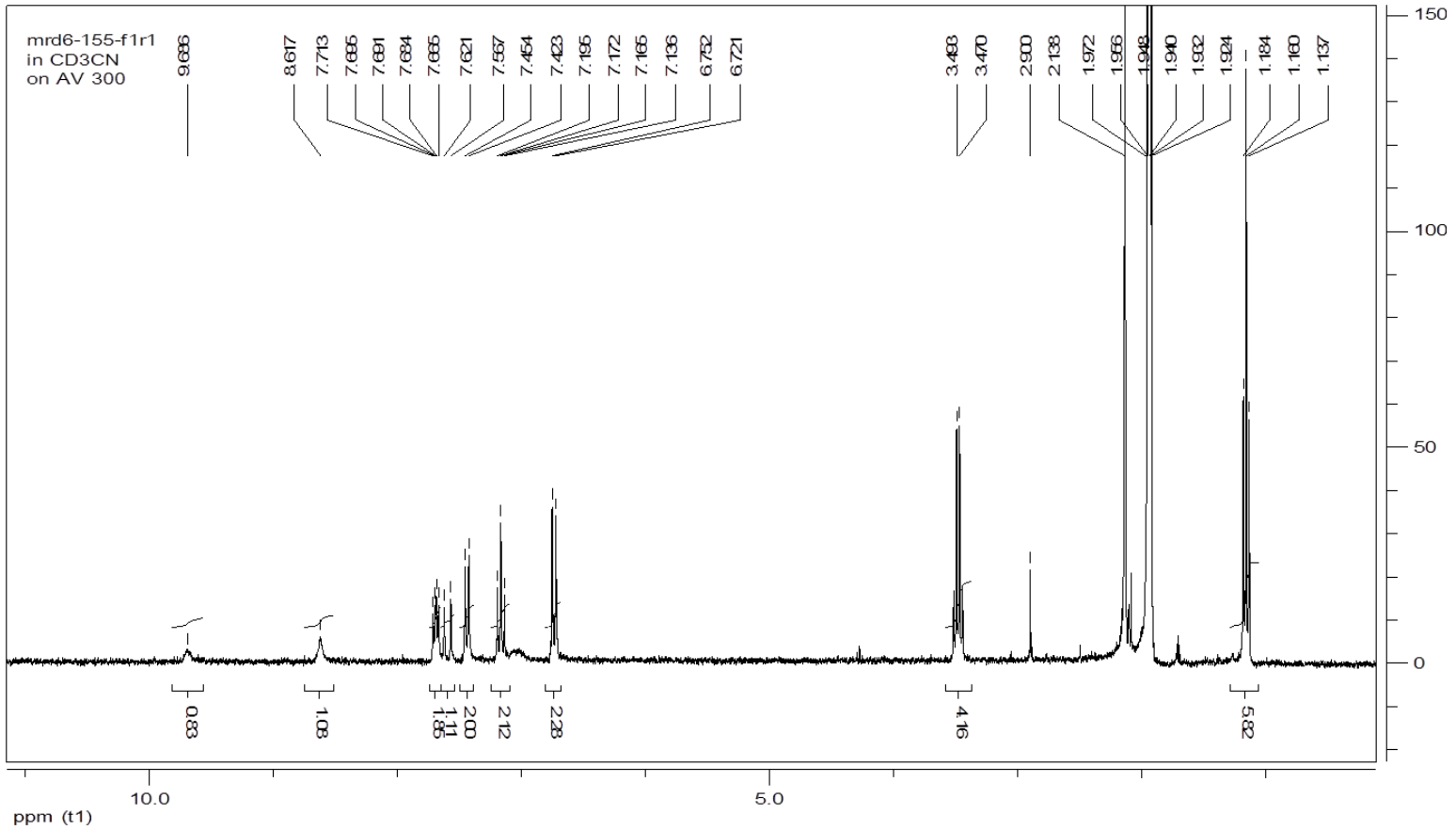

HRMS (ESI) of TCP-PhF

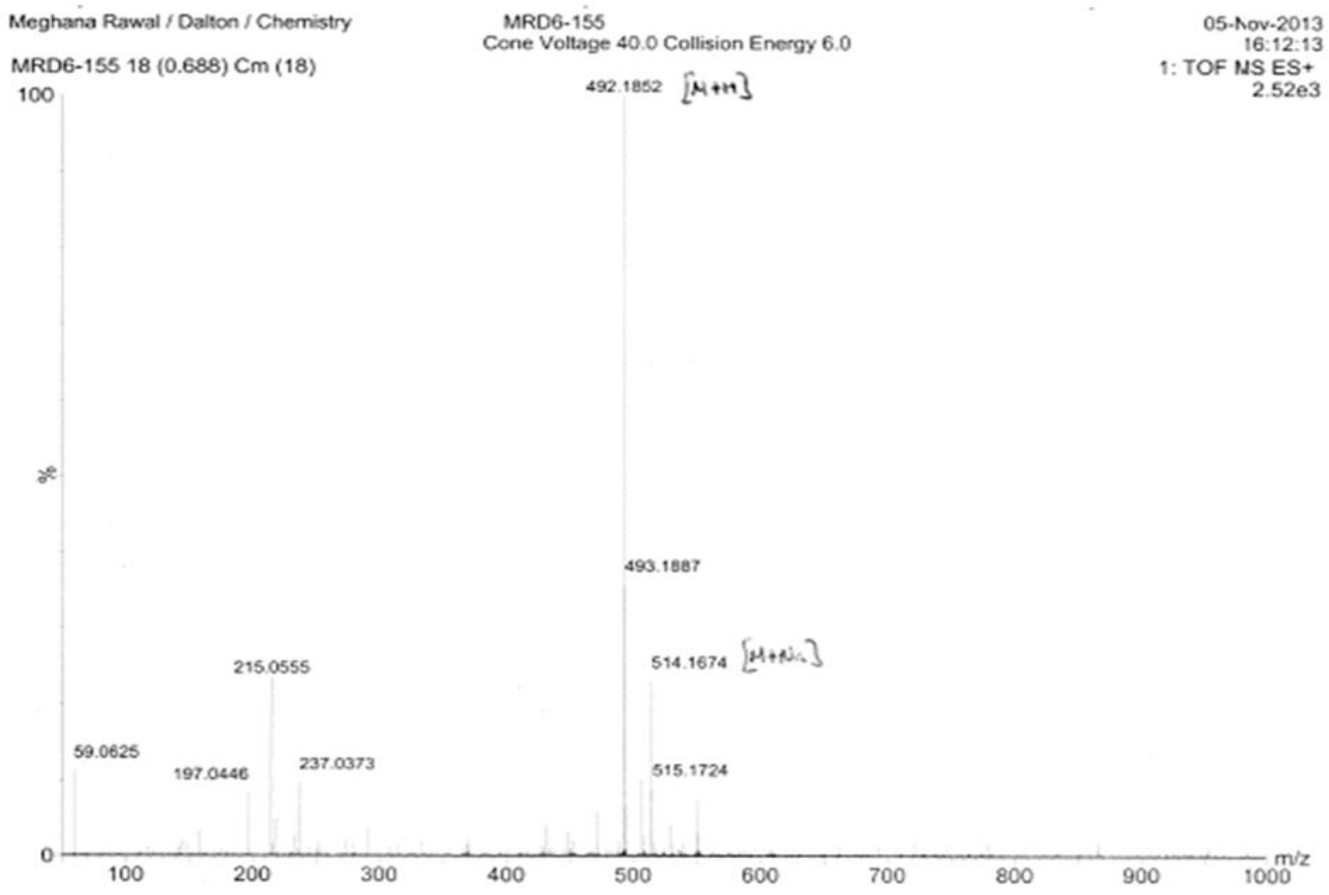

3.7.3 **X-ray diffraction data:**

TCP-Me Crystal Packing Structure

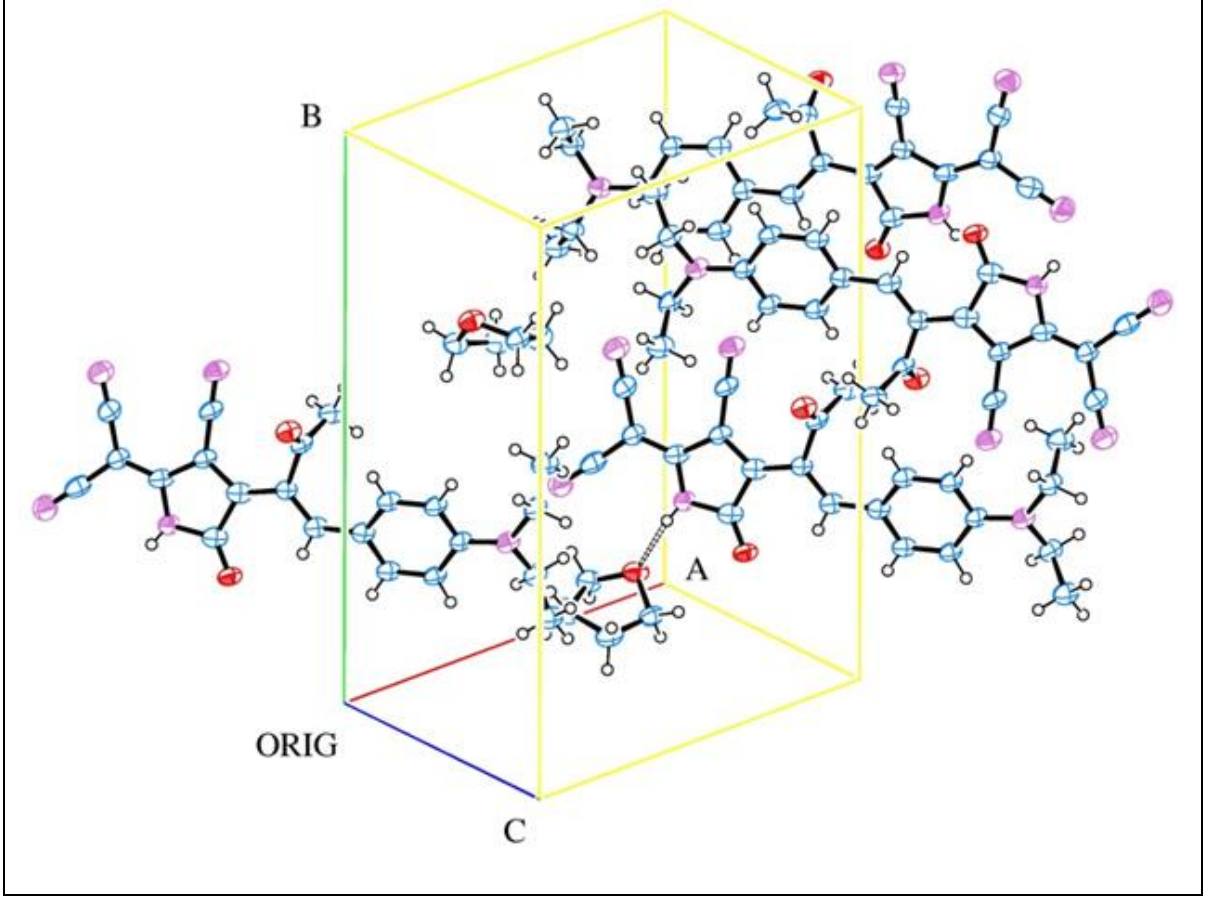

Crystal data for TCP-Me

Identification code	mrd_6_151_0ma	
Empirical formula	C26 H27 N5 O3	
Formula weight	457.53	
Temperature	100(2) K	
Wavelength	0.71073 Å	
Crystal system	Monoclinic	
Space group	P 2_1/c	
Unit cell dimensions	a = 13.755(4) Å	α = 90°.
	b = 17.446(5) Å	β = 103.54(2)°.
	c = 9.867(3) Å	γ = 90°.
Volume	2302.0(12) $Å^3$	
Z	4	
Density (calculated)	1.320 Mg/m^3	
Absorption coefficient	0.089 mm^{-1}	
F(000)	968	
Crystal size	0.10 x 0.07 x 0.02 mm^3	
Theta range for data collection	1.92 to 25.52°.	
Index ranges	-16<=h<=16, -21<=k<=21, -11<=l<=11	
Reflections collected	35966	
Independent reflections	4255 [R(int) = 0.1130]	
Completeness to theta = 25.00°	99.8 %	
Max. and min. transmission	0.9982 and 0.9912	
Refinement method	Full-matrix least-squares on F^2	
Data / restraints / parameters	4255 / 0 / 314	
Goodness-of-fit on F^2	1.011	
Final R indices [I>2sigma(I)]	R1 = 0.0782, wR2 = 0.1530	
R indices (all data)	R1 = 0.2192, wR2 = 0.2112	
Extinction coefficient	0.0109(18)	
Largest diff. peak and hole	0.372 and -0.297 $e.Å^{-3}$	

TCP-Ph Crystal Packing Structure

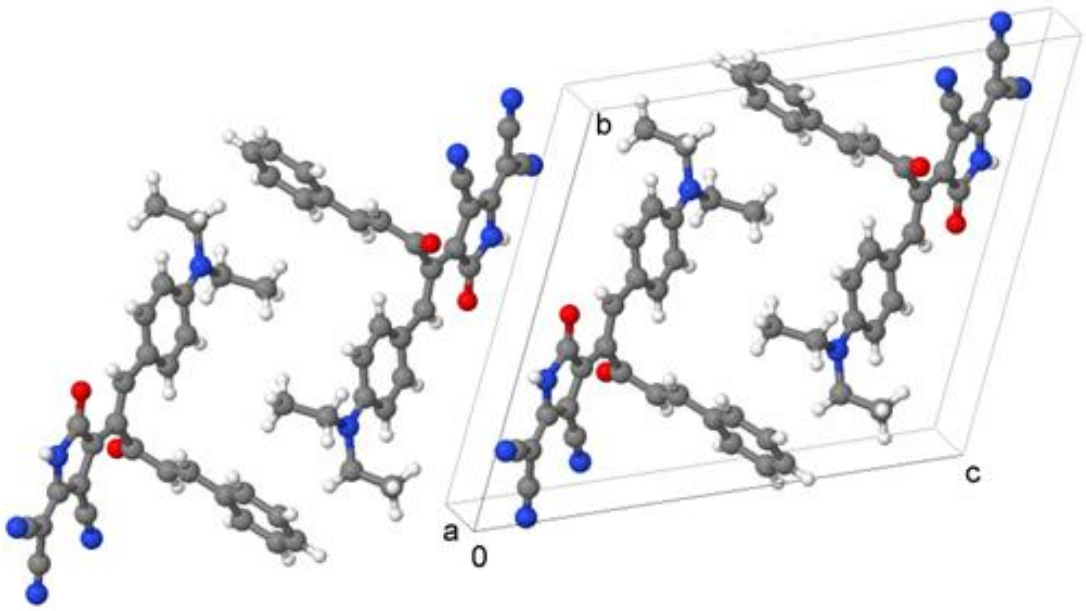

Crystal data for TCP-Ph

Identification code	mrd6_147_0ma	
Empirical formula	C29 H23 N5 O2	
Formula weight	473.52	
Temperature	100(2) K	
Wavelength	0.71073 Å	
Crystal system	Triclinic	
Space group	P -1	
Unit cell dimensions	a = 5.778(3) Å	α= 64.94(5)°.
	b = 14.455(8) Å	β = 89.61(5)°.
	c = 16.504(12) Å	γ = 78.92(3)°.
Volume	1221.1(12) $Å^3$	
Z	2	
Density (calculated)	1.288 Mg/m^3	
Absorption coefficient	0.084 mm^{-1}	
F(000)	496	
Crystal size	0.30 x 0.03 x 0.01 mm^3	
Theta range for data collection	2.50 to 25.19°.	
Index ranges	-6<=h<=6, -17<=k<=17, -19<=l<=19	
Reflections collected	31155	
Independent reflections	4149 [R(int) = 0.3053]	
Completeness to theta = 25.00°	94.8 %	
Max. and min. transmission	0.9992 and 0.9753	
Refinement method	Full-matrix least-squares on F^2	
Data / restraints / parameters	4149 / 18 / 254	
Goodness-of-fit on F^2	0.861	
Final R indices [I>2sigma(I)]	R1 = 0.0791, wR2 = 0.1616	
R indices (all data)	R1 = 0.2506, wR2 = 0.2211	
Largest diff. peak and hole	0.297 and -0.292 $e.Å^{-3}$	

3.7.4 **Hyper-Rayleigh scattering data:**

All HRS measurements were performed by Prof David Shelton (Department of Physics, University of Nevada, Las Vegas, NV).

The β values for the chromophores in CDCl3 solution were determined from hyper-Rayleigh scattering (HRS) measurements at a laser wavelength of 1064 nm (using a pulsed Nd:YAG laser) and sample temperature 25°C. Calibration of the HRS results used 4-nitroaniline (pNA) in CDCl3 solution as a reference standard. Dilute solutions of pNA (36.4mM), **TCP-1** (12μM), **TCP-Me** (35.3μM), **TCP-Ph** (36.1μM) and **TCP-PhF** (36.6μM) in $CDCl_3$ were freshly prepared for each measurement. The solution concentrations were chosen to give comparable signals for the chromophore and reference solutions, and the much smaller HRS signal measured for the neat solvent was subtracted. Sample and reference HRS signals were compared using the same laser focusing, collection optics and polarization configuration, using apparatus and techniques as previously described[15]. The laser power incident on the sample was adjusted without affecting the alignment or focusing of the laser beam using a half-wave plate and polarizer combination.

The 532 nm (second harmonic wavelength) HRS light is absorbed by the sample along the 1.5 mm path from the laser focus to the exit window of the cuvette. The self-absorption correction was determined using the 532 nm absorbance measured for the sample in the 10 mm sample cuvette.

The HRS signal at 532 nm selected by the 60 cm^{-1} bandpass filter may be contaminated with two photon fluorescence (2PF). The fraction of the total signal due to HRS is determined from a spectral scan, where the HRS and 2PF appear as a sharp peak and a flat background, respectively. The 2PF contribution was less that 7%.

HRS signal S is measured versus laser power P and S/P^2 is extrapolated to $P = 0$. This extrapolation is necessary since weak absorption of the focused laser beam in the sample heats the sample along the beam path, defocuses the beam, and reduces the HRS signal. In the absence of this thermal lens effect S/P^2 is independent of P. In the usual case of weak linear absorption by the sample at the laser wavelength the extrapolation is done by fitting $S/P^2 = A(1 - B \times P)$ to the data.

Sample	Conc μM	A_{532nm}	F = HRS/total	T(z)	S/P^2 (cps/W^2)	D (cps/W^2)	E (cps/μM W^2)	β/β_{PNA} ±2%
TCP-1	12.0	0.011	0.933(2)	0.966	3897(62)	3350	279.13	42.0
TCP-Me	35.5	0.025	0.972(1)	0.991	6094(34)	5676	160.80	31.9
TCP-Me	39.2	0.032	0.972(1)	0.989	6838(96)	6420	163.76	32.2
TCP-Ph	36.1	0.054	0.947(1)	0.982	10188(77)	9524	263.82	40.8
TCP-PhF	36.6	0.034	0.941(1)	0.989	11595(125)	10731	293.20	43.0

HRS Data Table For TCP-Me, TCP-Ph and TCP-PhF

A_{532}= absorbance at 532 nm for 1 cm of solution.

$T(z) = 10^{-Az}$

S/P^2 = power-normalized HRS signal extrapolated to $P^2 = 0$

$D = [(F/T)(S/P^2) - (S/P^2)_{CDCl3}]$

$E = D/conc$

$\beta/\beta_{PNA} = (E/E_{PNA})^{1/2}$

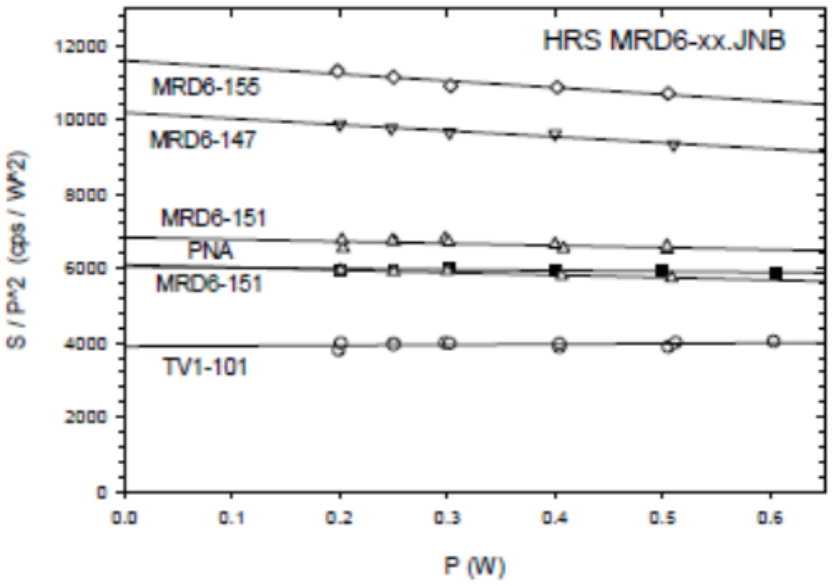

S/P^2 versus P for TCP-1 (TV1-101), TCP-Me (MRD6-151), TCP-Ph (MRD6-147) and TCP-PhF (MRD6-155)

The experimental static hyperpolarizability ratios, $\beta_{HRS(0)}/\beta_{pNA(0)}$ were extrapolated from the frequency dependent ratios, $(\beta_{HRS}/\beta_{pNA})_{1064}$ using the two level model (TLM) equation developed by Oudar and Chemla . Extrapolation to the static becomes increasingly unreliable however as resonance is approached as line broadening effects need to be taken into account. A correction factor known as thus applied to the TLM equation to give the damped two level model dispersion fit shown by **equations 2.1** and **2.2**:

$\beta^{SHG}(\omega,\omega_{eg},\gamma) = g(\omega,\omega_{eg},\gamma) * \beta^{HRS}(0)$	…….(2.1)
$g(\omega,\omega_{eg},\gamma) = \frac{\omega_{eg}^{\ 2}}{3}\left\{\frac{1}{(\omega_{eg}+i\gamma+2\omega)(\omega_{eg}+i\gamma+\omega)} + \frac{1}{(\omega_{eg}-i\gamma-2\omega)(\omega_{eg}-i\gamma-\omega)} + \frac{1}{(\omega_{eg}+i\gamma+\omega)(\omega_{eg}-i\gamma-\omega)}\right\}$	…….(2.2)

Compound	$(\beta_{HRS}/\beta_{PNA})_{1064}$	$\beta_{HRS(0)}/\beta_{PNA(0)}$
	Experimental	Experimental
pNA	1	1
TCP-1	42	38.37
TCP-Me	32	27.67
TCP-Ph	40.8	35.71
TCP-PhF	43	37.63

Experimentally obtained Frequency Dependent β_{HRS}/β_{pNA} Values and the Corresponding Extrapolated Static $\beta_{HRS(0)}/\beta_{pNA(0)}$ Values

The experimentally obtained value for β_{HRS} at 1064 for 4-nitroaniline, 11.4×10^{-30} was used to convert the $(\beta_{HRS}/\beta_{pNA})_{1064}$ ratios to $\beta_{HRS(1064)}$ for both molecules. The static $\beta_{HRS(0,TLM)}$ value for pNa 6.29×10^{-30} was extrapolated using the TLM expression in a fashion similar to that described above. This value was used multiplied with the $\beta_{HRS(0)}/\beta_{pNA(0)}$ values to give the static hyperpolarizibilities for both molecules. These results are tabulated below:

Compound	$\beta_{HRS(1064)}$ (10^{-30} esu)	$\beta_{HRS(0,TLM)}$ (10^{-30} esu)
	Experimental	Experimental
pNA	11.4	6.2902
TCP-1	479	241.35
TCP-Me	365	174.03
TCP-Ph	465	224.61
TCP-PhF	490	236.72

Frequency dependent $\beta_{HRS(1064)}$ and static $\beta_{HRS(0,TLM)}$ values

3.8 **References:**

(1) Carboni, R. A. 5-Cyanomethylene-2-oxo-3-pyrrolines. US 3013013, December 12, 1961.

(2) Cavanagh, D.; James, M. R.; Meyrick, B. H.; Wight, P. Pyrrolinone or -thione dyes with dicyanomethylene substituents, their mixtures, and their use in dyeing textiles. WO 9410248 A1, May 11, 1994.

(3) Li, D.; Zhao, M. Preparation methods of pyrrolinone dye compound and intermediate thereof. CN103232376 (A), August 7, 2013.

(4) Matsumoto, H.; Imai, H.; Tada, S. Process for manufacture of pyrroline derivatives as dyes for plastics and hydrophobic fibers. DE 3716840 A1, November 26, 1987.

(5) Akahori, K.; Nishikuri, M.; Nakamatsu, T. Dyeing or coloring by heterocyclic compounds. JP 60156760 A, August 16, 1985.

(6) Shuttleworth, L.; Mcmanus, M. J. In situ dye generation for thermal transfer printing. US5011811 (A), April 30, 1991.

(7) Matsumoto, H.; Imai, H.; Hirasawa, Y. Ink sheet for sublimation-type thermal-transfer recording process. JP 01042286 A, February 14, 1989.

(8) Maeda, S.; Kurose, Y.; Ozawa, T. Cyanomethyleneoxopyrroline dye optical information recording material., September 24, 1987.

(9) Nishigaki, J.; Yabuki, Y. Merocyanine photographic dyes and their manufacture. JP 09255883 A, September 30, 1997.

(10) Kaneko, A.; Lu, Z.; Wang, H.; Tweig, R. J.; Mao, G.; Singer, K. D.; Kaino, T. *Nonlinear Opt. Quantum Opt. Concepts Mod. Opt.* **2005**, *34*, 45–48.

(11) Jang, S.-H.; Luo, J.; Tucker, N. M.; Leclercq, A.; Zojer, E.; Haller, M. A.; Kim, T.-D.; Kang, J.-W.; Firestone, K.; Bale, D.; Lao, D.; Benedict, J. B.; Cohen, D.; Kaminsky, W.;

Kahr, B.; Brédas, J.-L.; Reid, P.; Dalton, L. R.; Jen, A. K.-Y. *Chem. Mater.* **2006**, *18*, 2982–2988.

(12) Leclercq, A.; Zojer, E.; Jang, S.-H.; Barlow, S.; Geskin, V.; Jen, A. K.-Y.; Marder, S. R.; Brédas, J. L. *J. Chem. Phys.* **2006**, *124*, 044510.

(13) Cho, M. J.; Lee, S. K.; Choi, D. H.; Jin, J.-I. *Dyes Pigments* **2008**, *77*, 335–342.

(14) Cho, M. J.; Lim, J. H.; Hong, C. S.; Kim, J. H.; Lee, H. S.; Choi, D. H. *Dyes Pigments* **2008**, *79*, 193–199.

(15) Shelton, D. P. *Rev. Sci. Instrum.* **2011**, *82*, 113103–113103–6.

(16) Oudar, J. L.; Chemla, D. S. *J. Chem. Phys.* **1977**, *66*, 2664–2668.

Vita

Meghana Rawal was born in Srinagar, India. She was raised in Pune, India, a city known for both its quality and quantity of academic and research institutes. Her father being a molecular biologist, she grew up in a scientific environment that encouraged curiosity and rational query. Her interests in school included Kathak, an Indian classical dance form and Karate. She competed and won accolades in state and district level martial arts tournaments. Due to an interest in polymers, she pursued an engineering degree and graduated first class with a BE (Polymers) from the Maharashtra Institute of Technology in 2003. In her senior year she and a few classmates spearheaded the organization of a student led national conference for undergraduates in polymers and macromolecules called Affinity 2003. Her final year project at the National Chemical Laboratory (NCL) exposed her to a world at the cross roads of polymers and nano-technology. After graduation she worked as a research assistant in the Polymer Science and Engineering department at NCL, developing synthetic methodologies for generation of meso-porous silica through polymerization. This created an interest in organic synthesis which culminated in a Ph.D. in December 2013 under Prof. Larry R. Dalton at the University of Washington, Seattle. She was the recipient of the B. Seymour Rabinovitch Graduate Student Fellowship Award in 2004. While in graduate school, she continued to pursue her passion for Kathak and her interest in martial arts training morphed into one in yoga. She intends to continue research either in academia or the industry in organic electronics and polymers.